

National Academy of Sciences of Ukraine
Ministry of Education and Science of Ukraine
Institute for Scintillation Materials NASU
O.Ya. Usikov Institute for Radiophysics and Electronics of the NASU
IV. E. Lashkaryov Institute of Semiconductor Physics NASU
Institute of Physics NASU
Kharkiv National University of Radio Electronics
V. N. Karazin Kharkiv National University
National Technical University of Ukraine
“Igor Sikorsky Kyiv Polytechnic Institute”
Odesa I.I. Mechnikov National University
Ukrainian Physical Society

Collection of Scientific Works

X INTERNATIONAL SCIENTIFIC CONFERENCE

Functional Basis of Nanoelectronics

September 16-21
Kharkiv – Odesa
2019

X International Scientific Conference “Functional Basis of Nanoelectronics”
Collection of Scientific Works. – Kharkiv, 2019. – 178 p.

Scientific works of the X International Scientific Conference “Functional Basis
of Nanoelectronics” are included in the Collection

Program Committee of the Conference

Program Committee Co-Chairs:

Ya.I. Lepikh	Prof., Dr., Odesa I.I.Mechnikov National University, Odesa, Ukraine
M.I. Slipchenko	Prof., Dr., Leading researcher, ISMA NASU, Kharkiv, Ukraine
S.I. Tarapov	correspondent member of NASU, Prof., Dr., O.Ya. Usikov Institute of Radio Physics and Electronics NASU, Kharkiv, Ukraine

Program Committee Members:

N.A. Azarenkov	Academician of the NASU, Prof., Dr., Vice-Rector of the V.N. Karazin Kharkiv National University, Kharkiv, Ukraine
A.E. Belyaev	Academician of the NASU, Professor, Director of the V.E. Lashkaryov Institute of Semiconductor Physics NASU, Kyiv, Ukraine
I.N. Bondarenko	Professor, Head of Dep. in Kharkiv National University of Radio Electronics, Kharkiv, Ukraine
Yu.E. Gordienko	Professor of Kharkiv National University of Radio Electronics, Kharkiv, Ukraine
Z.Yu. Gotra	Professor, Head of dep. Lviv Polytechnic National University, Lviv, Ukraine
B.V. Grynyov	Prof., Academician of NASU, Director of ISMA NASU, Kharkiv, Ukraine
V. Dyakonov	Prof., Dr., Head of Experimental Physics VI, Julius-Maximilians Universität Würzburg, Germany
I.V. Zavislyak	Professor of Taras Shevchenko National University, Kyiv, Ukraine
V.O. Katrich	Prof., Dr., Vice-Rector of the V.N. Karazin Kharkiv National University, Kharkiv, Ukraine
V.P. Kladko	Correspondent member of the NASU, Prof., Deputy. Director of the V.E. Lashkarev Institute of Semiconductor Physics NASU, Kyiv, Ukraine
V.P. Kostylev	Dr., Head. of the lab. of V.E. Lashkaryov Institute of Semiconductor Physics NASU, Kyiv, Ukraine
V.A. Kochelap	Correspondent member of the NASU, prof., Head of the Department of V.E. Lashkarev Institute of Semiconductor Physics NASU, Kyiv, Ukraine

A.P. Kuznetsov	Professor, Vice-Rector of the Belarusian State University of Informatics and Radioelectronics, Minsk, Belarus
A.L. Kukla	Dr., Head of the Department of the V.E. Lashkarev Institute of Semiconductor Physics. NASU, Kyiv, Ukraine
A.M. Negriyko	Correspondent member of NASU, Deputy Director of the Institute of Physics of NASU, Kyiv, Ukraine
S.L. Prosvirnin	Professor of Radio Astronomy Institute of NASU, Kharkiv, Ukraine
I. Yu. Protsenko	Prof., Dr., Head of dep. of Electronics, General and Applied Physics of Sumy State University, Sumy, Ukraine
F.F. Sizov	Correspondent member of NASU, Prof., V.E. Lashkaryov Institute of Semiconductor Physics NASU, Kyiv, Ukraine
V.A. Skryshevsky	Prof., Head. of dep. of the Institute of High Technologies, Taras Shevchenko National University, Kyiv, Ukraine
B.N. Chichkov	Prof., Dr., Gottfried Wilhelm Leibniz Universität / Institut für Quantenoptik, Hannover, Germany
Yu.I. Yakimenko	Academician of NASU, Professor, Vice-President of NTUU "KPI", Kyiv, Ukraine
V.A. Yampolsky	Correspondent member of NASU, Prof of O.Ya. Usikov Institute of Radio Physics and Electronics NASU, Kharkiv, Ukraine
A. Medvids	Dr., Prof., Riga Technical University, Latvia
E. Sheregij	Dr., Prof., Rzeszow University, Poland
Fukai Shan	Prof., Vice Dean of College of Microtechnology and Nanotechnology, China

**METHODS OF FORMATION,
DIAGNOSIS AND RESEARCH
OF NANOSTRUCTURES**

FORMATION OF SEMICONDUCTOR QUANTUM DOTS FOR ELECTROCHEMILUMINESCENT ASSAY BY LASER FRAGMENTATION

Yu.T. Zholudov^{*}, V.S. Vasylykovskyi⁺, M.I. Slipchenko⁺, O.V. Slipchenko[@], B.N. Chichkov[§]

^{*} Kharkiv National University of Radio Electronics

Nauky ave. 14, 61166, Kharkiv, Ukraine, tel. (057)7020369, E-mail: yurets.zh@gmail.com

⁺ Institute for Scintillation Materials NAS of Ukraine

Nauky ave. 60, 61001 Kharkiv, Ukraine, tel. (057)3410170, E-mail: naukovets.big@gmail.com

[@] V. N. Karazin Kharkiv National University,

Department of physical and biomedical electronics and integrated information technology
Svobody Sq. 4, 61022, Kharkiv, Ukraine, tel. (057)7052030 E-mail: elena.agidel@gmail.com

[§] Leibniz University of Hannover, Institute of Quantum Optics
Welfengarten 1, 30167 Hannover, Germany, tel. +49(511)2771666,

E-mail: chichkov@iqo.uni-hannover.de

The work describes the use of semiconductor quantum dots (QDs) for electrochemiluminescent assay of amine compounds and development of new method for production of shell-free semiconductor nanoparticles using laser fragmentation technique. The strategy of electroanalytical application of QDs is based on electrode modification with polymer films containing CdSe QDs that directly participate in ECL reaction with amine coreactants. We have also described efficient top-down method of fluorescent CdSe nanoparticles synthesis using laser fragmentation of its powder suspension in dimethylformamide, optical properties of produced QDs and discussed the applicability of produced nanoparticles for electroanalytical techniques.

Introduction

The development of new techniques for biologically important substances detection, in particular certain classes of amine compounds, is important considering vital role played by those biological amines in the living organisms. Thus their assay and monitoring are important tasks for biology and medicine, control of foods and beverages quality, pharmacy.

The method of electrogenerated chemiluminescence, also known as electrochemiluminescence (ECL) is a promising detection tool in the analytical chemistry of liquids. In ECL process electrochemically generated intermediates undergo a highly exergonic reaction to produce an electronically excited state that results in light emission. Currently, a number of substances are known as good coreactants for exciting ECL emission in aqueous and nonaqueous media, thus making them good analytes for the detection using ECL method. Among such coreactants are numerous amines, oxalate, peroxydisulfate, hydrogen peroxide and some others [1]. ECL has several attractive features (low background signal, precise control of reaction kinetics by the applied potential, compatibility with solution-phase and thin-film formats) that altogether make it a highly sensitive and selective analytical method.

In order to broaden the application area of ECL assay it is promising to replace commonly used organic luminophores with new emitting species, such as semiconductor QDs. They have a number of advantages over conventional luminophores (broad absorption spectrum, narrow and size dependent luminescence spectrum, high resistivity towards photo bleaching, high quantum yield) making a future assay more efficient and sensitive.

Research on nanomaterials with specific and pre-programmed properties is one of the most expanding fields in nanotechnology, at the crossroad of physics and chemistry and biology. Material properties in this size range are mainly determined by the quantum confinement effects. Ultrapure nanoparticles can be obtained using laser irradiation of solid materials or suspended microsols in liquid media. This green technology has become a reliable

alternative to traditional chemical reduction method for obtaining diverse sorts of nanoparticles. The synthesis enables formation of highly stable nanocolloids, nanoparticle size and size distribution control, and direct surface conjugation during the synthesis using a great variety of raw materials [2].

In this work we have developed an ECL approach for detection of amines of interest that is based on the use of amines as direct coreactants for electrochemical excitation of QDs emission. In this case fluorescent nanoparticles can be incorporated into conductive polymer films at the electrode surface and these modified electrodes can be used as compact and efficient ECL sensors.

Laser fragmentation synthesis of CdSe QDs

Laser ablation in liquids is commonly used to generate nanoparticles of noble metals and certain non-metallic substances in suspensions while the number of works devoted to production of semiconductor nanocrystals using laser ablation or fragmentation is relatively scarce [3]. Since our results indicate a number of advantages from using semiconductor QDs for electroanalysis, we believe that development of new methods for generation of ultrapure nanoparticles free from chemical precursors and byproducts is an important objective.

The fragmentation of CdSe nanoparticles was done using Trumpf TruMicro 5050 pulsed laser. Ultrasonicated suspension of CdSe powder in organic solvent was used as a fragmentation target. The target suspension was irradiated in quartz cuvette with the laser beam focused in the solution bulk. The fragmentation process was accompanied by mixing of the suspension to prevent sedimentation of CdSe powder grains (see scheme in Fig. 1).

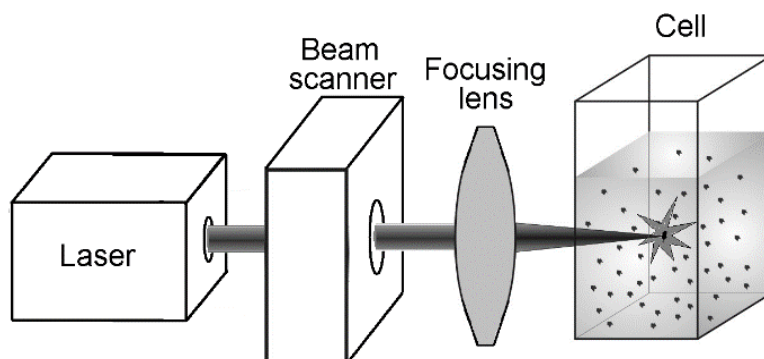


Fig. 1 - Scheme of laser fragmentation experiment

In order to choose appropriate media for laser fragmentation a number of solvents were first tested for their stability under laser irradiation. During preliminary studies several solvents were considered as potential media: nonpolar aprotic (toluene, chloroform, cyclohexane); lowpolar aprotic (dichloromethane); polar aprotic (dimethylformamide); polar protic (methanol, ethanol). These tests revealed strong damage of some solvents. Dimethylformamide (DMF), methanol and ethanol showed minimum changes of optical properties. When excited by 405 nm laser diode DMF showed weak fluorescence, while ethanol and methanol gave no emission.

Preliminary testing of CdSe nanoparticles synthesis revealed that only in DMF a distinct absorbance peak at 405 nm is present. This absorbance peak was rather unstable and was decaying with time. It was also noticed that depending on the concentration of fragmentation products there was different tendency towards aggregation. Flocculation of CdSe nanoparticles was only starting at relatively high concentrations when absorbance peak had value above 1.5 units.

Considering presence of fluorescent products of DMF degradation after laser irradiation in all studies the fragmentation products were removed from the original solution by

centrifugation and redispersed in a new DMF solvent. Obtained quantum dots possess weak broadband fluorescence with the peak position at about 660 nm. The position of absorption peak (~400nm) is characteristic for core-type CdSe quantum dots with the diameter below 2 nm [4].

The stability and fluorescent activity of CdSe nanoparticles in DMF is attributed to their surface stabilization with dimethylamine which is commonly present in DMF as its synthesis reagent and main product of decomposition during storage while it is well known that amines belong to the group of capping ligands that efficiently passivate CdSe surface and block nonradiative recombination centers.

In order to stabilize the properties of produced nanocrystals their surface modification was applied. Substances, commonly used for such purpose, mostly belong to the classes of phosphines and amines. In this study the modification of CdSe quantum dots was performed by trimethylolphosphine (TMP) and oleylamine (OLA) to provide their solubility on polar and nonpolar solvents accordingly. The reaction with TMP and OLA was performed in DMF at room temperature during 24 hours. After that quantum dots were separated by centrifugation and redispersed in appropriate solvent. Nanoparticles covered with OLA showed good solubility in toluene whereas those covered by TMP were well soluble in DMF.

The coverage of nanoparticles significantly enhanced their fluorescence efficiency due to blocking of surface defects. This is common behavior considering extremely high surface to volume ratio of nanoparticles of this size scale when surface states essentially contribute to the overall energetic structure of the nanoparticle. In all cases there was observed a shift of fluorescence maxima towards shorter wavelengths comparing to unmodified samples, especially in the case of modification with OLA.

Fig. 2a shows fluorescence and absorbance spectra of CdSe/ TMP QDs. An essentially stronger influence on both fluorescence and absorbance was found when OLA was used as a surfactant. Fig. 2b shows similar spectra of CdSe/ OLA QDs in toluene. As it is seen from the figure, the absorbance spectra exhibits well resolved narrow peaks corresponding to different energy levels of quantum dot. Also the shift of the fluorescence maxima due to surface passivation in this sample is the highest and emission peak occurs at 565 nm [5].

Due to rather small expected size of obtained CdSe nanoparticles the task of their visualization was rather challenging. Results of TEM study of particles modified with OLA show that due to insufficient contrast and resolution at the limit of microscope capabilities there are only well seen structures of the order of 2-3 nanometers in diameter, whereas diameter calculated on the base of the position of first absorbance peak corresponds to 1.5-1.6 nm.

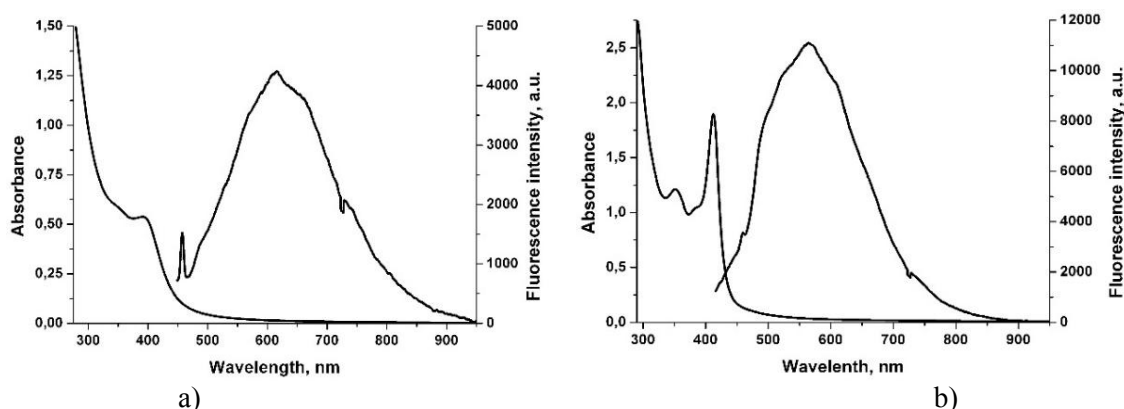


Fig. 2 - Fluorescence and absorbance spectra of CdSe quantum dots modified with a) TMP; b) OLA in DMF excited at 405 nm

ECL sensor for amines detection based on QDs

In analytical sciences there is a trend towards miniaturization of the instruments and their conversion into small, inexpensive and simple sensors. Many expectations for electrochemical and ECL analysis are related with the modification of sensor's electrodes by functional film comprising components for carrying out analytical reaction. The emissive properties of thin film can be achieved by its doping with nanomaterials such as semiconductor QDs acting as either redox mediators or emissive centers. The study was aimed at confirming the idea that polymeric films with CdSe QDs can generate ECL emission in reaction with amine coreactants.

CdSe/ZnS QDs stabilized with TOPO (diameter of 4 nm, $\lambda_{em} = 630$ nm) were deposited on conductive ITO glass substrates by spin coating technique in poly(9,9-di-n-octylfluorenyl-2,7-diyl) (PFO) conductive polymer matrix. ECL experiments were carried in 3-electrode electrochemical cell with film modified ITO glass working electrode, glassy carbon plate counter electrode and Ag/AgCl reference electrode. ECL was excited using cyclic linear potential sweep in phosphate buffer solution (pH = 6.85) as a supporting electrolyte with tripropylamine coreactant using ELAN-3D apparatus.

Fig. 3 shows ECL emission from QDs/ PFO film modified ITO electrode when electrode potential is swept in the 0 - 2.0 V range. The onset of weak ECL emission occurs at a potential of only 1.1V which is probably associated with the TPA oxidation itself while the main emission raise occurs at 1.4V (with peak at 1.55 V) that is probably associated with QDs oxidation. Presented results suggest that CdSe/ZnS QDs participate in redox reaction of oxidation at ITO electrode with further oxidative-reduction type ECL reaction with tripropylamine coreactant. Thus we believe that such QDs/polymer film modified electrodes are suitable for ECL detection of certain amines and for development of analytical ECL procedures on their base.

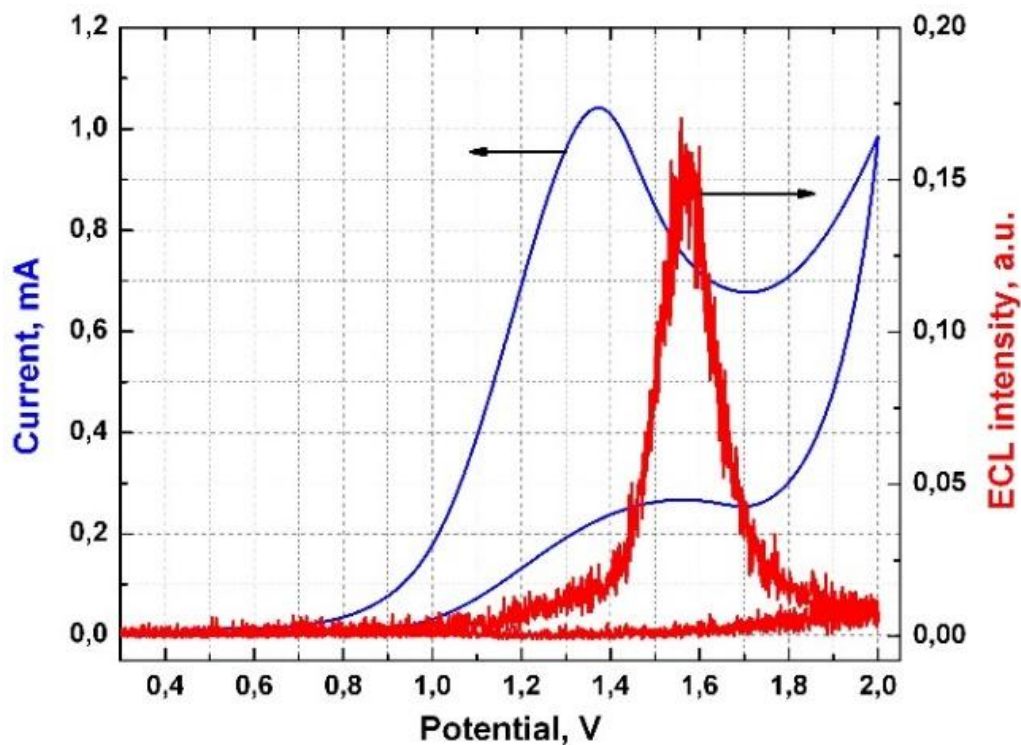


Fig. 3 - Cyclic voltammogram and ECL response from ITO electrode modified with PFO film containing CdSe/ZnS QDs, coreactant: 20 μ M tripropylamine

Conclusion

In this work we have demonstrated an approach for ECL detection of certain amine compounds using semiconductor quantum dots as emitters. We have shown that polymer films containing CdSe QDs can be used as a base for of new analytical ECL procedures and sensors. Feasibility of such approach was verified using ECL reaction with tripropylamine coreactant as a model of amine analyte. We have also shown that laser fragmentation is a new promising method for rapid and efficient production of shell-free semiconductor nanoparticles with high monodispersity and purity that possess unique optical properties and that can find their application in electroanalytical techniques.

Acknowledgment

The work was supported by DAAD grant A/14/02402 and Ostpartnerschaften program and Ukraine - China project M/109-2019 from Ministry of Education and Science of Ukraine.

References

- X1. W. Miao, "Electrogenerated chemiluminescence and its biorelated applications," *Chemical Reviews*, vol. 108, pp. 2506–2553, 2008.
- X2. F. Mafuné, J. Kohnno, Y. Takeda, T. Kondow, and H. Sawabe, "Formation of gold nanoparticles by laser ablation in aqueous solution of surfactant," *The Journal of Physical Chemistry B*, vol. 105, pp. 5114–5120, 2001.
- X3. H. Usui, Y. Shimizu, T. Sasaki, and N. Koshizaki, "Photoluminescence of ZnO nanoparticles prepared by laser ablation in different surfactant solutions," *The Journal of Physical Chemistry B*, vol. 109, pp. 120–124, 2005.
- X4. W. Yu, L. Qu, W. Guo, and X. Peng, "Experimental determination of the extinction coefficient of CdTe, CdSe, and CdS nanocrystals," *Chemistry of Materials*, vol. 15, pp. 2854–2860, 2003.
- X5. Y. Zholudov, C. Sajti, N. Slipchenko, and B. Chichkov, "Generation of fluorescent CdSe nanocrystals by short-pulse laser fragmentation," *Journal of Nanoparticle Research*, vol. 17, 2015.

TECHNOLOGICAL FEATURES FORMATION SPECTRA OF LUMINESCENCE CdS QD

V.A. Smyntyna¹, V.M. Skobeeva², K.A. Verheles¹, N.V. Malushin²

¹ I.I. Mechnikov National University of Odessa, Dvoryanskaya St. 2, 65082 Odessa, Ukraine,
E-mail: klara2010@meta.ua

² I.I. Mechnikov National University of Odessa, Pastera St. 27, 65082 Odessa, Ukraine

It are presented the results influence of two parameters of synthesis process of quantum dots sulfide cadmium (CdS QD) on the spectrum luminescence, namely, the acid-base balance of the growth solution and the correlation of reaction components (cadmium and sulfur salts). Carried out the syntheses in which the pH solution was changed in the interval of values from 2 to 10. There were also synthesized CdS QD with different ratios of the initial components. The results obtained by evidence of the fact that the technological process has a significant impact on the formation of bands luminescence CdS QDs . In both cases, the luminescence spectrum had three bands that are localized at $\lambda_1 = 462 \div 493$ nm, $\lambda_2 = 555 \div 598$ nm, $\lambda_3 = 660 \div 711$ nm. The observed features of the effect of these technological factors on the spectrum luminescence of CdS QDs are explained by the fact that, in the synthesis, the concentration of cadmium and sulfur ions is a determining parameter. In the first case, the ion concentration is controlled by the pH value of the solution, and in the second, by the initial concentration of $\text{Cd}(\text{NO}_3)_2$ and Na_2S .

INTRODUCTION

Semiconductor CdS QDs are cause significant interest due to their unique properties, which are absent in bulk materials due to the effect of quantum limitation of charge carriers. For a number of fields of science and technology, colloidal quantum dots are promising materials. They are of particular interest as a basis for creating biomedical markers and sensors [1].

From the point of view application of quantum dots (QD) of A_2B_6 compounds, their luminescent properties are of the greatest interest. The study of the luminescence of CdS QDs is a fairly large amount of work, however, the question of which luminescence bands are caused by intrinsic and impurity lattice defects and how the technology conditions affect the formation of the luminescence spectrum of CdS QDs remains topical [2]. In modern literary sources, only the possibility of the existence of defects is mentioned, but no attention is paid to the disclosure and description of their nature and the conditions of their creation in the process of synthesis [3]. This issue also includes the development of controlled synthesis of QDs, during which they form their own defects that determine the luminescence spectrum.

The colloid-chemical synthesis of CdS QDs is influenced by a large number of factors related to the conditions of the synthesis (duration, rate of introduction of the reaction components, temperature of synthesis). The formation of luminescence centers in CdS QDs depends on the concentration of cadmium and sulfur ions and their ratio, as well as on the acid-base balance in an aqueous growth solution. The results of the influence of these factors are presented in this study.

1. DESCRIPTION OF OBJECTS AND METHODS OF RESEARCH

The cadmium sulfide nanocrystals under study were obtained by a chemical method from solutions of cadmium and sulfur salts in a colloidal solution of gelatin. The formation of CdS particles occurs as a result of the exchange reaction: $\text{Cd}(\text{NO}_3)_2 + \text{Na}_2\text{S} \Rightarrow \text{CdS} + 2\text{NaNO}_3$.

The pH value of the solutions was changed by adding a solution of alkali or hydrochloric acid to an aqueous solution of gelatin with cadmium nitrate to obtain the necessary pH values (2 ÷ 10).

The pH value of the solutions was changed by adding a solution of alkali or hydrochloric acid to an aqueous solution of gelatin with cadmium nitrate to obtain the necessary pH values (2 ÷ 10). Samples were also synthesized, in which the concentrations of cadmium and sulfur ions and their ratio changed. The pH value in the synthesis process was constant and was equal to 7. In the course of the study, four combinations of solutions with different ratios of the initial components of cadmium and sulfur were created. The ratio of the molar concentrations of the initial components of $Cd(NO_3)_2 / Na_2S$ was: 1/4, 1/2, 1/1, 2/1. In each of these combinations, the following samples were obtained: with a constant volume of $Cd(NO_3)_2$, namely 5 ml, in each of the four combinations, the volume of injected Na_2S changed: 0.25; 0.5; 1.2; 3, 4 and 5 ml. The luminescence was excited by a LCS-DTL-374QT pulsed laser with a wavelength of 355 nm. Laser power - 35 mW.

2. DESCRIPTION AND ANALYSIS OF RESULTS

2.1. Effect of acid-base balance in aqueous solution with Cd CdS.

It is known that salt solutions are carried out in aqueous solutions. In our case, the hydrolysis of cadmium and sulfate. The molar concentration of ions is calculated by the formulas (1 - 2) and is graphically presented in Figure 1.

$$C_0 = [Cd^{2+}] + Cd(OH)^+ + Cd(OH)_2^0, \quad (1)$$

$$\alpha_1 = \frac{[Cd^{2+}]}{C_{Cd(NO_3)_2}} = \frac{1}{1 + \frac{k_1}{[H^+]} + \frac{k_1 k_2}{[H^+]^2}}, \quad \alpha_2 = \frac{k_1 \alpha_1}{[H^+]}, \quad \alpha_3 = \frac{k_1 k_2 \alpha_1}{[H^+]^2}, \quad (2)$$

where α - is the molar concentration of the components; k - is the ionization coefficient (taken up from the table [4]).

It is seen that at pH values < 8 the concentration of cadmium ions in solution dominates, and up to pH = 6 it remains unchanged. At pH > 6, the concentration of cadmium ions decreases and $Cd(OH)^+$ is formed. At pH value > 9, cadmium hydroxide $Cd(OH)_2$ is formed.

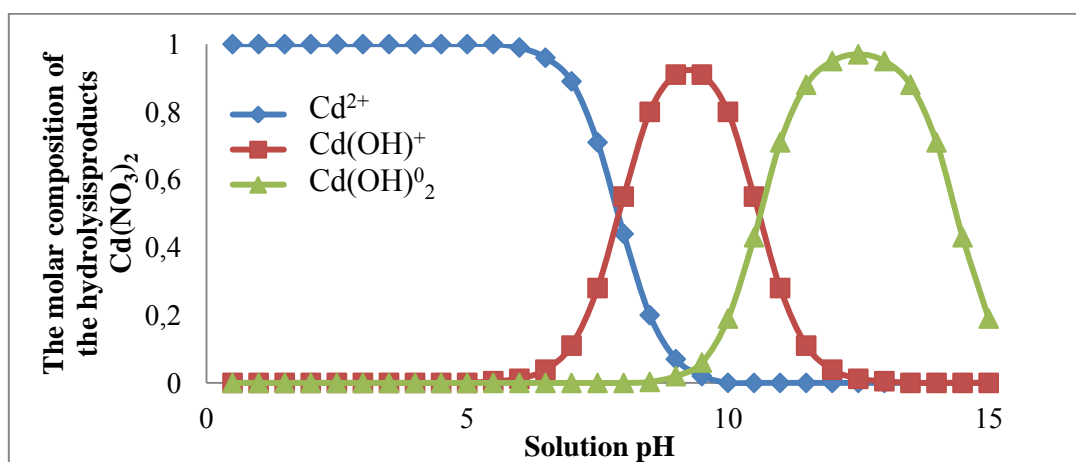


Fig. 1 - Dependence of ion concentration on solution pH

Cadmium sulfide nanocrystals were synthesized at the following pH values of the solution: 2, 4, 7, 10. Regarding the hydrolysis of sulfur sulfide, it is known that the hydrolysis of sulfur salts occurs at pH values > 6 . At lower pH values, the source of sulfur is impurity sulfur, which is present in gelatin.

In fig. 2 shows the normalized luminescence spectra of CdS QDs, which were synthesized at different pH values. It can be seen that the luminescence spectra of samples obtained at low pH (2 and 4) and at pH (7 and 10) differ sharply. At low pH values, the short-wavelength emission band with a wavelength $\lambda_{\max} = (480-490)$ nm dominates, and at large pH, the longwave band, localized at $\lambda_{\max} = (700 - 720)$ nm.

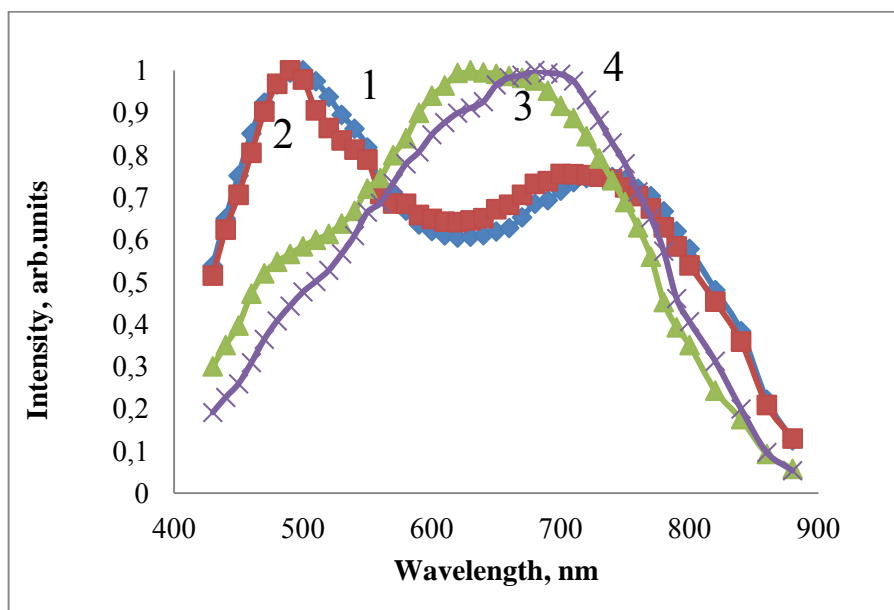


Fig. 2 – Normalized luminescence spectra of CdS QDs grown at different pH values of the solution: 2 (1), 4 (2), 7 (3), 10 (4)

2.2. The effect of the relative concentration of the starting components on the fluorescence spectrum of the QD of CdS

The graphs presented in Figure 3 correspond to the relative concentrations of the $\text{Cd}(\text{NO}_3)_2 / \text{Na}_2\text{S}$ components: 1/4, 1/2, 1/1, 2/1 (Fig. 3 a, b, c, d, respectively). It is seen (Fig. 3 (d)) that with an increase in the concentration of cadmium, the shortwave ($\lambda_{\max} = 490$ nm) band is dominant, and in Fig. 3 (a), where the concentration of cadmium is rather low, this band is hardly noticeable. This confirms the nature of the evolution of the spectra of rice. 3 (a, b, c, d) in which Na_2S was added to the initial solution: 0.25; 0.5; 1.2; 3, 4 and 5 ml, (curves 1-7), respectively. Indeed, it can be seen that the addition of sulfur contributes to an increase in the intensity of the long-wavelength band. In experiments, samples containing a short-wavelength emission band ($\lambda = 462 \div 493$ nm) have an excess of cadmium, and a long-wavelength band ($\lambda = 660 \div 711$ nm) is an excess of sulfur.

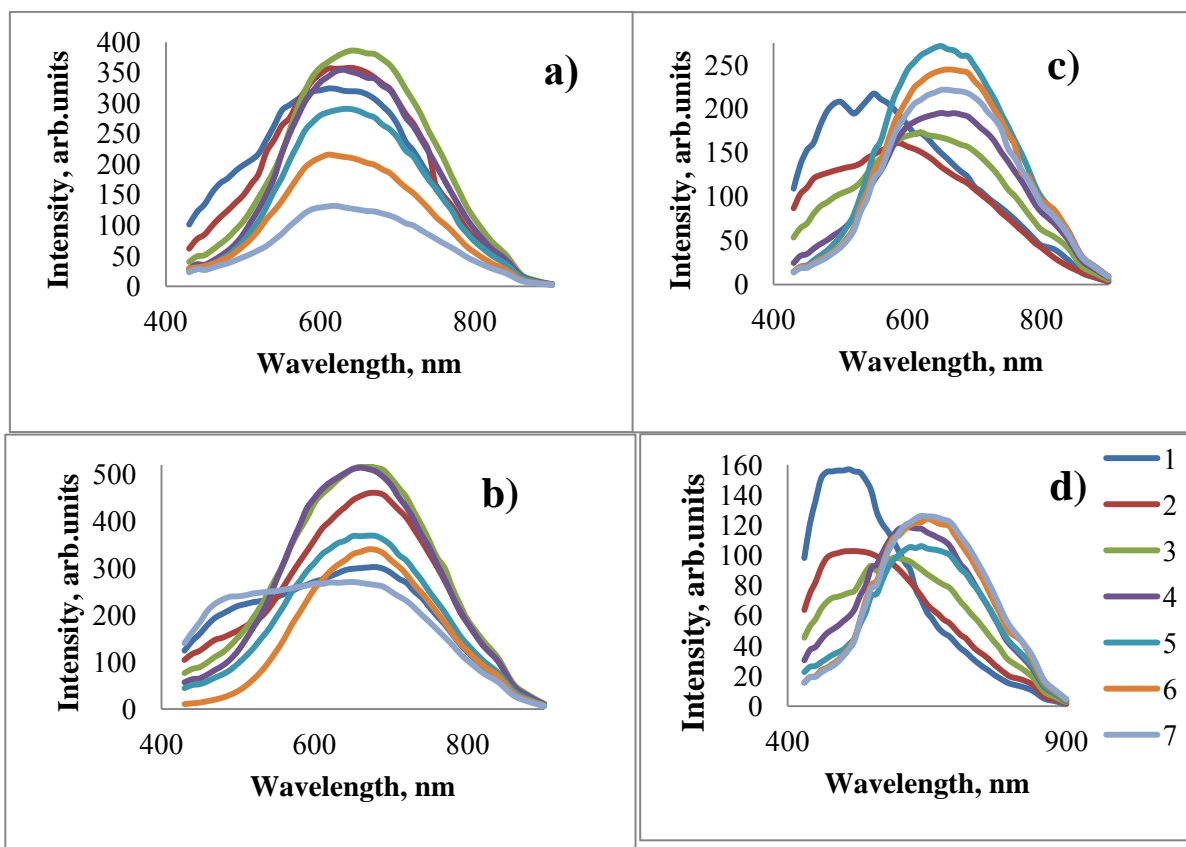


Fig. 3 – Spectrum of luminescence CdS obtained at a molar ratio of the original components of $CdNO_3/Na_2S$: 1/4 (a); 1/2 (b); 1/1 (c); 2/1 (d).

Since the curves of the luminescence spectra in both experiments are complex and consist of several elementary bands, the approximation of the luminescence spectra by Gauss curves was carried out, with the result that three bands of emission in CdS were identified. The results of decomposition are shown in table 1.

Table 1. Dependence of the positions of the maximums of the luminescence bands of QDs, obtained as a result of the decomposition of the spectrum, on the value of the solution and for different ratios of the original components

<i>Effect of acid-base balance in aqueous solution with QDs CdS (Fig. 2)</i>				<i>The effect of the relative concentration of the starting components on the PL of QDs of CdS (Fig. 3)</i>			
<i>pH</i>	λ_1 , nm	λ_2 , nm	λ_3 , nm	$CdNO_3/Na_2S$	λ_1 , nm	λ_2 , nm	λ_3 , nm
2	490	-	716	2/1 (curve 1)	462	555	660
4	493	-	708	1/1 (curve 3)	462	573	690
7	483	592	694	1/2 (curve 5)	464	598	703
10	481	578	703	1/4 (curve 7)	-	593	711

Note that in the photoluminescence spectra of nanocrystals, the band in the region $\lambda = 555 \div 598$ nm is also recorded. This band develops in nanocrystals, the synthesis of which was carried out at the same concentration of cadmium and sulfur ions.

Thus, the above results indicate that the luminescence of CdS QDs obtained by the method of colloidal chemistry due to its own defects and this is due to the influence of the

stoichiometric composition of cadmium and sulfur. Some discrepancy in the localization of the luminescence maxima of individual bands can be explained by the spread in the size of the QD.

CONCLUSIONS

In this work, the influence of two parameters of the process of QD synthesis on the spectrum of their luminescence, namely, the acid-base balance of the growth solution and the ratio of the components of the reaction (cadmium salts of sulfur), is investigated. Syntheses were carried out in which the pH of the solution varied in the range of values from 2 to 10. Also, CdS QDs were synthesized with different ratios of the starting components.

The results obtained indicate that the technological process has a significant impact on the formation of cadmium sulfide QD emission bands. In both cases, the emission spectrum had three bands, which are localized in the wavelength range $\lambda_1 = 460 \div 490$ nm, $\lambda_2 = 555 \div 598$ nm, $\lambda_3 = 660 \div 720$ nm. The observed features of the influence of these technological factors on the luminescence spectrum of CdS QDs are explained by the fact that, in the synthesis, the determining parameter is the concentration of cadmium and sulfur ions. In the first, the ion concentration is regulated by the pH of the solution, and in the second, by the initial concentration of $\text{Cd}(\text{NO}_3)_2$ and Na_2S .

RERERENCE

1. The nature of the luminescence centers in CdS / [VG Klyuev, Fam Thi Khan Mien, Yu. S. Bezdtko] nanocrystals. - Condensed matter and interphase boundaries, V. 16, № 1, 2014. - 27 p.
2. Features of the formation of CdS nanocrystals at a fixed synthesis time / [Yu. S. Bezdtko, V. G. Klyuev]. - Bulletin of VSU. Series: Physics. Mathematics, № 1, 2014. - 6 p.
3. Quantum Dots Synthesized Morphological and Optical Properties of CdS with different pH values / [Akeel M. Kadim, Wasan R. Saleh]. - Iraqi Journal of Science, Vol. 58, No.3A, 2017. – 1207 p.
4. Hydrolysiions of metals in diluted solutions / [V. A. Nazarenko, V. P. Antonovich, E. M. Nevskaya]. - M. : Atomizdat - 1979. - 192 p.

SYNTHESIS AND CHARACTERIZATION OF ORGANIC-INORGANIC PEROVSKITE WITH NON-CONTACT METHODS

V.P. Kostylyov¹, A.V. Sachenko¹, V.M. Vlasiuk¹, S.D. Kobylanska², P.V. Torchyniuk²
¹*V. Lashkaryov Institute of Semiconductor Physics, National Academy of Sciences of Ukraine, 41 pr. Nauki, Kiev 03028 Ukraine, e-mail: vkost@isp.kiev.ua*
²*Vernadsky Institute of General and Inorganic Chemistry, National Academy of Sciences of Ukraine, 32/34 Prospect Palladina, Kiev 03142, Ukraine*

Abstract

Presented in this work are the results of our study of the photoelectric properties of perovskite $\text{CH}_3\text{NH}_3\text{PbI}_{2.98}\text{Cl}_{0.02}$ films deposited on a glass substrate using the spin-coating method. The unit cell parameters of the perovskite are determined using x-ray diffractometry. It is shown that the film morphology represents a net of non-oriented needle-like structures with significant roughness and porosity.

Was shown the non-contact method of spectral characteristics of the low-signal surface photovoltage and the transmission method reveal information about the external quantum yield in the films studied and about the diffusion length of minority carriers in the perovskite films. It has been established that the films obtained are naturally textured, and their bandgap is 1.59 eV. It is shown that in order to correctly determine absorption coefficient and the bandgap values, Urbach effect should be accounted for. Minority carriers' diffusion length is longer than the film thickness, which is equal 400 nm. The films obtained are promising materials for solar cells.

Introduction

The promising candidates that can increasing the efficiency of photovoltaic energy conversion and decreasing the production cost are solar cells (SCs) based on the organic-inorganic chalcogenides of metals with perovskite structure [1]. These are direct-bandgap materials, implying high optical absorption coefficient value. As compared to the traditional SCs based on monocrystalline silicon, their fabrication technology is simpler, because it does not require high temperatures, which reduces the price of these SCs. Besides, during the several years of their investigation, the efficiency of these elements has increased to 20,9% for the SC with the area of 1 cm² and to 22.7% for the area of 0.09 cm²[2].

In this work, it is proposed to use the method of spectral characterization of the small-signal surface photovoltage together with the measurements of the optical properties (transmittance and reflectance) for characterization and development of fabrication technologies of perovskite films of different microstructures. By definition, the small-signal surface voltage V_{ph} is always much smaller than the thermal voltage, $V_{ph} \ll kT/q$, where k is Boltzmann's constant, T is the temperature, and q is the elementary charge. At $T=300$ K, $kT/q = 25.9$ mV.

The methods proposed allow one to establish the mechanism of short-circuit current formation, to obtain the bandgap value in a perovskite film as well as the diffusion length of the non-equilibrium minority charge carriers, and to estimate surface recombination velocity from the short-wavelength part of the photosensitivity spectrum.

Experimental methods

Synthesis method. Lead iodide PbI_2 , methylammonium chloride $\text{CH}_3\text{NH}_3\text{Cl}$ (C.P.), and methylammonium iodide $\text{CH}_3\text{NH}_3\text{I}$ that was pre-synthesized were used as the input reagents. In order to stabilize the perovskite structure, partial replacement of iodine with chlorine was carried out using methylammonium chloride $\text{CH}_3\text{NH}_3\text{Cl}$ (C.P.). Dried dimethylformamide (DMF, C.P.) was used as a solvent.

To obtain the $\text{CH}_3\text{NH}_3\text{PbI}_{2.98}\text{Cl}_{0.02}$ films, the input reagents PbI_2 , $\text{CH}_3\text{NH}_3\text{I}$, and $\text{CH}_3\text{NH}_3\text{Cl}$ were dissolved in DMF in stoichiometric proportions and mixed for 1 hour at 70°C. The synthesis was performed in a dry box. The so obtained transparent solution was then deposited onto a pre-cleaned substrate by spin-coating at 1200 rotations per minute during 30 seconds. Glass or ITO-coated glass (denoted hereafter as ITO/glass) were used as substrates. Thermal treatment of the films was carried out on a pre-heated stove at 90°C for 30 minutes.

The products were characterized by x-ray powder diffraction taken on the apparatus DRON-4-07 (CuK α -radiation, 40 kV, 18 mA) in the $2\theta=10-120^\circ$ range with the step size of $0,02^\circ$ and exposition time of 6 s.

Measurements of the physical characteristics. The spectral characteristics of the surface photovoltage were measured in the wavelength range $\Delta\lambda = 400-900$ nm on the perovskite $\text{CH}_3\text{NH}_3\text{PbI}_{2.98}\text{Cl}_{0.02}$ films deposited on glass with an ITO layer. The measurements were performed at a constant flux of photons of monochromatic light according to ASTM standards [3]. Surface photovoltage measurements were performed with a non-destructive method using a press-on ITO electrode with the area $\sim 7 \times 7$ mm² deposited on mica of ~ 5 μm thickness. The transmission spectra in the wavelength range $\Delta\lambda = 400-900$ nm were measured on the perovskite $\text{CH}_3\text{NH}_3\text{PbI}_{2.98}\text{Cl}_{0.02}$ film samples deposited on glass without an ITO layer. The reflection measurements at the wavelength of 632.8 nm have revealed that reflection had diffusive character, and the reflection coefficient was quite small, estimated to be $\sim 5\%$.

Results and discussion

To determine the unit cell parameters of the $\text{CH}_3\text{NH}_3\text{PbI}_{2.98}\text{Cl}_{0.02}$ material synthesized using the full-profile Rietveld method, the x-ray diffraction patterns of the single-phase samples were used, one of which is shown in Fig. 1. Calculations of the structure parameters indicate that this diffractogram corresponds to the tetragonal symmetry ($I4/mcm$ space group, № 140), which agrees with the literature data.

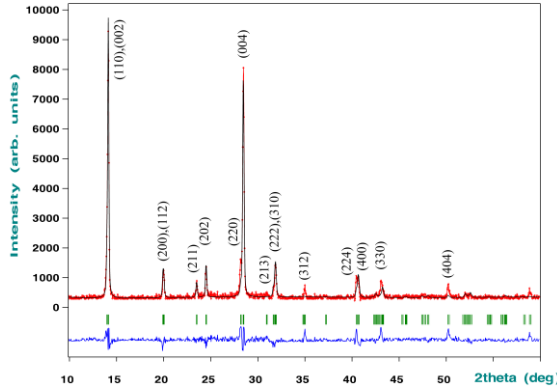


Fig 1 – Experimental (symbols) and theoretical (curves) x-ray diffractograms of a $\text{CH}_3\text{NH}_3\text{PbI}_{2.98}\text{Cl}_{0.02}$ film sample after thermal processing at 90°C . The vertical lines indicate peak locations, with Miller indices given in the brackets. The difference curve is shown below

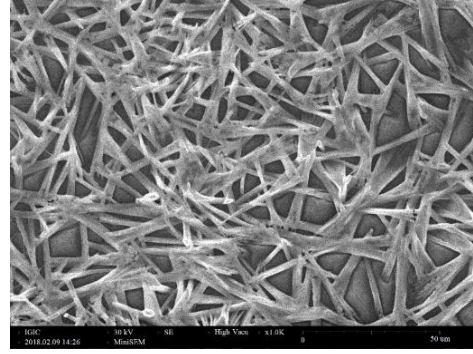


Fig 2 – $\text{CH}_3\text{NH}_3\text{PbI}_{2.98}\text{Cl}_{0.02}$ film microstructure after its thermal processing at 90°C

For the calculations, the atomic coordinates from this work were used for Pb (4c) 000; I1(8h) $xy0$; I2(4a) $00\frac{1}{4}$; C (16l) xyz ; N (16l) xyz . For the $\text{CH}_3\text{NH}_3\text{PbI}_{2.98}\text{Cl}_{0.02}$ film the following lattice parameters were obtained: $a = 0.8870(2)$ \AA , $c = 1.2669(8)$ \AA , $V = 0.9968(7)$ \AA^3 .

The microstructure analysis of the films obtained, see Fig. 2, shows that the ITO/glass substrate is incompletely covered by $\text{CH}_3\text{NH}_3\text{PbI}_{2.98}\text{Cl}_{0.02}$. The film morphology can be described as a net composed of non-oriented needle-like structures with a broad range of length to width ratio and significant film roughness and porosity.

In general, the spectral dependence of the low-signal surface photovoltage $V_{ph}(\lambda)$ can be described as [4]

$$V_{ph}(\lambda) = A(\varphi_s, \lambda)EQE(\lambda) = A(\varphi_s, \lambda) \cdot (1 - R(\lambda))IQE(\lambda), \quad (1)$$

where φ_s is the band bending on the illuminated side of the film, λ is the light wavelength, A is the coefficients with the dimensions of Volts, $\alpha(\lambda)$ is light absorption coefficient, $R(\lambda)$ is the reflection coefficient and $EQE(\lambda)$ and $IQE(\lambda)$ are the external and internal quantum efficiencies of photogeneration.

As shown in [4], the probability of photon absorption increases due to an increase of its path length from the value of $2d$ in a plane-parallel structure to the value of $4n_r^2d$ in a textured structure, which leads to a broadening of quantum efficiency with λ and to its shifting towards the longer wavelengths; it is also occur a reduced reflection coefficient value. It was established in [4] that the absorption edge when the minority carrier diffusion length L is much longer than the film thickness d can be described by the generalized expression

$$IQE(\lambda) = \left(1 + \left(4\alpha(\lambda)d n_r^2 / b\right)^{-1}\right)^{-1}, \quad (2)$$

where $b \geq 1$ is a non-dimensional parameter equal to the ratio of the longest photon path length possible, $4n_r^2$, to its real value. This ratio depends on the texturing quality and film thickness.

Fig. 4 shows the experimental spectral dependence of the absorption coefficient $\alpha(\lambda)$ for the perovskite $\text{CH}_3\text{NH}_3\text{PbI}_3$ obtained in [5].

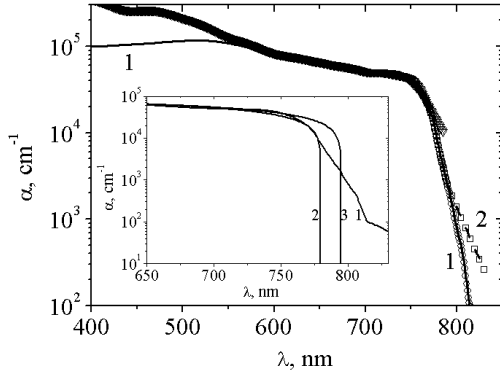


Fig. 3 – Spectral curves of the absorption coefficient in $\text{CH}_3\text{NH}_3\text{PbI}_3$. Curve 2 – Urbach shift. The inset shows the solution of the inverse problem (curve 1) and the results of Eq. (4) with $E_g = 1.59$ eV (curve 2) and 1.56 eV (curve 3)

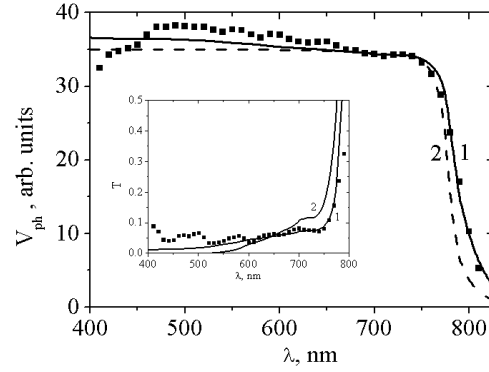


Fig. 4 – Spectral curves of $V_{ph}(\lambda)$ for a film with an ITO layer. Dark circles are the experimental data, curve 1 was obtained theoretically using Eq. (1) and (2), curve 2 was obtained using Eq. (1) and equation for a parallel-plane structure with a single reflection. The parameters used: $d = 400$ nm, $b = 4$. The inset shows transmission spectra

It is well known that the absorption edge in the structurally imperfect films is described by Urbach rule. The empirical absorption coefficient depends on the photon energy in this wavelength range as

$$\alpha_{ur} = \alpha_{ur0} \exp(E_{ph} / E_0), \quad (3)$$

where α_{ur0} is the initial absorption coefficient, E_{ph} is photon energy, and E_0 is the characteristic energy, which is of the order of a few tens of meV for not too big deviations from the perfect films.

Having analyzed the $V_{ph}(\lambda)$ values near the absorption edge, we established that for the films investigated, Urbach parameters are $\alpha_{ur0} = 2.5 \cdot 10^3$ cm^{-1} and $E_0 = 27$ meV. Using the corrected $\alpha(\lambda)$ dependence (Fig. 4, curve 2), we obtain a curve (see squares), which we will use in the theoretical calculations.

Because organic-inorganic perovskites are direct-bandgap semiconductors, the absorption coefficient $\alpha(\lambda)$ near the absorption edge is given by the formula

$$\alpha(\lambda) = B \frac{\left(1240 / \lambda - E_g\right)^{1/2}}{1240 / \lambda}, \quad (4)$$

where B is a constant, E_g is the bandgap value, and λ is the wavelength in nm.

The inset in Fig. 4 shows the using $\alpha(\lambda)$ curve (curve 1), and using the expression (4) for the bandgap value of 1.59 eV (curve 2) and 1.56 eV (curve 3). One can conclude that the bandgap in the films investigated is 1.59 eV.

Shown in Fig. 4 are the experimental and theoretical values of $V_{ph}(\lambda)$ for a film with an ITO layer, obtained using the expression (2) and the generalized value of $\alpha(\lambda)$ (curve 1). As seen from Fig. 4, the experimental $V_{ph}(\lambda)$ values near the absorption edge agree with the theoretical curve 1 very well if we set $d = 400$ nm and $b = 4$.

Thus, it follows from this analysis that the film studied here captures light efficiently due to its natural texturing. This conclusion agrees with the microstructure data, see Fig. 2.

Let us note that the spectral curves of the low-signal surface photovoltage for film illumination from the opposite sides are close to each other. This provides an additional evidence of the high diffusion length (exceeding the film thickness), which, according to literature data, are of the order of 1 μ m in the samples with chlorine added.

Shown in the inset of Fig. 4 are the transmission spectra for a perovskite $\text{CH}_3\text{NH}_3\text{PbI}_{2.98}\text{Cl}_{0.02}$ film without ITO. The respective theoretical formula for a textured structure (with the coefficient b taken into account) is

$$T_t = (1 - R) \left(1 + (\alpha(\lambda) l_{ph}(d, b)) \right)^{-1}, \quad (5)$$

where $l_{ph}(d, b)$ – photon free path.

The agreement between experiment and theory is quite good in the wavelength range from 500 nm to 800 nm for a film without the ITO layer using the generalized value for $\alpha(\lambda)$ and the values $d = 400$ nm and $b = 4$ (curve 1). However, the transmittance according to the theoretical formula for the plane structure (curve 2) gives no agreement between theory and the experiment in the whole spectral range. Thus, the experimental transmission spectra of the film without the ITO layer also confirm that the film is naturally textured.

Conclusions

The efficiency of the method of surface photovoltage spectral dependence was demonstrated together with the measurements of the optical properties (transmittance and reflectance) for the characterization of perovskite films. In particular, the methodology proposed allows one to consistently determine the bandgap value of a perovskite film, as well as its minority carriers diffusion length in the case $L \leq d/3$ or to estimate its value in the opposite case.

As a detailed analysis of the absorption coefficient has shown, in the films mentioned above, Urbach effect plays an essential role near the absorption edge. One can obtain good agreement of the theory with experiment and to deduce an accurate value of the perovskite film bandgap of 1.59 eV only by taking this effect into account.

It has been established that the films studied are naturally textured and that the diffusion length of the non-equilibrium charge carriers in the $\text{CH}_3\text{NH}_3\text{PbI}_{2.98}\text{Cl}_{0.02}$ perovskite films exceeds the film thickness. This is also supported by the results of a comparison between the spectra of the low-signal surface photovoltage obtained when the film was illuminated from the opposite sides.

References

1. M.A. Green, A. Ho-Baillie, H.J. Snaith, Nature Photonics, 8, 506 (2014)
2. Green MA, Hishikawa Y, Dunlop ED, Levi DH, Hohl - Ebinger J, Ho - Baillie AWY. Solar cell efficiency tables (version 51). Prog. Photovolt. Res. Appl. 2018;26:3–12.
3. Standard test methods minority carrier diffusion length in extrinsic semiconductors by measurement of steady-state surface photovoltage. Annual book of ASTM standards 10.05, F 391-96. – 1996. – P. 150-158.
4. A.V. Sachenko, V.P. Kostylyov, A.V. Bobyl, V.M. Vlasyuk, I.O. Sokolovskyi, E.I. Terukov, and M. Evstigneev, Technical Physics Letters, 43 (7), 633 (2017).
5. Stefaan De Wolf, Jakub Holovsky, Soo-Jin Moon, Philipp L per, Bjoern Niesen, Martin Ledinsky, Franz-Josef Haug, Jun-Ho Yum, and Christophe Ballif.- J. Phys. Chem. Lett.- 2014, 5, 1035–1039.

MOBILE COMBINED PHOTOVOLTAIC / WIND POWER STATION FOR POWER SUPPLY OF ELECTRONIC EQUIPMENT IN THE FIELD CONDITIONS

R.M. Korkishko, V.M. Vlasyuk, B.F. Dvernikov, V.V. Chernenko and V.P. Kostylyov
V. Lashkaryov Institute of Semiconductor Physics NAS of Ukraine,
03680 Kyiv, Ukraine, e-mail: *romkin.ua@gmail.com*

Introduction

Solar photovoltaic power stations, which operate on the principle of direct conversion of solar energy into electrical energy, are reliable, highly efficient, compact energy sources in the absence of stationary electrical networks. The analysis of proposals for mobile solar power station [1-5] has shown that their main disadvantage is a rather significant duration of charge (exceeding 10 hours) of low-power equipment, even at a high level of energy illumination, due to insufficient output power of solar panels. Such devices do not have an internal buffer accumulator that accumulates energy during the day. And then it allows to carry out power supply or charging low-power equipment at low light (at night). Also, the low reliability of the design, does not allow to effectively use them in the field.

The purpose of this work is the development and manufacture of a mobile combined photovoltaic / wind power station that provides power or charging a wide range of low-power equipment (laptops, radio stations, smart phones, tablets, dosimeters, etc.) in extreme conditions, even at low energy levels that is an advantage over the range of chargers on the market.

Results and discussion

The power station relates to the field of renewable energy sources, the principle of which is based on the combined use of direct conversion of solar energy and wind energy into electrical energy, namely to mobile devices based on semiconductor photoelectric converters and a wind generator, which are designed to charge batteries with a rated voltage of 4 up to 12 V and power supply of a wide range of low-power equipment in field conditions. Such devices can be used by employees of the State Service of Ukraine for Emergencies, the Ministry of Internal Affairs, members of the Armed Forces of Ukraine, tourists, geologists and representatives of other professions, in the absence of access to centralized power supply.

The problem is solved in that the mobile combined photovoltaic / wind power station for powering and charging equipment in the field, contains a semiconductor photovoltaic module and a wind generator placed on the mast. The power station differs from analogs in that additionally contains a rechargeable battery, a charge controller for powering the photovoltaic module, the output of which is connected to a rechargeable battery and a charge controller for powering the wind generator, the output of which is also connected to a rechargeable battery and contains a car coaxial connector, which is connected with the output of the battery. For visual inspection of the battery capacity, the power station additionally contains a digital display unit, the output of which is connected to the battery, and the battery, charge controllers and digital display unit and their connections are placed in a sealed metal case of the photovoltaic module. The digital display screen is displayed on its outer surface. Photovoltaic modules of a mobile combined photovoltaic / wind power station are made in the form of a book. And the mast on which the wind generator is located is made folding.

In fig. 1 shows a block diagram of a device that includes: 1 – a semiconductor photovoltaic module that directly converts the energy of solar radiation into electrical energy; 2 – a photovoltaic module charge controller, which provides control over charging / discharging a battery from a photovoltaic module; 3 – a wind generator that converts the energy of air

masses into electrical energy; 4 – charge controller of the wind generator, which provides control of the charge / discharge of the battery from the wind generator; 5 – rechargeable battery; 6 – digital display unit that implements the function of indicating the current capacity of the battery; 7 – output coaxial automotive connector for connecting the load through the appropriate adapter.

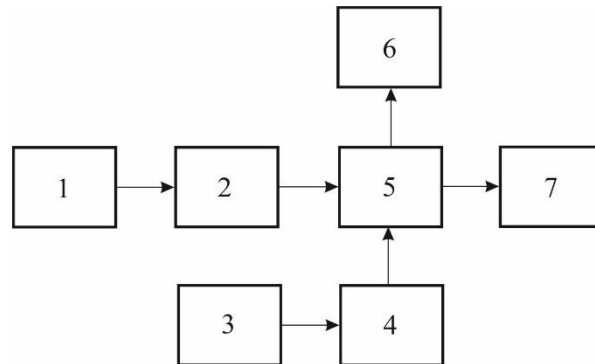


Fig. 1 – The block diagram of a mobile combined photovoltaic / wind power station, where: 1 – semiconductor photovoltaic module; 2 – photovoltaic module charge controller; 3 – wind generator; 4 – wind generator charge controller; 5 – rechargeable battery; 6 – digital display unit; 7 – output coaxial automotive connector

The proposed power station works as follows. Solar radiation hits the photoactive surface of a semiconductor photovoltaic module (1), where direct conversion of solar radiation into electrical energy occurs. Further, the received energy through the charge controller from the photovoltaic module (2) is supplied to the battery (5). In the presence of wind, energy is obtained from the wind generator (3). The received energy through the charge controller from the wind generator (4) goes to the battery (5). When this happens charging the battery. The capacity of the battery can be visually monitored using a digital display unit (6). The battery in turn is connected to the original coaxial car connector (7). The connector terminals serve as terminals for connecting the load through the appropriate adapter.

To implement the technical solution, a mobile combined photovoltaic / wind power station was assembled according to the scheme shown in Fig. 1. The appearance of the mobile combined photovoltaic / wind power station in its “working” state is shown in Fig. 2. The device uses a semiconductor photovoltaic module with a power of 40W (power is indicated for standard measurement conditions: energy illumination 1000 W/m², temperature 25 °C), which is made in the form of a book, overall dimensions 530x470x75 mm (folded). The photoactive surface of the photovoltaic module is protected by hardened glass. The wind generator with a horizontal axis of rotation is made in the form of a folding mast on which the gondola is fixed. On the gondola there is a 40W generator, overall dimensions 1200x540x500 mm (when folded). The base of the generator is fixed with three removable blades. The diameter of the wind wheel is 1100 mm. Orientation in the direction of the wind is carried out by means of a weather vane, which is also fixed on the gondola.

On the case of the wind generator is fixed metal carrying handle. When installing a wind generator, the mast is expanded and fixed with the help of three special steel stretch marks. The height of the mast in the unfolded form is 3000 mm. The case of the photovoltaic module contains a charge controller for powering the photovoltaic module, a charge controller for powering a wind generator, a rechargeable battery (LiPo) with a capacity of 20 Ah, which allows powering or charging low-power equipment even at night when there is no wind. Visual

inspection of the battery capacity is carried out using a digital display unit. As an output connector, a coaxial automotive connector is built into the housing of the photovoltaic module. Each connector is closed with a sealed cover to prevent moisture and dust from entering. The connector terminals serve as terminals for connecting the load through the appropriate adapter. At the output of the coaxial automotive connector, the nominal voltage is 12 V. If it is necessary to obtain alternating voltage, a 12/220 V portable inverter can be connected. The corresponding adapters and inverters are commercially available for vehicles and are selected depending on the specific needs of the user.



Fig. 2 – Appearance of mobile combined photovoltaic / wind power station in its “working” state

From the back side, the housing of the photovoltaic module is protected by metal aluminum plates 2 mm thick, which increase the rigidity and reliability of the design. All folding parts, including connectors, are sealed with a wear-resistant sealant, which prevents moisture and dust from entering the body. A metal carrying handle and a clasp are attached to the case.

The power station is adapted to power and charge a wide range of low-power equipment (laptops, radio stations, smart phones, tablets, dosimeters, etc.) in field (extreme) conditions. In

this case, the weight of the device is 20 kg, and the overall dimensions in the folded state: the photovoltaic part is 530x470x75 mm, the wind generator is 1200x540x500 mm.

Conclusions

This paper presents the results of the development and manufacture of a mobile combined photovoltaic / wind power station that provides power or charging a wide range of low-power equipment (laptops, radio stations, smart phones, tablets, dosimeters, etc.), in extreme conditions, even at low energy levels light, which is an advantage over a number of chargers on the market. Due to the fact that the device uses a rechargeable battery, it improves the efficiency of the device, since it can provide power or charging low-power equipment even at night in the absence of wind. The device uses a battery charge controller to power the photovoltaic module and a wind generator, which prevents the battery from completely discharging or recharging. An indication of the capacity of the battery, which allows you to visually monitor the capacity of the battery, is implemented. All electronic components are located in a sealed metal case of a photovoltaic module, which provides high mechanical strength and prevents ingress of moisture and dust inside, which significantly increases the reliability and mobility of the device. The photovoltaic module and wind turbine mast are collapsible, which significantly increases the mobility of the power station by reducing its size.

Such devices can be used by employees of the State Service of Ukraine for Emergencies, the Ministry of Internal Affairs, members of the Armed Forces of Ukraine, tourists, geologists and representatives of other professions, in the absence of access to centralized power supply.

References

1. Литовченко В.Г. Сонячна енергетика: порядок денний для світу й України / В.Г. Литовченко, М.В. Стріха. - Київ: К.І.С, 2014. - 40 с.
2. Оксанич А.П. Сучасні технології виробництва кремнію та кремнієвих фотоелектричних перетворювачів сонячної енергії / А.П. Оксанич, В.А. Тербан, С.О. Волохов, М.І. Ключ, В.А. Скришевський, В.П. Костильов, А.В. Макаров. - Кривий Ріг: Мінерал, 2010. - 300. - 266 с.
3. Жданович Л.О., Паламарчук І.П., Цуркан О.В., Янович В.П., Вітросонячна електроенергетична транспортабельна установка (ВЕСТРА); Патент України номер 61262, опубл. 11.07.2011, бюл. № 13.
4. Боровий Я.А., Андрєєв О.А., Борова В.Є., Берник В.О., Замлинний В.Ю., Остапін І.С., Сонячна фотоелектрична вітрова електростанція; Патент України номер 93895, опубл. 27.10.2014, бюл. № 20.
5. Щур І.З., Климко В.І., Вітросонячна електростанція; Патент України номер 107030, опубл. 25.05.2016, бюл. № 10.

PHOTOELECTRIC CHARACTERISTICS OF DIFFUSION-FIELD SILICON SOLAR CELLS AT HIGH EXCITATION LEVELS

R.M. Korkishko, V.M. Vlasyuk, V.V. Chernenko, O.A. Serba and V.P. Kostylyov
V. Lashkaryov Institute of Semiconductor Physics NAS of Ukraine,
03680 Kyiv, Ukraine, e-mail: *romkin.ua@gmail.com*

Introduction

The intensive use of traditional fuels and the ever-growing influence of the global environmental crisis have led mankind to search for alternative, environmentally friendly, renewable sources of energy. The active use of alternative energy sources is primarily due to the rise in prices for the extraction of traditional fossil fuels, primarily oil, gas and coal, which are the basis of modern energy. In this regard, all the countries of the world community are paying more and more attention to actively seeking alternative energy supply. [1, 2].

Solar photovoltaic stations, which operate on the principle of direct conversion of solar energy into electrical energy, are reliable, highly efficient, compact sources of energy in the absence of stationary electrical networks. Increasing the efficiency of photoconversion of solar cells (SC), and as a result, reducing the cost of solar power plants is the main and priority direction in the development of solar energy.

The electrophysical, photoelectric, and generation properties of solar cells based on silicon for the case of low excitation levels, when the concentration of nonequilibrium charge carriers Δn is substantially less than the equilibrium concentration n , are studied in sufficient detail

At the same time, photoelectric processes in silicon SCs at elevated excitation levels, when $\Delta n \geq n$, have not been studied sufficiently and a number of problems remain to be solved, which are related to determining the nature and features of the generation-recombination, optical and photoelectric processes in them, in particular in the case of high values of the bulk lifetime of minority charge carriers (diffusion lengths of minority charge carriers in the order, or more than the thickness of the SC), when it is necessary to consider and take into account additional mechanisms of generation-recombination processes, which have so far been neglected due to their smallness compared with the Shockley-Reed-Hall bulk mechanism. Increased excitation levels are realized when silicon SCs are operated in the concentration of solar radiation ($C = 1 \div 200^X$ AM1.5) or in the so-called HITTM (Heterojunction with Intrinsic Thin Layer is a registered trademark of Sanyo-Panasonic) SC based on heterostructures amorphous silicon - crystalline silicon with minimized and surface recombination losses. The open-circuit voltage V_{oc} in such a solar cell reaches 0.75 V.

Fig. 1. illustrates the modes of operation of the SCs, namely: low excitation level, when the criterion is fulfilled $\Delta n = \Delta p \ll n_0(p_0)$, high excitation level, when $\Delta n = \Delta p \gg n_0(p_0)$ and elevated excitation level, when $\Delta n = \Delta p \geq n_0(p_0)$ [3]. To build dependencies $V(N)$, the equation was solved:

$$\Delta p = -\frac{p_0}{2} + \sqrt{\frac{p_0^2}{4} + n_i^2 \exp\left(\frac{qV_{oc}}{kT}\right)}.$$

where is the Δp – excess concentration of charge carriers; p_0 – equilibrium concentration of charge carriers; n_i – intrinsic concentration of charge carriers; q – elementary charge; V_{oc} – open circuit voltage; k – Boltzmann constant; T – thermodynamic temperature.

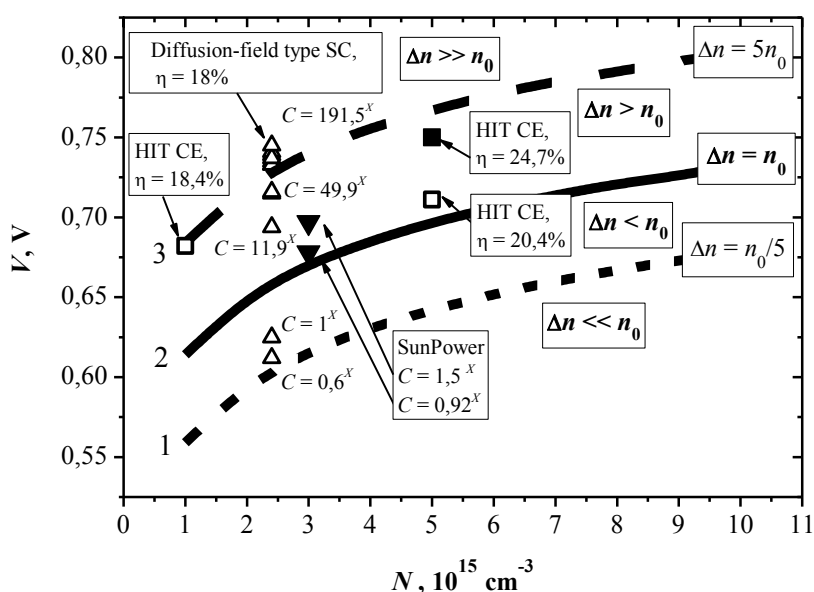


Fig. 1 – Criteria for the implementation of the level of excitation, depending on the level of doping base SC. Where: (curve 1, low excitation level), (curve 2, increased excitation level), (curve 3, high excitation level) [3]

The dots on the graph denote experimental samples that were studied in this work and the record for its time of SCs produced by the Japanese company Sanyo Electric Co. (HIT SCs with an efficiency of 24.7% [4]).

The purpose of this work was to study the features of the work of the developed and manufactured diffusion-field silicon SCs with a concentrated solar radiation of 200^X .

Results and discussion

The study of the photoelectric characteristics of the experimental experimental samples of silicon SCs of diffusion-field type was carried out under the conditions of the natural Sun. The concentration of solar radiation was carried out using the developed setup for conducting phototechnical tests of silicon SCs under AM1.5 spectral conditions, where a Fresnel plastic lens was used as a concentrator. The degree of concentration varied widely $C = 1 \div 200^X$. The results of experimental studies of the light current-voltage characteristics and photoelectric parameters calculated from them – short circuit current I_{sc} , open circuit voltage V_{oc} , fill factor FF , and efficiency η , depending on the degree of concentration of solar radiation are shown in Fig. 2-3.

It should be noted that the SC samples under the AM1.5 conditions were characterized by slightly lower values of the main photoelectric parameters: short circuit current, open circuit voltage, and efficiency. In particular, η , was obtained within 15.5 ÷ 16% (AM1.5) compared with the prototype – space SCs. Such deterioration is caused by a decrease in the relative photoactive area, an increase in the doping level of the emitter (Auger recombination). Reducing the dimensions of the SC to 5×5 mm also led to a decrease in the open circuit voltage, as the proportion of the periphery and its contribution to recombination along the edges of the SC increased.

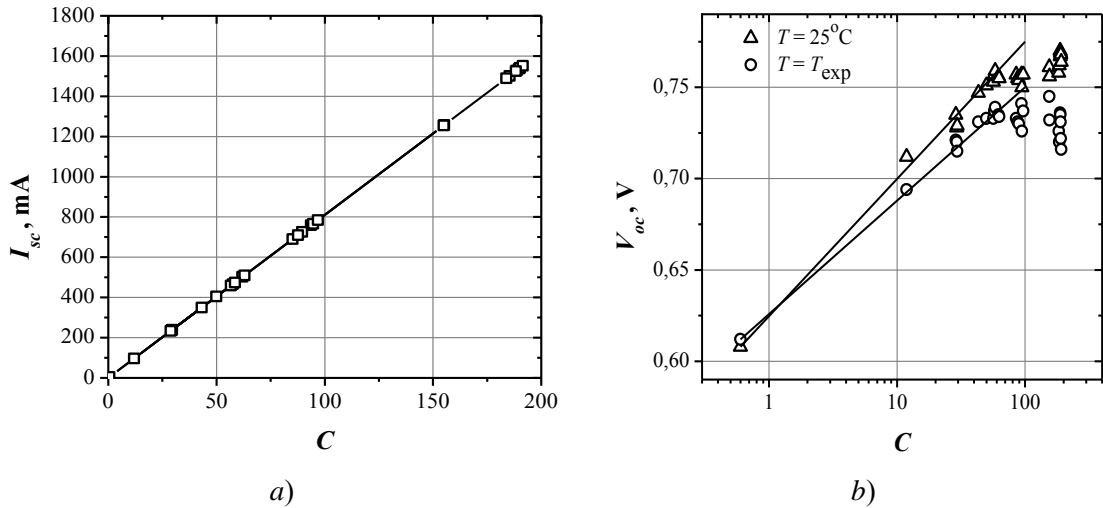


Fig. 2 – Dependence I_{sc} (a) and V_{oc} (25°C) and V_{oc} (T_{exp}) (b) developed SC diffusion-type field of the degree of concentration of solar radiation

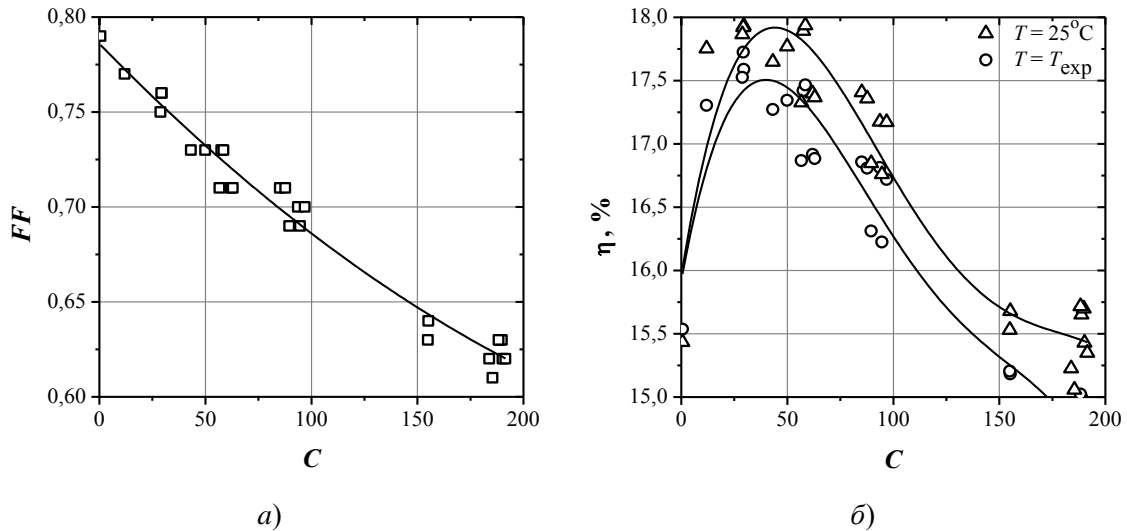


Fig. 3 – Experimental dependencies of FF (a) and η (b) developed by diffusion-field type SEs on the degree of concentration of solar radiation. The theoretical (line) and experimental (dots) dependences for the temperature of the experiment (triangles) and a temperature of 25°C (squares)

From the presented results it can be seen that in the whole range of changes in the level of illumination $C(0,6^X \div 200^X)$, the samples developed by the SCs are characterized by a linear relationship $I_{sc}(C)$ (Fig. 2, a). The dependence $V_{oc}(C)$ shown in Figure 2, b, on the semilogarithmic scale to the degrees of concentration $50^X \div 60^X$ is linear (that is V_{oc} , it depends logarithmically on the degree of concentration) and then stabilizes and then begins to subside. The reason for the decrease in V_{oc} is the effect of heating the sample with concentrated solar radiation, and to a lesser extent, an increase in recombination losses due to Auger recombination through impurity centers involving excitons [5].

As can be seen from Fig. 2, 3, developed by a diffusion-field solar cell based on silicon effectively work in the range of natural solar radiation concentrations of $C = 1 \div 150^X$, while the dependence of photoconversion efficiency (Fig. 3, *b*) and open circuit voltage (Fig. 2, *b*) have the form of a curve a maximum at $C \approx 25^X$. An increase of V_{oc} to values of 0.750 V can be seen, and an efficiency up to 18.1% at $C = 20^X \div 25^X$. The limitation on the value of V_{oc} and its further decline is associated with the effect of heating the sample (Fig. 2, *b*). The efficiency value of the solar cell at $C = 150^X$ is equal to the initial (at $C = 1^X$) value – 15.5%.

Comparison of the simulation results with the results of experimental studies of diffusion-field-type concentrator SCs allows us to conclude that the technological route has been fairly well optimized, which made it possible to implement in practice the value of series resistance close to $0.035 \text{ Ohm}\cdot\text{cm}^2$, as evidenced by the coincidence of theoretical and experimental efficiency photoconversion η at $C \approx 180^X$. The reduced level of η compared with theory in the range of $C = 10^X \div 150^X$ is explained by lower values the initial η (15.5% in the experiment compared to 16.5% in theory) and the effect of the heating of the SC.

Conclusions

In this paper, the results of the study of the photoelectric characteristics of experimental samples of silicon solar cells of diffusion-field type with concentrated solar radiation in the range of $C = 1 \div 200^X$ are presented.

It is shown that such SCs have minimized specific series resistance, close to $0.035 \text{ Ohm}\cdot\text{cm}^2$, which made it possible to obtain high values of operational parameters in the range of natural solar radiation concentrations $C = 1 \div 150^X$.

References

1. Литовченко В.Г. Сонячна енергетика: порядок денний для світу та України / В.Г. Литовченко, М.В. Стріха. – Київ: К.І.С., 2015. – 40 с.
2. Кюрчев В.М. Альтернативне паливо для енергетики АПК: навч. посібник / В.М. Кюрчев, В.А. Дідур, Л.І. Грачова; за ред. В.А. Дідура. – Київ: Аграрна осв., 2012. – 416 с.
3. Процеси фотоелектричного перетворення енергії в кремнієвих фотоперетворювачах при підвищених рівнях збудження / [В.П. Костильов, Р.М. Коркішко, М.В. Герасименко та ін.]. // 7-а Міжнародна науково-технічна конференція «Сенсорна електроніка та мікросистемні технології»: тези доп. – Одеса, 30 травня – 3 червня. – 2016. – С. 77.
4. 24.7% Record efficiency hit solar cell on thin silicon wafer / [A. Yano, S. Tohoda, K. Matsuyama et al.]. // 28th European Photovoltaic Solar Energy Conference and Exhibition. – 2013. – P. 748-751.
5. Сучасні технології виробництва кремнію та кремнієвих фотоелектричних перетворювачів сонячної енергії / [А.П. Оксанич, С.О. Волохов, В.А. Тербан та ін.]. – Кривий Ріг: Мінерал, 2010. – 267 с.

LOW-TEMPERATURE FREEZE-DRYING METHOD FOR THE SYNTHESIS OF ZnO:Mn NANOKRYSTALS

O.V. Kovalenko, V.Y. Vorovsky, M.F. Bulaniy, O.V. Khmelenko, O.I. Kushnerov
Oles Honchar Dnipro National University, 4901072, Dnipro city, Gagarin ave., 72,
dep. Radioelectronics, tel. (056)373-12-63, *E-mail: kovalenko.dnu@gmail.com*

In the work, the NC ZnO and ZnO:Mn with a concentration of Mn 2 and 4 at.% was obtained by the low-temperature freeze-drying method. For this purpose, solutions of zinc acetates $\text{Zn}(\text{CH}_3\text{COO})_2 \cdot 2\text{H}_2\text{O}$ and manganese $\text{Mn}(\text{CH}_3\text{COO})_2 \cdot 4\text{H}_2\text{O}$ were used. By means of XRD, it has been established that nanocrystals (NCs) have a pure phase and wurtzite-type hexagonal lattice, their size is $d \sim 65$ nm. The EPR spectra of the samples have a wide absorption line, which is caused by the presence in the NC of a large number of intrinsic and impurity defects. These defects are the result of the destructive action of hydrogen, which is a product of the thermal decomposition of zinc and manganese acetates. It is shown that there is a relationship between the number of crystal lattice defects in the ZnO:Mn NCs and their ferromagnetic properties at room temperature. Samples of ZnO:Mn with a concentration of Mn 2 and 4 at.%. They have a specific magnetization value of M_s equal to 0.089 and 0.045 emu/g, respectively. The results can have great potential in spintronic devices and spin-based electronic.

Introduction

Diluted magnetic semiconductors (DMS) have unique electrical, piezoelectric, optical and magnetic properties. They can be used in the field of microelectronics and spintronics. To obtain DMS, a nonmagnetic nanocrystalline (NC) semiconductor is required to be doped with a small amount of transition metal admixtures that leads to appearance in this NC of ferromagnetic properties (FP) at room temperature. The main problem of obtaining DMS is to achieve a high degree of homogeneity and purity of the initial product. From this point of view, the freeze-drying synthesis (FDS) has significant advantages, since it allows the components to be mixed at the molecular level at the solution preparation stage, and also ensures high purity of the technological process.

The FDS method is based on the thermal decomposition of salts of the initial components, the solutions of which were previously frozen in the form of small droplets and dried by the sublimation method [1]. It is known that high temperatures of DMS synthesis result in disappearance of FP in the samples. At the same time, the temperatures for the production of NC by the FDS method from inorganic precursors are, as a rule, rather high. So, when using sulfate as initial components, the temperature of NC synthesis exceeds $T = 850$ °C, which leads to the formation of NCs of large sizes and, as a result, to disappearance of quantum-size and FP in the samples. Therefore, there is a need to search for other precursors for low-temperature synthesis of nanomaterials by the FDS method. Possible precursors for low-temperature FDS of ZnO:Mn NCs can be zinc acetates $\text{Zn}(\text{CH}_3\text{COO})_2 \cdot 2\text{H}_2\text{O}$ and manganese $\text{Mn}(\text{CH}_3\text{COO})_2 \cdot 4\text{H}_2\text{O}$, which have the thermal decomposition temperature of $T_d = 325 - 350$ °C [2].

The work purpose was to obtain ZnO:Mn NCs by the low-temperature FDS method and study of their magnetic properties.

Essence

For the synthesis of samples, a 10% aqueous solution of zinc acetate was used, to which an appropriate amount of manganese acetate was added. Thus, the solutions were created to obtain samples of the ZnO and ZnO:Mn NCs with a Mn concentration 2 and 4 at.%. The solutions were sprayed into droplets of size $d = 20-100$ μm, which were then frozen with liquid nitrogen. Drying of the obtained cryogranules was carried out in a sublimation unit during 16 hours [3]. NC synthesis occurred during the thermal decomposition of dry zinc and

manganese acetate salts at a temperature $T = 350\text{ }^{\circ}\text{C}$. The duration of thermal decomposition affects the efficiency of the doping process of ZnO NCs with Mn admixtures, as well as the dimensions of NCs. In order to obtain small sizes of ZnO:Mn NCs, short-term heat treatment was carried out for 20 minutes in air. Examination of the sample by the X-Ray phase method (Fig. 1) made it possible to establish that the ZnO:Mn NCs have a wurzite-type hexagonal lattice.

At the given X-ray diffraction patterns, there are no additional reflections of the products of synthesis. This suggests that the duration of heat treatment (20 minutes) is sufficient for complete decomposition of the initial components. For the ZnO:Mn NC sample under study (4 at.%), the lattice parameters a , c , the average NC size d , and the unit cell volume V were calculated. The following results were obtained: $a = 3.236\text{ }\text{\AA}$, $c = 5.197\text{ }\text{\AA}$, $d = 65, 3\text{ nm}$, $V = 47.14\text{ }\text{\AA}^3$. At the same time, the volume of the unit cell V of the synthesized sample differs significantly from that for single-crystal ZnO, for which $V_m = 47.58\text{ }\text{\AA}^3$. This fact indicates the presence of deformation stresses in the crystal lattice of the ZnO NC. Comparing the X-ray patterns of the synthesized NC and ZnO:Mn NC, obtained by ultrasonic pyrolysis of aerosol [4], we can make conclusion that during the synthesis of NC by low-temperature FDS the solubility of Mn ions in them increases (Fig. 1).

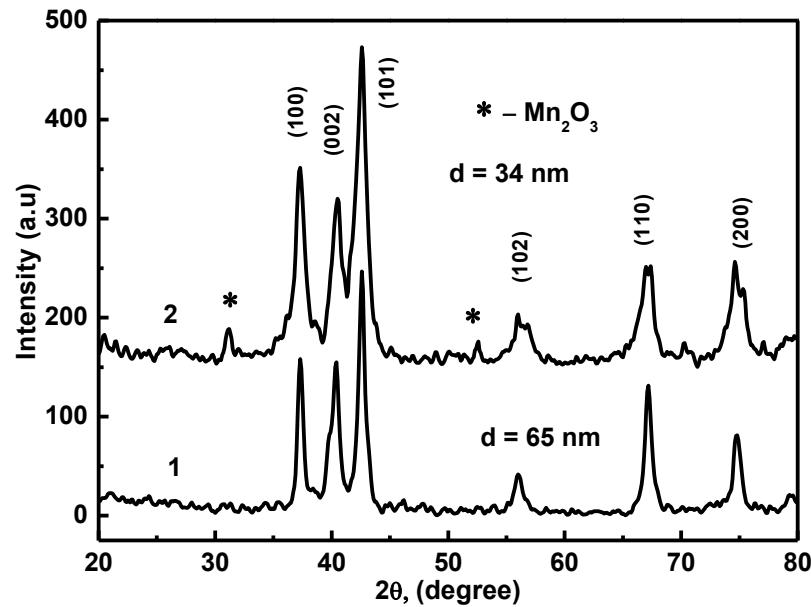


Fig. 1 – X-ray diffraction patterns of samples of ZnO: Mn NC (4 at.%) synthesized by the method: 1 - low-temperature FDS, 2 - ultrasonic pyrolysis of aerosol [4]

The EPR spectra of the synthesized samples (Fig. 2) have a wide asymmetric absorption line of high intensity. In this case, the sample of undoped ZnO has an absorption line of the highest intensity. An increase in the Mn admixture concentration leads to a decrease in the intensity of the broad absorption line and the appearance on it of signs of the presence of lines of the EPR spectrum of the hyperfine structure (HFS) of Mn^{2+} ions. This structure is due to Mn^{2+} ions located at the sites of the ZnO crystal lattice. Annealing the ZnO:Mn sample (4 at.%) at a temperature $T = 550\text{ }^{\circ}\text{C}$ in air for 20 minutes also changes the structure of the EPR spectrum. In it, the intensity of the main absorption line decreases and the intensity of the HFS lines of the Mn^{2+} ions increases. After annealing this sample at $T = 850\text{ }^{\circ}\text{C}$ for 20 min. in its EPR spectrum the wide absorption line completely disappears, only the HFS lines of Mn^{2+} ions remain (Fig. 2a, line 5).

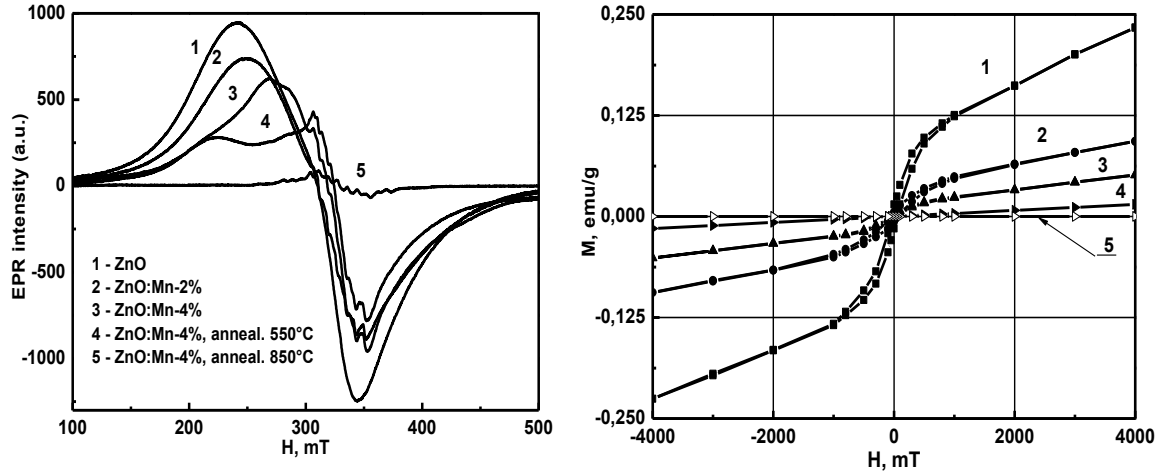


Fig. 2 – EPR spectra (a) and magnetization curves (b) of ZnO and ZnO: Mn NCs: a - ZnO (1), ZnO: Mn with Mn concentration 2,4 at.% (2) and (3) respectively (4) and (5) - sample (3) after annealing for 20 minutes at $T = 550\text{ }^{\circ}\text{C}$ and $T = 850\text{ }^{\circ}\text{C}$, respectively; b - ZnO:Mn with Mn concentration 2,4 at.% - (1) and (2), respectively (3) and (4) - sample (3) after annealing for 20 minutes at $T = 550\text{ }^{\circ}\text{C}$ and $T = 850\text{ }^{\circ}\text{C}$ respectively, (5) - sample (3) after annealing for 1 h. at $T = 850\text{ }^{\circ}\text{C}$

Such a transformation of the EPR spectra in ZnO and ZnO:Mn NCs is caused by the redistribution in the synthesized samples of the concentration of intrinsic defects, such as interstitial zinc (Zn_i), oxygen vacancy (V_o), and OH hydroxyl groups. In the samples of ZnO: Mn NCs, impurity defects are also added to these defects - interstitial manganese (Mn_i) and Mn^{2+} ions, which substitute Zn^{2+} ions isovalently in the ZnO lattice. All these defects are formed as a result of the destructive action of hydrogen, which is a product of the thermal decomposition of zinc and manganese acetates [2]. During prolonged heat treatment of the samples, as a result of recrystallization of the samples and their post oxidation, the concentration of defects in the NC decreases, therefore, only the HFS of Mn^{2+} ions are recorded in the EPR spectra.

It is known that lattice defects play a decisive role in the onset of FP in DMS. In [5], it was shown that FP in ZnO:Mn NCs are due to the presence of intrinsic and impurity defects in them. In this case, intrinsic defects, for example, oxygen vacancies (V_o), act as intermediaries in the exchange interaction between impurity defects as interstitial Mn ions. Therefore, a decrease in the number of participants in the exchange interaction during annealing (vacancies V_o and admixture Mn ions) should lead to a decrease in the FP in ZnO:Mn NC at room temperature. This conclusion is confirmed by our results (Fig. 2b). The absence of a saturation state on the magnetization curves of the samples indicates that, in addition to the ferromagnetic one, there is also a paramagnetic phase, the amount of which is determined by the angle of inclination of the lines relating to these curves. After separation of this paramagnetic component, the magnetization curves of the ferromagnetic phase were constructed and the specific magnetization values M_s of the samples in the saturation state were obtained. So, for a ZnO:Mn sample with Mn concentration 2 at.% this value is $M_s = 0.089\text{ emu/g}$, and for samples with Mn concentration 4 at.% $M_s = 0.045\text{ emu/g}$. Such a decrease in FP can be explained by the fact that an increase in the Mn concentration leads to the formation of smaller nanocrystals with a more ordered crystalline structure. Such NCs have fewer intrinsic defects, including V_o oxygen vacancies.

Annealing the sample in air at a temperature $T = 550\text{ }^{\circ}\text{C}$ also leads to a decrease in the specific magnetization value due to a decrease in the number of oxygen vacancies V_o . After heat treatment at $T = 850\text{ }^{\circ}\text{C}$ (20 min), the sample becomes completely paramagnetic (Fig. 2b, curve 4), possibly because under such conditions oxygen V_o vacancies completely disappear, but some

amount of admixture defects (ions Mn), which have paramagnetic properties, remains. Annealing the sample for 1 hour leads to a complete loss of magnetic properties (Fig. 2b, curve 5). This may be due to the absence in the sample of both intrinsic (oxygen vacancy V_o) and admixture (interstitial Mn ions) crystal lattice defects necessary for exchange interaction start.

Conclusions

The paper shows the possibility of producing ZnO:Mn NC by the low-temperature FDS, which have ferromagnetic properties at room temperature. The main synthesis modes were obtained, namely: the admixtures Mn concentration is 2 at. %, the synthesis temperature is $T = 350$ °C, the synthesis time is 20 min. It was established that the specific magnetization of the ZnO:Mn sample with Mn concentration 2 at.% is $M_s = 0.089$ emu/g. It is shown that the feature of the structure of the EPR spectra and the magnetic properties of the samples can be explained on the assumption that during the synthesis ZnO:Mn NCs are formed in a gaseous hydrogen medium. It is a product of thermal decomposition of zinc and manganese acetates and provokes the formation of a large number of defects, which, in turn, cause the ferromagnetism of the ZnO:Mn NC at room temperature. The results obtained can be used in the synthesis of ZnO:Mn NCs for use in nanoelectronic and spintronics devices.

List of references

1. M.B. Generalov. Cryochemical nanotechnology. (Moscow: Akademkniga: 2006) - 325 p.
2. V.G. Anil, L. Bertrand, T. Shin-Hwa, G. Kalyani, C. Hua, C.L.Yong. Simultaneous thermogravimetric analysis and in situ thermo-Raman spectroscopic investigation of thermal decomposition of zinc acetate dehydrate forming zinc oxide nanoparticles. *Chemical Physics Letters*. – 2003. – Vol. 381. – p. 262 – 270.
3. M.F. Bulanyi, V.Y. Vorovsky, A.V. Kovalenko, O.V. Khmelenko. Structure of granules magnetic nanocrystals nickel-zinc ferrite obtained by cryochemical method. *J. Nano- Electron. Phys.* - 2017.- Vol. **9** – No 3. – p.36-41.
4. V.Y. Vorovsky, A.V. Kovalenko, A.I. Kushneryov, O.V. Khmelenko. Preparation of zincoxide nanopowders doped with manganese which have ferromagnetic properties at room temperature. *J. Functi-onal Materials* – 2018 - Vol. 25, No. 1. – p. 61 – 66.
5. S. Chattopadhyay, S.K. Neogi, A. Sarkar, M.D. Mukadam, S.M. Yusuf, A. Banerjee, S. Bandyopadhyay. Defects induced ferromagnetism in Mn doped ZnO. *J. Magn. Magn. Mater.* – 2011 - Vol. 323 – p. 363–368.

FORMATION OF NANOSTRUCTURAL $\text{PbI}_2\text{-PbMnI}_2$ COMPOSITE MATERIALS

A.P. Bukivskii¹, I.G. Vertegel¹, R.V. Gamernyk², Z.D. Kovalyuk³ and Yu.P. Gnatenko¹

¹Institute of Physics of NASU, 03028 Kyiv, 46 Nauky Ave., Dep. of Optics and Spectroscopy of Crystals

²Lviv National University, 29005 Lviv, 8 Kyrylo and Mefodiy Str., Dep. of Experimental Physics

³Institute for Problems of Materials Science, NAS of Ukraine, Chernivtsi Branch
tel. (044) 525-1395

E-mail: ap.bukivskii@gmail.com

1. Introduction

PbI_2 semiconductor crystals are of considerable interest because they are used for elaboration of high-sensitive non-cooled radiation detector materials for x- and γ -rays. PbI_2 has a type of layered structure with a repeating unit of hexagonal close-packed layer of Pb^{2+} sandwiched between two layers of I^- in the crystal. Recently, it was shown that their solid solutions, namely $\text{Pb}_{1-x}\text{Cd}_x\text{I}_2$, exhibit intense photoluminescence (PL) and luminescence excited by X-rays (XRL) at room temperature¹. These properties of the materials are due to the peculiarity of their crystal structure caused by the formation of nanostructural solid solutions. The use of $\text{Pb}_{1-x}\text{Mn}_x\text{I}_2$ alloys can expand the luminescence spectral range of such materials and thus improve their scintillator characteristics. Besides, PbI_2 crystals doped with magnetic atoms are of interest for the development of new materials – layered diluted magnetic semiconductors. It is also expected that, in the case of $\text{Pb}_{1-x}\text{Mn}_x\text{I}_2$ alloys of MnI_2 compound can be formed, which, as shown recently², exhibit multiferroic properties.

Comparative studies of optical absorption, photoluminescence and EPR spectra of PbMnI_2 bulk crystals and nanocrystals have been carried out in the work³. It was shown that exciton lines are shifted to the short-wavelength region with increasing concentration of Mn atoms. It is evident that this behavior of excitons is due to the formation of $\text{Pb}_{1-x}\text{Mn}_x\text{I}_2$ solid solutions. EPR measurements indicate that the basic spectrum consists of typical hyperfine structure. It indicates that local symmetry of Mn^{2+} ions is D_{3d} -symmetry and Mn^{2+} ions replace Pb^{2+} ions.

In this paper, for the first time, the results of studies of morphology, the XRD, SEM, EDX, photoluminescence and nuclear quadrupole resonance (NQR) spectra of the investigated crystals are presented in order to establish the mechanism of formation of PbMnI_2 crystals and their structural and optical properties.

2. Results and discussion

XRD measurements show that $\text{Pb}_{1-x}\text{Mn}_x\text{I}_2$ crystals with $X=0.03$ present single phase of 2H-polytype. A decrease of the crystal lattice parameters is observed, which may be caused by the replacement of Pb^{2+} ions with Mn^{2+} ions, which have an ionic radius of 1.26 Å and 0.91 Å, respectively. At the same time, for $X=0.10$, PbI_2 of 4H- polytype as well as PbMnI_2 of 2H-polytype were observed. Thus, in this case, inhomogeneous PbI_2 crystals exist, where PbMnI_2 solid solutions of micron and submicron sizes have been introduced into PbI_2 crystal, i.e. such crystals present $\text{PbI}_2\text{-PbMnI}_2$ composite. EDX measurements of the crystals with $X=0.10$ also confirm inhomogeneity of these crystals. In this case, the Mn concentration corresponds to the X-values from 0.020 to 0.035. Sometimes there are also regions of the crystal, where the concentration of manganese exceeds $X = 0.20$.

In order to observe the changes in the photoluminescence spectra caused by the formation of $\text{Pb}_{1-x}\text{Mn}_x\text{I}_2$ solid solutions we also studied pure PbI_2 single crystals which have mainly 2H-polytype. In this case, the exciton photoluminescence spectrum contains several lines at 2.497 eV, 2.492 eV, 2.484 eV, 2.472 eV and 2.459 eV. These lines correspond to the bound excitons and their phonon replicas with the participation of low-frequency optical phonons. In particular, the intense line at 2.492 eV corresponds to the emission of excitons localized on the neutral

donors, i.e., (D^0X)-line for PbI_2 crystal of 2H-modification. The weak line at 2.492 eV also corresponds to the emission of other bound excitons in PbI_2 crystal of 2H-polytype. The line at 2.503 eV may be associated with the exciton line in PbI_2 crystal of 4H-polytype or correspond to the emission of free excitons. The latter assumption is supported by the observation of free excitons for this crystal in the exciton reflection spectrum at 2.503 eV. In addition, another two intense broad lines at 2.435 eV and 2.385 eV are also observed, which are associated with the emission of donor-acceptor pairs with the participation of two different acceptor levels. In this case, the phonon replicas of these zero-phonon lines are also observed.

An analysis of the low-temperature photoluminescence spectrum of the investigated materials shows that for $X=0.03$, free and bound excitonic lines for PbI_2 crystal of 2H-polytype are observed. Besides, in the short-wavelength region a new line at 2.546 eV has been found. Since the energy position of this line is bigger than the band gap of PbI_2 crystal, it can be caused by the exciton emission in $Pb_{1-X}Mn_XI_2$ solid solutions, which are present in the crystal regions of small sizes distributed heterogeneously in PbI_2 crystal. The short-wavelength shift of the energy position for free excitons can also be caused by the appearance of the quantum size effect. In this case, the crystal region of $Pb_{1-X}Mn_XI_2$ solid solutions presents platelet-shaped nanoparticles with the width of 1-2 single layers. In addition, we also observed a line in the long-wavelength region at 2.435 eV associated with the emission of donor-acceptor pairs.

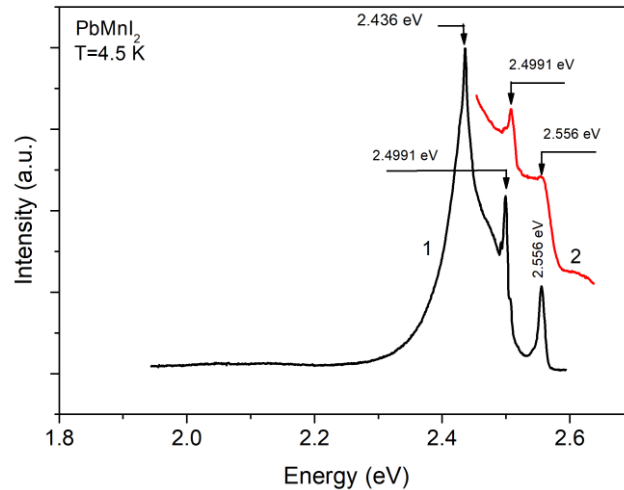


Fig. 1 – Photoluminescence (curve 1) and exciton reflection (curve 2) spectra of $Pb_{1-X}Mn_XI_2$ crystals with $X=0.05$ at $T=4.5$ K

As can be seen from Figure 1, for $Pb_{1-X}Mn_XI_2$ crystals with $X=0.05$ the photoluminescence spectrum (curve 1) contains two intense excitonic lines at 2.507 eV and 2.556 eV as well as the line at 2.436 eV, which corresponds to the radiative recombination of donor-acceptor pairs. The first line corresponds to the excitonic emission of bound excitons for PbI_2 of 4H-polytypes. Here, the exciton reflection spectrum is also present, which is associated with the formation of free excitons. This spectrum contains two lines at 2.515 eV and 2.573 eV. The first line corresponds to the formation of free excitons in PbI_2 crystal of 4H-polytype. At the same time, the other line is evidently due to the emission of free excitons in $Pb_{1-X}Mn_XI_2$ solid solutions. It should be noted that the energy position of photoluminescence line at 2.556 eV coincides with the maximum of the exciton reflection line. Therefore, this emission is associated with the formation of the localized excitons in $Pb_{1-X}Mn_XI_2$ solid solutions. Such localization occurs on the crystal field fluctuations. Thus, we have a strongly heterogeneous crystalline system, in which separate regions of solid solutions are embedded in the crystal matrix of PbI_2 . For $X=0.10$ the photoluminescence spectrum shows excitonic lines at 2.509 eV and 2.502 eV, which correspond to the emission of bound excitons in PbI_2 crystal of 4H polytype. At the same time,

another two lines at 2.496 eV and 2.492 eV are also observed, which are associated with exciton emission in PbI_2 crystal of 2H polytype. It should be noted that new lines appear in the short-wavelength region at 2.559 eV and 2.669 eV. In our opinion, these lines correspond to the exciton emission for the crystal region where $\text{Pb}_{1-x}\text{Mn}_x\text{I}_2$ solid solutions are formed. We assume that other crystal regions exist with different concentration of Mn atoms. We observe exciton emission from relatively homogeneous crystalline regions with a concentration of Mn atoms of about (2-3) %. Sometimes we observe the photoluminescence spectra for the crystals with $X=0.10$, which also contain broad bands at 2.204 eV and 1.890 eV. These bands may be caused by the intracenter emission of Mn^{2+} . In this case such emission may be caused by the formation of MnI_2 compound in the crystal region with very large concentration of Mn atoms (about 20%).

The NQR spectra of I^{127} for the investigated crystals were measured at 77 K in the frequency range of 5-300 MHz. The dependence of NQR spectra parameters on Mn concentrations have been studied. This allows us to determine the constant $e^2Qq_{zz}(x)$ of the quadrupole interaction and the parameter $\eta(x)$ associated with the asymmetry of the gradient electric tensor fields. It was found that the frequencies of NQR line for PbI_2 crystal of 2H- and 4H-polytypes correspond to 8.9 MHz and 9.8 MHz, respectively. The obtained results show that for the crystals with ($0 \leq x \leq 0,05$), Mn^{2+} ions preferably replace Pb^{2+} ions in the crystalline layers, which causes a change in the width of the I^{127} NQR line, but does not change the NQR frequency of I^{127} line ($\pm 3 / 2 \leftrightarrow \pm 5/2$). For $x = 0.10$, the I^{127} NQR spectrum changes significantly. It was shown that the investigated crystals have a heterogeneous composition, which includes 4H- and 2H- polytypes. It is evident, that such composite is due to the formation of the crystal region containing PbMnI_2 solid solutions.

3. Conclusions

The complex structural and optical studies of PbMnI_2 crystals were carried out. XRD measurements show that PbMnI_2 crystals with $X=0.03$ present single phase of 2H-polytype. At the same time, for $X=0.10$, PbI_2 of 4H- polytype, as well as PbMnI_2 of 2H-polytype were observed. Thus, in this case inhomogeneous PbI_2 crystals exist, where $\text{Pb}_{1-x}\text{Mn}_x\text{I}_2$ solid solutions of small sizes are embedded in PbI_2 crystal, that is, such crystals are a PbI_2 - PbMnI_2 composite. These results are confirmed by the optical measurements for the crystals with $X=0.05$, where two bands are observed in the exciton photoluminescence and reflection spectra. These bands in the exciton reflection spectrum correspond to free excitons in PbI_2 crystals of 4H-polytype and in $\text{Pb}_{1-x}\text{Mn}_x\text{I}_2$ solid solutions. For crystals with $X=0.10$, the emission caused by intracenter transitions of Mn^{2+} ions is observed. Such emission may be caused by the formation of MnI_2 compound in the crystal region with very large concentration of Mn atoms (about 20%). Thus, the investigated crystals present composite materials of the type PbI_2 - PbMnI_2 - MnI_2 . This conclusion coincides with the results of NQR measurements. It is expected that these materials can also exhibit multiferroic properties inherent to the MnI_2 compound.

References

1. A.P. Bukivskii, Yu.P. Piryatinskii, R.V. Gamernyk, Yu.P. Gnatenko, Nature of radiative recombination processes in layered semiconductor PbCdI_2 nanostructural scintillation material, *Journal of Luminescence*, 185, 2017, 83–91.
2. Xianxin Wu, Yingxiang Cai, Qing Xie, Hongming Weng, Heng Fan, and Jiangping Hu, *Physical Review B* 86, 2012, 134413.
3. A.I. Savchuk, I.D. Stolyarchuk, O. A. Savchuk, O.A. Shporta, I. Stefaniuk, I. Rogalska, E. Sheregii, *Semiconductor Physics, Quantum Electronics & Optoelectronics*, 2014. 17, 2014 41-45.

DIELECTRIC PROPERTIES AND ELECTRICAL CONDUCTIVITY OF 6CB LIQUID CRYSTAL WITH $\text{Cu}_6\text{PS}_5\text{Br}$ SUPERIONIC NANOPARTICLES

I.P. Studenyak¹, O.V. Kovalchuk^{2,3}, S.I. Poberezhets³, M. Timko⁴, P. Kopčanský⁴

¹Uzhhorod National University

88000, Uzhhorod, Pidhirna Str. 46, dep. Applied Physics,

tel. (099) 797-30-16

E-mail: studenyak@dr.com

²Kyiv National University of Technologies and Design

01011, Kyiv, Nemyrovycha-Danchenka Str. 2, dep. Physics

³Institute of Physics, National Academy of Sciences of Ukraine

03028 Kyiv, Nauky av. 46, dep. Molecular Photoelectronics

⁴Institute of Experimental Physics, Slovak Academy of Sciences

04001, Košice, Watsonova Str. 47, dep. Magnetism

The given work is devoted to the study of the influence of $\text{Cu}_6\text{PS}_5\text{Br}$ superionic nanoparticles on the dielectric properties of planar-oriented 6CB liquid crystal in the frequency range from 6 to 10^6 Hz and at the temperature of 293 K. The concentration of nanoparticles varied from 0 to 0.1 wt.%. It has been shown that $\text{Cu}_6\text{PS}_5\text{Br}$ nanoparticles significantly less influence the conductivity of 6CB than the $\text{Cu}_6\text{PS}_5\text{I}$ nanoparticles. Moreover, at concentrations of 0.01-0.05 wt.% of $\text{Cu}_6\text{PS}_5\text{Br}$ nanoparticles, the conductivity of the LC decreases. It is assumed that the nonmonotonic dependence of 6CB conductivity on the concentration of $\text{Cu}_6\text{PS}_5\text{Br}$ superionic nanoparticles is caused by two competing mechanisms: an increase in conductivity due to the introduction of conductive impurities with nanoparticles and a decrease in conductivity due to adsorption of impurities on the surface of nanoparticles.

Introduction

Liquid crystals (LC) are now widely used in display technology. In order to significantly expand the limits of the practical application of LC it is necessary to be able to predictably change their properties. One of the methods for expanding the functional properties of the LC is the introduction of various types of nanoparticles [1-3]. As we have shown in Refs. [1-3], significant changes in the properties of LC are observed when introducing superionic nanoparticles. The introduction of $\text{Cu}_6\text{PS}_5\text{I}$ nanoparticles into 6CB LC leads to an increase in conductivity by almost two orders of magnitude due to the dissociation of nanoparticles in the LC with the formation of Cu ions [1]. The purpose of this work was to investigate the influence of $\text{Cu}_6\text{PS}_5\text{Br}$ superionic nanoparticles on the dielectric properties of a planar-oriented nematic 6CB LC and to compare it with the results of the influence on this LC of $\text{Cu}_6\text{PS}_5\text{I}$ superionic nanoparticles.

Experimental

$\text{Cu}_6\text{PS}_5\text{Br}$ powders were milled with a planetary ball-mill. The maximum milling time of the powder was 30 min. 6CB LC without/with $\text{Cu}_6\text{PS}_5\text{Br}$ superionic nanoparticles was studied in a sandwich-type cell with transparent ITO electrodes. The electrodes were coated with an appropriately processed polymer layer to provide the planar orientation of the LC molecules. The concentration of nanoparticles of a near-spherical shape with the average size of 200 nm in the LC was 0.1, 0.5, 1 wt. %. The cell thickness was 18 μm . The LC cell was filled using the capillary method at a temperature by 5–10 K above the nematic-to-isotropic phase transition temperature. The dielectric properties of the sandwich cells were investigated in the frequency range from 6 to 10^6 Hz at a temperature of 293 K using an oscilloscopic method.

Results and discussion

Fig. 1 shows the frequency dependences of the real component of the complex dielectric permittivity ϵ' of 6CB LC with the different concentration of $\text{Cu}_6\text{PS}_5\text{Br}$ superionic nanoparticles. It follows from Fig. 1 that $\text{Cu}_6\text{PS}_5\text{Br}$ nanoparticles have a significantly less impact on the value

of ϵ' than $\text{Cu}_6\text{PS}_5\text{I}$ nanoparticles have [1]. It is shown that the influence of nanoparticles essentially depends on the frequency range. Therefore, for analysis, it is logical to divide the frequency dependence ϵ' into two regions A and B (Fig. 1).

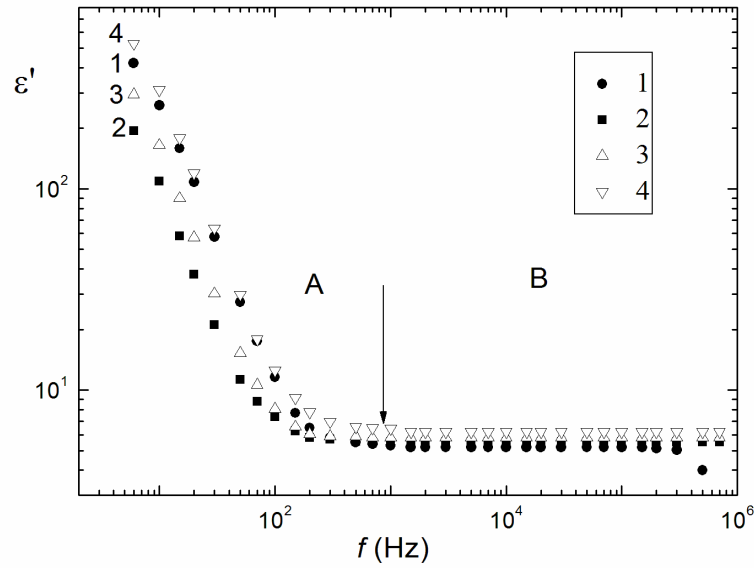


Fig. 1 – Frequency dependences of the real part ϵ' of complex dielectric permittivity at 293 K for 6CB LC (1) and 6CB LC with different content of $\text{Cu}_6\text{PS}_5\text{Br}$ superionic nanoparticles: 0.01 (2), 0.05 (3) and 0.1 wt.% (4)

As it follows from Fig. 1, there is a sharp increase in the value of ϵ' with a decrease in frequency in the section A ($f < 10^3$ Hz). As we have shown in Ref. [4], this effect is due to the fact that in order to ensure the charge transfer in the electrode section, the intensity of the electric field in the sample is redistributed in such a way that almost the entire voltage of the measuring signal will be applied to a thin (dozens of nanometers) near-electrode layer. It was shown in Ref. [4] that the dispersion of ϵ' in the A region of dielectric spectrum can be described by the Debye equation. This dispersion is caused by the rotation of the dipoles of the LC molecules at angles corresponding to fluctuations of the order parameter. Since the electric field is mainly concentrated in near-electrode section, it is there that the charge transfer occurs due to oscillations of the molecules dipoles. In the bulk of LC, charge transfer occurs due to the motion of ions. Therefore, the parameters of the relaxation process in the A region depend not only on the parameters of the near-electrode section, but also on the conductivity of the sample.

Significantly less influence of $\text{Cu}_6\text{PS}_5\text{Br}$ nanoparticles on the value of ϵ' of 6CB LC than the influence of $\text{Cu}_6\text{PS}_5\text{I}$ nanoparticles is obviously caused by the fact that $\text{Cu}_6\text{PS}_5\text{Br}$ nanoparticles significantly less influence the conductivity of 6CB LC than $\text{Cu}_6\text{PS}_5\text{I}$ nanoparticles. As we will show below, the lower influence of $\text{Cu}_6\text{PS}_5\text{Br}$ nanoparticles on the conductivity of the 6CB LC determines the essential difference between the frequency dependences of ϵ' at different concentrations of nanoparticles.

As follows from the analysis of Fig. 1 for frequencies $f > 10^3$ Hz (region B of the dielectric spectrum), the value of ϵ'' does not depend on the frequency. This corresponds to the condition where the electric field intensity in the thickness of the sample will be the same. In this case, the value of ϵ' will be equal to the bulk dielectric permittivity. It is concluded that the presence of impurities of $\text{Cu}_6\text{PS}_5\text{Br}$ even at maximum concentrations (0.1 wt.%) results in a small (less than 20%) increase in dielectric permittivity of a 6CB LC with nanoparticles (Fig.1).

One more important conclusion can be drawn from the analysis of the frequency dependences of ϵ' in region A. At 0.01 wt.% and 0.05 wt.% of $\text{Cu}_6\text{PS}_5\text{Br}$ nanoparticles, the dielectric permittivity is less than the dielectric permittivity of a pure LC. According to Ref. [4], this fact may be caused by the influence of nanoparticles on the LC conductivity. Therefore, it is

logical to consider how the $\text{Cu}_6\text{PS}_5\text{Br}$ superionic nanoparticles influence the conductivity of 6CB LC.

Fig. 2 shows the frequency dependence of conductivity σ_{AC} of 6CB LC with the different concentration of $\text{Cu}_6\text{PS}_5\text{Br}$ superionic nanoparticles.

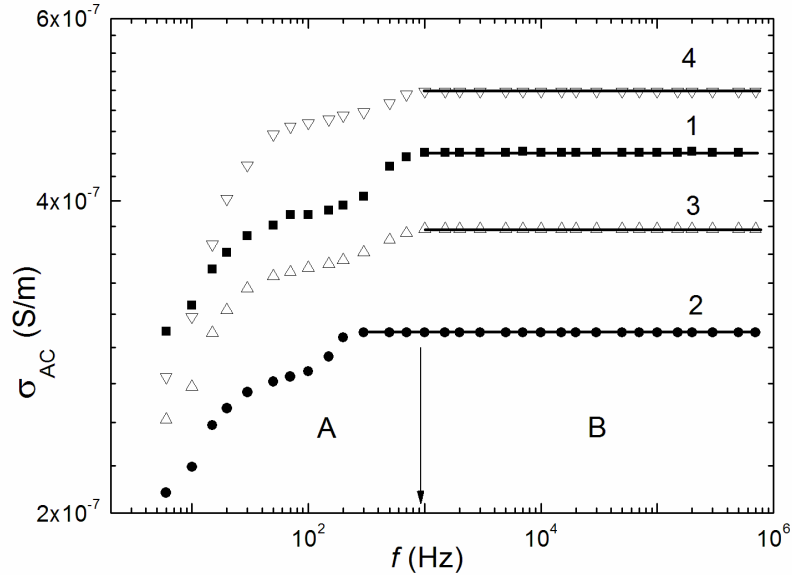


Fig. 2 – The frequency dependences of the electrical conductivity σ_{AC} at 293 K for 6CB LC (1) and 6CB LC with different content of $\text{Cu}_6\text{PS}_5\text{Br}$ superionic nanoparticles: 0.01 (2), 0.05 (3) and 0.1 wt.% (4)

It follows from the analysis of Fig. 2, that the frequency dependence of conductivity also can be divided into two regions A and B. At A region ($f < 10^3$ Hz), the value of σ_{AC} decreases with decreasing frequency. In fact, for these frequencies, we can not talk about the conductivity since, as noted above, the electric field is applied not to the entire bulk of the LC, but to a thin near-electrode layer. For the frequencies $f > 10^3$ Hz (region B of the dielectric spectrum), as follows from Fig. 2, the conductivity does not depend on the frequency. It is these values of conductivity that correspond to the bulk conductivity. It is shown that the value of σ_{AC} of nematic LC is a nonmonotonic function of the content of $\text{Cu}_6\text{PS}_5\text{Br}$ nanoparticles (Fig.2).

Fig. 3 shows the dependence of 6CB LC conductivity on the concentration of $\text{Cu}_6\text{PS}_5\text{Br}$ superionic nanoparticles. From these data, it follows that the conductivity of 6CB LC is a nonmonotonic concentration function of $\text{Cu}_6\text{PS}_5\text{Br}$ nanoparticles. At small concentrations of nanoparticles (0.01 - 0.05 wt.%), the LC conductivity decreases. However, with maximum concentration, the LC conductivity becomes larger (almost in 1.1 times). To explain this effect, we must assume that $\text{Cu}_6\text{PS}_5\text{Br}$ nanoparticles affect the 6CB LC by two different mechanisms. Firstly, along with the nanoparticles, the certain impurities are introduced into LC, which can be the charge carriers. In addition, the LC conductivity can increase due to the dissociation of nanoparticles in LC [1]. However, in the case of $\text{Cu}_6\text{PS}_5\text{Br}$ nanoparticles such mechanism of conductivity increase is not observed (no color of LC was detected as for $\text{Cu}_6\text{PS}_5\text{I}$ nanoparticles [1]). Secondly, the conductivity of LC may decrease as a result of the adsorption of ions that transfer the charge to the LC, on the surface of the electrodes. Each of the above mechanisms may vary in different ways from the concentration of nanoparticles. It is obvious that in the case of a nonmonotonic dependence of the conductivity of 6CB LC on the concentration of $\text{Cu}_6\text{PS}_5\text{Br}$ superionic nanoparticles, two such mechanisms act simultaneously. At 0.01-0.05 wt.% of nanoparticles, adsorption of ions on the surface of nanoparticles is prevalent, and at 0.1 wt.% conductivity increase occurs due to the introduction of additional (to those existing in LC) ions.

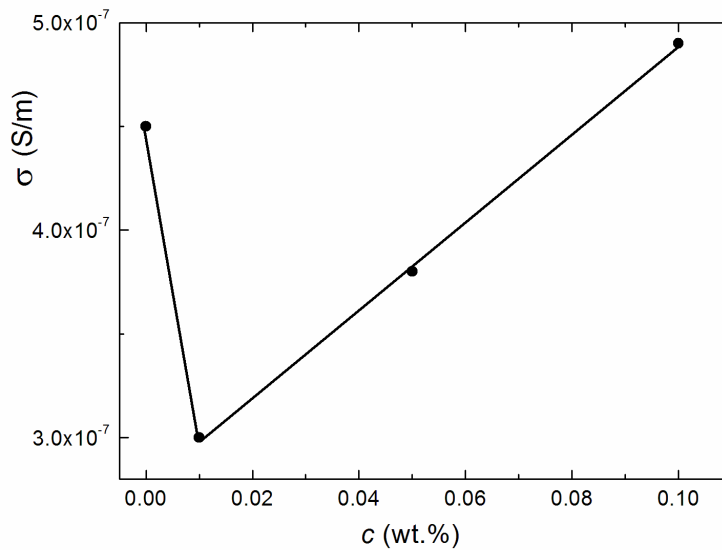


Fig. 3 – Concentrational dependence of the electrical conductivity σ_{AC} at 293 K for 6CB LC with Cu_6PS_5Br superionic nanoparticles

From the comparison of the data we obtained with the data presented in Ref. [1], we can conclude that Cu_6PS_5Br nanoparticles significantly less influence the conductivity of 6CB LC (increasing the conductivity by only 1.1 times with a maximum concentration of 0.1 wt.%) than nanoparticles in Cu_6PS_5I (increase in concentration by almost two orders of magnitude). Thus, the substitution of I atoms by Br atoms in Cu_6PS_5X ($X=I, Br$) nanoparticles leads to a significant difference in their effect on 6CB LC conductivity.

Conclusions

It has been shown that Cu_6PS_5Br superionic nanoparticles significantly affect the conductivity of 6CB LC, more than they influence its dielectric permittivity. Conductivity of 6CB LC in the range of 0-0.1wt.% is a nonmonotonic function from the concentration of Cu_6PS_5Br nanoparticles. The mechanism of this effect is proposed on the basis of the existence of two competing and closely related processes: the increase of conductivity due to the introducing of additional (to those existing in LC) ions and decrease of conductivity due to adsorption on the surface of nanoparticles of ions that are charge carriers in LC. It is shown that Cu_6PS_5Br nanoparticles significantly less influence the conductivity of 6CB LC than Cu_6PS_5I nanoparticles.

References

1. I.P. Studenyak, V.Y. Izai, V.I. Studenyak, etc, Influence of Cu_6PS_5I superionic nanoparticles on the dielectric properties of 6CB liquid, crystal, *Liquid Crystals* 44 (2017) 897-903.
2. O.V. Kovalchuk, I.P. Studenyak, V.Yu. Izai, etc, Saturation effect for dependence of the electrical conductivity of planar oriented nematic liquid crystal 6CB on the concentration of Cu_7PS_6 nanoparticles, *Sem. Phys. Quant. Electr. & Optoelectr.* 20 (2017) 437-441.
3. I.P. Studenyak, P.Yu. Demko, A.V. Bendak, etc, Influence of superionic nanoparticles Cu_6PS_5I on dielectric properties of nematic liquid crystal 6CHBT, *Sem. Phys. Quant. Electr. & Optoelectr.* 18 (2015) 205-208.
4. O. Yaroshchuk, A. Kovalchuk, R. Kravchuk, The interfacial dipole-to-dipole interaction as a factor of polar anchoring in the cells with planar liquid crystal alignment, *Mol. Cryst. Liquid Cryst.* 438 (2005) 195-204.

ESTIMATION OF THE RESOLVING ABILITY OF OPEN COAXIAL UHF SENSOR

Slipchenko N.I.¹, Liu Chan², Borodkina A.N.³, Panchenko A.Yu.⁴

¹ Institute for Scintillation Materials NAS of Ukraine,
60, Nauky Ave., Kharkiv, 61000, Ukraine

² Heilongjiang Bayi Agricultural University External Relations Department
Xinfeng Str. 5, Daqing, 163319, China

³ Kharkiv National Medical University
4, Nauky Ave., Kharkiv, 61022, Ukraine

⁴ Kharkiv National University of Radio Electronics
14, Nauky Ave., Kharkiv, 61166, Ukraine, Dep. DOED
Tel.: (057) 702-14-94

E-mail: oleksandr.panchenko@nure.ua

Theoretical analysis of the microwave sensor spatial resolution is presented. The sensor is an open coaxial aperture. It allows you to concentrate the electromagnetic field in a small area that is significantly less than the wavelength. This allows using it as a sensor of nano-objects. Such a sensor can operate in a wide frequency range. This increases information efficiency in indirect measurements. A rigorous analytical model can be created for it. But it admits the possibility of strict solution of the problem only for the case of multilayer samples. The solution to this problem makes it possible to evaluate the ability of the sensor resolution in the axial direction. The paper sets the problem of the prospects of creating an analytical model for estimating the radial resolution. The solution of the problem is based on an analytical description of the fields in the working area of such a sensor using an existing model. Based on the analysis of the field distribution in the working area, factors that influence resolution are identified. The obtained distributions allow us to estimate the axial and radial resolution. The results of calculations of the components of the electromagnetic field in the working area of the sensor are discussed.

1. Introduction

Currently, there is a rapid development of nanotechnology. An urgent task is the creation of non-destructive means for nano-scale objects control. An open coaxial aperture makes it possible to concentrate the electromagnetic field (EMF) in a small area that is substantially less than the wavelength. This allows using it as a sensor of nano-objects. Open coaxial sensors (OCS) of the microwave range have several advantages. They require minimal processing of the sample. Reducing the size of the OCS allows you to extend the frequency range of measurements in the region of higher frequencies. The possibility of measurements in a wide frequency range increases the amount of the primary information. This contributes to increasing the reliability of the information obtained from indirect measurements. In addition, it is possible to create a fairly accurate analytical model of the OCS. This simplifies the process of creating specific meter designs.

The analytical solution for the distribution of the EMF components in the working area of the sensor is most easily recorded for a layered sample. This allows you to study thin films. Various variants of the influence of thin layers were considered, including the analysis of the emitted wave [1]. Less attention has been paid to the assessment of radial inhomogeneities. This requires fundamentally new, more complex analytical models. Prospects for creating such models must be justified. Evaluation of prospects can be carried out on the basis of already known models.

The purpose of this work is a preliminary assessment of the spatial resolution of the OCS, including the radial one. The objective of the work is to analyze the components of the EMF in the workspace of the OCS.

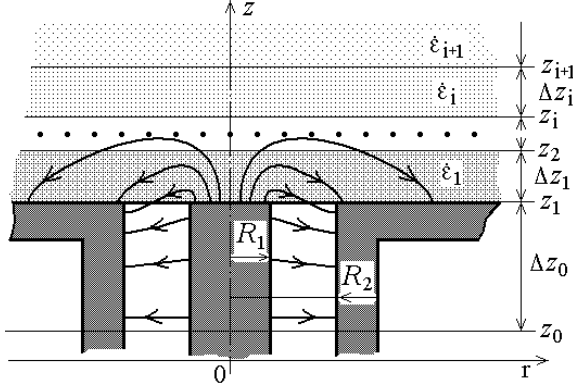


Fig. 1 – Structure of the OCS and the electric field in a layered sample

1. Basic ratios for OCS

Rigorous mathematical representation of the components of the EMF in the working area of the OCS can be obtained on the basis of tensor Green functions of Maxwell's equations for cylindrical regions. Single-mode operation of the OCS is provided with TEM wave in the supply line. Therefore, there is only one component of the magnetic field – H_ϕ in the OCS. The electric field has two components: radial – E_r , and axial – E_z . The structure of the electric field of the OCS in this case is shown in Fig.1. But the solution is easier to

write for the field \vec{H} , it has the form [2]:

$$\vec{H}(\vec{r}, z) = \int_V \tilde{A}^M(\vec{r}, \vec{r}') \vec{j}^i(\vec{r}') dv, \quad (1)$$

where \tilde{A}^M – is the magnetic field tensor;

\vec{j}^i – are the magnetic field sources.

With such a structure of the EMF, H_ϕ is associated with only one component of the source – j_ϕ^i . In this case $j_\phi^i = E_r$, and from 9 \tilde{A}^M components, it suffices to use one transverse one to determine $\vec{H} = \vec{\varphi}_0 H_\phi$. Compliance with the real distribution of $E_r(z, r)$ choice determines the accuracy of the result of solving this problem.

With a small aperture ($R_2 \ll \lambda$), the distribution $E_r(z, r)$ differs from the TEM field in the supply line only in the upper part of the region Δz_1 . If you place the plane $z_0 = const$ in the lower part of the area Δz_1 , you can specify $E_r(z, r)$ in the form $E_r(z_0, r) = U_0 r^{-1}$. Then, the value U_0 is associated with the voltage in the line U_L as $U_L = U_0 \ln(R_2 / R_1)$. A solution of the integral equation with respect to $E_r(z_1, r)$ – the field in the plane of the aperture is required [3] to determine rigorously the field in the sample under study. However, a rigorous analysis shows that the difference of $E_r(z_1, r)$ from $U_0 r^{-1}$ appears only near the edges of the aperture. With a small aperture, this difference slightly affects the output parameters of the OCS [4].

With $R_2 \ll \lambda$ the most informative output parameter is the capacity of the OCS – \dot{C}_a . When calculating the capacitance in the plane z_0 , you can get a strict solution [5]. To assess the properties of OCS at a qualitative level, \dot{C}_a behavior can be analyzed based on known physical factors. As it is known, the electrical capacitance of the system is related to the energy of the electric field. Therefore, an assessment of distribution of the electric field components will make it possible to determine the area that makes the greatest contribution to \dot{C}_a . Thus, the assessment of the EMF components distributions solves the problem set in the report. When determining the field in the working area of the OCS, you can use the case of a homogeneous sample. When $E_r(z_1, r) = U_0 r^{-1}$, the expressions for E_z , E_r and H_ϕ are simplified to integrals with respect to wave numbers

$$H_\phi(r, z) = -j\omega\varepsilon_0\varepsilon_1 U_0 \int_0^\infty \frac{[J_0(\kappa R_1) - J_0(\kappa R_2)] J_1(\kappa r) \exp[-\gamma_1(z - z_1)]}{\gamma_1} d\kappa, \quad (2)$$

$$E_r(r, z) = -U_0 \int_0^{\infty} [J_0(\kappa R_1) - J_0(\kappa R_2)] J_1(\kappa r) \exp[-\gamma_1(z - z_1)] d\kappa, \quad (3)$$

$$E_z(r, z) = U_0 \int_0^{\infty} \frac{[J_0(\kappa R_1) - J_0(\kappa R_2)] J_0(\kappa r) \exp[-\gamma_1(z - z_1)]}{\gamma_1} \kappa d\kappa, \quad (4)$$

where J_0 and J_1 are Bessel functions;

ω – is the circular frequency of the probing field: $\omega = 2\pi f$, f – is the operating frequency;

$\gamma_1 = \sqrt{\kappa^2 - \varepsilon_1 k_0^2}$ – is the propagation constant;

ε_0 – is the dielectric constant;

k_0 – is the propagation constant in vacuum.

Numerical analysis will be carried out for $U_a = 1\text{ V}$, $f = 10\text{ GHz}$, $R_2 = 2\text{ mm}$ and the dielectric constant $\varepsilon_1 = 1 - i0,0001$ of the sample.

2. Distribution of field components in the workspace of the OCS

Estimation of the intensity of the electromagnetic field components distribution in the sample will show the size of the area being investigated. Figure 2a, b, c shows the distributions $H_\varphi(r, z)$ for three values of R_1 / R_2 ratio.

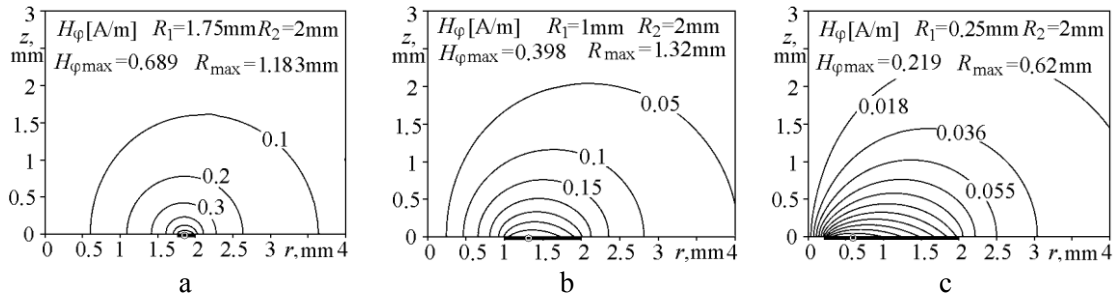


Fig. 2 – The intensity of the magnetic component in the sample

The maximum values of the magnetic field strength in the aperture plane – $H_{\varphi \max}$, as well as the position of the points corresponding to these values – R_{\max} are shown for comparison. The change of $H_{\varphi \max}$, when the ratio R_1 / R_2 changes, corresponds to changes in the wave resistance of the supply line. Naturally, the total energy of the EMF changes.

In most practical cases, the dielectric properties of objects are subject to measurement. They define the electric field energy in the capacitive structure. The distribution of the electric field component E_r is shown in Fig.3a, b, c, E_z – in Fig.4a, b, c.

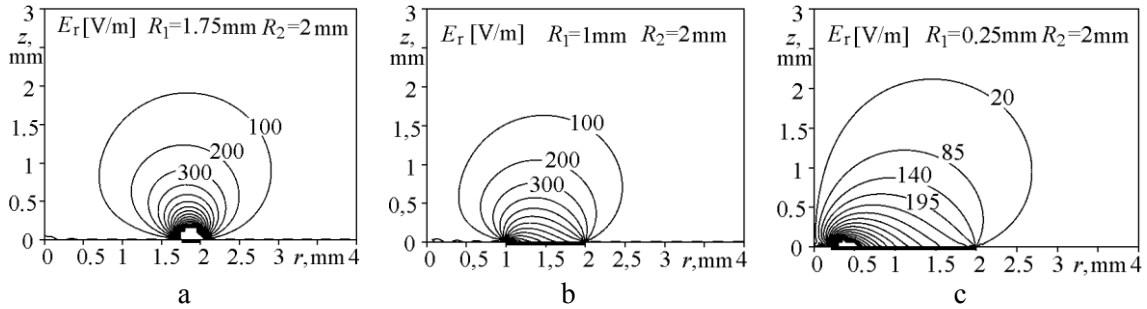


Fig. 3 – The intensity of the radial electrical component in the sample

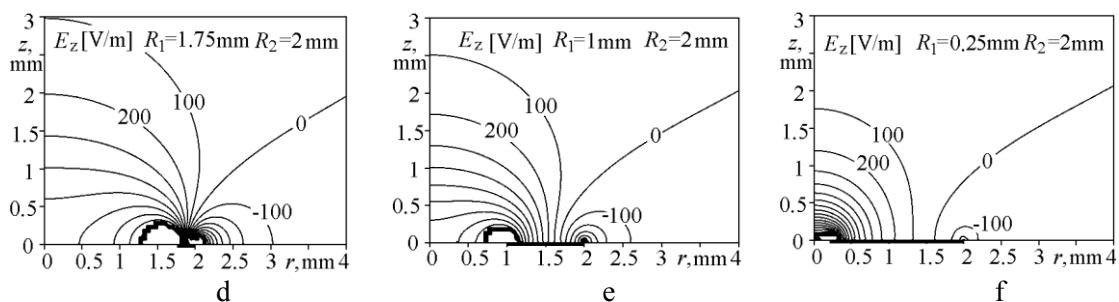


Fig. 4 – The intensity of the axial electrical component in the sample

As these distributions show, the highest concentration of the electrical component is near the edges of the aperture. Note that with a more rigorous analysis, an increase in this factor is observed [3].

The presented distributions show the areas that contribute the most to the overall value \dot{C}_a . The transformation of the distributions of all components of the EMF with $R_1/R_2 \rightarrow 0$ shows that the concentration \vec{E} near the center conductor increases. Moreover, the increase in the directions of the axes \vec{r}_0 and \vec{z}_0 is about the same. This is especially clearly shown by the distribution E_z in Figure 4c. Therefore, reducing the radius of the central rod increases proportionally the resolution both in axial and radial directions. But in this case the field penetrates less deeply into the sample under study.

On the other hand, with $R_1/R_2 \rightarrow 1$ penetration is comparable to the size of the gap $\Delta R = R_2 - R_1$. Moreover, the axial penetration of the EMF corresponds to the radial one.

In general, both radial and axial resolution is comparable to the size of the minimum element forming the aperture.

Conclusions

The analysis performed corresponds to real measuring transducers and has practical value. In particular, this design of the OCS makes it possible to carry out the operational control of films of nano-scale thickness. The presented results show that the axial and radial spatial resolution of the OCS depends on the minimum dimensions of the elements forming the aperture. In this case, the resolution in both directions has approximately the same values.

The analysis indicates perspective of using the OCS in the study of nano-scale objects. The results of this analysis are the basis for further development of mathematical models of this kind of sensors.

References

1. Wen Mingming, Ch. Liu, Panchenko A.Yu, Slipchenko N.I. (2015) Evaluation of influence of microwave radiation sensor in the form of an open end of the coaxial line on its metrological characteristics. *Telecommunications and Radio Engineering*, №74 (15), pp.1355-1366. DOI: 10.1615/TelecomRadEng.v74.i15
2. Panchenko B.A. Green tensor functions of Maxwell's equations for cylindrical areas // *Radiotekhnika: All-Ukr. Interdep. Sci. Mag.* 1970. № 15. P.p. 82-91. (In Russian)
3. Lu Ch., Panchenko A.Yu., Slipchenko M. I. (2016) An integral equation for the field distribution within the aperture plane of the coaxial sensor. *Telecommunications and Radio Engineering*, №75(7), pp.587-594. DOI: 10.1615/TelecomRadEng.v75.i7 20
4. Panchenko A.Yu. Modeling a small aperture resonator type microwave meter of substance parameters // *Telecommunications and Radio Engineering*. 1998. V.52 No.8. P. 42-22. DOI: 10.1615/TelecomRadEng.v52.i8.80
5. Panchenko A.Yu., Slipchenko N.I., Borodkina A.N. (2014) On the development of a practical technique of theoretical calibration of resonant sensors for near-field microwave diagnostics. *Telecommunication and Radio Engineering*, №73(15), pp. 1397-1407. DOI: 10.1615/TelecomRadEng.v73.i15.

LOCAL MICROWAVE HEATING

I.N. Bondarenko, G.N. Bendeberya, E.A. Gorbenko
Kharkiv National University of Radio Electronics
61166, Kharkiv, Nauky ave. 14, dep. Microelectronics,
Electronic Devices and Appliances
tel.: (057) 702-13-62,
E-mail: d_meda@nure.ua

Experimental studies of the possibilities of practical implementation of local microwave heating technology have been carried out. The correspondence of the existing theoretical models of the process to what is happening in practice is shown. The results of measuring the temperature distribution over the sample when exposed to a radiating microwave coaxial probe are given. The directions for further improvement of the operating modes and the main components of the microwave modifier are determined.

Introduction.

The use of microwave energy of the electromagnetic field for heating different media is widely known and well-studied. As a rule, the developers of various directions of practical use of this method were faced with the task of ensuring a spatially uniform microwave heating. The task of localization arose very rarely, for example, during hyperthermia of tumors, and had a macro-dimensional nature. At the same time, micro-dimensional heating can be relevant in the interests of modifying micro-objects, and especially for micro- and nanoelectronics.

The development of high-local microwave heating allows doping and re-doping, thermal oxidation, recrystallization and annealing of various materials in the surface layer of the object, including those ones in film structures.

However, to achieve micron and submicron localization of microwave heating, it is necessary to solve the problem of optimal heat dissipation. For this, it is necessary to have an appropriate theoretical description of the method adapted to the type of the microwave transmitter used, for example, with a coaxial aperture.

The practical possibility of microlocalization of microwave heating appeared as a result of the development of near-field sources of microwave radiation, in particular, for scanning microwave microscopy [1].

The main part.

Theoretical studies of the localization characteristics of microwave heating of semiconductor and dielectric objects are based on the joint solution of electrodynamic and thermal problems for near-field sources of microwave radiation. The theoretical foundations of local microwave heating modeling are described in detail in [2, 3].

Fig. 1 schematically shows the possible functional scheme for the implementation of local microwave heating, as well as the type of electrodynamic structure of the micromodifier.

In modeling, a radiator based on a conical coaxial probe with a spherical and flat tip shape was considered as a local micromodifier. The radius of the tip is ~ 10 microns. The object of study is the "film on the substrate" structure.

As a result of model studies in [23-26], the following was established:

- temperature distribution inside and along the sample surface substantially depends on the size of the gap between the micromodifier point and the sample surface;
- the spatial distribution of temperature in the sample, depending on the shape of the point of the tip (flat or spherical) also changes - for a spherical one, it is of more localized nature;
- local heating of the sample leads to a local change in the electrical characteristics, which additionally accelerates the heating process;
- during long-term (more than 10^{-3} s) exposure of the microwave radiation to the sample, heat spreads over the sample due to its thermal conductivity, which leads to a decrease in the degree of localization of heating.

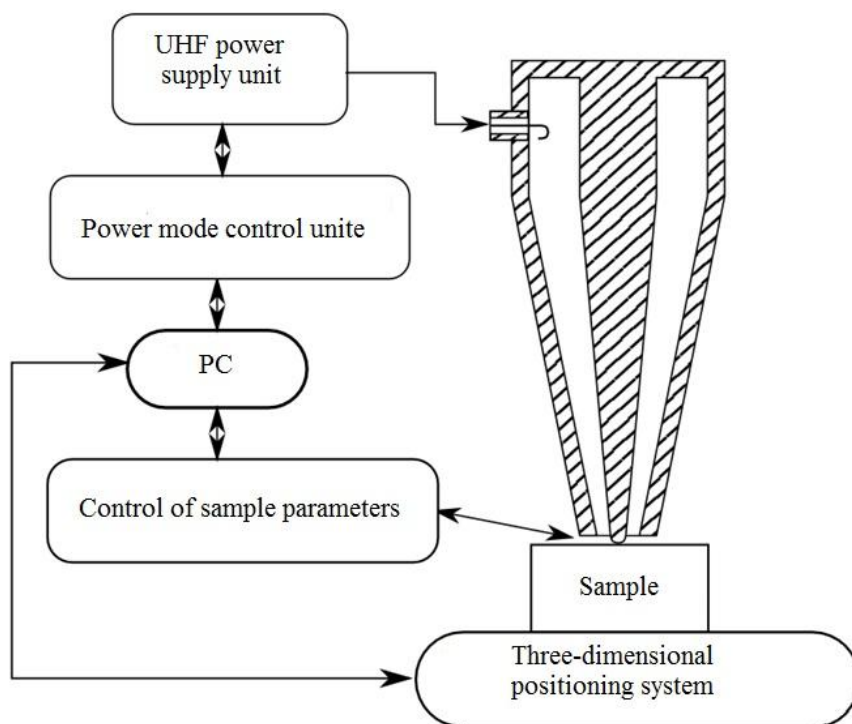


Fig. 1 – Functional diagram of the microwave micromodifier main nodes

An installation, based on a magnetron type generator M-857 with a generation frequency of ~ 9.480 GHz with output power of up to 10 W, was assembled for experimental studies of microwave heating. A general view of the installation is shown in Fig.23. Fig. 3 shows a general view of the radiator with a tuning screw.

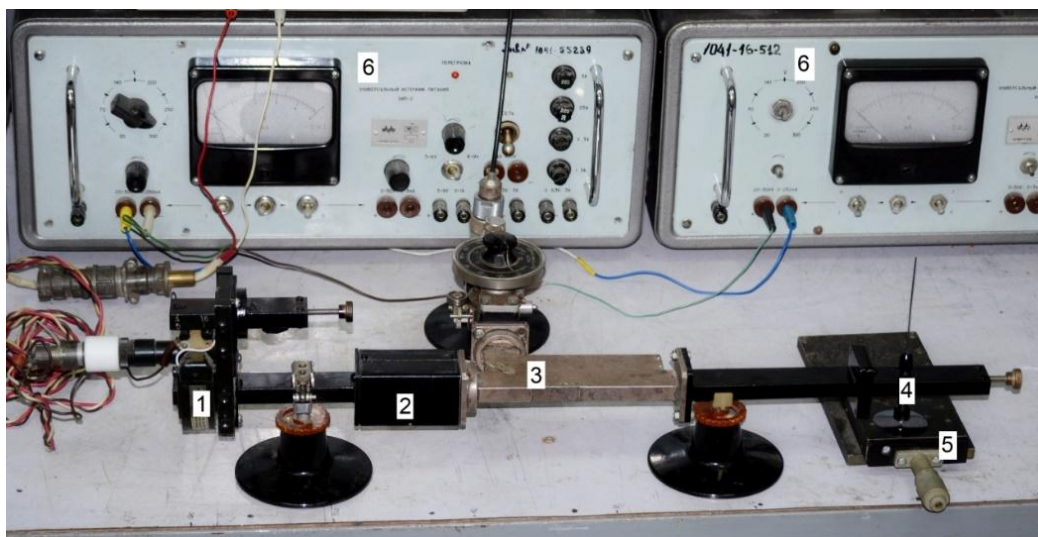


Fig. 2 – Installation for formation of the local EMF power up to 10 W: 1 - M-857 magnetron, 2 - ferrite valve, 3 - directional coupler with attenuator and detector head, 4 - emitter (impact tool), 5 - objective table, 6 - power supply units of the magnetron

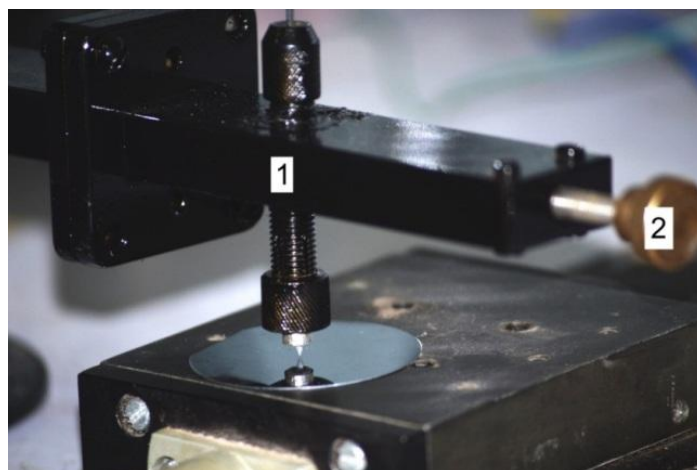


Fig. 3 – General view of the emitter with setting screw:
 1 - waveguide-coaxial transition, 2 - short-piston setting screw

A gas discharge occurs at some ratios of the electric field intensity between the emitter and the object, the gap between them and the ambient pressure.

Substrates of monocrystalline silicon and polycore coated with a layer of photoresist were used as objects for studying the temperature distributions. Studies of thermal fields on substrates were carried out both in the mode of a probe touching their surface and in the mode of a plasma action with a gap.

The thermal distribution was recorded using a FLIR E60 type thermal imaging camera with a FOL17 lens. The temperature resolution of the camera is 0.05°C . Thermal images were processed using the FLIR Quick Report 1.2 firmware.

Fig. 4 show the thermal fields in the field of view of the camera (a) and the temperature at the points of the substrate (b), which are located along the radius of the region centered on the tip of the working probe (Sp1 ... Sp7), the probe tip temperature Sp8.

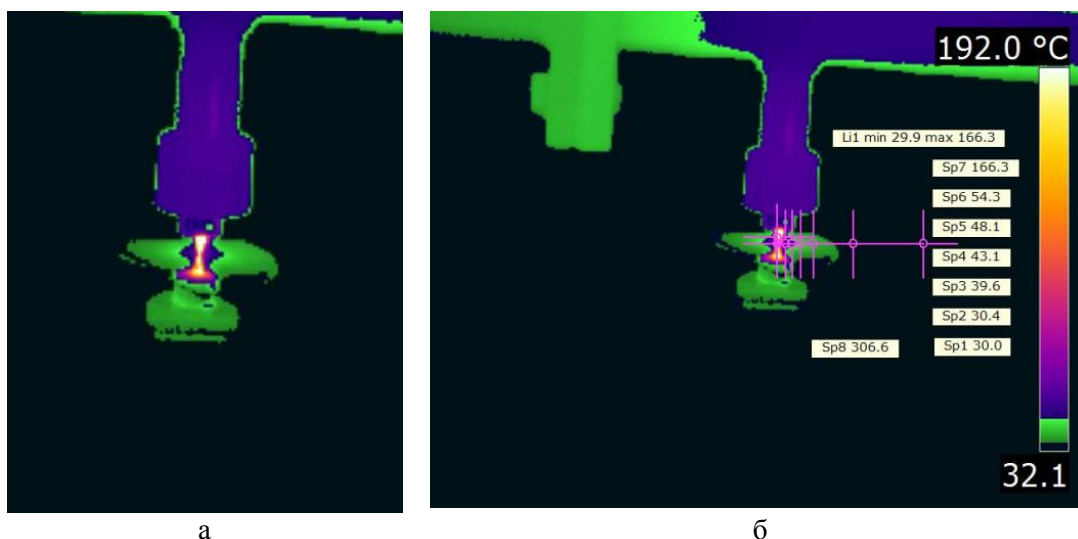


Fig. 4 – Thermogram of the silicon substrate heating. Thermal field (a) and temperature at the points of the Sp1 ... Sp7 substrate, located along the radius of the region centered on the tip of the working probe Sp8 (b)

In all cases, the effect of microwave power was constant, without modulation in time of exposure. The nature of the distribution is generally the same with slight differences in

steepness, probably due to different thermal conductivities and the effect of photoresist on heat distribution.

Conclusions.

Experimental studies of microwave local heating confirm the main provisions of the conditions for its implementation, obtained by model consideration. This leads to the need to take into account most of the factors identified by the simulation, when implementing the process of microwave local heating.

If the requirements for positioning and the geometric shapes and sizes of nodes and elements can be met with the help of existing technical and practical possibilities, then the questions of dynamic control of the microwave (electromagnetic) effect process imply the development of special support.

In this regard, it seems promising to use devices for generating amplified pulse signals based on microwave resonator storage devices [28–30]. Such devices make it possible to receive pulse signals with an amplitude several orders of magnitude higher than the generator signal from generators of continuous microwave radiation of low power and to

Integrated use of the available theoretical and experimental results allows us to raise the question of the possibility of creating technological devices for microwave local effects on small-sized objects and structures, including those ones of the micro- and nano-level.

References:

1. Chen, L.F. *Microwave Electronics: Measurement and Materials Characterization* / L.F. Chen, C.K. Ong, C.P. Neo, V.V. Varadan, V.K. Varadan – John Willy & Sons, Ltd, 2004. – 537 p.
2. Gordienko Yu. Ye., Poletaev D.A., Prokasa A.M., Slipchenko N.I. High-local microwave heating of semiconductors and dielectrics // *Applied Radio Electronics*. –Kharkiv: Publishing house KNURE, 2013. Vol. 11, №3.-P.426-430. (In Russ.).
3. Gordienko Yu. Ye., Shcherbak Ye. L., Levchenko A.V. Basic principles of the theory of high-local scanning microwave heating of semiconductors and dielectrics // *Physical surface engineering*. - Kharkov. KNU– 2015. - V.13, №3. - P.348-355. (In Russ.).
4. Bondarenko I.N., Gorbenko E.A., Krasnoshok V.I. Microwave switch based on waveguide T-junction for compression resonant pulse former // *Telecommunications and Radio Engineering*. Begell Hous, Inc., NY, (USA). – 2017. – Vol. 76, N 6. pp. 469-475.
5. Bondarenko I.N., Gorbenko E.A., Krasnoshok V.I. Microwave switch based on a combined coaxial-waveguide tee for a cavity pulse shaper // *Telecommunications and Radio Engineering*. Begell Hous, Inc., NY, (USA). – 2018. – Vol. 77, N 5. pp. 391-397.
6. Bondarenko I.N., Gorbenko E.A. Formation of powerful microwave pulses using resonator storage // *Telecommunications and Radio Engineering*. Begell Hous, Inc., NY, (USA). – 2018. – Vol. 77, N 15, pp.1311-1319.

MICROWAVE LOCAL DIAGNOSTICS OF BIOOBJECTS

I.N. Bondarenko, Yu.Ye. Gordienko, A.S. Nechiporenko, A.Yu. Panchenko
Kharkiv National University of Radio Electronics
61166, Kharkiv, Nauky ave. 14, dep. Microelectronics,
Electronic Devices and Appliances
тел.: (057) 702-13-62
E-mail: d_meda@nure.ua

Information on the content and changes in the distribution of free and bound water in biological objects allows for the diagnosis of their condition. Microwave diagnostics of bioobjects using resonator transducers with coaxial probe structures provide an opportunity for non-destructive analysis with millimeter and submillimeter spatial resolution. Analytical methods were used to study the nature of the interaction of electromagnetic fields created by coaxial apertures of various configurations with samples. On the basis of the obtained results, directions for the implementation of microwave high-local diagnostics techniques are determined.

Introduction

In comparison with other electrophysical methods, microwave methods, due to the possibility of measurements in the wide frequency range, which lie in the relaxation frequencies of macromolecules, have significantly higher information capacity. Most of the molecules of bioreactors are electrically neutral. The electrophysical properties of the molecule of bioreactors are acquired when they are bound to molecules of water that have a pronounced dipole moment. Therefore, solving the problem of determining the relationship of water with biological macromolecules and the creation of methods for controlling the state of water in biological substances is a step in the overall problem of diagnosing the state of bio objects.

Therefore, there is a significant set of physical factors that are related to obtaining information on the status of bioobjects on the basis of determining the amount and distribution of free and embedded water in the macromolecule of biological substances using microwave sensors relative to bio objects in vivo and in vitro, as well as in the period external influence on them, and corresponding to these sensors of secondary converters.

With the development of microwave diagnostics there was a need for concentration of efforts on the development of methods and controls for small-scale objects. This determined the use of the so-called near-field interaction of a sensitive element with the object, which led to the construction of primary measuring transducers on the basis of resonators [1].

The need for non-destructive control of objects of arbitrary shape caused, in addition, the advantage of the so-called aperture interaction of the field of measuring resonators with the object [2]. It is these principles that were the basis of most developments with microwave sensors in recent years.

In such a statement, the basic foundations were the base of the necessary alternative solutions to use near-field resonator sensitive elements. Their application allowed to create multi-parameter microwave sensors with wide possibilities of unification, accurate theoretical description of the characteristics of the transformation, dynamic positioning and substantial minimization of requirements to the sizes and form of the object of control.

This complex of properties provided an opportunity to implement the necessary locus of control of the heterogeneity of the distribution of values of parameters on the object surface and multidimensional diagnostics.

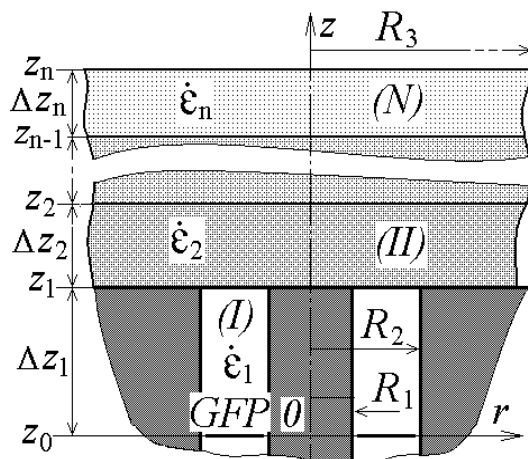
The main part

The dielectric properties of biopolymers in the field of dispersion of free water are largely determined by the state of water inclusions. As a result, dielectric characteristics are an informative material for obtaining data, first of all, about the state of water in the investigated system. In a number of processes there is a possibility to observe changes in these characteristics in moist specimens and solutions of biopolymers, as well as in cell suspensions.

In this way, the method of microwave dielectrometry, at achieving a certain level of accuracy, provides an opportunity to obtain effective methods of quantitative and qualitative estimates of changes in the state of bound water in the system, which correspond to structural changes in its components. To study the dielectric characteristics of biological objects, there is a method for measuring the complex permittivity of a wide class of biopolymers: solutions and suspensions, gels, films and powders, tissues and cell cultures under various external influences.

For instruments of operational control of the parameters of materials in the microwave range as a sensor, the open end of the coaxial line is very attractive (Fig. 1). It features simplicity, processability, the ability to work in a wide range of frequencies, high field location, easy preparation of samples to measurements. It is not difficult to make changes to the design of an open coaxial sensor (OCS), which opens the possibility of variation of measured samples and areas of application.

To realize the benefits of OCS, a strict assessment of its metrological properties is required. This requires the most accurate calculation of the distribution of the electromagnetic field. Modern software provides an opportunity to accurately calculate it. But to determine the relationship and understanding its properties, it is necessary to develop analytical methods.



R_1 – inner radius of coaxial line; R_2 – external

[1] **Fig. 1** – Geometric measurement scheme using OCS

Microwave control can be an effective addition to traditional methods for monitoring the status of bio objects, in particular, in clinical examination of patients. This requires the creation of specialized diagnostic equipment, the development of new and development of known methods of research. When creating a specific, small-scale equipment, a significant role is played by reducing the cost of development. Thus, there was a need to conduct a series of studies to answer a number of specific issues.

Among them it is especially important to note the following:

1. Justification and selection of the type and design of the microwave meter, which allows to increase the informativeness of the measurements and reduce the volume of biological samples.

2. Provision of measurements over a wide frequency range, which lies in the region of relaxation frequencies of free and bound water.

3. Development of a technique ensuring the elimination of the main errors of the theoretical calibration, in particular, guided by the criteria of hardware errors and the necessary accuracy of measurements in clinical conditions.

4. Conduct an analysis of the procedure for obtaining the final results and themselves for the creation of a model that allows the calculation of the properties of a microwave meter with a complex structure. Create a perfect model that provides further upgrades to sensors.

5. Development of procedure and algorithm of numerical solution of the problem of calculating the parameters of the microwave meter.

Resonator methods are most sensitive to changes in the parameters of samples of small sizes while preserving the necessary accuracy of measurements. Bulk resonators provide high accuracy, but require internal placement of the sample, which is inconvenient for current measurements. Quarter-wavelength coaxial resonator measuring transducers (RMT) through a coaxial measuring aperture (CMA) are coupled to the surrounding space. In doing so, they also provide sufficient accuracy of measurements [3]. In addition, the theoretical calibration of sensors based on RMT with CMA, estimation of their parameters is possible. They have the ability to localize the field in a given volume of the sample, a wide frequency range.

The quarter-wave RMT is a transitional link between open and closed types of resonator meters. They are most consistent with the requirements of minimizing sample volumes while maintaining high sensitivity. Execution of the open end of the RMT in the form of a coaxial measuring aperture of small size makes it possible to concentrate the electric field of the resonator in a small volume. This ensures a maximum change in the resonance frequency of the RMT, depending on the dielectric properties of the object. At the same time, the size of such a work area is determined not by the wavelength, but by the size of the CMA. In addition, the semi-open system is convenient for current measurements.

To solve problems of microprobe structures, the method of a given field was convenient. This method allows the integral parameters of the RMT (resonance frequency f and Q factor) to be replaced by the complex value of the equivalent concentrated CMA C capacitance. In this case, the electromagnetic wave base of the solution is preserved. The method of a given field greatly simplifies analytical calculations, but gives an approximate solution. Nevertheless, it has a fundamental opportunity in all the most important cases to provide the necessary precision.

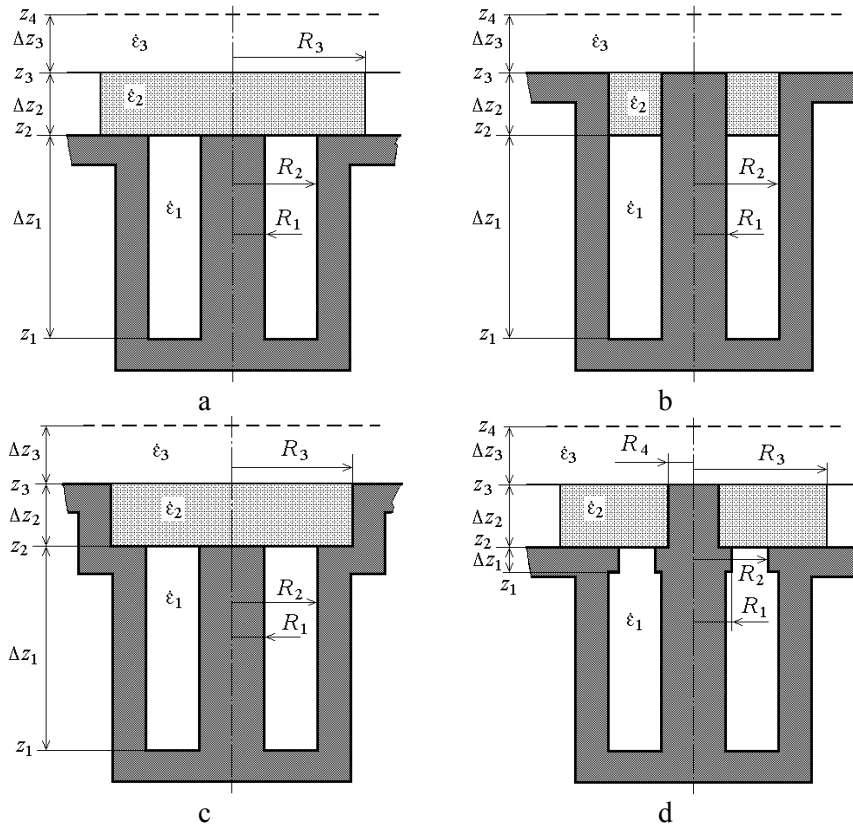


Fig. 2 – Examples of geometrical circuits of RMT with CMA and variants of placement of cuvettes with biomaterial into the working area

If we take into account that the relaxation properties of free water are most pronounced at frequencies near 10 GHz, and for the frequency bound in the macromolecules this will be lower than the design of such RMT will have acceptable dimensions, and the required volume of samples will be determined only by biological criteria.

An adequate mathematical model and the creation of an efficient calculation algorithm open the possibility of determining the distributions of an electric field inside the sample, which is necessary to take into account the characteristics of heterogeneous biological samples.

The geometric schemes of some variants of the performance of the CMA and the placement of the sample cuvette (Δz_2 , ϵ_2) are presented in Fig. 2, a-d. Only a sample (layer Δz_2) is shown. The effect of possible gaps and cuvettes for placing the sample can be taken into account with further refinement of the model.

Conclusion

The use of analytical methods for describing the processes of interaction of electromagnetic fields formed by coaxial measuring apertures with the studied structures of various types, combined with numerical methods of mathematical modeling, make it possible to more clearly visualize the nature of the processes and even define a number of requirements for measuring instrument designs.

Moreover, the results obtained in this case can be applied to the already existing and used in practice RMT based on different types of resonant structures, since in all of them the working body providing the local measurement is a coaxial probe [4 – 6].

At the same time, for calibration of RMT, it is necessary to determine the transfer function, which relates the change in the electrophysical characteristics of the local areas of the objects under study with the measured changes of the quality factor and the resonant frequency. It should be borne in mind that for each specific design RMT and the sample placement options will have its own transfer function.

The solution to this problem is possible by conducting for each case a series of measurements with reference materials and building approximation conversion functions based on them taking into account a possible analytical description.

References

1. Chen, L.F. *Microwave Electronics: Measurement and Materials Characterization* / L.F. Chen, C.K. Ong, C.P. Neo, V.V. Varadan, V.K. Varadan – John Willy & Sons, Ltd, 2004. – 537 p.
2. Gordienko Yu. Ye., Petrov V.V., Khamud F.M. Estimation of Numerical-Analytical Models of Microwave Cavity Detectors with a Coaxial Measuring Aperture // *Telecommunications and Radio Engineering*. vol. 65, № 9-10, pp. 789-798, 2006.
3. Steinhauer D.E., Vlahacos C.P., S. Dutta S.K. at all. Quantitative imaging of sheet resistance with a scanning near-field microwave microscope // *Appl. Phys. Lett.* № 72. pp. 861–863, 1998.
4. Ch. Lin, Bondarenko I.N., Panchenko A.Yu., Slipchenko N.I. Electrodynamic sensor for assessing transformations of the state of water in biological objects // *Telecommunications and Radio Engineering*. vol. 77, № 12. pp.1103-1112, 2018.
5. Gordienko Yu.Ye., Bondarenko I.N., Slipchenko N.I. Biological objects parameters meter based on microwave microscope with coaxial resonant sensor // *Proc. of the 10-th International Conference “Modern problems of radio engineering, telecommunications and computer science” (TCSET 2010), Ukraine. Lviv-Slavske, Feb. 23-27, 2010.* art. no. 5446176, p.137-138.
6. Bondarenko I.N., Gordienko Yu.Ye., Levchenko A.V. Submillimetric localization of microwave diagnostics and modification of objects of various nature // *9th International Kharkiv Symposium on Physics and Engineering of Microwaves, Millimeter and Submillimeter Waves (MSMV'2016), Kharkiv, Ukraine, 2016.* № 7538014.

LUMINESCENCE STUDIES OF THE DYE SELF-DESENSITIZATION PROCESSES OF TYPE II

Tyurin A.V., Bekshaev A.Ya., Zhukov S.A.
Research Institute of Physics Odessa I.I. Mechnikov National University
65023, Odessa, Paster st., 27,
tel. (048)723-80-36
E-mail: zhukov@onu.edu.ua

Abstract

Spectral sensitization of photosensitive systems by dyes of the positive and negative charge states, adsorbed on the surface of a condensed medium, leads to the interaction of their molecular and J-aggregated forms, which is reflected in the low-temperature ($T = 77\text{ K}$) luminescence spectra and causes the anti-Stokes anomalously slowed fluorescence of molecular dyes at excitation of their J-aggregates. We have proved that it is these electron-hole processes that are responsible for the dyes' self-desensitization of type II.

For photosensitive and sensory systems, a luminescent method is proposed to control the interaction of molecular and polymolecular forms of dyes, which is responsible for the self-desensitization processes.

Introduction

Both the separate and J-aggregated dye molecules absorb light of different spectral ranges with high efficiency, which is used in photochemical elements where the photoexcited dyes transfer the non-equilibrium charge carriers, the electron and the hole, to active centers, being the basis of optoelectronic devices. The most wide applications of the dyes is coupled with the spectral sensitization of photosensitive systems.

The effectiveness of the dye sensitizer is determined by the transfer of electrons and holes, photoexcited in the dyes, to active centers contained in a condensed medium on the surface of which they are adsorbed. However, not all photo-excited in the dye electrons and holes are delivered to these centers. Part of the charge carriers is lost due to recombination in the dye itself, as a result of the interaction of the polymolecular forms of the dye with the molecular dye [1], which determines the so-called self-desensitization effect [2].

For the case of photosensitive emulsions, two types of the dye-induced self-desensitization are defined in [2]:

1) if an electron and a hole of the photoexcited dye-sensitizer migrate inside the dye itself and recombine there, then this process is called self-desensitization of type I

2) the electron of the photoexcited dye is delivered to the active center while the hole remains in the dye, due to which a radical cation of the dye D^+ appears on the surface of a condensed medium containing the active centers. Then, D^+ captures the electron from the active center and, as a result of recombination, the radical cation D^+ relaxes to the ground unexcited state. This process of the electron-hole recombination is most likely for J-aggregating dyes and is called self-desensitization of type II.

Therefore, in order to evaluate the effectiveness of the dye in all areas of its application, it is necessary to take into account the processes of self-desensitization. It is very difficult for realization on the basis of only spectrosensitometric tests; that is why in this paper we have proposed a luminescent technique for this purpose that allows one to control the interaction processes of molecular and multimolecular forms of the dye responsible for the self-desensitization.

Experimental data

The luminescence measurements were performed based on the experimental setup described in [3] with mechanical modulation of the signal and under the condition that the

sample was excited and its radiation was recorded during 10^{-4} s, the dark interval was $1.1 \cdot 10^{-3}$ s and at the modulation frequency 400 Hz. This technique allows recording phosphorescence and anomalously slow fluorescence, with an optimal relaxation time, which is decisive in the self-desensitization processes.

As objects of the luminescent investigations at $T = 77$ K, two types of emulsion were chosen:

Emulsion-1. Homogeneous emulsion containing microcrystals (MC) AgBr(I) (3% AgI) of the mean size $d \approx 0.24 \mu\text{m}$, generated in the gelatine environment by means of the two-stream controllable emulsification at $p\text{Br}=2$. The spectral sensitization of the emulsion was performed by the anion J-aggregated dye – of 3,3'-di- γ -sulfurpropyl-9-ethyl-4,5,4',5'-dibenzocarbocyaninbetaine pyridinium salt (D1);

Emulsion-2. Homogeneous AgBr-emulsion with the MC of the mean size $d \approx 0.15 \mu\text{m}$, subjected to the sulfur sensitization during 1.5 hour at 47°C in presence of $2 \cdot 10^{-4}$ mol of $\text{Na}_2\text{S}_2\text{O}_3$ / mol AgBr. The spectral sensitization of the type-2 emulsion was performed by the cation J-aggregated dye 3,3',9 - trietil- 5,5'-difeniloxycarbocyaninnitrat (D2).

To register the self-desensitization processes, the dye concentrations were used that allow formation of polymolecular forms of the dye J-aggregates.

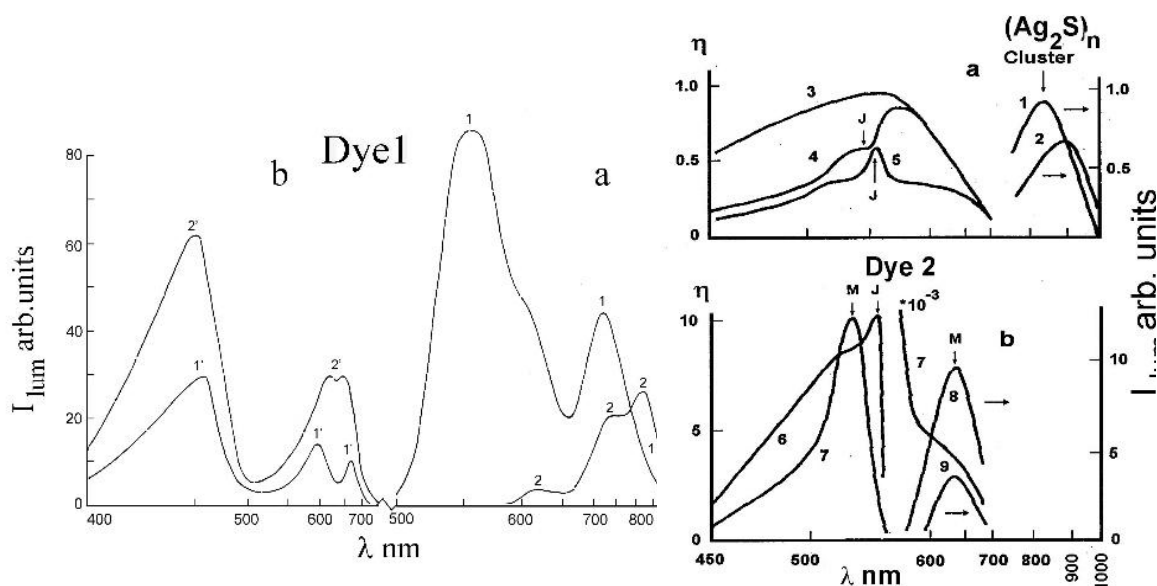


Fig. 1

Fig. 2

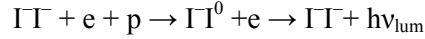
Fig. 1. Spectra of luminescence (a) and excitation (b) of the Emulsion-1 with introduced D1 (10^{-3} mol D1 / mol AgBr). The luminescence spectra 1, 2 were registered upon excitation by the monochromatic light with λ (nm): 1 – 450; 2 – 670. The excitation spectra were registered for the luminescence with λ_{max} (nm): 1' – 750; 2' – 800.

Fig. 2. (a) Luminescence spectra of the $(\text{Ag}_2\text{S})_n$ clusters excited by the monochromatic light with λ (nm): 1 – 615; 2 – 690. Spectra of the luminescence excitation of clusters $(\text{Ag}_2\text{S})_n$ for $\lambda_{\text{max}} = 850$ nm in the type 2 emulsion with the dye D2 concentration (mol D2 / mole AgBr): 3 – 0; 4 – $5 \cdot 10^{-5}$; 5 $3 \cdot 10^{-4}$.

(b) Spectra of the fluorescence excitation of the D2 J-aggregates for $\lambda_{\text{max}} = 570 - 580$ nm (6); phosphorescence spectra of the molecular D2 for $\lambda_{\text{max}} = 640$ nm (7) and phosphorescence spectra of the molecular D2 introduced into the Emulsion-2, at the excitation by the monochromatic light with λ (nm): 8 – 530; 9 – 690.

In the luminescence spectrum of the Emulsion-1, excited by monochromatic light with $\lambda = 450$ nm, four emission bands are observed (Fig. 1a, curve 1):

(1) luminescence band of paired iodine centers with $\lambda_{\max} \approx 560$ nm corresponds to the recombination scheme:



(2) luminescence band with $\lambda_{\max} \approx 640$ nm is associated with the anomalously slowed fluorescence of D1 adsorbed on the surface of MC AgBr(I) in the molecular state (M_{ASF});

(3) luminescence band with $\lambda_{\max} \approx 750$ nm, according to our data [4], is associated with centers ($I\Gamma - Ag_2^+$) in the emulsion AgBr(I), which are formed due to the dye adsorption on the MC surface described by the scheme



where Ag_i^+ is the interstitial silver ion, and the occurrence of luminescence with $\lambda_{\max} \approx 750$ nm can be described by a recombination scheme:



(4) The luminescence band with $\lambda_{\max} \approx 710$ nm in the excitation spectrum, as well as the luminescence band with $\lambda_{\max} \approx 750$ nm, is associated with the three maxima with $\lambda = 450, 600$ and 690 nm, which are related to the silver halide, molecular and J-aggregated D1, respectively (Fig. 1b, curve 1'). The luminescence band with $\lambda_{\max} \approx 710$, in its spectral position corresponds to the fluorescence band of the J-aggregate of D1, and, therefore, it can be attributed to the anomalously slowed-down fluorescence of the D1 J-aggregate (J_{ASF}).

For the Emulsion-1, the following should be particularly noted: when excited by the monochromatic light corresponding to the absorption band of the D1 J-aggregates ($\lambda = 670-690$ nm) (Fig. 1a, curve 2), the anti-Stokes anomalously slowed fluorescence of the molecular D1 M_{ASF} ($\lambda_{\max} = 610-640$ nm), the D1 band J_{ASF} ($\lambda_{\max} \approx 710$ nm), and the band overlapped with it with $\lambda_{\max} \approx 750$ nm, are observed in the luminescence spectrum as well as the phosphorescence band of the molecular D1 M_F ($\lambda_{\max} \approx 800$ nm) (Fig. 1a, curve 2).

– The luminescence of the Emulsion-2 (Fig. 2a, curves 1 and 2) is accompanied by the appearance of a luminescence in the near infrared region with $\lambda_{\max} \approx 820 - 880$ nm, which is due to the luminescence of $(Ag_2S)_n$ -clusters adsorbed on the surface of AgBr MC. When the adsorption of D2 additionally occurs on the $(Ag_2S)_n$ -cluster surface, the luminescent properties of the system “cluster-adsorbed D2” are distinguished by a number of features:

– During adsorption of a small amount of dye ($5 \cdot 10^{-5}$ mol D2 / mol AgBr) on a cluster, a decrease in the efficiency of cluster luminescence excitation in the absorption bands of D2 is observed (Fig. 2a, curve 4). This decrease in the excitation efficiency occurs due to the overlap of the system of excited states of the dye and cluster, which causes the so-called Fano effect [5];

– An increase of the D2 concentration in the AgBr emulsion to $3 \cdot 10^{-4}$ mol D2 / mol AgBr is accompanied by the appearance of typical dye-sensitized luminescence of clusters (on the cluster emission curve, maxima appear at $\lambda = 525$ and 550 nm, coinciding with the absorption maxima of the M and J bands of D2 (Fig. 2a, curve 5)). This is due to the fact that, at high concentrations of the adsorbed dye, the clusters are covered not by monomolecular, but by polymolecular layers of the dye, and therefore it is possible to transfer the energy of the excited D2 from the “outer” layers. In this case, two interrelated effects are observed: a decrease in the cluster luminescence excitation efficiency (for D2, this is the region $\lambda > 580$ nm (Fig. 2a, curve 5), and the excitation of the molecular dye in the same spectral region (Fig. 2b, curve 9). These effects are determined by the energy transfer from the excited J-aggregate of D2 to the levels of the molecular D2. Consequently, upon the multilayer adsorption of D2 in the “cluster – D2” system, energy transfer from the excited J-aggregate of D2 is possible not only to a cluster but

also to a molecular D2, which leads to an anti-Stokes abnormally slowed fluorescence of molecular D2 during the absorption of two light quanta by the J-aggregate D2 (Fig. 2b, curve 9).

Therefore, depending on the frequency of the light used to excite the luminescence of the “cluster – adsorbed D2” system, switching of the electron-hole processes is possible, which can be used in molecular electronics

Discussion

As follows from the above experimental results, the adsorption of molecular and multimolecular forms of the dye in various charge states is possible both on the surface of the AgHal MCs and on the surface of $(Ag_2S)_n$ clusters adsorbed on the AgBr MC surface. In both cases, the photoexcitation of J-aggregates of adsorbed dye is accompanied by the occurrence of anti-Stokes anomalously slowed-down fluorescence of the molecular dye (M_{AASF}). Based on the definition of self-desensitization, the M_{AASF} , when excited by light from the absorption region of J-aggregates, corresponds to self-desensitization by a dye of type II.

Therefore, the luminescent method allows to associate the self-desensitization with specific electron-hole processes, which are caused by the interaction of the polymolecular forms of the dye with the molecules of the dye-sensitizer. In our case, when J-aggregates of the dye are excited, self-desensitization of type II occurs only in the molecular dye and is controlled in detail by the proposed luminescence technique, which can be used to control self-desensitization processes

The control of electron-hole processes of this sort is especially important for the case of spectral sensitization of fine highly-dispersed silver-halogen emulsions used in the holography.

Conclusions

When the dyes of two charge states, adsorbed on the surface of the AgHal and $(Ag_2S)_n$ MC clusters in the molecular and J-aggregated state, are used for spectral sensitization of photosensitive systems, the anti-Stokes anomalously slowed fluorescence of the molecular is revealed when the dye J-aggregates were excited. This fluorescence is responsible for the dye self-desensitization of the type II.

For photosensitive and sensory systems, a luminescent technique has been proposed that enables not only controlling the interactions of molecular and polymolecular forms of the dye responsible for the self-desensitization processes, but also opens ways to the most efficient utilization of photocarriers due to suppression of the self-desensitization effects.

References

1. Тюрин А.В., Чурашов В.П., Жуков С.А., Манченко Л.И., Левицкая Т.Ф., Свиридова О.И. Оптика и спектроскопия. Т. 104, №1. С. 97.
2. Шапиро Б.И. Теоретические начала фотографического процесса. М.: Эдиториал УРСС, 2000. 209 с.
3. Жуков С.А. Люминесценция кристаллов галогенидов серебра смешанного состава. Дисс. канд. физ.-мат. наук. Одесса 1991. 121 с.
4. Belous V.M., Akhmerov A.Yu., Zhukov S.A., Orlovskaya N.A., Sviridova O.I. Sci. Appl. Photo. 1997. V.38(6). P.529.
5. V. Fano. Phys. Rev. 1961. V. 124. P. 1866.

FEATURES OF THE USE OF MICROWAVE MICROSCOPY IN NANO-ELECTRONICS TECHNOLOGY

I.M. Shcherban, Yu.Ye. Gordienko
Kharkiv National University of Radio Electronics
61166, Kharkiv National University of Radio Electronics,
tel. (057) 702-13-62
E-mail: ihor.shcherban@nure.ua

The basic principles for the diagnostics of nanoelectronic materials using Scanning Microwave Microscopy (SMM) based on resonator transducers (RT) with coaxial microprobe aperture is discussed in the report. The prospects for multi-parameter diagnostics are discussed, as well as the elimination of difficulties associated with the separation of the contribution of all influencing parameters. In particular, the effect of the gap between the sample and the RT probe, as well as changes in the tip radius in the process of diagnostics, is considered in detail. It is proposed to form a so-called combined signal, which is invariant to such interfering factors as the non-reproducibility of the gap between the tip of the relay and the object, as well as changing the geometry of the tip during operation. It is shown that the invariance of the formed signal is not always perfect, and at small values of the gap, it may deteriorate. A detailed analysis of factors that worsen the degree of suppression of the influence of interfering factors is presented, and methods for their exclusion are discussed.

Introduction

Nanoelectronics is an area in which the achievements of nanophysics receive the most rapid implementation and development. The rapid progress in this area requires, accordingly, the development of new methods for controlling the properties of the structures of materials, on the basis of which modern electronic equipment and devices will be formed.

One of the main criteria for monitoring the studied objects in nanotechnology is the resolving power of the diagnostic tool, both spatial and measured physical quantity. Spatial and physical locality, achievable when using methods of scanning probe microscopy allows it to occupy a leading position in this area [1].

SMM is one of the youngest and very rapidly developing tools of probe monitoring methods. Nevertheless, the SMM is capable not only of unite a range of tasks solved using Scanning Tunnel Microscopy (STM), Atomic Force Microscopy (AFM) and Scanning Capacitive Microscopy (SCM), but also significantly multiply them. The main feature of the SMM is the multiparameter diagnosis. Since, unlike AFM and STM, it becomes possible not only to measure the surface profile, but also the profiles of the main electrophysical parameters of the objects ϵ , $\text{tg}\delta$ and σ both in depth and on the surface of the material under study. However, together with that, the dependence of the SMM scanning signals on the influence of many factors, as well as their combinations, creates difficulties in obtaining adequate measurement results. As shown in our work [2], the obtained diagnostic results need a so-called reconstruction.

In some works, the hybrids that are SMM with a sensitive element formed of an AFM or STM cantilever are often found. In work [3], the authors use AFM to maintain the gap constant between the sensor and the object during scanning. This simplifies the procedure for reconstructing the resulting figure, in the event that the surface profile of the object under study does not interest us or has a constant value.

According to the type of physical phenomena used in the primary measuring transducers, microwave sensors can be divided into waveguide and resonator. Resonator sensors (RS) have always been an alternative to waveguide, mainly due to the higher sensitivity and hardware compactness of building on the basis of them technical diagnostic tools. Higher sensitivity is determined by the accumulation of measurement information against the background noise in Q times (resonator quality factor).

Information about the properties of an object with this approach is extracted through a shift in the resonant frequency and a change in the quality factor of the RS. Often these signals

are called fundamental. In practice, vector analyzers of microwave circuits are usually used for their registration. Also, quite a lot of works is devoted to the formation of a packet of fundamental signals based on an automatic frequency control system (AFC) of the generator according to the RS [5]. However, the obtained measurement information signals by the two methods mentioned above are not without influence of the so-called interfering factors. These include the uncontrolled gap between the tip of the resonator probe (RP) and the object, changing the shape and radius of the tip during operation, changing or deviating from the calculated values of the parameters of the microwave tract. [4]. These and other factors can change not only the amplitude of the signals $\Delta Q/Q_s$ and $\Delta f/f$, thereby introducing an error in the measurements, but also a view of the conversion characteristics of RS [4]. These factors significantly limit the use of SMM compared to STM and AFM. Naturally, this also applies to local microwave diagnostics, in general.

Basic provisions

To search for possible directions for solving the problems involved, let us consider the physical nature of the signals formation from the position of resonator perturbation by an object through the aperture. In the approximation of small perturbations that are permissible in measurement situations, the fundamental signals $\Delta f/f$ and $\Delta Q/Q_s$ can be expressed as follows [4]

$$\frac{\Delta Q}{Q_s} = \frac{\int_{V_r} \sigma E^2 dV}{2 \cdot \int_{V_r} E^2 dV} \cdot \varepsilon_s \cdot \text{tg} \delta \cdot Q_0 \quad (1) \quad \frac{\Delta f}{f} = \frac{\int_{V_s} E^2 dV}{2 \cdot \int_{V_r} E^2 dV} \cdot (\varepsilon_s - 1) \quad (2)$$

$$\frac{\Delta Q}{Q_s} = \frac{\Delta f}{f} \cdot \left(\frac{\varepsilon_s}{\varepsilon_s - 1} \right) \cdot \text{tg} \delta_s \quad (3) \quad N = \frac{\Delta Q}{Q_s} / \frac{\Delta f}{f} = \frac{\varepsilon_s}{\varepsilon_s - 1}_0 \text{tg} \delta_s \cdot Q_0 \quad (4)$$

It follows from the above relations that both signals are essentially determined by a physically uniform process of interaction of the microwave electric field with the object's matter through the real and imaginary parts of the dielectric constant of the object. Therefore, in it is shown that it is advisable to determine the distribution profile of $\text{tg} \delta$ through the ratio of the fundamental signals $\Delta Q/Q_s$ and $\Delta f/f$. Such a signal is called a combined one and the degree of influence of interfering factors on it turns out to be significantly less, which suggests its invariance to interfering factors. However, more thorough numerical studies carried out by us in this work show that the presentation of the invariance of such a signal to the gap is highly idealized.

In fig. 1 shows the dependence of the fundamental signals on the gap between the tip and the sample, as well as on the tip radius in relative units.

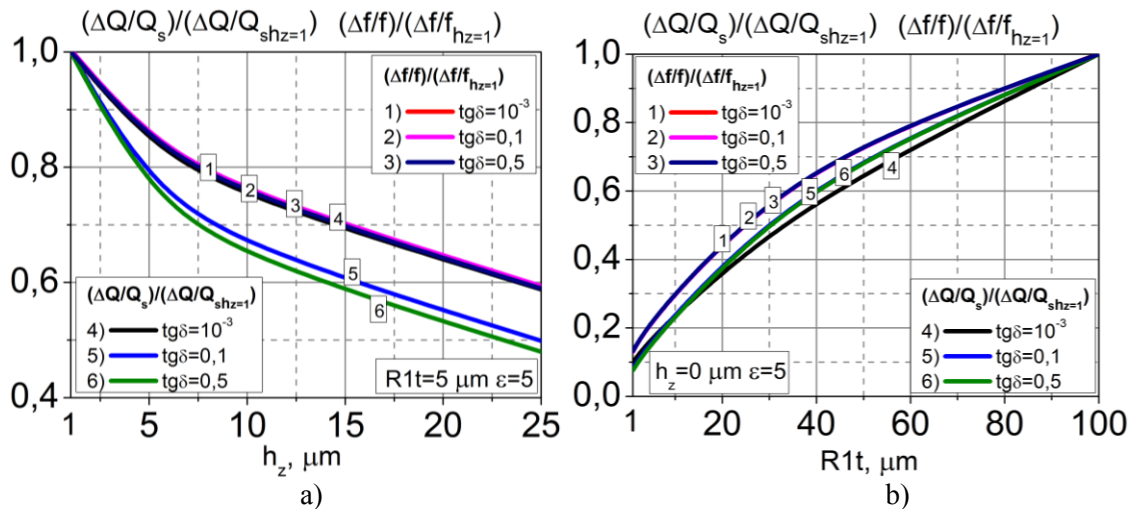


Fig. 1 – The peculiarity of the influence of the gap (a) and the tip radius (b) on the fundamental signals presented in relative units

As you can see, the nature of changes in the fundamental signals is quite close in character, and in some cases even identical. A sufficiently high correlation of signals is achieved at low values of ε and $\text{tg}\delta$. However, when $\text{tg}\delta > 10^{-3}$, the identity of the waveform is violated, and the degree of suppression of the influence of interfering factors in the diagnosis decreases accordingly.

Violation of invariance with increasing radius of the tip is presented in detail in Fig. 2.

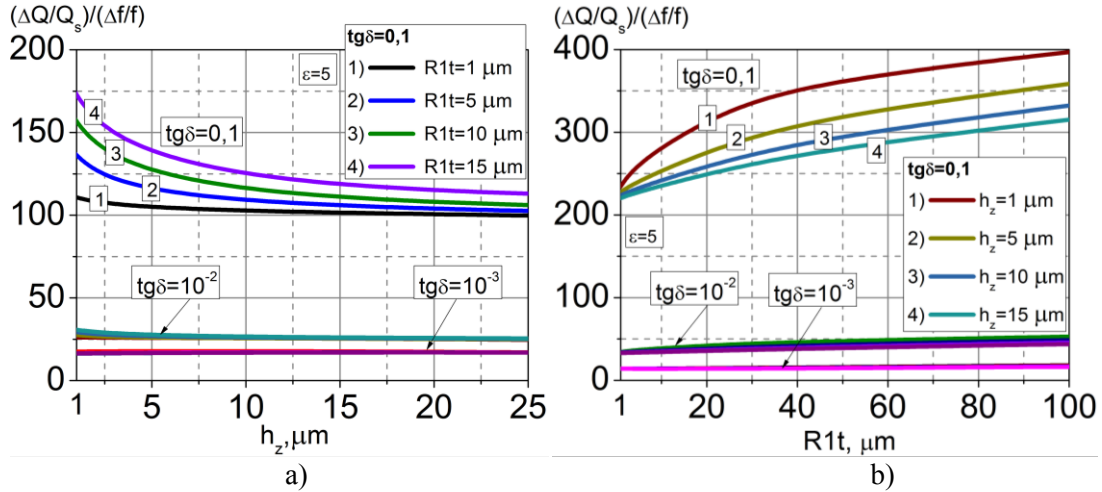


Fig. 2 – Invariance of the combined signal to the gap between the RP and the object for several values of $R1t$ (a), and to a change in the tip radius for several values of the gap h_z (b)

As can be seen from fig. 4, invariance is not observed at small gaps “ $h_z < R1t$ ”. To clarify the physical causes of this feature, we carried out numerical studies, the results of which are shown in Fig. 3.

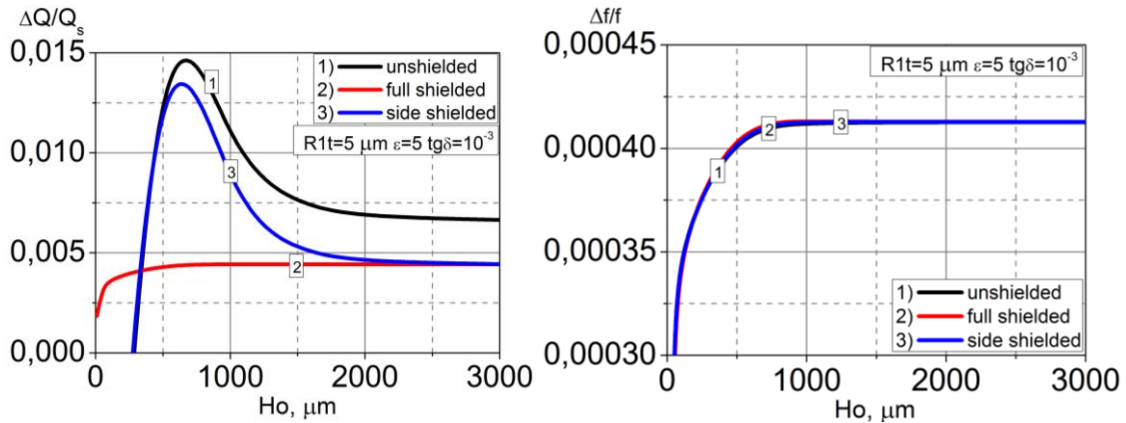


Fig. 3 – Changes in the fundamental signals of the RP, depending on the sample thickness at various degrees of shielding

From the presented dependences, it can be seen that shielding of thin samples does not affect the signal $\Delta f/f$ and sufficiently reduces the signal $\Delta Q/Q_s$. From this it follows that the cause of the non identity of these signals is the loss to the radial line on the gap. These losses can be reduced for samples with a low $\text{tg}\delta$ by side shielding. Diagnostics of samples with $\text{tg}\delta > 10^{-2}$ should be carried out at $h_z > R1t$. Therefore, to improve the gap invariance, it is necessary to sacrifice the locality of the scan.

Invariance to a change in the radius of the tip for such a combined signal apparently occurs because of the compensating influence of the gap, which changes with the change in the radius of the tip.

Conclusion

The report discusses the prospects for the use of SMM for the diagnosis of nanoelectronics structures. The study of various electromagnetic properties of materials using SMM based on resonator probes with a coaxial aperture provides not only high spatial resolution, but also a significant increase in the contrast of images.

Particular attention is paid to the expansion of ideas about the possible multiparameter high local microwave diagnostics. First of all, this is due to the basing of the fundamental SMM signals indicated in the report for such universal physical parameters of the object as the effective dielectric constant ϵ and magnetic permeability μ . These parameters, in turn, are determined by a wide range of properties of materials and structures, which ensures the expansion of diagnostics in the area of influencing factors.

The report substantiates the possibility of subdivision of various affecting and influencing factors on diagnosed and interfering. Accordingly, in addition to the fundamental scan signals, it has been proposed to form combined signals that in one way or another reduce the influence on the diagnostics of interfering factors and emphasize the functionally important ones. An illustrative example of such combined signals are signals built on the ratio of fundamental signals “for example, $(\Delta Q/Q_s) / (\Delta f/f)$ ” or their relation to the initial signals “for example, the signal of the initial quality factor of the probe Q_0 ”.

The features of the dependence of the degree of invariance on the range of change in the interfering factor and the range of change of the diagnosed property are theoretically established. An example of the interfering factors are taken: the gap, the irreproducibility of the geometry of the probe and its shape. An example of a diagnosed property is taken: $\text{tg}\delta$ and relative dielectric constant of the local region of the material of the object.

It is shown that the invariance declared on the basis of the theory of small perturbations often is not observed due to the variation of interfering factors of the magnitude of the microwave losses of the probe to radiation into formed up radial line is not being taken into account.

References

1. Bhushan B. Scanning Probe Microscopy - Principle of Operation, Instrumentation, and Probes Springer Handbook of Nanotechnology / B. Bhushan, M. Othmar // Springer-Verlag Berlin Heidelberg. – 2007. – p. 591.
2. Gordienko Yu. Ye. Principles of physical interpretation of images in the SMM / Yu. Ye. Gordienko, I.M. Scherban, A.V. Levchenko // Journal of Surface Physics and Engineering. – 2018. – Vol. 3. – № 1. – p. 17–23.
3. Ju, Y. A microwave probe nanostructure for atomic force microscopy / Y. Ju , M. Hamada , T. Kobayashi, H. Soyama // Microsyst. Technol. – 2009. – Vol. 15. – № 8. – p. 1195–1199.
4. Gordienko Yu.Ye. Suppressing the effects of interfering factors in local microwave diagnostics / Gordienko Yu.Ye., Shian O.P., Shcherbban I.M. / Telecommunication and Radio Engineering. – 2016. – Vol. 75. – № 13. – p. 1221–1229.
5. Xiang D. Quantitative complex electrical impedance microscopy by scanning evanescent microwave microscope / D. Xiang, C. Gao // Materials Characterization. – 2002. – № 48. – p. 117–125.

**NANOELECTRONIC SENSORS
AND INFORMATION SYSTEMS.
NANOELECTRONIC SENSORS
FOR BIO-ENGINEERING**

NEW APPROACHES TO CREATION OF HIGH- EFFICIENCY RECEIVERS OF SOLAR RADIATION FOR CONCENTRATOR SOLAR MODULES

V.N. Borshchov, N.I. Slipchenko, O.M. Listratenko, O.V. Kravchenko, O.V Syddia.
Limited liability company «Research and Production Enterprise «LTU»
61145, Kharkov, st. Novgorodskaya, 3, 1st floor, office 104
tel. (050) 591-24-55
E-mail: kravcenkoaleksandr671@gmail.com

Current state and trends in development of solar photovoltaic, including technology of concentrator solar modules on Fresnel lenses and mirror concentrators, are considered. New approaches to creation of high-performance receivers of concentrated solar radiation based on aluminum-polyimide Chip-On-Flex (COF) assembly technology and gallium-arsenide solar cells with efficiency of 46-48% have been proposed. Experimental samples of innovative solar radiation receivers for point concentrator modules on Fresnel lenses were manufactured and investigated.

Keywords: concentrator solar photovoltaic, gallium-arsenide solar cells, solar radiation receivers, design-technological solutions.

Growth rates and development plans of "solar" photovoltaic in industrialized countries are impressive in scale. Solar photovoltaic is becoming a key sector in the global power industry. Forecast of the long-term development of solar energy in the world suggests a global installed solar energy capacity of 4,500 GW by 2050. In this case, solar energy will generate approximately 16% of the world's electricity, which confirms its relevance and importance for the global electric power industry.

Achieving economically acceptable values of solar electricity cost in Ukraine, even under insufficiently good insolation conditions, is also quite realistic, but due to creation of new generation solar systems with high concentration ratio based on the concept of small-size (500mmx500mm) high-efficiency gallium photovoltaic modules. At creating such modules it becomes possible to reduce cost of semiconductor materials for production of a given electrical power in proportion to solar radiation concentration ratio. At concentration ration up and more than 800 times, cost of gallium-arsenide solar modules even now can be reduced to less than 1 Euro per watt. And creation of large solar stations on their case will provide cost of produced electricity less than 0.1 Euro per kWh.

Goal of the work is development of new approaches to creation of more advanced design and technological solutions of radiation receivers for concentrator solar modules based on using modern high-performance materials and components. Including gallium-arsenide solar cells (SC) with efficiency of 46-48% which are able to provide high competitive ability of concentrator solar systems with low energy costs up to 5-10 euro cents per kWh. Carrying out studies to confirm of correctness of choice of design solutions, assembly technology and justification of the required lifetime of concentrator receivers for solar point focus modules with high concentration ration on Fresnel lenses [1, 2].

At the research were developed few high-concentration solar radiation receiver designs (HCPV modules) on Fresnel lenses based on triple-junction gallium-arsenide solar cells manufactured by ENE (Belgium) and AZUR Space (Germany) with an efficiency of 30-36% and own development of innovative aluminum-polyimide Chip-On-Flex (COF) assembly technology. The objects of research were samples of quality test structures (QTS) and experimental samples of concentrated-radiation receivers with secondary optical elements (SOE).

Also was carried out works on the analysis and selection of materials, design studies for development of designs of secondary optical elements (SOE). For testing manufacturing technology of receivers, test structures of quality and various types of samples of receivers of concentrated radiation were developed and manufactured (Fig. 1, 2). Accelerated thermo cycle tests of receiver samples were also performed to assess their reliability and lifetime in accordance with standard IEC 62108 (item 10.6.3) "Concentrator photovoltaic (CPV) modules and assemblies - Design qualification and type approval". This standard defines requirements for electrical, mechanical and temperature characteristics of concentrator photovoltaic modules and their assemblies (receivers) that are acceptable for long-term operation in normal climatic conditions [3, 4].



Fig. 1 – Receivers of concentrated solar radiation based on triple-junction gallium-arsenide SC with types of integrated secondary optics: a) truncated cone, b) truncated pyramid

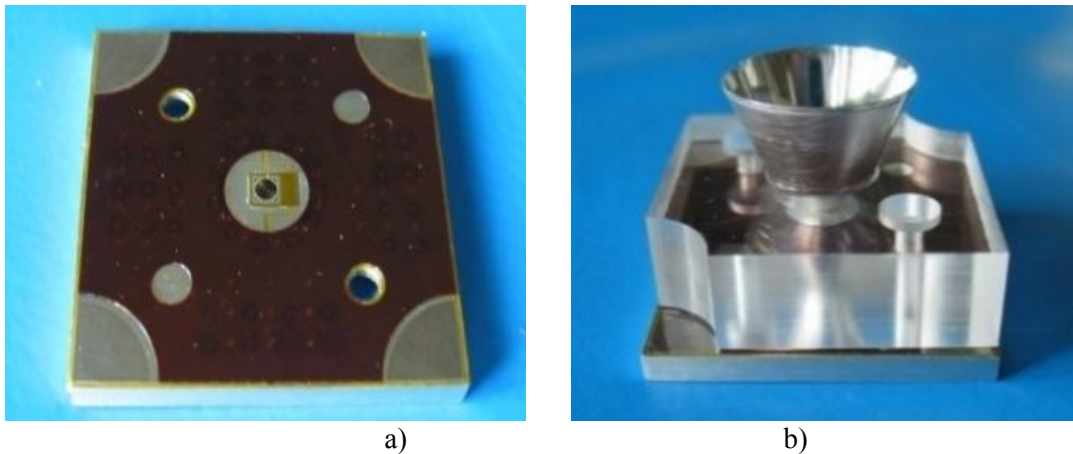


Fig. 2 – Quality testing structures based on gallium-arsenide SC: a) without SOE; b) with integrated SOE

The QTS consisted of triple-junction InGaP / GaAs / Ge solar cells, encapsulated by silicon compound ELASTOSIL S690 (Waker Silicones, Germany). Holder with the truncated cone SOE, interconnection board based on adhesiveless aluminum-polyimide carrier, protective diode and an aluminum flat heat sink. The solar concentrating radiation receivers included triple-junction InGaP / GaAs / Ge solar cells — 9 pcs., SOE — 9 pcs., interconnection flexible aluminum-polyimide board, protective diode and heat sink.

Accelerated forced thermo cycle tests of above described samples were carried out to confirm the correctness of choice of design solutions and receiver assembly technology. The

influence of simultaneous effect of alternating temperature changes and repeated short-term current load in the forward direction on the solar cell and the SC group of $1,25 I_{sc} = 500\text{mA}$ at $T > 25^\circ\text{C}$ and ten electric cycles per thermo cycle was also determined. At the same time, the influence of thermal cycling effects on electrical parameters and durability of the receivers designed for operation in normal conditions for 20 years (8 hours / day, total time 58400 hours) with solar concentration ratio up to 750 times and output power from 1.5W up to 15W.

Parameters of the test mode were determined taking into account the physics and mechanical properties of used materials, kinetics of changes in characteristics and recommendations of international standards in order to prevent conditions exceeding the temperature limits of used materials, and conditions accelerating atypical failure mechanisms.

According to IEC 62108 (clause 10.6.3) standard, taking into account properties of used materials, financial constraints, saving time and resources, test option TCA - 2 has been chosen with maximal temperature in the thermal cycle plus 110°C and minimum temperature minus 40°C with total number of thermal cycles at least 500. For testing 9 QTSs with SOE on the basis of triple-junction gallium-arsenide SC from Azur Space Company and ENE Company were manufactured. In three versions of QTS based on triple-junction gallium-arsenide SC from Azur Space Company for assembly flexible boards made of FDI-A-50 with a Ni-coating $1-2\ \mu\text{m}$ thick on Al-conductors were used. For investigations of corrosion resistance of welded joints of flat aluminum leads without nickel coating, obtained by ultrasonic welding with Au / Ag contact pads of solar cells, batch of 6 QTS with SOE was produced. Also 3 concentrated solar radiation receivers were manufactured on the basis of triple-junction gallium-arsenide solar cells from ENE Company with SOE using flexible board made of FDI-A-50 adhesiveless aluminium-polyimide dielectric (aluminum flat leads $30\ \mu\text{m}$ thick).

After conducting 100 thermal cycles electro-energy parameters both in the QTS and in the receivers did not change. After 500 thermal cycles output power of eight of the nine tested QTS decreased by no more than 5.5% (Fig. 3). For receivers output power decreased by no more than 2.5% (Fig. 4). This allows to conclude that the chosen design and technological solutions of concentrator receivers based on triple-junction GaInP/GaAs/Ge SC and innovative COF assembly technology meet the requirements of IEC 62108 (clause 10.6.3) standard. Expected lifetime of concentrator receivers with SOE is at least 20 years.

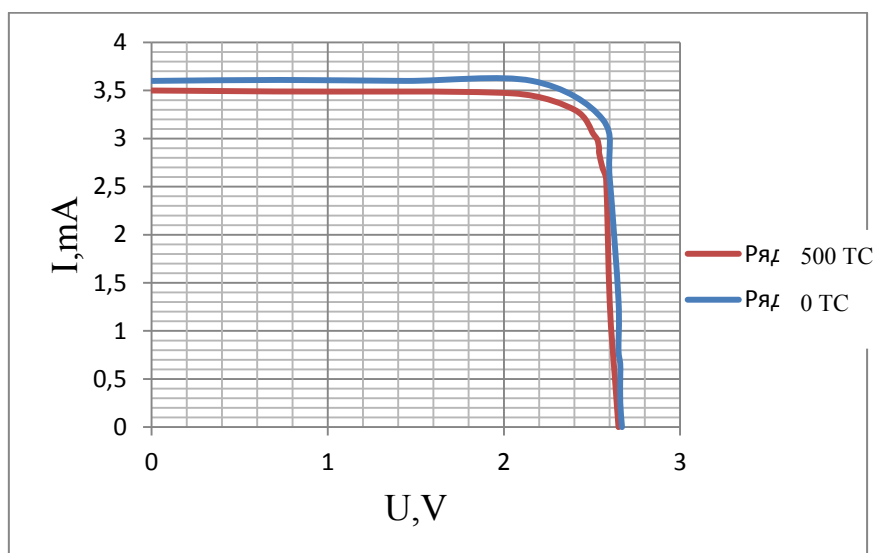


Fig. 3 – Averaged light IV characteristics of TSC after assembly and thermal cycling tests (for AM1.5 conditions; $T = 25 \pm 2^\circ\text{C}$, one sun)

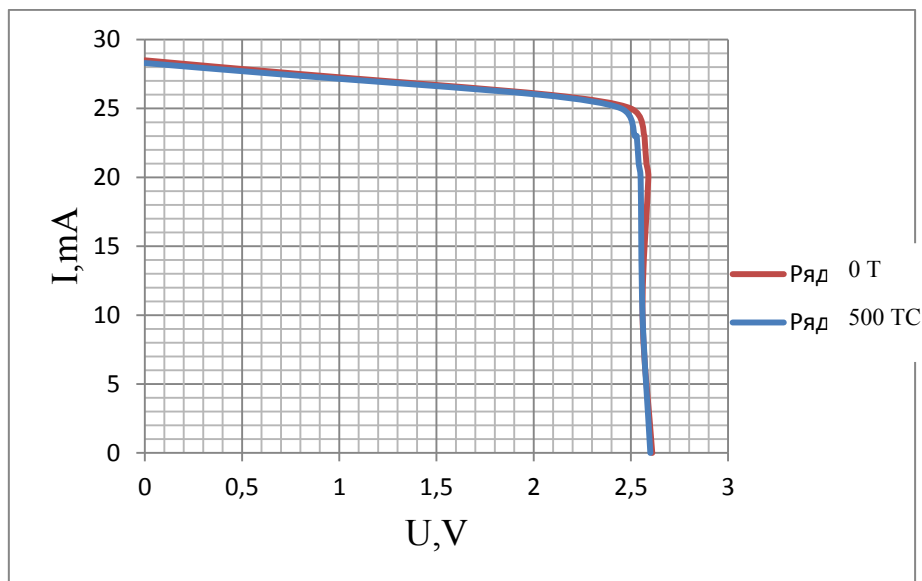


Fig. 4 – Averaged light IV characteristics of receivers after assembly and thermal cyclic tests (for AM1.5 conditions; $T = 25 \pm 2^\circ\text{C}$, one sun)

On the basis of the obtained positive results, LLC Research and Production Enterprise LTU, first time in Ukraine, now develop and organize production of new types of laminated materials for flexible and flexible-rigid aluminum-polyimide printed circuit boards. Proposed innovative technical solutions made it possible to create such methods for manufacturing domestic adhesiveless flexible materials that ensured using more simple, cheaper and reproducible manufacturing techniques for laminated materials with required geometrical dimensions of wide range of used metal foils and operating in the temperature range from minus 200°C up to plus 250°C (Fig. 5). At the same time it was possible to reduce cost of layered materials in comparison with world analogues by half to 1.6 Euro per dm^2 .

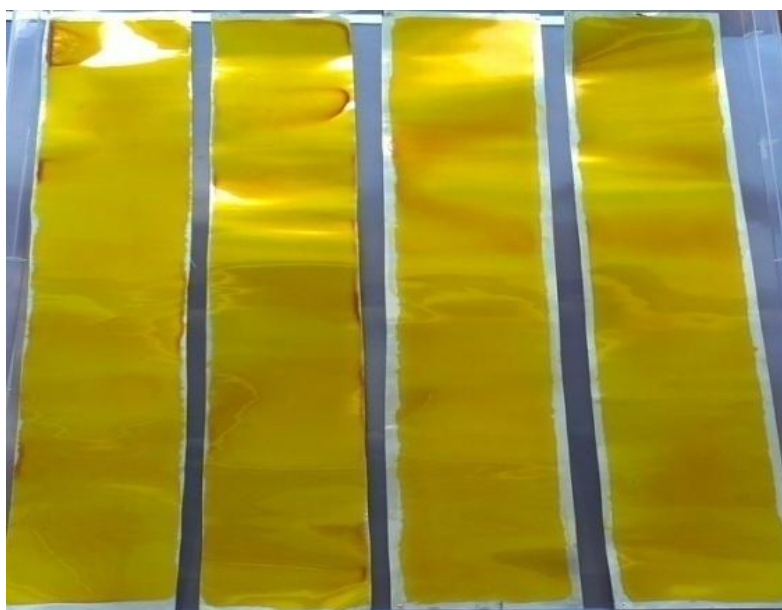


Fig. 5 – Samples of adhesiveless aluminium-polyimide materials

This allows significantly reduce cost of manufacturing promising receivers of concentrated solar radiation for HCPV focal-point modules on Fresnel achromatic lenses as the simplest (not requiring using SOE) and a cheap way to quickly implement concentrator modules with efficiency of more than 40% with concentration ratio exceeding 500 times. At development of industrial production of most advanced four-junction GaInP/GaAs//GaInAs/Ge SC from Azur Space Company with an efficiency of 48% it is possible to achieve requirements for the commercially acceptable cost of domestic concentrator solar modules not worse than the best world analogues [1, 5, 6].

After reasonable and careful selection of materials with necessary physical parameters, optimization of volumetric and geometric characteristics of structural elements of the receivers, as well as taking into account the commercially reasonable cost and availability for purchase of chosen materials and components following composition and design of the receiver based on aluminum COF assembly technology was defined (Fig. 6).

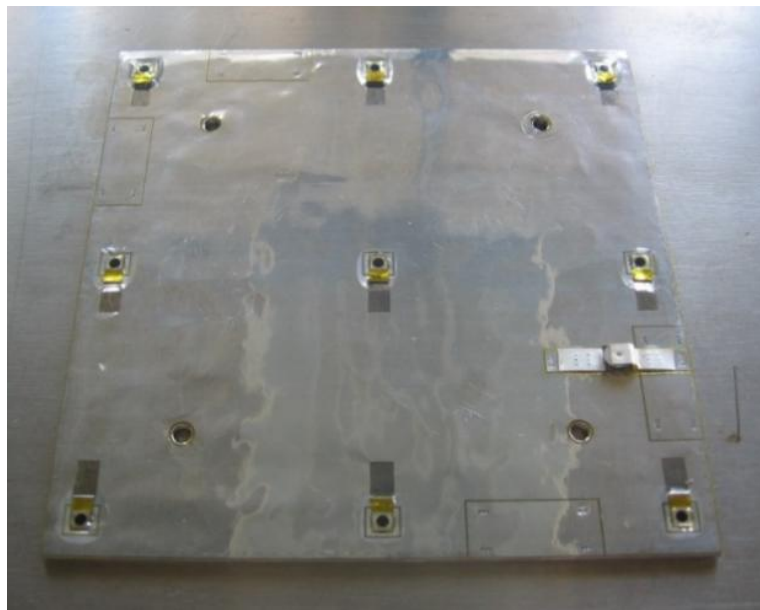


Fig. 6 – Sample of receiver manufactured using aluminum COF technology on flat aluminum radiator

Conclusions

1. On the basis of comprehensive analysis of the state and modern technological level of development of solar concentrator technologies in the world authors proposed new commercially acceptable design and technological solutions of solar radiation receivers for HCPV focal point modules on achromatic Fresnel lenses as most simple (not requiring SOE) and cheapest way of fast practical implementation of concentrator modules with efficiency of more than 40% with concentration ratio more than 500 times less than and not worse than the best world analogues.

2 To implement the proposed approaches for creating receivers for more high-efficiency mirror concentrator modules with concentration ration up to 800 times with efficiency of 40%, needed:

– additional carrying out research works on selection of design and technological solutions for concentrating solar radiation receivers based on COF (Chip-on-flex) assembly technology for bare four-junction arsenide-gallium solar cells (SC) with GaInP/GaAs

//GaInAs/Ge with efficiency of 48% with flexible interconnection boards. Including creation of printed circuit assemblies with mirrored secondary optical elements integrated into receivers based on Mirosilver type materials with reflection coefficient of 95-98%.

– manufacture of experimental samples and carrying out functional investigations of receivers of concentrated solar radiation, as well as carrying out accelerated tests in accordance with IEC 62108 standard to confirm of correctness of chosen design solutions, assembly technology and lifetime of ground-based concentrator photoelectric receivers with concentration ratio up to 800 times.

3. Results of work will potentially allow to achieve values of competitive capacity of electricity generated by serial solar concentrator modules based on the developed designs of new solar receivers at level of 0,2–0,5 Euro per watt.

References

[1] Key industry trends in solar energy. Economy and Technology 2019 Access mode: https://elektrovesti.net/65157_klyuchevye-otraslevye-tendentsii-solnechnoy-energetiki-ekonomika-i-tekhologii. – Access date 29.05.2019.

[2] The State Of Renewable Energies In Europe Edition.– 2018.–18th Eur Observ'ER Report.– P. 70, P. 195.– Access date 29.05.2019.

[3] IEC 62108 Design certification and type approval of concentrator photovoltaic modules and subassemblies. Supplement 1.0 2007-12.

[4] Borschev V.M. Study of the thermal characteristics of high-performance receivers of concentrated solar radiation of a new generation / V.M. Borschev, V.A. Antonova, O.M. Listratenko, Ya.Ya. Kostyshin, G.V. Buyer, I.T. Tymchuk, M.A. Protsenko // Instrumentation technology. - 2012. - №1. - P.3-9.

[5] Borshchov V.M., Listratenko O.M., Protsenko M.A., Tymchuk I.T., Fomin O.O. Innovative microelectronic technologies for high-energy physics experiments // Functional materials. – 24. – No.1 (2017) . – P. 1-11.

[6] Patent of Ukraine for utility model number 119126 "A method of manufacturing a flexible laminate for products based on foil." Registration date 11.09.2017 Inventors: Nikitsky G.I., Borschev V.M., Listratenko A.M., Tymchuk I.T. and etc.

NANOCOMPOSITES BASED ON RUTHENIUM SEMICONDUCTOR COMPOUNDS FOR GIC ELEMENTS AND SENSORS

Lepikh Ya.I., Borshchak V.A., Lavrenova T.I., Zatovskaya N.P., Balaban A.P.
Interdepartmental Scientific and Educational Physical and Technical Center of the MES and
NAS of Ukraine at the Odessa I.I. Mechnikov National University
65026, Odesa, 2, Dvoryanska str.,
tel. (048) 723-34-61,
Email: ndl_lepikh@onu.edu.ua

New heterophase nanocomposite semiconductor materials have been created for GIC elements and sensors that have significantly better electrophysical parameters (EPhP) and stability than existing ones. The glass formation processes and electrophysical properties of glassy materials containing no lead toxic compounds have been investigated.

Methods for the composite materials degradation processes reducing have been developed and methods for the basic characteristics stabilization increasing, variation and regulation of the electro-physical parameters of hybrid integrated circuits (GIC) elements and microelectronic sensors have been proposed [1-2].

Dependences of the electrophysical parameters (EPhP) of the film elements based on nanodispersed "ruthenium compounds - dielectric matrix" on the dispersion, the ratio of the initial component concentrations, the nanoscale structural-phase transformations and the annealing temperature have been determined.

Introduction

One of the important problems of micro- and nanoelectronics is the imperfection of functional materials used in GIC. GIC film elements formed on the basis of existing composite materials do not meet the current requirements for the electrophysical parameter stability, which is especially important in the special equipment composition. The main causes of this state of affairs are insufficiently studied structural-phase transformations, nanocomposite conductivity mechanisms, degradation processes, both as a result of internal processes and external destabilizing factors. Another important problem in this field is the toxicity of the used today starting materials (lead compounds, etc.).

Thus, the actuality of the study of nanocomposite heterophase materials based on the systems "glass - clusters RuO_2 , $\text{Bi}_2\text{Ru}_2\text{O}_7$, $\text{Pb}_2\text{Ru}_2\text{O}_{7-x}$ " is determined by the relevance of determining the structural-phase transformation processes features, heterophase nanocomposites electrophysical properties and physical mechanisms of the electrical conductivity depending on different factors.

Results of the research

The conductive properties of heterophase composites are formed by selecting the components and in the heat treatment process. In the case where there is no interphase interaction between the metal and non-metallic components, the conductivity of the composites is determined by the properties of the phase components and depends only on the concentration of the metal volume fraction. The general law of current flow in such systems are described by a theory that assumes the presence of some threshold concentration, near which there is a sharp change in the nature of the conductivity. In the presence of interfacial interaction, the annealing process can be accompanied, on the one hand, by the formation of new phase components, on the other - by changing the component electrophysical properties. As a result, composites not

only have the properties of the original components, but often acquire new, qualitatively different characteristics. One of the most important applied problem is to determine the nature of the influence of physicochemical processes occurring in heterophase systems depending on the component concentration, temperature, time of heat treatment on the phase composition, structure and, as a consequence, on the composites electrical conductivity. The second task is to establish the mechanisms implemented in them.

The nanocomposite elements are formed by annealing the pastes, which are a mixture of functional material powders, glassy bond, and organic bond. At paste annealing the glass powders are melted and sintered into a glass matrix, in which the particles of the functional phase fixes, forming conductive circuits. Therefore, nanocomposite elements complex of electrophysical properties is largely conditioned by the properties and composition of the glass binder. Glass binders include lead-boron-alumina-silicate glass as a binder. The main disadvantages of the known materials: high annealing temperature of pastes (870 - 900° C); the presence in the glass binder of toxic lead compounds; high linear thermal expansion coefficient (LTEC); low reproducibility of their EPhP. The processes of glass formation and crystallization investigation technique has been developed, as well as the physico-chemical properties of the system "SiO₂-B₂O₃-Bi₂O₃-ZnO-MgO-CdO" at different ratios of the concentrations of the initial components and alloying impurities has been studied in order to choose the optimal glass compositions for thick GIC elements resistive, conductive and dielectric layers of etc.

It has been found that as the main glass-forming component, the best results are obtained by the use of bismuth oxide, which makes it possible to obtain more fusible glasses. It has been shown that Bi₂O₃ oxide does not interact with conductive elements and is introduced into the glass as a material neutral in this respect. It helps to improve the wetting and adhesion of the glass to the substrate. In high-bismuth glass, Bi₂O₃ is involved into the matrix construction as a glass-forming agent. Synthesis of glasses in the SiO₂-B₂O₃-ZnO-BaO-Bi₂O₃ system was carried out for the following compositions: $x\text{SiO}_2 \cdot y\text{B}_2\text{O}_3 \cdot 10\text{ZnO} \cdot z\text{BaO}$; $x\text{SiO}_2 \cdot y\text{B}_2\text{O}_3 \cdot 10\text{ZnO} \cdot z\text{BaO}$; $x\text{SiO}_2 \cdot y\text{B}_2\text{O}_3 \cdot z\text{ZnO} \cdot 10\text{BaO} \cdot 5\text{Bi}_2\text{O}_3$; $x\text{SiO}_2 \cdot y\text{B}_2\text{O}_3 \cdot z\text{ZnO} \cdot 10\text{BaO} \cdot 10\text{Bi}_2\text{O}_3$; $x\text{SiO}_2 \cdot y\text{B}_2\text{O}_3 \cdot z\text{ZnO} \cdot 10\text{BaO} \cdot 15\text{Bi}_2\text{O}_3$. Here, x varied from 30 to 60 mol. %, y - from 5 to 10 mol. %, z - from 10 to 40 mol. %.

The glasses ability to crystallize was studied by studying the diagram glasses composition. The multicomponent system diagram technique based on the graphical representation of cross sections of multidimensional figures (multidimensional simplex), which represent systems in multidimensional space, hyperplanes with a given percentage of one or more components has been developed. The softening beginning temperature was measured by dipping the tip of the rod into the glass under a load of 100 g. The softening beginning was fixed by an indicator with a separation price of 2 microns. The coefficient of thermal expansion was measured by the dilatometric method in the temperature range (20-400) ° C. The glass samples chemical stability was determined by the shortcut method of determining the stability of the glass powder with respect to the water, alkali and acids action.

Based on the glass formation processes study, physico-chemical properties (LTEC, softening beginning temperature, specific surface resistance, chemical resistance), the optimal compositions for the fusible glasses production for thick-film elements of integral and functional electronics were selected

A low-melting glass for thick-film nanocomposites containing no toxic lead compounds was obtained [3]. The obtained glasses have high water resistance. The advantages of glass are: reduction of softening beginning temperature (400 - 450°C); an increase in the specific surface resistance tenfold (10^{14} - $5 \cdot 10^{14}$ Ohm·cm), the absence of toxic lead compounds, which leads to a decrease in environmental pollution. Glasses can be used at nanocomposites production for high-

voltage equipment at voltage 10 - 25 kV as well as for glass bonding thick-film nanocomposites and dielectric layers of multilevel GIC.

A method for determining the mechanisms of the processes of direct influence of internal and external factors on structural-phase transformations and element GIC electrophysical parameters has been created. The study of nano-dimensional structural-phase transformations in GIC elements combined with the influence of external factors makes it possible to obtain elements with stable EPhPs.

The dispersion of glass powders used in the pastes manufacture plays a significant role in ensuring the reproducibility and stability of the EPhP thick films. In today's requirements, the dispersion of powders is not regulated. Therefore, the size and dispersion of the glass powders particles were investigated. The objects of study were powders of lead-boron-alumina-silicate glasses №№ 279, 2005, 2006 - 2, 2006 - 3 and 2006 - 8, as well as functional material RuO₂.

Histograms of glass powders particle size distribution have been obtained. Analysis of histograms allows to draw the following conclusions: the best dispersion is characterized by the powders of glass No. 2006-3, 2005 and 2006-8, their particles projection area is mainly from fractions to 8 ... 13 μm², the largest uniformity in size with a relatively high particles dispersion is characterized by RuO₂ powder.

It has been established that a large variation in the powder particle size of the pastes original components is one of the essential factors that affect the electrophysical parameters reproduction. That's why, the dependence of the electrophysical properties of thick-film structures based on the "glass- RuO₂ clusters" on the dispersion of the starting material particles and the ratio of their concentrations at a fixed annealing temperature (870 ° C) has been investigated. The films were made on the basis of powders of lead-borosilicate glass (PbO, SiO₂, B₂O₃, Al₂O₃) with fixed particle sizes (0, 5 μm, 1 μm, 3 μm, 5 μm) and functional material RuO₂ with particle sizes of 0.05 - 0, 1 μm.

It has been established that with increasing ratio of conductive phase – glass the films surface resistivity decreases, and the resistance temperature coefficient passes from the region "-" to the region "+" of values. The greatest influence of the glass particles size on the resistor resistance occurs in samples with a low content of ruthenium dioxide. The films resistance increases with increasing glass content, the highest growth rate of ohmic resistance occurs for the glass frit with a particle size of 0.5 μm. As the RuO₂ concentration increases, the resistance approaches a constant value and is independent the glass particle size. The obtained dependences of the electrophysical properties of the thick-film nanocomposites on the phase, particle size distribution of the glass binder, at different ratios of the concentrations of the original components, allow the variation of their EPhPs and their use as temperature sensors. The obtained results make it possible to create qualitatively new heterophase nanocomposite materials for GIC elements and non-ideal heterojunctions of microelectronic sensors that have significantly better electrophysical parameters than existing ones.

The functional basis of resistive nanocomposites is typically ruthenium oxide compounds, such as RuO₂. Pb₂Ru₂O₆ is used to save precious ruthenium dioxide.

It has been established that during thick films annealing there is an interaction between the film conductive phase and the glass components. The influence of glass properties on the processes of structural-phase interaction of the glass matrix with the conductive phase in the system "glass - Pb₂Ru₂O₆" has been investigated. It has been established that phase composition of nanocomposite based on lead ruthenium is substantially related to the chemical composition of glass. Lead ruthenium reacts with some metal oxides. This interaction is related to the acid-base properties and is realized because these metal oxides have acidic properties more pronounced than in ruthenium,

Conclusions

The distinguishing features of the results are that, for the first time, bismuth oxide was chosen as the main glass-forming component, instead of lead oxide, which makes it possible to obtain more fusible glasses with a softening temperature of 400 - 430° C. Alloying impurities (SiO₂, CdO, ZnO, MgO, B₂O₃) are selected in such a way as to provide the necessary physical and technical glass characteristics. Significantly reduced softening temperature and LTEC, increased surface resistivity, which allows it to be used in the manufacture of thick-film resistors for high-voltage equipment, and there are no toxic lead compounds. The glass does not crystallize during heat treatment in the temperature range of 300-900° C. The technology of glass manufacturing in relation to known compositions is characterized by a decrease in the cooking temperature to 900 - 1000 ° C.

Mechanisms of nanoscale structural-phase transformations in glass-clustered RuO₂, Pb₂Ru₂O_{7-x} systems has been determined for the first time. During this system annealing occur the tenfold increase of the specific surface resistance (10^{14} - $5 \cdot 10^{14}$ Ohm·cm), achieved high water resistance (II dimming class). The absence of toxic lead compounds, lead to reduced environmental pollution. Glasses can be used to produce nanocomposites for high-voltage instrumentation, as well as glass binder of thick-film nanocomposites and dielectric layers of the multilevel GIC.

List of references

1. Valentyn Smyntyna, Vitalii Borshchak and Ievgen Brytavskiyi. Nonideal Heterojunctions for Image Sensors // Copyright © 2018 by Nova Science Publishers, Inc. Published by Nova Science Publishers, Inc. † New York.— 175 pp. <https://novapublishers.com/shop/nonideal-heterojunctions-for-image-sensors/>
2. Lepikh Ya.I., Lavrenova T.I., Sadova N.M., Borshchak V..A., Balaban A.P., Zatovskaya N.P. Structural-phase transformations and electrophysical properties of SiO₂-B₂O₃-Bi₂O₃-ZnO-BaO-based composites // Sensor electronics and Microsystem Technologies. - 2018— Vol.15, № 4 - RR. 77-84.
3. Patent for invention No. 113565 Lepih YI, Lavrenova TI Light-melting glass for nanocomposites // Publ. Bul. # 3/2017 of 10/02/2017.

NANOSTRUCTURED ELECTROCONDUCTIVE COMPOSITE MATERIALS FOR DETECTING PHOSPHORUS AND CHLOROROGANIC SUBSTANCES

Kukla O.L.¹, Mamykin A.V.¹, Pud A.A.², Ogurtsov N.A.², Noskov Yu.V.², Mikhaylov S.D.²

¹V.E. Lashkaryov Institute of Semiconductor Physics, NAS of Ukraine

03028, Kyiv, Nauki prosp., 41, tel. (044) 525-55-84, E-mail: kukla@isp.kiev.ua

²V.P. Kukhar Institute of Bioorganic Chemistry and Petrochemistry, NAS of Ukraine

02160, Kyiv, Kharkivske shose, 50, tel. (044) 559-70-03, E-mail: alexander.pud@gmail.com

A number of hybrid nanocomposites based on electroconductive polymers and nano- and submicron particles of other materials have been synthesized and investigated, which have been used as sensitive layers for chemoresistance sensors suitable for the detection of some phosphorous- and chlorine volatile organic compounds (simulators of poisonous substances) and nitro-aromatic compounds (simulators of explosive substances). These materials have a structure of type core (inorganic or polymeric particle) - nano-shell (electroconductive polymer). It is shown that the array of the most effective sensor films, due to variations in selectivity to different types of analytes, is able to confidently identify these toxic and explosive substances as classes, regardless of the concentrations by principle of "electronic nose". It is established that the creation of a chemoresistive sensor system is possible when using only 2 types of the most sensitive chemoresistive films, which simplifies the development of a portable gas analyzer device for the detection of tested substances.

Introduction. Intrinsically conducting polymers are very attractive for various applications due to their high conductivity, thermal and atmospheric stability, luminescence ability, nonlinearity of optical parameters, sensory properties, and others. The spectrum of potential applications of these polymers, both in the pure state and in composites with different materials, is very wide: field-effect transistors, polymer light-emitting diodes, solar panels, sensors, capacitors, etc. In particular, their nanocomposites with core-shell structure can be considered as promising materials for sensor electronics due to the high specific surface area, nanoscale thickness of the shell, and the availability of sensitive centers in this shell for analyte molecules [1, 2].

The purpose of this work was to investigate the possibility of rapid detection and subsequent identification of toxic (poisonous) gases and explosives using arrays of chemoresistive sensors based on electroconductive nanocomposite layers and using statistical methods of chemical pattern recognition. The task of the work was also to create a prototype of a portable gas analyzer device for environmental monitoring and detection of toxic molecules in the air, with the possibility of subsequent analysis of the obtained responses for qualitative identification of the investigated substances by the technology of "electronic nose".

To achieve this goal, the sensitivity and selectivity of detecting a number of simulators of poisonous and explosive substances (PS and ES) were carried out using arrays of chemoresistive sensors with electroconductive nanocomposite layers [3], which change their electrical conductivity under the gas action.

Materials and methods. Five types of electroconductive films have been selected for chemoresistive electrodes: CNT/P3MT-Cl (nanocomposite carbon nanotubes/poly(3-methylthiophene), chlorine dopant), TiO₂/PANI-DBSA (nanocomposite polyaniline with particles TiO₂, dodecylbenzenesulfonic acid (DBSA) dopant), PVDF/P3MT-Cl (polyvinylidene fluoride/ poly(3-methylthiophene), chlorine dopant), CNT/PANI-DBSA (nanocomposite carbon nanotubes/polyaniline, dopant DBSA), P3MT-Cl (pure poly(3-methylthiophene), chlorine dopant), sensitive to the analyzed analytes in the concentration range of 10-1000 ppm. At the same time only the first three types of films were used for identification of explosives.

As simulators of PS were chosen phosphorous- and chlorine organic compounds, which, in their molecular structure and physicochemical properties, are close to real PS but they are not

one's (though they are toxic) due to certain differences in the chemical formula: dimethylmethyl phosphonate (DMMP) (simulator of poisonous gas "sarin"), trimethyl phosphate (TMP), diethyl phosphite (DEP), 1,4-dichlorobutane (DCB) and dichloroethyl ether (Chlorex). Several types of nitroaromatic substances from a range of nitrotoluenes were selected as simulators of ES: O-Nitrotoluene (2-MNT), Nitrobenzene (MNB).

Synthesized according to [1, 4] nanocomposite electroconductive polymers (ECP) have a structure of type core (template inorganic or polymeric nano- or submicron particle) - shell (ECP) (Fig.1). The films of these materials were deposited on the raster gold microelectrodes on glass-ceramic substrates by irrigation of nanoparticles in chlorobenzene.

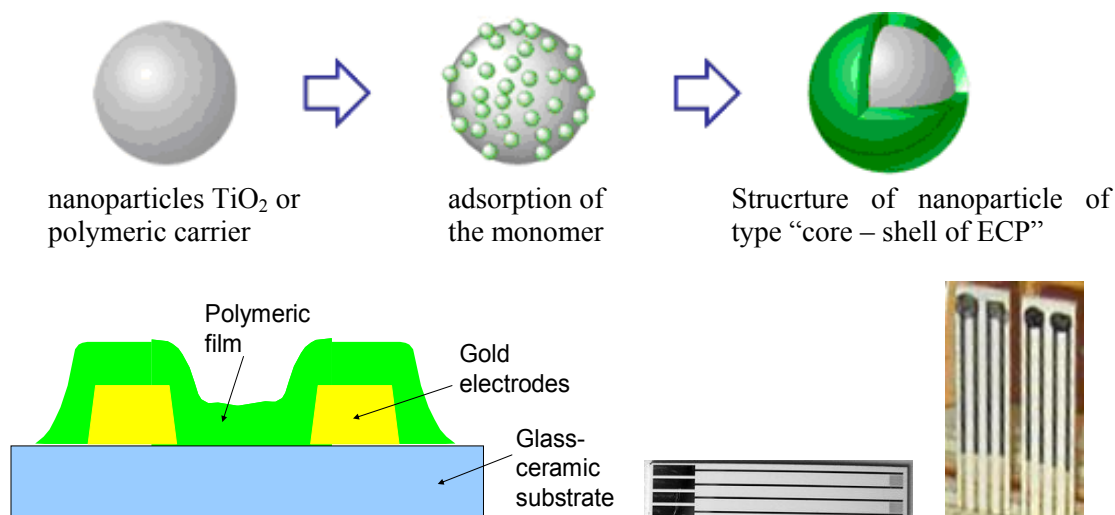


Fig. 1 – Formation and structure of synthesized nanocomposite materials and view of chemoresistive microelectrodes with deposited electroconductive sensitive films

As sensor response, a change in the electrical conductivity of the polymer resistors was recorded by measuring the change in direct current through each chemoresistor with the adjustable reference voltage applied to it when chemoresistor was exposed to the gas environment. The current was measured using the converter of type input current - output voltage based on a operational amplifier coupled to an analog-to-digital converter.

Exposure of the individual analytes was carried out using an injection syringe system, the measurement was carried out for 2 min, after which the chamber was repeatedly purged with room air. The desired concentration of the analyte was formed by consecutive dilutions of its saturated vapor (taken at 20°C) with room air.

Determination of phosphorous and chlorine organic simulators of toxic substances

The gas sensitivity of the above types of chemoresistor films was tested. For most phosphorus and chlorine organic PS concentrations of 100, 200, 500 and 1000 ppm were taken. However, lower concentrations of 10 and 50 ppm analytes were additionally used to detect the high sensitivity of individual films to individual analytes. The detection thresholds of the analyzed PS ranged from 10 ppm (for DMMP and Chlorex) to 100 ppm (for other analytes-simulators). The maximum relative responses were of about 4-5% at concentrations of toxic compounds of hundreds of ppm, the response rate was 1-2 minutes.

Figure 2 shows, for example, the relative responses of all types of chemoresistive films under study to the simulator of PS "Sarine" DMMP and the chlorineorganic simulator of PS Chlorex. This example is interesting because both sensors have opposite responses signs from all sensors. This is important for the next step - processing the sensor array data and recognizing different classes of PS using "electronic nose" technology.

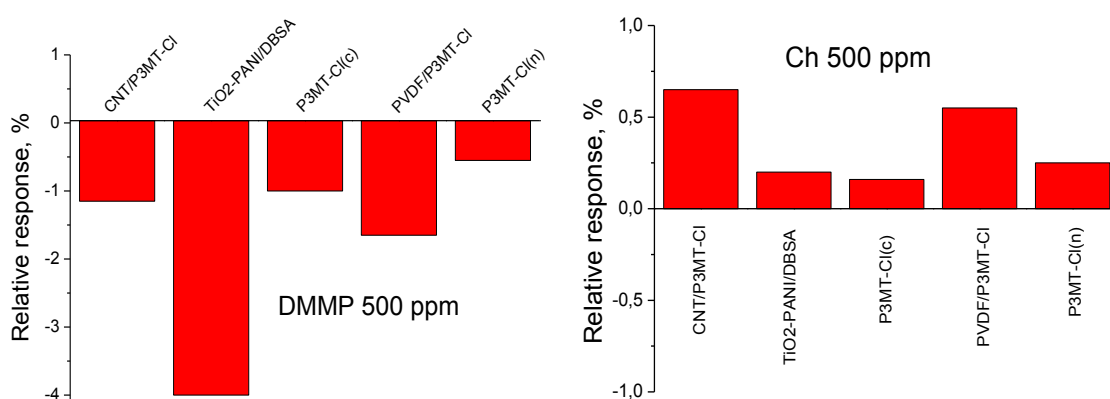


Fig. 2 – Response diagrams of 5 types chemosensors on fixed concentration of 500 ppm for analytes DMMP and Chlorex

For further analysis, the above 5 types of chemosensors were assembled into sets of 2, 3, 4, and 5 types of films, which made it possible to form all possible variants of construction of two-, three-, four- and five-element sensor arrays. The purpose of such analysis is to investigate the possibility of identifying (separating) the studied types of phosphorus and chlorine organic volatile compounds at any of their concentrations.

Using the statistical method of principal component analysis [5], the responses of all these sensor sets were projected on the respective factor plane. As can be seen from Fig.3, a rather successful identification of the PS simulators was observed already when using two sensors in the sensor array. In particular, it was very successful to use a pair of TiO₂/PANI-DBSA and PVDF/P3MT-Cl films, in which the DMMP is confidently separated from other analytes, as well as chlorine organic analytes DCB and Chlorex. Further increase in the number of chemosensors in the array composition (up to 3-5 types of films) did not significantly change the quality of visualization of chemical images.

At the same time, the array of two types of composite films CNT/P3MT-Cl and TiO₂/PANI-DBSA was the most optimal for the reliable identification of the investigated explosive nitroaromatic substances (data not shown).

Conclusions. As a result of the research, five types of chemoresistive sensors, suitable for the detection of phosphorous- and chlorine organic volatile compounds (simulators of poisonous substances), were selected. Due to variations in the selectivity of different sensors to different analytes (especially to groups of phosphorus and chlorine organics, which have the opposite sign), the sets of such sensors have been shown to be able to confidently identify these poisonous substances as classes regardless of concentrations by “electronic nose” principle. In this case, the practical construction of the sensor array is possible when using only two types of films, which simplifies the development of a portable gas analyzer device for detecting the analytes under study.

In particular, it was found that when designing a portable device for determining the poisonous substances it is advisable to use the two most sensitive composite films of types TiO₂/PANI-DBSA and PVDF/P3MT-Cl. An array of two composite films of CNT/P3MT-Cl and TiO₂/PANI-DBSA types was found to be the most optimal for detecting explosive substances.

Some disadvantages of the developed chemoresistive sensors can be attributed to their low selectivity, which requires some time for the subsequent mathematical processing of signals from the sensor array by "electronic nose" technology, as well as the need for pre-adaptation and "training" of sensors in evaporations of analyzed matters with aim of stabilization of sensor base line. At the same time, the advantages of these sensors include their high speed, small size,

ease of measurement, which makes it possible to create a portable device with a standalone rechargeable battery.

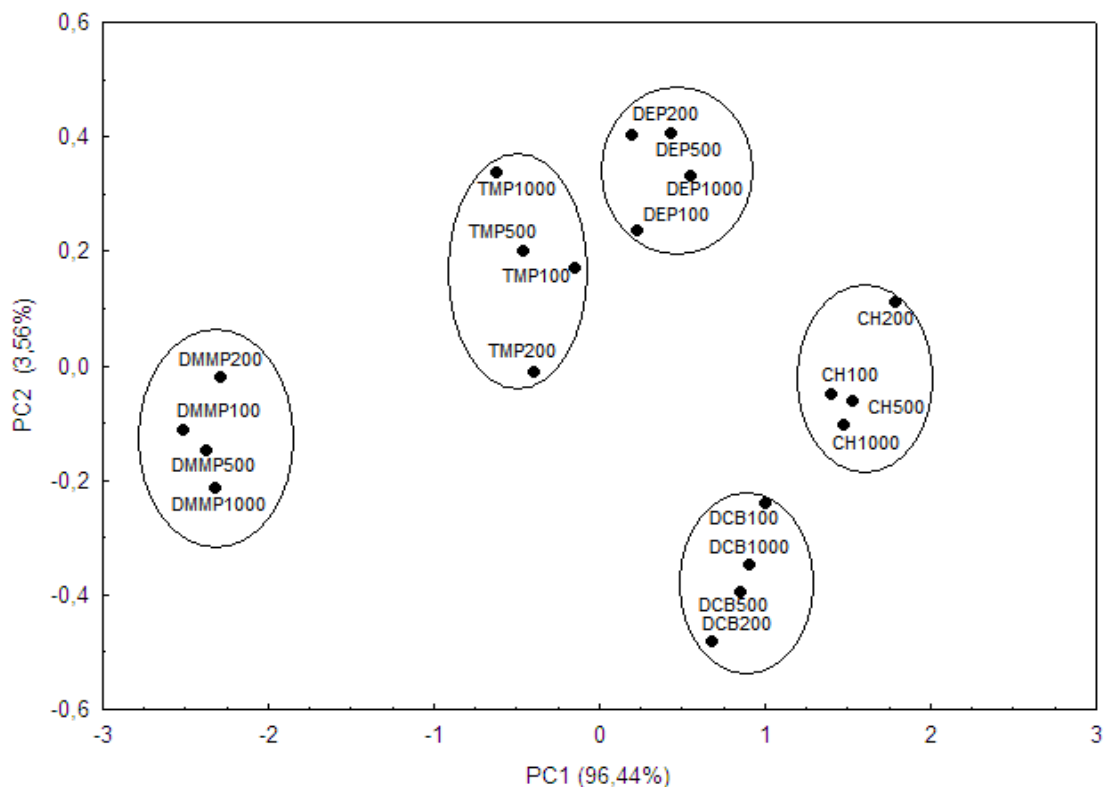


Fig. 3 – The projection on the plane of the principal components of the responses of two-element sensor array based on the $\text{TiO}_2/\text{PANI-DBSA}$ and $\text{PVDF}/\text{P3MT-Cl}$ films. The location on the plane of the investigated PS simulators at all their tested concentrations is indicated by the corresponding circles

References

1. Ogurtsov N.A., Bliznyuk V.N., Mamykin A.V., Kukla O.L., Piryatinski Yu.P., Pud A.A. Poly(vinylidene fluoride)/poly(3-methylthiophene) core-shell nanocomposites with improved structural and electronic properties of the conducting polymer component // Physical Chemistry Chemical Physics journal. – 2018.- Vol. 20.- P. 6450-6461.
2. Ogurtsov N., Bliznyuk V., Mamykin A., Kukla O., Piryatinski Yu., Pud A. Enhanced properties of the conducting polymer in the PVDF/poly(3-methylthiophene) nanocomposites // Abstracts of 11th International conference “Electronic processes in organic and inorganic materials”, Ivano-Frankivsk, Ukraine, May 21-25, 2018, P. 56.
3. Kukla O.L., Mamykin A.V., Kazantseva Z.I., Koshets I.A., Drapailo A.B., Kalchenko V.I., Ogurtsov N.A., Noskov Yu.V., Mikhaylov S.D., Pud A.A. Chemosensors systems based on different types of transducers specified for determination of toxic gaseous matters // Abstracts of 11th International conference “Electronic processes in organic and inorganic materials”, Ivano-Frankivsk, Ukraine, May 21-25, 2018, P. 209.
4. Ogurtsov N.A., Noskov Yu.V., Bliznyuk V.N., Ilyin V.G., Wojkiewicz J.-L., Fedorenko E.A., Pud A.A., Evolution and Interdependence of Structure and Properties of Nanocomposites of Multiwall Carbon Nanotubes with Polyaniline // J. Phys. Chem. C. 2016, 120, 230-242.
5. Jurs P.C., Bakken G.A. and McClelland H.E. Computational Methods for the Analysis of Chemical Sensor Array Data from Volatile Analytes // Chemical Review. - 2000. - Vol. 100. - P. 2649–2678.

INTEGRATION OF HARD BLOCKS INTO FPGA NANOSTRUCTURE

V.P.Karnaushenko, A.V.Borodin, Y.S.Vasyliev, M.I. Piataikina.

Kharkiv National University of Radio Electronics

61166, Kharkiv, Nauky ave. 14, dep. Microelectronic devices and appliances,

tel. (057) 702-13-62

E-mail: vladimir.karnaushenko@nure.ua;

Field Programmable Counter Arrays (FPCAs) have been recently introduced to close the gap between Field Programmable Gates Arrays (FPGA) and Application Specified Integrated Circuits (ASICs) for arithmetic dominated applications. FPCAs are reconfigurable lattices that can be embedded into FPGAs to efficiently compute the result of multi-operand additions.

Field Programmable Counter Arrays, arithmetic applications, integration, shadow cluster.

I FPCA Integration with FPGAs

This thesis presents a study of the issues related to integration of hard blocks (and/or coarse-grained blocks) into FPGAs. It then proposes some integration scenarios for FPCAs and describes a generic platform for implementation and evaluation of some of these scenarios based on Stratix II devices and the FPCA architecture.

- The Problem

The introduction of hard logic blocks and coarse-grained blocks for FPGAs creates a new problem: their seamless integration. In simple words, the problem asks how should these blocks be floor planned and placed in the homogeneous array of soft logic, and how should they be connected to the routing fabric efficiently? The floor plan should result in shorter critical paths and reduced congestion and an interface must be designed for the block that meets the following requirements:

- It should provide the required level of connectivity (i.e. all typical circuits using the block should be routable).
 - It should be fast and consume minimum chip area.
- It should minimize the negative impact on the rout ability of other blocks.

II Related Works

Although there has been significant study on new architectures for hard and coarse-grained blocks for FPGAs, few of them have studied their detailed interface. In [1], formal optimization methods are used to design mixed-granularity FPGA architectures. Integer Linear Programming (ILP) is incorporated to determine the best floor plan to optimize the architecture for a set of DSP applications, including the choice of the best mix of hard 18*18-bit multipliers.

A similar problem is studied for block RAMs in [2]. In this work, without any investigation and inspired by commercial FPGAs, it is assumed that a row of block RAMs is located in the middle of the chip (like figure 1). The authors have tried to determine the ideal flexibility of the memory/logic interconnect block (illustrated in figure 2). The flexibility of a memory/logic block is defined as the number of (or portion of) available routing wires to which each memory pin is connected. This study shows that if the flexibility is too low, many

circuits become unroutable, while excessive large flexibility values increase the memory access time and also waste chip area. Alternatively, the authors have made several enhancements to the routing architecture based on the characteristics of memory-to-memory connections, such as busses, in their benchmark circuits. Since nets connecting to multiple memory blocks are common in many circuits' blocks, the authors have proposed to add additional programmable switches between adjacent memories to support these nets. This significantly improved the results on architectures with lower interconnect block flexibility.

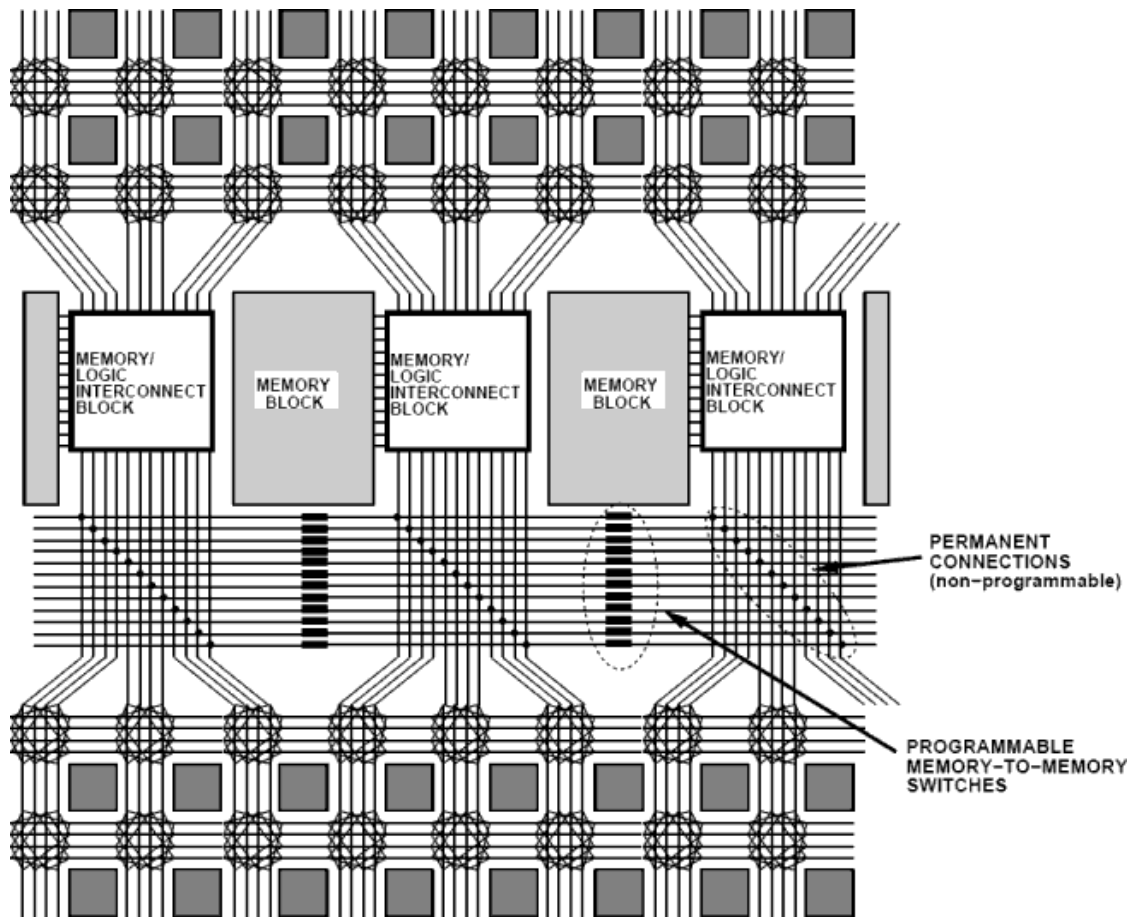


Fig. 1 – An example of integrating RAMs as hard blocks [1]

The large M-RAM blocks in Stratix II device resemble this style of integration. This solution enhances the ability to tile island-style architecture, and requires a completely new design for interfacing with the rest of routing fabric. Greater integrity and speed are achieved with larger hardwired blocks, but the layout design and interface design becomes a more complicated.

It doesn't seem that the results obtained for memory block integration could be used for arithmetic blocks such as FPCAs. The functionality of the pins and their contribution to total routing resource demand are different for blocks with different functionalities.

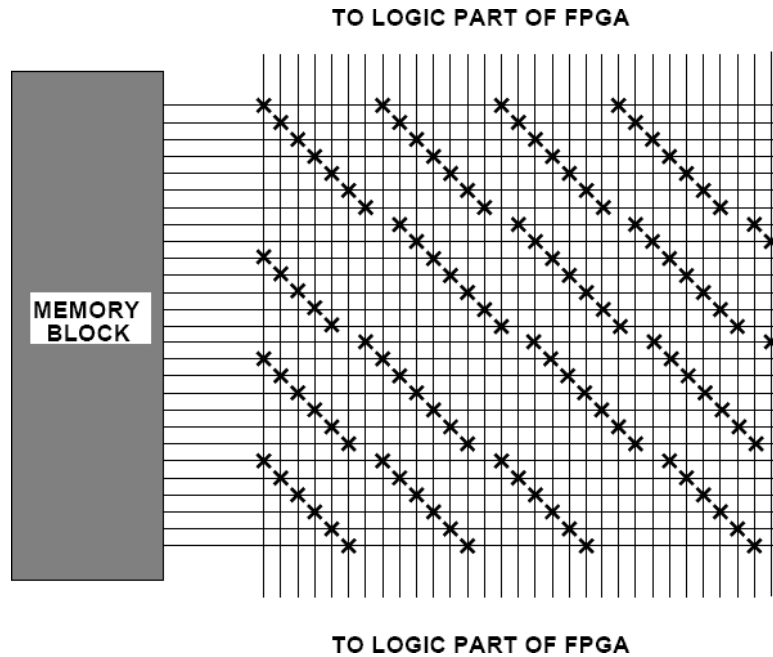


Fig. 2 – Example of memory/logic interconnect block [1]

A very recent work [3], has studied the integration of coarse grained Floating Point Units (FPUs) in a fine-grained soft logic array. Different floor planning strategies for placement of the FPUs, different aspect ratios and possible pin placement methods are evaluated to find the optimum architecture. The approach taken is again an empirical one based on the delay and minimum channel width requirement of a set of benchmarks. Unlike the previous approach, they have assumed that the gridded routing fabric extends over their Embedded Blocks (EBs). Figure 3 shows a scenario where a 3*3 super-tile is replaced by an embedded block.

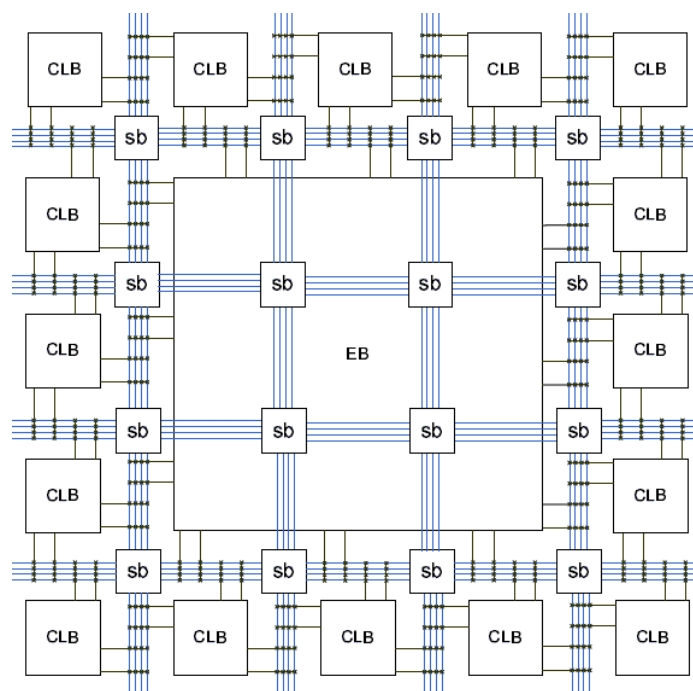


Fig. 3 – Expansion of the gridded routing fabric over the embedded block [3]

The M512 RAMs, M4K RAMs, and the DSP blocks in Stratix II devices are examples of this approach, but with a small difference. Tiles in the same column are all of the same kind. These tiles are all the same height (or multiples of same height) but their widths may slightly differ. In this way, the general routing fabric could be designed as easily as the general island-style routing fabric consisting of horizontal and vertical channels of routing wires with switch blocks in their intersections points. The problem of interconnect interface block design in this approach; will be to minimize the re-design of the intra-cluster connections in such a way that matches the actual pin-demand of the new hard blocks.

As an example, the DSP blocks in the Stratix II architecture span 4 blocks vertically. The blocks are designed in such a way that they can be decomposed into four tiles. Each tile has the same height as other logic tiles and has a switch box, intra-cluster connections and the DSP core itself. The intra-cluster connection design for DSP blocks is interesting. LAB tiles in Stratix II devices have 45 local interconnect lines that are selected by a level of switches from the general routing network. These lines drive all the ALM inputs which are around 65 input pins. For the DSP tiles (¼ each DSP block), there are 60 local lines that drive approximately 40 input pins. This information is summarized in table 1. The reason for this local interconnect-input pin difference is that it is the actual pin-demand of the tiles which is important, not just the number of input pins. Many of the 65 input pins of the ALMs in each LAB could be shared or driven by the local feedback lines. This lowers the actual pin demand to 44. On the other hand, DSP block input pins are arithmetic bits, which are all distinct, and needed to be routed separately. Thus, more connections than the total number of input pins are provided by the local lines to ensure the required routing flexibility. FPCAs, from this point of view, are more similar to DSP blocks than to block RAMs.

Table 1: Intra-cluster design of LAB and DSP tiles

<i>Tile Type</i>	<i>Local Interconnect Lines</i>	<i>Input Pins</i>
<i>LAB Tile</i>	44	=65
<i>DSP Tile</i>	60	=40

Hard blocks improve the area and speed of the designs mapped to FPGAs, but only if they are used. Otherwise, the silicon area devoted to them and, the expensive routing resources around them are wasted. This also suggests that the integration of hard blocks is only feasible if they are used often. Shadow clusters are introduced in [4,5] to take better advantage of the routing resources around hard blocks, when they are not used. A shadow cluster is a soft logic block, placed “behind” the hard block so that if the design doesn't use the hard block, then some general FPGA logic within the shadow cluster can be used to implement a portion of the real circuit. Shadow clusters come at the expense of additional area, but, if properly used, the advantage obtained by making better usage of the routing network dominates this extra area overhead. Figure 4 depicts this idea. The inputs, which come from the routing network, are shared between the shadow cluster and the hard block. Depending on the mode of operation, either the output of hard block or the shadow cluster is selected.

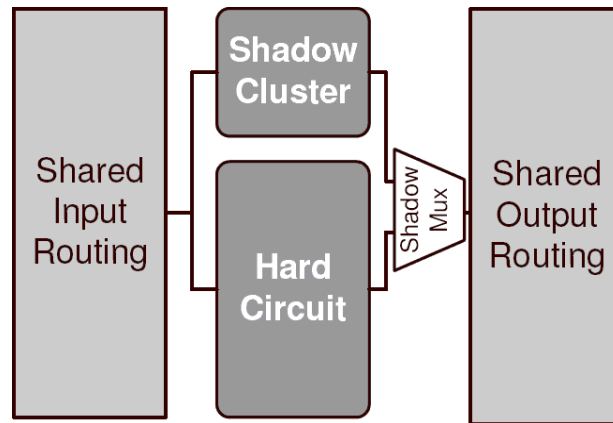


Fig. 4 – Illustration of shadow cluster concept [3, 4]

III Summary and Conclusions

A design space exploration tool for FPCAs consisting of a generic model of FPCAs, a mapping heuristic with synthesis and report automation facilities were developed. An analysis of the design space was performed and a new metric called utilization was suggested to prune the DSE.

A set of benchmarks were chosen and the DSE were performed, and some of the best performing architectures in terms of speed and area were highlighted.

The problem of integrating FPCAs with FPGAs was also studied.

References

- [1] A.M. Smith, G.A. Constantinides, and P.Y.K. Cheung, "Integrated Floorplanning, Module-Selection, and Architecture Generation for Reconfigurable Devices," *Very Large Scale Integration (VLSI) Systems*, IEEE Transactions on, vol. 16, 2008, pp. 733-744.
- [2] S. Wilton, J. Rose, and Z. Vranesic, "The memory/logic interface in FPGAs with large embedded memory arrays," *Very Large Scale Integration (VLSI) Systems*, IEEE Transactions on, vol. 7, 1999, pp. 80-91.
- [3] C.W. Yu et al., "The Coarse-Grained / Fine-Grained Logic Interface in FPGAs with Embedded Floating-Point Arithmetic Units," *Programmable Logic, 2008 4th Southern Conference on*, 2008, pp. 63-68.
- [4] Peter Jamieson and Jonathan Rose, "Enhancing the area-efficiency of FPGAs with hard circuits using shadow clusters," *Field Programmable Technology, 2006. FPT 2006. IEEE International Conference on*, 2006, pp. 1-8.
- [5] P. Jamieson and J. Rose, "Architecting Hard Crossbars on FPGAs and Increasing their Area Efficiency with Shadow Clusters," *Field-Programmable Technology, 2007. ICFPT 2007. International Conference on*, 2007, pp. 57-64.

THERMORESISTIVE TRANSDUSERS USED HEAT EXCHANGE TECHNOLOGY

S. N. Osinov, V. F. Zavorotnyi, B. I. Lupyna, O. V. Borisov

National Technical University of Ukraine "Igor Sikorsky Kyiv Polytechnic Institute"
03056, Kyiv, Polytechnichna str. 16, b. 12, apt. 07-b, Ukraine, Microelectronics department
E-mail analog2@ukr.net

Systematization of electronic, thermal and hydrodynamic physical models distinctive for sensing processes into devices manufactured by the silicon micro-electro-mechanical systems technology was been considered in the paper. The physical and technical characteristics, structural and topological aspects of the micromechanical thermo-resistor active heating converters synthesis for fluid (gas and liquid) parameters determination are considered. The mathematical model which is accepted as the basis for synthesis of the library of CAD system elements and designing of information electronics devices with the registration of various physical parameters is proposed. The analytical calculation on the basis of the proposed model for a gas flow sensor of the temperature dependence from the fluid flow velocity in the MEMS structure was performed

I. Introduction

Development of the sensing device for any physical value and carrying out of scientific researches with its using imply the both sensor and research field detailed elaboration. Revealing regularities of the investigated measuring processes into the research object is solved within the problem framework. Synthesis of a new generation semiconductor submicron or nanoscale structures is mainly based on the use of laws and phenomena of solid state physics and is largely used into an empirical process. Many authors have attempted to systematize and present comprehensively such knowledge [1], but the result does not create the impression of completely systematic one. The variety of phenomena and laws allowed to create a variety of semiconductor structures and devices based on them. This process has not completed but constantly develops and discovers of nanoscale effects. The variety of effects should be considered in a certain methodological manner. First of all, it concerns measured values, by means of which quantitative description of the phenomenon (effect) is given; secondly, established relationships take the form of mathematical models at certain approximation; finally the synthesis of a semiconductor device can be considered. Modern researches is hardly to imagine without the active use of software products based on basic mathematical models to formalize a process of semiconductor individual element design and a converter synthesis as a whole [2]. Such information and analytical systems with a communication interface are developed for circuit design and do not affect the design and technological constraints of particular classes of semiconductor structures. In terms of systematization of knowledge about phenomena in solids and in micromechanical thermocouples in particular, the creation of such an information system remains an urgent task, since a detailed analysis of the processes occurring in the semiconductor structure opens up possibilities for the new measuring methods implementation and the characteristics of devices improving. The systematization of knowledge in this direction can not be reduced to a formal table or a simple algorithm for defining a feature of systematization. A vivid example is the study of electron-hole transition phenomena, which made it possible to obtain a variety of semiconductor devices, and this variety has become possible thanks to Computer Aided Design (CAD) systems - a separate tool for their research [3]. Nowadays, there are classes of instruments for which the physical principles of functioning are presented in the form of a CAD. For devices not studied or new expediency of the system approach is justified and the synthesis of the information system for the study of devices is a necessary step. With the rapid development of MEMS there is a rising need for CAD. This is an unsolved part of sensing device synthesis task for the both scientific purposes and educational ones for devices based on MEMS structures using electrothermal phenomena.

II. Multifunctional Microelectronic Thermoresistive Sensor

A. Application Fields and Technology.

The functional dependences of the overheated by enforcement thermoresistor from environmental parameters such as temperature, pressure, fluid (gas or liquid) flow, absorbed electromagnetic power are an essential physical principle of developments. The unified sensitive element includes a resistor assembly properly co-located either freely or at a thin-film dielectric membrane. The membrane being made by backside through etching of a monocrystalline silicon wafer. The membrane thermal properties, geometry and on the substrate location provide a high thermal isolation of the sensitive element from the substrate and reliable contact with ambient fluid. Micro Electro Mechanical System (MEMS) technology is used for the such sensitive element fabrication. It mainly includes standard operation steps of microelectronic manufacturing and micromechanical engineering for many types of sensors. Atomic layer deposition technology is possible for a fabrication of the sensitive element.

Sensor signal processing circuits are individual for each type of sensor and usually include a heating power supply circuit, a measuring amplifier, an analog-to-digital (ADC) converters, heat loss and offset compensation circuits, interface electronics (lately made by IoT technology).

Fields of application of microelectronic thermal sensors are the next:

- temperature measurement,
- absolute gas pressure measurement, vacuum measurement (Pirani type),
- volume or mass flow of gas and liquid measurement,
- gas analysis by heat exchange and mass transfer technologies,
- differential pressure and velocity variation measurement,
- optical power measurement.

B. Basic Constructive Constraints.

The presented phenomena of electrothermal transformations are basic for describing the ongoing physical processes. At this stage, it is necessary to understand the essence of the physical phenomenon, how to describe it and what structural characteristics are basic.

Thus, in the analysis of the gas flowmeter an electro-hydraulic analogy was been used. To characterize the flow forming channel, a pneumatic resistance is introduced - a parameter that is defined as the ratio of the pressure drop ΔP [Pa] to the channel length L_y (analogue of the voltage drop on the element) to bulk charges moving medium in the channel Q [m³ / sec] (analog of electric current):

$$R_h = \lambda_m \lambda_r \frac{\Delta P}{Q} \quad (1),$$

where λ_m – scale parameter of model, λ_r – dimensionless parameter of the form of the flow-forming channel cross-section, depending on the Reynolds number.

Any fluid movement in the flow-forming channel is accompanied by vortices and fluxes, especially in transition modes. If the reaction rate of the measuring system is higher than the rate of the changes in the channel, then the semiconductor structure can be treated as quasi-static. In this detail, the study of the laminar flow of the medium in the channel based on the calorimetric method is predominant.

For a cylindrical channel in a mode of laminar speed, the Reynolds number, taking into account the parameters of the medium, can be expressed through volume flow or through pressure drop ΔP on the length of the L_y channel in accordance with the following expressions:

$$Re(Q) = \frac{4\gamma Q}{\pi\eta D}, \quad Re(\Delta P) = \frac{\gamma D^3 \Delta P}{32 \eta^2 L_y} \quad (2),$$

where γ [kg/m³], η [Pa·s] – respectively, density and kinematic viscosity of the medium in the channel.

In the worst case scenario for numbers $Re < 200$, the length of the channel, which provides the formation of a laminar flow, has an order of ten hydraulic diameters. Then, for channels up to 1 mm high, the sensing element of the converter should be located 10 mm from the beginning of the channel for the implementation of the laminar mode at the upper region of the measuring range; as a result the transducer package must accordingly have dimensions of at least 20 mm.

C. Simulation

At this stage, the mathematical equations of electrothermal transformations is synthesized, and, in essence, a mathematical model for calculating phenomena in the MEMS structure [6].

The study is carried out iteratively according to the calculation algorithm for calculating the basic characteristics of the micromechanical primary converter with active heating.

III. Electrothermic transformations in the thermoresistive transducers

Micromechanical thermistor transducers operate on the basis of electrothermal transformations, and it is envisaged to create the given temperature gradients in the thermally insulated structure (TIS) and control the heat exchange between its individual elements and the environment. Structurally simple membrane, bridge or cantilever insulated TIS are multifunctional and meet the need for temperature, pressure, composition of the gas mixture, linear velocity, volume or mass flow of liquid and gas, acceleration, sound vibrations (microphones), electromagnetic radiation (bolometers) etc. The development of electronic transformer devices on their basis requires a complex statement of the problem with the obligatory consideration of both electrical and thermophysical processes directly in the TIS, as well as in the thermophysical and hydrodynamic processes in the environment fluid. Automatisation of an optimal design for such TIS and secondary converters electronic circuits development are the up to date subject of active research in the leading scientific institutions of the world.

The determination of the fluid flow velocity by methods of active heating implies either the estimation of the fraction of thermal losses of the heater into the surround flow due to its mechanical motion

(thermoanemometric method) or the analysis of the change in the spatial temperature distribution into the both TIS around the heater and the flow-forming channels (calorimetric method). The solution of the heat transfer problem in precise formulation requires finding a common solution of the following system of equations:

- Navier-Stokes equation for a non-mopping environment (equation of moments),
- equation of continuity of a flow in a channel,
- the energy transfer equation in the filled medium channel for the temperature field $T(x; y; z)$ in the moving flow without taking into account heat allocation due to the work performed by the forces of friction and compression,
- equation of conductive and convective heat transfer in the structural elements of the TIS taking into account heat sources geometry and heat exchange processes from the TIS' top and down surfaces.

These equations solutions require taking into account the processes occurring in the MEMS flow-forming channel; it is necessary to determine the velocities and pressures distribution for a given instant of time at any point in space. It is necessary to take into account both the initial and the boundary conditions for the completeness of the situation, depending on the type of the problem being solved. The complexity of the named equations systems prejudices a possibility of an exact solution obtaining in the general form; this is a well-known fact; therefore, different scenarios of the approximate solution are considered. There are certain solutions that establish links between the parameters of the motion of the medium and the

structural elements of the semiconductor MEMS. One of such scenarios is the use of a solution in the form Gagen-Poiseuil equations.

The detailed solution by an analytical method with due consideration for simplifications described in [6] establishes links with parameters that can be influenced by manufacturing technology [5]. The common solution also is a complex task for real TRST designs. In practice, when analyzing the physical processes of measuring the transformation of the TRST, it is expedient to perform a reasonable simplification of their geometry to simple models and using of the similarity theory methods.

IV. Results Of Analytical Simulation By Calorimetric Method

The simulation of processes in the structure should be considered successful if the results obtained on the basis of the both calorimetric and thermoconduometric method including:

- the study of the stationary temperature distribution in the flow-forming channel;
- the research on the heat exchange of the microbridge heat-generating element with the analysed medium in a flow-forming channel of a rectangular cross-section.

We've took into account the specific energy exchange between the next heat exchange bodies:

- elements inside of the TIS;
- the roof and bottom of the flow-forming channel;
- the moving fluid into the channel.

We have analysed conductive and convective heat transfer in the typical structural elements of the TIS taking into account the simplified heater geometry like a beam placed on a closed dielectric membrane. We have took into account heat exchange processes from the TIS top and down surfaces into a rough approximation of liner temperature distribution towards the outer normal to TIS surfaces [4] into the both the flow-forming channel and the etching cavity. Finally we have obtained the next heat-exchange equation for TIS one-dimension temperature distribution along the flow channel:

$$\left(\frac{1}{2}k_f d_{ch} + k_m d_m\right) \frac{d^2 T}{dy^2} - C_f \gamma_f d_{ch} \frac{V_y}{2} \frac{dT}{dy} - (h_t + h_b) T = \frac{P_h}{S_h} \quad (3),$$

where k_f , C_f , γ_f – the fluid heat conductivity, heat capacity and density respectively, d_{ch} – the flow-forming channel height, k_m and d_m – the TIS supporting membrane heat conductivity and thickness, h_t and h_b – the TIS heat exchange coefficients from the top and bottom surface respectively, P_h and S_h – the heater active power and heat-exchange surface respectively.

The last equation solution gives the temperature distribution into the proposed simple model for the both flow velocity depending heater T_h and TIS $T(y)$ towards the flowing fluid:

$$T_h = \frac{P_h/S_h}{\frac{k_f}{d_{ch}} + \frac{k_{air}}{d_b} + S_{ch} C_f \gamma_f \sqrt{\frac{V^2 + 16a_f^2 \left(\frac{1}{2} + \frac{k_m d_m}{k_f d_{ch}}\right) \frac{h_t + h_b}{k_f d_{ch}}}{1 + 2 \frac{k_m d_m}{k_f d_{ch}}}}}$$

$$T(y) = T_h \exp(\lambda y) \quad (4),$$

where: k_{air} – air heat conductivity (the proposed model supposed the bottom under-TIS etching cavity filled by stagnant air), a_f – fluid thermal diffusivity, S_{ch} – the flow-forming channel cross-section,

The analytical solution takes into account the electrothermal feedback between processes in the primary and secondary transducers, allows to perform the above-mentioned studies and results the numerical estimation.

V. Conclusions

The task of systematization of models of physical processes in a multifunctional primary converter, designed by MEMS on silicon based on electrothermal transformations, was solved.

The mathematical model which is accepted as the basis for synthesis of the library of CAD system elements and designing of information electronics devices with the registration of various physical parameters is proposed.

The analytical calculation on the basis of the proposed model for a gas flow sensor of the temperature dependence from the fluid flow velocity in the MEMS structure was performed. The results shown calculations for the sensor model described above show that the conversion characteristic is not symmetrical. This result requires an appropriate asymmetrical arrangement of the sensors relative to the heater. Therefore, for the bidirectional measurement of the linear velocity and the simultaneous preservation of the maximum sensitivity of the method, a matrix of sensitive elements will be required. This is the main conclusion of the analysis described in the proposed model.

VI. References

[1] "Handbook of MEMS for Wireless and Mobile Applications", Edited by Deepak Uttamchandani, Woodhead Publishing Limited, 2013.

[2] I.Sh. Nevlyudov, VV Evseev, VO Bortnikova, Ya.O. Zamirets, "Analysis of modern means of automated design of microelectromechanical systems", *Technology of administration*, №1, pp. 3 - 8, 2014.

[3] V.M. Tesliuk, "Models and Information Technologies for the Synthesis of Microelectromechanical Systems", Lviv, Tower and Co, 2008.

[4] A.G. Kozlov, "Error and adequacy of analytical modeling of temperature distribution in thermal microsystems", Problems of the development of promising micro and nanoelectronic systems 2014 Collected works in common. Ed. Academician of the Russian Academy of Sciences Stempkovskogo M., IPPM RAS, part II, pp. 167 - 172, 2014.

[5] "A method for manufacturing a matrix of thermoresistive converters", Patent of Ukraine №76885, published on January 25, Bulletin No. 2, 2013.

[6] Lupyna B.I. "Micromechanical surface thermo-resistor converter of linear velocity of medium in a channel of a rectangular cross-section", *Electronics and communication*, vol. 21, no 3 (92), pp. 17 - 28, 2016.

**PHYSICS AND THEORY
OF NANOSTRUCTURES
FOR ELECTRONICS**

EVALUATION OF EFFECTIVE PERMITTIVITY OF QUARTZ NANOCOMPOSITES WITH FULLERENE INCLUSIONS

Yu. M. Penkin, V. A. Katrich, M. V. Nesterenko, S. L. Berdnik
V. N. Karazin Kharkiv National University, 61022, Svobody Sq. 4, Kharkiv, Ukraine
E-mail: berdnik@karazin.ua

The possibility to reduce permittivity of radiotransparent materials made of silicon ceramics by embedding into their structure a lattice of fullerene inclusions is investigated. The proposed principle of creating new nanocomposites allows us to preserve main technical characteristics of ceramics: mechanical strength, erosion resistance, and ablation absence up to temperatures of about 1400°C. It was shown that inclusions of the fullerenes C_{720} allow to reduce the effective permittivity of the nanocomposites up to 10–17%.

Keywords — radio-transparent nanocomposite; fullerene inclusion; effective permittivity.

I. Introduction

Dielectrics are called radio-transparent materials if electromagnetic waves propagates through a dielectric layer practically without attenuation and random phase fluctuations. In other words, the radiotransparent materials have small dielectric losses and weakly reflect electromagnetic waves at operating frequencies. The radiotransparent materials are primarily used as radomes and protective covers for various types of ground-, air- and sea-based antenna systems. The development of radio-transparent fairings for aircrafts aimed at improving their mechanical, thermal, and radio-technical properties remains the most actual problem, due to need for increasing speed, maneuverability, improving radio-technical characteristics and all-weather capability of aircrafts. Currently, researchers in different countries pay great attention to the problem of developing new fairing materials [1], which have the high strength, significant erosion resistance, maximum possible radio transparency and absence of ablation at high temperatures. Ablation is defined as removal of mass from the surface of the fairing by high-temperature high-speed aggressive gases.

In modern practice, sitalls are widely used as materials for high-temperature antenna radomes and radiotransparent windows. The glass-ceramic materials, sitalls, are obtained by addition into molten glass fine powders of noble metals, copper, or titanium dioxide. However, sitalls have insufficient heat resistance and dielectric characteristics at temperatures above 1100 °C, since their softening temperature do not exceed 1500 ° C. From this point of view, refractory materials with melting points of 2000 °C and above, for example, silicon nitride ceramics can be used as radiotransparent materials [1].

A series of materials based on silicon nitride was developed by *Ceradyne Incorporated* (USA). The company produces several types of antenna radomes made of the following materials: fused silica ($\epsilon = 3.3$; $tg\delta \approx 0.003$), IRBAS ($\epsilon = 7.6$; $tg\delta \approx 0.002$), Ceralloy 147-31N ($\epsilon = 8.0$; $tg\delta \approx 0.002$) and Ceralloy 147-01EXP ($\epsilon = 4.0 \div 6.0$; $tg\delta \approx 0.002 \div 0.005$). These materials are used in modern rocket systems subjected to high mechanical and thermal loads, their dielectric properties are stable up to 1400°C [2]. Since the permittivity of these materials is in the range $3.3 \leq \epsilon \leq 9.0$, it would be highly desirable to reduce the permittivity while maintaining the rest of the material characteristics. To solve this problem, the authors propose to consider the possibility to include the lattice of fullerene inclusions into the structures of the silicon ceramics [3]. This work is aimed at the quantitative estimate of the effective dielectric constant made of the quartz nanocomposites with fullerene-like inclusions C_{720} .

II. Assessment of nanocomposite permittivity

The nanocomposites are defined as multicomponent solid materials, in which one of the components in 1D, 2D or 3D has dimensions not exceeding 100 nanometers. Also, as

nanocomposites are called materials whose structures consist of many repetitive components, known as layers or phases placed at distances of less than tens of nanometers. In the case of double nanocomposites, a component that is continuous throughout the entire material volume is called a matrix, and a composite discretely distributed over volume is called a reinforcement or reinforcing element. Usually, the reinforcing element is included into the matrix to change some of its properties.

The physical and electrical characteristics of the nanocomposite can significantly differ from the properties of conventional macro-composite material made from the same basic matrix substances and reinforcing elements. For example, silicon-carbon nanocomposites differ from conventional composite materials by lower weight, improved wear and impact resistances as well as increased resistance to chemical aggression. Therefore, fullerene inclusions [3] due to achieved level of technology for producing carbon nanomaterials can be considered as a promising type of reinforcing elements for matrix ceramics.

Let us consider a ceramic matrix with material parameters $(\epsilon_1; \mu_1)$. Suppose, that reinforcing elements are included as single fullerenes located at the nodes of 3D cubic lattice with a period s , as shown in Fig.1, and also assume that regardless of the fullerenes type used [3], the form of inclusion can be approximated by a sphere with radius a . If the model of fullerene inclusions in the form of a lattice of dielectric balls with material parameters $(\epsilon_2; \mu_2)$ is considered, the electrodynamic problem of finding the electrical characteristics of a nanocomposite can be reduced to problem of artificial dielectrics [for example, 4].

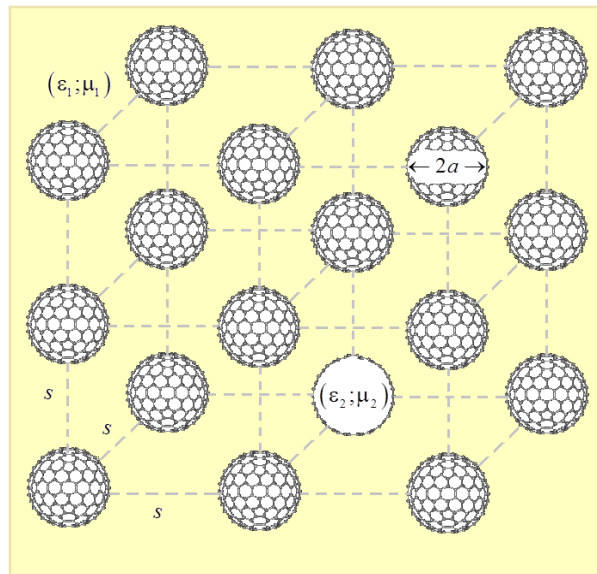


Fig. 1 – The nanocomposite internal structure

The corresponding electrodynamic problem can be solved under assumptions that a medium with small periodic inclusions is infinite and the characteristics of the electromagnetic field propagating in it can be obtained by using the effective permittivity (ϵ_{eff}) and permeability (μ_{eff}) of the composite medium. That is, the process of field propagation in such a medium can be described in terms of the electromagnetic wave with a wavelength λ_{eff} and the wave number $k_{eff} = 2\pi/\lambda_{eff}$ under conditions $k_1 a \ll 1$ ($k_1 = k\sqrt{\epsilon_1 \mu_1}$, $k = 2\pi/\lambda$, λ is the wavelength in free space). The above problem formulation allows rigorous analysis of the wave diffraction at the single spherical inclusion by satisfying boundary conditions for electric and

magnetic fields. The total field acting on the reinforcing particle can be found as a superposition of the excitation wave field and the fields scattered by the other inclusions. As is customary, these fields can be determined using approximating discrete summations by integrations.

Let us use the final expressions for ε_{eff} and μ_{eff} , obtained in [4]:

$$\varepsilon_{eff} = \varepsilon_1 \left(1 + \frac{3f}{(\varepsilon_2 + 2\varepsilon_1)/(\varepsilon_2 - \varepsilon_1) - f} \right), \quad \mu_{eff} = \mu_1 \left(1 + \frac{3f}{(\mu_2 + 2\mu_1)/(\mu_2 - \mu_1) - f} \right), \quad (1)$$

where $f = (4\pi a^3/3s^3)$ is the ratio of the volumes of the reinforcing inclusion and the cube with a side equal to the lattice period, that is, the filling factor of the matrix with spherical inclusions. As can be seen, the formula (1) for non-magnetic materials, transforms into the well-known Clausius-Mossotti formula, and the inequality $\varepsilon_{eff} < \varepsilon_1$ holds if $\varepsilon_2 < \varepsilon_1$. Hence, the permittivity the reinforcing inclusions should be relatively lower of the matrix substance.

Let us select, based on the formula (1), the fullerene type which can be used for the nanocomposite reinforcement. As is known [3], the fullerene molecules consist of n carbon atoms C located at vertices of hexagons or pentagons forming the surface of a sphere or ellipsoid (see Fig. 2). The number n of the carbon atoms determines both the type of fullerene C_n and the sphere radius, approximating the surface of the molecule.

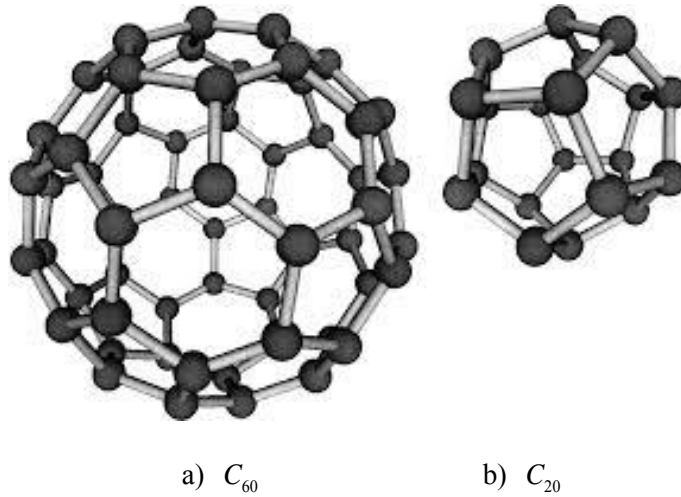


Fig. 2 – The fullerene structures

The concept of effective dielectric constant for different types of fullerenes was proposed in [5], where results based on numerical simulations were obtained, some of which are presented in the Table 1.

Table 1. Fullerene parameters

C_n	C_{20}	C_{60}	C_{180}	C_{720}
a [nm]	0.199	0.355	0.613	1.259
ε_2	10.632	3.041	1.922	1.365

The analysis of the data presented in the Table 1 shows that the radius of the fullerene molecular increases while its effective permittivity decreases if the number of atoms in the molecule n increases. Therefore, the simulation results represented bellow were obtained for the fullerene C_{720} , the highest type considered in [5]. Based on the relation (1) and table data,

the dependences of the relative value of the ratio $\varepsilon_{eff}/\varepsilon_1$ upon the period of the nanoinclusion lattice were calculated for different matrices of silicon nitride ceramics. For example, the plots $\varepsilon_{eff}/\varepsilon_1$ as functions of the lattice period s are shown in Fig. 3, where curve 1 corresponds to the silica matrix ($\varepsilon_1 = 3.3$), and curve 2 corresponds to the matrix of Ceralloy 147-31N ($\varepsilon_1 = 8.0$) made by *Ceradyne Incorporated* (USA).

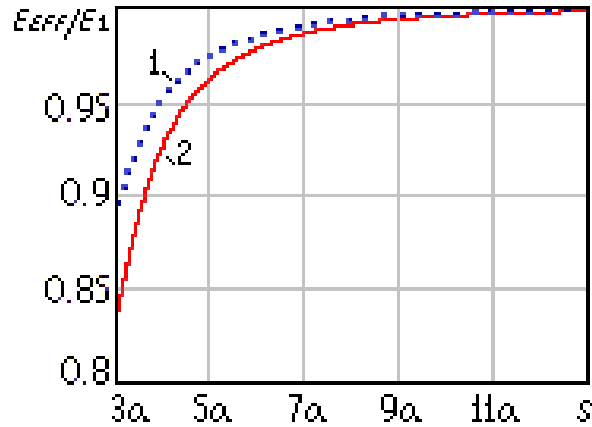


Fig. 3 – The permittivity of nanocomposites:
1- silica matrix, $\varepsilon_1 = 3.3$, 2- Ceralloy 147-31N, $\varepsilon_1 = 8.0$

As can be seen from fig. 3, the inclusion of fullerene lattices into silicon matrices makes it possible to reduce the effective permittivity of the nanocomposites by 10–17%. As expected, the denser is the filling of the matrix substance with fullerene inclusions, the greater is the effect of the ε_{eff} reducing.

III. Conclusion

The results of theoretical studies to reduce the permittivity of radio-transparent materials made of silicon ceramics are presented. To achieve the effect, it has been proposed to use fullerene inclusions located at the nodes of cubic lattices as a reinforcement for silicon matrices. The proposed approach to creating new nanocomposites consists in that the technical characteristics of ceramics: mechanical strength, erosion resistance, and ablation absence, are preserved up to temperatures of about 1400 °C. The simulation results show that inclusions of fullerenes C_{720} reduces the nanocomposite permittivity ε_{eff} by 10–17%. It can also be stated that using higher types of fullerenes in nanocomposites of larger molecule sizes and, hence, with a lower effective permittivity will improve the effectiveness of the approach.

References

- [1] Rusin M.Yu. Design of rocket head fairings made of ceramic and composite materials, Moscow, Izd-vo MGTU im. N.E. Baumana, 2005, 64 p. (in Russian).
- [2] MatWeb [Электронный ресурс] // Online Materials Information Resource. URL: <http://www.matweb.com> (дата обращения: 15.03.2019).
- [3] Kroto H. W., Heath J. R., O'Brien S. C. et al. "C60-Buckminsterfullerene," Nature, vol. 318, No 6042, pp. 162—163, 1985.
- [4] Lewin L. "Theory of waveguides: techniques for the solution of waveguide problems," Newnes-Butterworths, p. 346, 1975.
- [5] Penkin D. "Selected Aspects of Wireless Communication between Nano-devices," PhD Dissertation, Delft University of Technology, p. 155, 2015.

MORPHOLOGY AND MICROSTRUCTURE OF CATHODE DEPOSIT OBTAINED AT PLASMA-ARC SYNTHESIS OF CARBON NANOTUBES

^{1,2} V.G. Udovitskiy, M.I. Slipchenko³, O.Yu. Kropotov²,
P.V. Turbin^{1,2}, B.M. Chichkov⁴, O.V. Slipchenko²

¹ Scientific Center of Physical Technologies MES and NAS of Ukraine
61022, Kharkiv, Svobody Sq., 6, a/c 4499, Tel. (057)707-53-82

E-mail: udovvg@meta.ua, petro_turbin@ukr.net

²V.N. Karazin Kharkiv National University,
61022, Kharkiv, Svobody Sq., 6, Tel. (057)705-20-30

E-mail: germany@karazin.ua

³Institute of Scintillation Materials, NAS of Ukraine
61001, Kharkiv, Nauky Ave.

E-mail: naukovets.big@gmail.com

⁴Leibniz University, Hannover, Germany

E-mail: b.chichkov@lzh.de

Synthesis of carbon nanotubes (CNTs) and other carbon nanostructures in the arc discharge is one of the first and best methods for obtaining them. It's based on ablation of the graphite anode and the deposition of carbon nanostructures on the cathode surface and on other surfaces of the vacuum chamber. The formed cathode deposit (CD) plays an important role in maintaining the arc discharge and, accordingly, the synthesis processes. The article presents the original experimental results of our own authors research. For the first time, a CD has been obtained, which inside the hard outer shell contains two layers – a soft core and a soft black interlayer between core and the outer shell.

Introduction

Progress in the development of microelectronics over the past few decades has been extraordinarily large and impressive, in particular in the scaling and development of silicon large integrated circuits both in terms of functionality and the number of elements in them and the complexity of their structure. The cost of one transistor on a silicon chip has decreased more than 10^6 times in the previous 40 years, and the number of transistors in one chip has also increased more than 10^6 times [1]. Advanced manufacturers have long overcome the fundamental barrier of the number of transistors in a single chip, viz., 10^9 units. This was made possible due to the successful use of miniaturization, which was a major trend in the development of silicon microelectronics technology during the period when electronics evolved in accordance with Moore's Law. Intel company reported that in 2017 it began producing chips using 10-nanometer technology, in 2018 it planned to master 7-nanometer technology, and in 2021 - 5-nanometer one [2].

In most cases microelectronics, actually, has already become nanoelectronics. But its further development in the traditional way of reducing the size of individual elements and increasing the density of packaging now faces extreme technological (and therefore financial) difficulties. However, the main thing is that on the way to the further reduction in the size of the individual elements are the physical constraints caused by the fundamental laws of quantum physics. Therefore, one of the main trends in the development of nanoelectronics now is the search for new materials that, with a high level of miniaturization of devices already achieved, could significantly increase their performance and reduce energy consumption compared to silicon-based devices. Extremely promising in this sense are the new carbon 1D- and 2D-dimensional nanostructures - carbon nanotubes (CNTs) and graphene.

Comparative model studies of the performance (speed of logic transitions) and energy consumption for these operations of one of the most advanced Si 3D transistors with 3D

architecture (FinFET) and transistors based on CNTs of similar sizes confirmed that transistors based on CNTs in these parameters are significantly ahead of the transistors with Si (Fig. 1) [3].

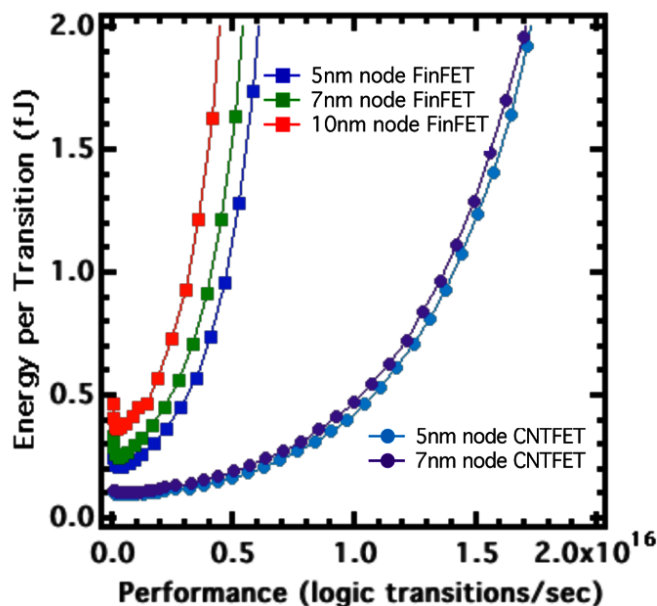


Fig. 1 – Comparative characteristics of the speed of logic transitions and energy consumption for these operations for Si-FinFET and FETs based on CNTs

The great potential of using new carbon materials in electronics, both practically implemented and potentially possible, has led to the creation of a new direction in electronics at the turn of the millennium, the so-called "carbon-based electronics", which is now actively developing. The concept of carbon electronics envisages the possibility of manufacturing a variety of electronic devices, in particular flexible, stretchable and bio-integrated, solely (or mainly) based on different carbon materials. Experts anticipate significant advances for carbon electronics in the future.

Among new carbon nanostructures, CNTs (1D nanostructures) are now the most widely used in electronics, transistors (even single-electron ones), diodes, various sensors, supercapacitors, solar cells, light-emitting panels, electrochemical power supplies, and so on like that, have been made on their basis. They open wide prospects for the further development of nanoelectronics, in particular, new areas of electronics - ionoelectronics, spintronics. Manufacturing of nanoelectronic devices based on separate CNTs requires the development and implementation of sophisticated technologies that would allow the manipulation of separately selected CNTs with the required properties, in particular, to position and fix them in the desired place of the solid state circuit and to provide them with a reliable electrical switch. Such technologies are now available only in modern laboratories, and therefore, while manufacturing the CNT-based devices, their arrays, pre-synthesized by different methods, are now mainly used, or their thin films are applied directly to the desired substrates. Methods for making thin CNT films for use in electronics were previously considered by us in [4].

All of the above causes the high relevance of the development of productive reproducible methods of the CNTs synthesis. Now there are many known methods and technologies for the CNT production, but three methods are the most suitable for mass and controlled production: ablation of graphite in arc discharge (plasma arc method), laser ablation of graphite, chemical vapor deposition (CVD synthesis). The plasma-arc method (ARC-synthesis) is currently the most commonly used method, which has historically been the first method to be widely used for the synthesis of various carbon nanostructures.

A so-called cathode deposit (CD) is formed at the cathode in plasma-arc synthesis of CNTs with the ark powered by direct current. A lot of work is devoted to studying the properties of CD, in particular, its morphology, composition, structure, since it significantly influences the synthesis process, as well as the properties and quantity of the obtained CNTs. However, quite often results published by different authors are weakly correlated with each other. This can be explained by the great dependence of the process of plasma-arc synthesis and the properties of the CD, formed in this case, on many factors - plasma-forming gas, pressure in the chamber, the size of the chamber, the size and configuration of the anode and cathode, voltage at the electrodes, current densities, etc. These factors usually do not exactly match in studies of various authors. Detailed overview of various properties of the CD obtained by other authors, is done by us in [5].

The purpose of this work is to present the original results of our own experimental studies of the morphology, composition and structure of the CD obtained in the course of plasma-arc synthesis of CNTs.

Experimental part

Arc synthesis of the CNT was carried out using the modernized domestic vacuum unit VUP-5M (Vacuum Universal Post-5M). During the modernization, the vacuum chamber was effectively cooled with an arc discharge in it. The windows in the chamber were made of quartz glass with fluoroplastic seals. Rods with a diameter of 6 mm of ultra high purity graphite were used as anodes, the same rods with a diameter of 6 mm, or massive cylindrical billets of graphite with a diameter of 50 mm were used as cathodes.

Ar is the gas generating plasma, its pressure was 200 - 500 Torr. The anode - cathode distance after ignition of the arc discharge was maintained at the level of 1 - 2 mm using a specially designed electric actuator. It could be directly controlled with a specially designed camera-obscura attached to the window of the vacuum chamber. The current of the arc discharge was regulated by the voltage of the power source (20 - 30 V) and maintained at the level of 50 - 80 A. The location of the electrodes is vertical. Experiments were performed with the cathode arrangement above or below. The vertical configuration, unlike the horizontal arrangement of the electrodes, provides a fairly uniform flow of cathode and anode on all sides by convective heat fluxes with vapor or carbon nanoparticles formed in the surrounding electrode space at ablation of the anode. Figure 2 shows a photo of the electrodes (cathode with CD on top of it) after 5 cycles of arc discharge for 3 to 4 minutes each.



Fig. 2 – Photo of electrodes (cathode with CD on top of it) after 5 cycles of arc discharge

Results and their discussion

Fig. 2 shows that the CD grew long enough on the cathode. After 5 cycles of arc discharge, its length was ~ 100 mm. The discharge was carried out with intermittent cycles to

prevent overheating of the camera and the equipment installed therein. The publications sometimes provide information on the length of the formed CD, which was usually 10 - 70 mm, and sometimes reached 100 mm [5]. In our experiments we managed to grow cathode deposits of a record length, namely, 180 mm and even slightly more (Fig. 3).

The outer surface of the upper part of the CD, that is, its shell is ~ 4 mm long from the end, which was on the side of the anode, has a grayish-steel color. Further, the surface of the CD shell is covered in many places with loose soot-like black particles which have a weak bond with this shell and are easily separated from it even with slight shaking of the CD.



Fig. 3 – Photo of 180 mm long cathode deposit obtained by ablation of an anode 6 mm in diameter

The deposit of the maximum possible length in our studies was formed with a dual purpose - to evaluate how the length of the CD influences the arc discharge process, and also to apply the resulting CD already as an anode that evaporates in the arc discharge in the following experiments. There was no significant effect of the length of the cathode deposit on the arc discharge.

Fig. 2 also shows that after 5 cycles of the arc process not only the CD but also the deposit on the anode was formed. Its formation substantially complicates theoretical consideration and modeling of the already sufficiently multifactorial process of arc synthesis of carbon nanostructures, since this means that after some time the process of the arc discharge is no longer in the graphite (cathode) - graphite (anode) system, as this is the case at the beginning of the process, and in fact in the CD (cathode) - an anode deposit (anode) system. The role of the anode deposit in the arc discharge is still poorly understood.

When characterizing the CD morphological structure in the radial direction it was indicated in many publications that it consisted of a soft porous core of black or black and gray color, in which various carbon nanostructures were found and multiwall CNTs were distributed between them [5]. The core is inside a fairly solid but fragile shell of gray-steel or gray-silver color, which consists mainly of pyrolytic carbon and hardly contains the CNTs. The boundary between the inner layer and the outer shell is clear and the fragile material of the inner layer can be easily removed mechanically from the shell. It was also often noted that the CD had a three-layer structure - around the solid shell with the core inside there was also an outer very porous layer of amorphous carbon, in which both single-walled and multi-walled CNTs were found, as well as other carbon nanostructures. This outer layer is very poorly bonded to the shell and can easily crumble upon mechanical action. The publications of other researchers stated that there was only one layer inside the solid shell, in which different carbon nanostructures were found and multi-walled CNTs distributed between them.

A typical two-layer structure of the CD was obtained in our studies as well while conducting an arc discharge between the graphite cathode and the anode of equal diameters of 6 mm (Fig. 4a). This diameter of graphite electrodes was most commonly used in the vast majority of published studies. During the process the anode positioning was mistakenly displaced relative to the cathode by about 2.5 mm and therefore the CD, as can be seen in Fig. 4a, grew on the cathode also with a corresponding offset relative to its axis. This random experimental result indicates that the CD grows on the cathode, focusing mainly not on the axis of the cathode but on the axis of the anode that evaporates.



Fig. 4 – The CD photo: a - cathode D 6 mm, anode D 6 mm; b - cathode D 50 mm, anode D 6 mm

The cathode deposit, which grew on the cathode with a diameter of 50 mm at ablation of the anode with a diameter of 6 mm. (Fig. 4b), had a completely different radial structure. This CD contains not more than one layer inside the hard shell, but two (see Fig. 5) - a core of dark gray (as in other publications), around which there is a thin fragile layer of rich black color, and then a solid outer shell of gray-steel color is placed.

Subsequent electron microscopic studies have shown that the core, as in other studies, contains various carbon nanostructures, including multistage CNTs (Fig. 6a). A thin layer of black between the core and the outer shell consists of amorphous carbon and turbostrate graphite nanoparticles (Fig. 6b). The outer hard shell, as in other studies, consists mainly of porous carbon material similar to pyrolytic graphite (Fig. 6c).

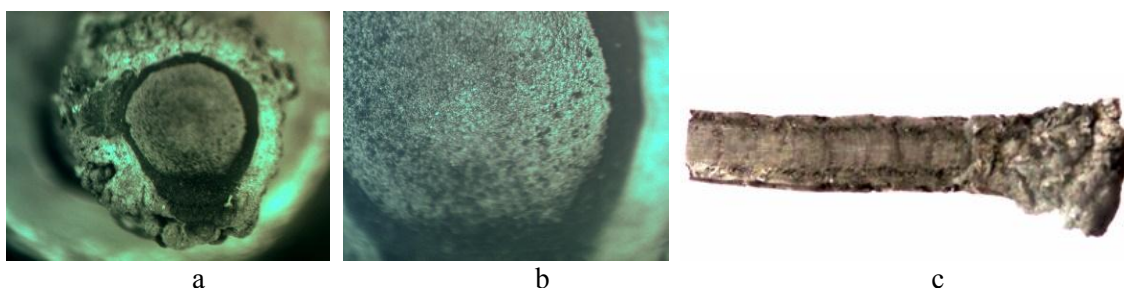


Fig. 5 – Photo of the three-layer CD: a, b – is a photo of the grinders of the end part of the CD; c – is a photo of a longitudinal section of this CD

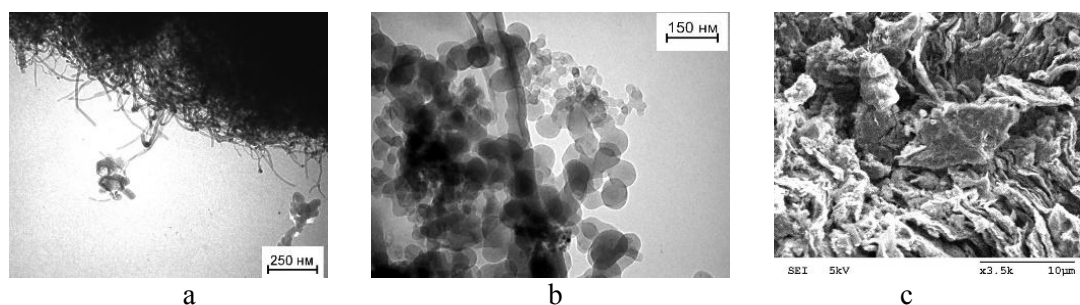


Fig. 6 a, b – are TEM photographs of particles taken from: a - the CD core; b - from the gap between the CD core and the sheath; c – from SEM photograph of the CD outer shell

The presence of a layer between the core and the outer shell, is observed not in one place, but along the entire length of the CD (Fig. 5c). This confirms the law of the CD formation of such structure during the whole process of its growth.

The boundaries between all three components of the obtained CD are clear and well observed when examined both with the naked eye and in an optical microscope. We did not find

information about the experimental observation of such a structure of CD, namely, the presence of a clear gap between the core and the outer shell in other publications, but the possibility of its formation was already theoretically foreseen [6].

Conclusions

Research into various issues related to the synthesis of CNTs is very relevant, as CNTs have already been identified and still have considerable potential for use in various fields, including electronics. The CD is synthesized using the plasma-arc method for the first time, it contains not one fragile core inside the solid outer shell, as observed in many studies, but a core with a clear transition layer between it and the outer shell. This result is an experimental confirmation of the previously published theoretical model, where the assumption of the possibility was made of three temperature zones formation in the CD under certain conditions, located concentrically in the radial direction. Electron microscopic studies have shown that the core, as in other studies, contains a variety of carbon nanostructures, including multiwalled CNTs. The thin layer of black color between the core and the outer shell consists of amorphous carbon and turbostrate graphite nanoparticles. The outer hard shell consists mainly of porous carbon material similar to pyrolytic graphite.

References

- 1 Micro- and Nanoelectronics: Emerging Device Challenges and Solution. CRC Press 2015, 363 p.
2. R. Courtland. Moore's law's next step: 10 nanometers // IEEE Spectrum Magazine. - 2017. – Vol. 54, Iss. 1. – P. 52-53.
3. G. S. Tulevski, A. D. Franklin, D. Frank, J. M. Lobe, Q. Cao, H. Park, A. Afzali, Shu-Jen Han, J. B. Hannon, W. Haensch. Toward High-Performance Digital Logic Technology with Carbon Nanotubes // ACSNANO. – 2014. – Vol. 8, No. 9. – P. 8730-8745.
4. A.Yu. Kropotov, N.I. Slipchenko, V.G. Udovitskiy, B.N. Chichkov. Thin films of carbon nanotubes for the purpose of creating various electronic devices // Proc. of IX Int. Scientific Conference "Functional Base of Nanoelectronics", September 18 - 23, 2017, Odessa, Ukraine P. 5-8. (In Russian)
5. V.G. Udovitskiy, O.Yu. Kropotov, M.I. Slipchenko, P.V. Turbin, B.M. Chichkov Features of growth and structure of cathode deposit obtained using plasma-arc synthesis of carbon nanotubes // Radioelektronika i informatika. - 2018, No. 4 (83). – P. 4-19. (In Ukrainian)
6. S.N. Mohammad. Arc Discharge and Laser Ablation Processes for Nanotube Synthesis: Exploration, Understanding and Rediscovery // Rev. Nanosci. Nanotechnol. – 2013. – Vol. 2, No. 5. – P. 309-345.

GENERAL KINETICS OF Pb-Sn SOLID SOLUTIONS CELLULAR PRECIPITATION

Yu.A. Vronska, S.M. Zakharov, I.O. Shmatko, O.A. Shmatko, S.M. Kedrovskiy

G. V. Kurdyumov Institute for Metal Physics of the NAS of Ukraine,

36 Acad. Vernadsky Blvd,

03680, Kiev 142, Ukraine

тел. (066) 342-17-48

E-mail: igorshmatko989@gmail.com

General kinetics of Pb-Sn solid solutions cellular precipitation with content of Sn with 5,15; 7,60; 10,03; 12,38; 14,73; 19,22; 23,55; 27,70 та 29,05 at. % was studied at a temperature of 293 K by methods of optical microscopy, X-ray diffraction analysis and resistometry.

The aging process of Pb-Sn alloys takes place in two stages: primary and secondary cellular reactions. As a result of the primary cellular reaction, a thin-plate structure (cells), consisting of alternately located tin plates and a depleted lead-based solid solution, is formed.

The primary plate structure continues to decompose during the secondary cellular reaction or non-sloping roughness. Secondary cellular reaction occurs at a much lower rate than the primary cellular reaction, forming a plate structure of lower dispersion.

Measuring the lattice parameter indicates that the concentration of the depleted solid solution in the primary cells is substantially higher than the equilibrium, whereas its concentration in the secondary cells is closer to the equilibrium.

The representation of experimental isothermal resistorgrams in the coordinates $d\rho/dlgt$ - lgt , where ρ -electrical resistance, τ - time of aging of the alloy, provides the possibility of precise determination of the time intervals for the flow of primary and secondary cell reactions and their speed parameters.

The staged nature of the discontinuous (cellular) precipitation of metallic supersaturated solid solutions was observed in earlier studies of this process by the method of optical metallography [1]. The formation of cells of significantly lower dispersion of the microstructure was called the coalescence process by the investigators, not taking into account the non-complete depletion of the initial supersaturated solid solution during its initial stage of precipitation [2].

Secondary cellular reaction occurs in a depleted solution during the primary reaction, the concentration of which is usually higher than that of the alloy at the given aging temperature. The lower saturation of the solid solution determines the lower velocity of the secondary cell reaction, as well as the dispersion of the new microstructure. Despite the fact that the process of secondary cellular reaction is a widespread and well-known phenomenon, its systematic studies have not been carried out to date. Only in Pb-Sn alloys, based on the results of isothermal resistometric studies of cellular precipitation kinetics, a method for data differentiation for primary and secondary reactions was proposed. [3].

This technique is the newest approach to the quantitative processing of kinetic data of aging of alloys. The microstructural investigations revealed that the general picture of the transformed volume during the cellular precipitation in Pb-Sn alloys consists of primary and secondary cell reactions, but the time intervals of these reactions with ordinary kinetic isotherms (in this case resistometric ones) can not be determined. That is achieved by the method of numerical differentiation of the function in (x) given analytically or tabulated.

This method consists of replacing this function with the interpolation polynomial $P(x)$, the derivatives of which $d^n P(x)/dx^n \approx d^n y(x)/dx^n$ are extracted analytically from the corresponding relations. Numerical differentiation for uniformly located three nodes with interpolation is realized by the relation:

$$y'(x_0 + ph)_3 = \frac{1}{h} [(p - 0,5)y_{-1} - 2py_0 + (p + 0,5)y_1].$$

Here $p \approx (x - x_0)/2h$, h – interval of x increment.

In general, the numerical differentiation equation for nodes $y(x)$ is more elemental than the given relation, since P in the nodes acquires a fixed value. The equation for a central node is particularly simple and quite accurate ($P=0$):

$$y' = (y_{i-1} - y_{i+1})/2h \quad (1)$$

$$y'' = (y_{i-1} - 2y_i + y_{i+1})/h^2 \quad (2)$$

These relationships are convenient for numerical differentiation of tabulated functions at a point $x=x_0$. Thus, they are suitable for processing not only resisto-, dilato- and volumurons, but also similar experimental results in relation to the general kinetics of phase transformations in metallic alloys. By help of them the isothermal resistograms of the studied alloys were processed. The data on the dependence of their electrical resistance from aging time are combined into four groups due to the significant difference in the rate of decomposition process, which increases with increasing the saturation of the solid solution, and in order to optimize the mathematical analysis of the resistograms.

The first group involves alloys with Sn content up to 10.03 at.%, with low aging rates. The corresponding resistograms (Fig. 1a) are graphically redrawn on the equilateral nodes with the following definition of the function values for specific nodes in mm. Subsequently, these values by elemental transformations are transformed into absolute values, by which, using the relation (1), the dependences $y' - x$ (Fig. 1b) are constructed, which are curves with clearly expressed peaks corresponding to the time of the maximum reaction rate.

The second group consists of alloys with 12.38 and 14.73 at.% Sn (Fig. 2a), whose aging rate is significantly higher than the previous group has. The result of mathematical processing (Fig. 2 b) makes it possible to establish the fact of the start of the secondary reaction, which begins before the end of the primary. The shift of the maximum reaction rate is noted.

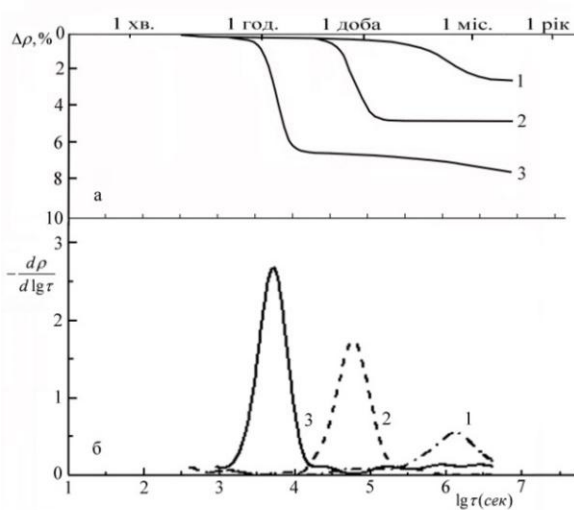


Fig. 1 – Dependences $\Delta\rho - \lg\tau$ (a) i $d\rho/d\lg\tau - \lg\tau$ (б) for alloys with Sn content 5,15 (1), 7,60 (2) and 10,03 (3) at.%

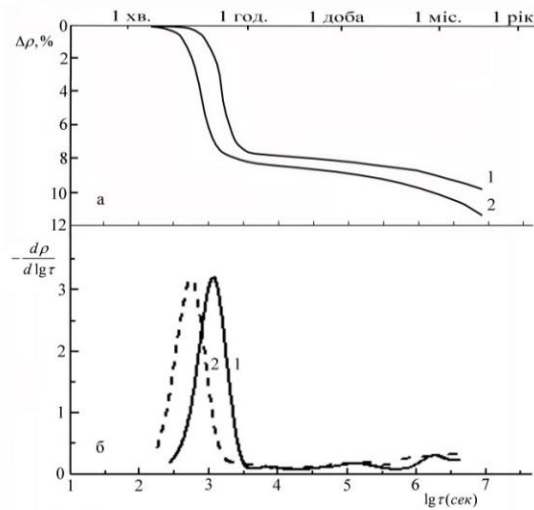


Fig. 2 – Dependences $\Delta\rho - \lg\tau$ (a) i $d\rho/d\lg\tau - \lg\tau$ (б) for alloys with Sn content 12,38 (1) and 14,73 (2) at.%

The third group contains experimental data for alloys with 19.22 and 23.55 at.% Sn (Fig. 3a), which are aging even faster than the previous ones. By their processing (Fig. 3 b), the first and second stages of the cellular reaction are clearly identified. And in these alloys the secondary reaction also begins before the end of the primary.

Finally, for the fourth group of alloys with 27.70 and 29.05 at.% Sn (Fig. 4a) we have an extremely high aging rate. At the same time, the secondary reaction begins at some time after

the end of the primary and, unlike the alloys of the third group, is characterized by a lower velocity (Fig. 4b).

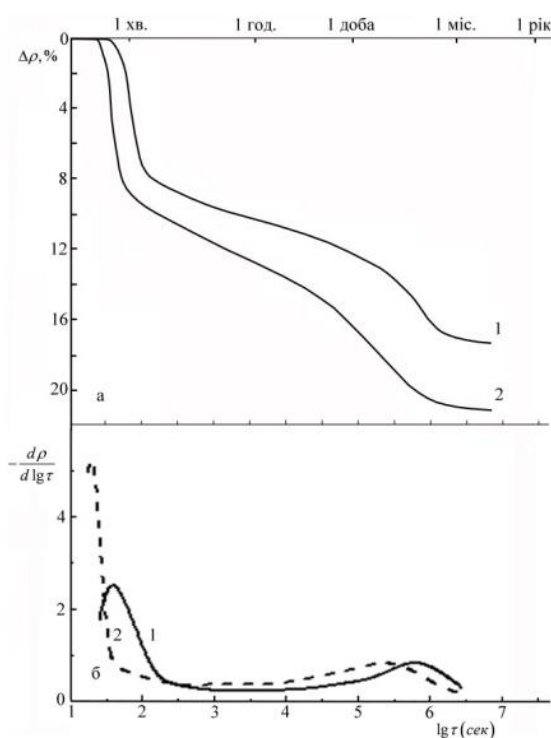


Fig. 3 – Dependences $\Delta\rho - \lg\tau$ (a) i $dp/d\lg\tau - \lg\tau$ (б) for alloys with Sn content 19,22 (1) and 23,55 (2) at.%

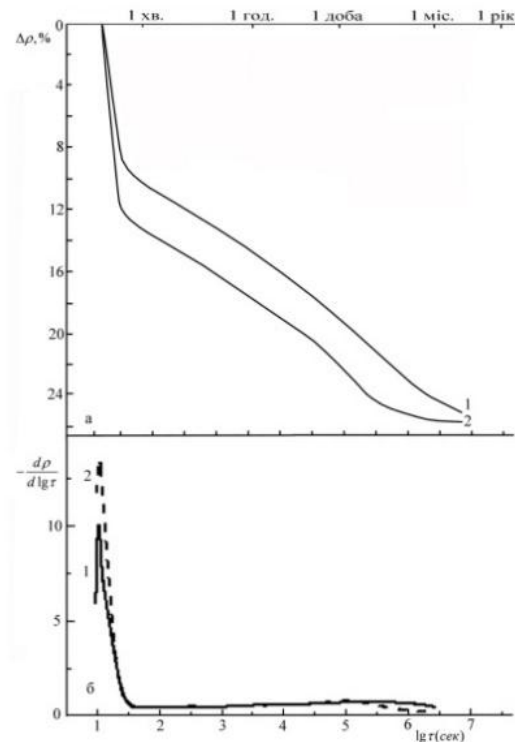


Fig. 4 – Dependences $\Delta\rho - \lg\tau$ (a) i $dp/d\lg\tau - \lg\tau$ (б) for alloys with Sn content 27,70 (1) and 29,05 (2) at.%

The conclusion regarding the above-mentioned flow of these reactions can be confirmed by analyzing the dependence of the maximum speed of the primary reaction (the first derivative) on the concentration of Sn (Fig. 5). Almost a horizontal plot on the graph exactly matches the alloys of the second and third groups, in which the secondary reaction actively develops before the end of the primary. Thus, the rate of the primary reaction is practically constant for alloys in which the secondary reaction is activated before the end of the primary. In those cases, when competition between primary and secondary reactions is not significant, there is a uniform increase in the speed of the primary reaction.

From the dependencies shown in Fig. 1b and 2b it is simply determined the finishing time of the primary cellular reaction for alloys of the first group and the primary reaction for alloys of the first and second groups, and from Fig. 3b and 4b of the primary and secondary reactions for alloys of the third and fourth groups. These time parameters are necessary for obtaining data on the change in the converted volume of alloys during their isothermal aging to analyze the general kinetics of cellular precipitation based on the theory of J. Cahn [4]. The precise definition of these parameters can be obtained by the second derivative of our function, which transforms to zero at the start and end of the analyzed process.

In addition, note that the data shown in Fig. 5 correlated satisfactorily with the results of a series of studies of the volume fraction of the precipitation phase (Sn) during the primary cellular reaction (Fig. 6). It has been established that in Pb alloys containing about 12-17 at.% Sn, the degree of exhaustion of the initial saturation of the solid solution is \sim (57-65)%. A rather high degree of residual supersaturation is the driving force of a relatively intense secondary cellular reaction. At lower and higher initial concentrations (c_0) of Sn in investigated alloys, the proportion of exhaust c_0 increases, correspondingly weakening the stimulus to the development of the secondary reaction.

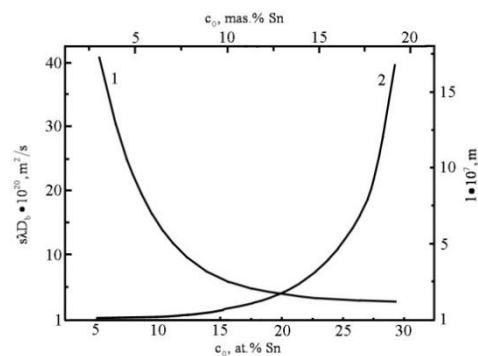
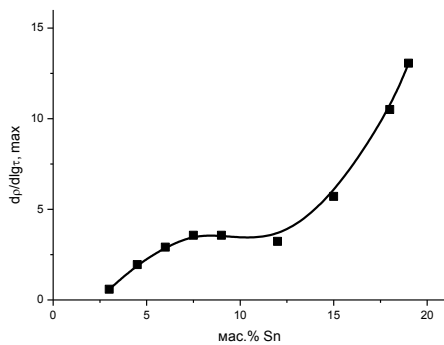


Fig. 5 – Dependence of the maximum rate of the primary reaction in Pb-Sn alloys on the Sn content
Fig. 6 – Concentration dependences l (1) and $s\lambda D_b$ (2)

To a certain extent this situation can be connected with the dependence of the mobility of the grain boundary (the front of the cellular reaction) $M \sim s\lambda D_b/l^2$. Here D_b – the diffusion coefficient of the atoms of the dissolved element by a moving grain boundary, s – segregational factor, λ – grain boundary thickness ($\approx 0,5$ nm), and l – interlamellare distance in a cell. From Fig. 6, where the concentration dependences $s\lambda D_b$ and l are given, it is evident that for $c_0 < 12$ at.% Sn the determining contribution to the growth of M is the change l , whose value decreases with increasing c_0 . For $c_0 > 17$ at.% Sn as a control factor in accelerating the movement of the front of the cellular response begins to prevail D_b . Thus, the equilibrium in the competition of the two indicated kinetic parameters of the cellular reaction determines a certain stability of the process velocity in the concentration range of 12-17 at.% Sn, which is illustrated by a distinct "plateau" depending on the given velocity from c_0 (Fig. 5).

1. L.N. Larikov, O.A. Shmatko. Cellular precipitation of supersaturated solid solutions. - Kyiv: Naukova dumka, 1976. - 221 p.

2. G. Borelius, Larsson L.E. A Resistometric Study of the Kinetics of Precipitation in Lead-Tin Alloys. // The Materials of Symposium organised by the Institute of Metals and held at the Royal Institution „The Mechanism of Phase Transformations in Metals” (London, on 9 November 1955). Institute of Metals Monograph and Report Series. - 1956. - № 18.

3. Yu.M. Koval, V.F. Mazanko, I.O. Shmatko, O.A. Shmatko. The stage of cellular precipitation of supersaturated lead-tin solid solutions. // Reports of the NAS of Ukraine. - 2013. - №2. - P. 71 - 74.

4. Cahn J.W. The Kinetics of Grain Boundary Nucleated Reactions. // Acta met. - 1956. - 4. - № 5. - C. 449 - 459.

SIZE INFLUENCE OF SILVER NANOPARTICLES ON THE COEFFICIENT OF Ag LINEAR THERMAL EXPANSION

O.V. Filatov^{1,2}, O.M. Soldatenko², S.M. Soldatenko²

¹ G.V. Kurdyumov Institute for Metal Physics of the NAS of Ukraine
03142, Kyiv, Academician Vernadsky Boulevard, 36, dep. Physics of Atomic Transport
Processes

² National Technical University of Ukraine “Igor Sikorsky Kyiv Polytechnic Institute”
03056, Kyiv, Prosp. Peremohy, 37, dep. Metal Physics, Faculty of Physical engineering
tel. (066) 450-54-43

E-mail: oksana.hubina2811@gmail.com

This work is devoted to study silver nanoparticles as a material that may be used in MEMs/NEMs technologies. Thermal property such as a coefficient of linear thermal expansion (CLTE) of silver nanoparticles is investigated there by the molecular dynamics method. Parameters of modelled systems and a way of CLTE investigation are given. The CLTEs of silver nanoparticles with different sizes and different percentage of atoms on the surface are described. The size of nanoparticle with stable CLTE on the temperature range from 150 K to 450 K is defined.

Introduction

For today different nanoobjects, especially carbon nanotubes, are widely used in MEMs/NEMs technologies [1]. They found an application in sensors, actuators and energy storages. More over a lot of metallic nanoparticles, including metal nanotubes, are developing as an alternative of usage of standard components in electronic systems. One significant property of such nanoparticles is the coefficient of linear thermal expansion (CLTE) which is important for understanding how does the material behave under different thermal conditions. This knowledge gives an information about areas of material application. For example the CLTE of carbon nanotubes increases with the temperature growth [2] that can limit areas of their application. To provide the material with the stable CLTE on the whole temperature range of material exploitation could expand the possibilities of based on them devices.

The main aim of this work is to find the correlation between size of silver nanoparticle and its CLTE. As a research method there was used the method of molecular dynamics (MD) using potential based on the Embedded Atom Method (EAM).

Earlier studies of CLTE and thermal stability of silver nanotube [3] showed that the CLTE of silver nanotube decreases with a temperature growth. It was caused by stresses on internal and external surfaces of nanotube. Later study of this task showed that the CLTEs of silver nanotube and silver nanofiber (structure without internal surface) are similar if the percentage of atoms on both surfaces of nanotube is equal to the percentage of atoms on the single fibers surface. Modelling of nanofibers is an easier way than modelling of nanotubes because they have no internal emptiness and they don't depend significantly on elected crystallography in contradiction to metal nanotubes [3].

This study shows how the CLTE depends on the percentage of atoms on nanofibers surface that mean the size of the nanostructure. Eight silver nanofibers with different diameters and an identical length – 10 nm were chosen for this research. These systems were modelled with periodic boundary conditions in the direction of main fiber axis and free boundary conditions in two other directions. Temperature range of study was 150 K – 450 K, temperature step was 100 K. All systems were relaxed for 0,4 ns at each temperature and the equilibrium lattice parameters were calculated. Changes of the CLTEs were calculated using changes of the equilibrium lattice parameters.

Results

The CLTE decreases with the temperature growth in the case of very small nanofibers, where 12 % of atoms or more are on the surface of the nanostructure. It may be connected with high uncompensated stresses on the nanostructures surfaces. The increasing of nanostructure size that mean the decreasing of surface atom percentage changes line slope.

Figure 1 shows how does the CLTE depend on temperature for structures with different percentages of atoms on the surface – from 0 % (periodic boundary conditions in all directions) to 63 %.

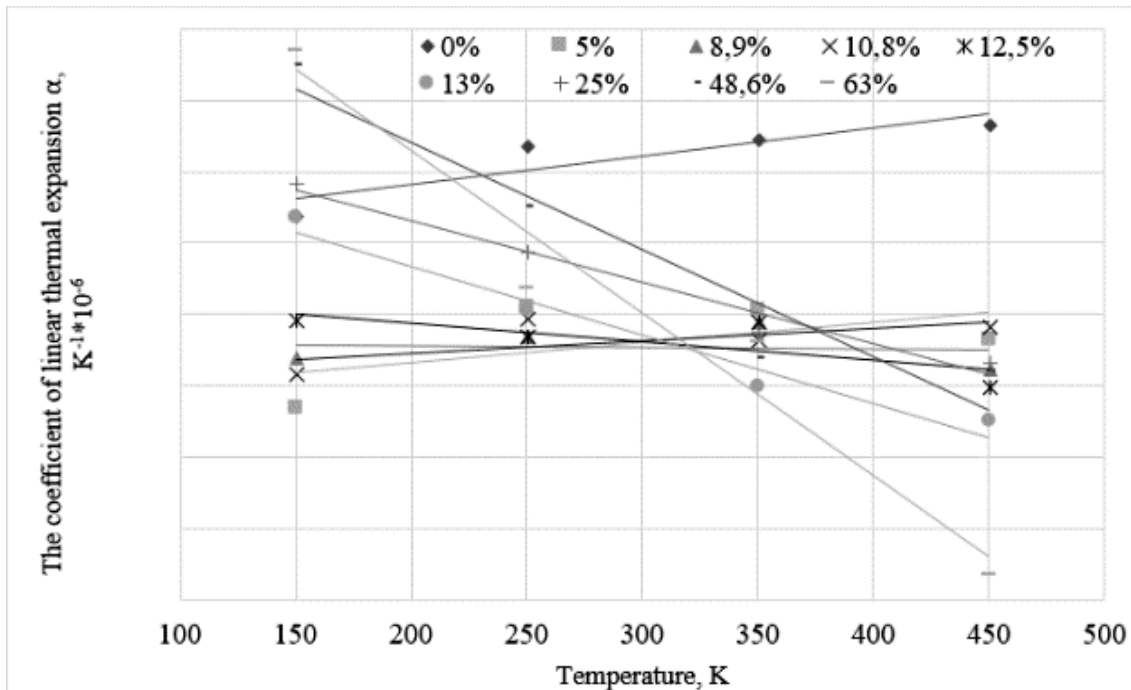


Fig. 1 – The dependence of the coefficient of linear thermal expansion on temperature for silver nanofibers with different percentages of atoms on the surface

The most stable CLTE is in case of 8,9 % of surface atoms. The dependence of surface atoms percentage on the approximate diameter of nanoparticle is given in Tab. 1.

Table 1. The conformity of percentage of surface atoms to the diameter of nanofiber

Atoms on the surface, %	Diameter of nanofiber, nm
5	30
8,9	10,8
10,8	8,8
12,5	7,6
13	7,2
25	3,6
48,6	2
63	1,2

Approximation lines ($\alpha = bT + c$, where α is the CLTE, T – temperature, b and c – coefficients of equation: $b, c = \text{const}$) for the CLTEs of each nanostructure with different percentage of atoms on the surface were built to understand what percentage of surface atoms is the most correct for creating the structure with the stable CLTE on all temperature range of potential exploitation. Coefficient b in the equation of approximation shows how rapidly the

CLTE changes with the temperature growth. Zero value of b indicates the size of nanostructure with stable CLTE (in this case $\alpha = c$). Changing of the coefficient b is shown at Fig. 2.

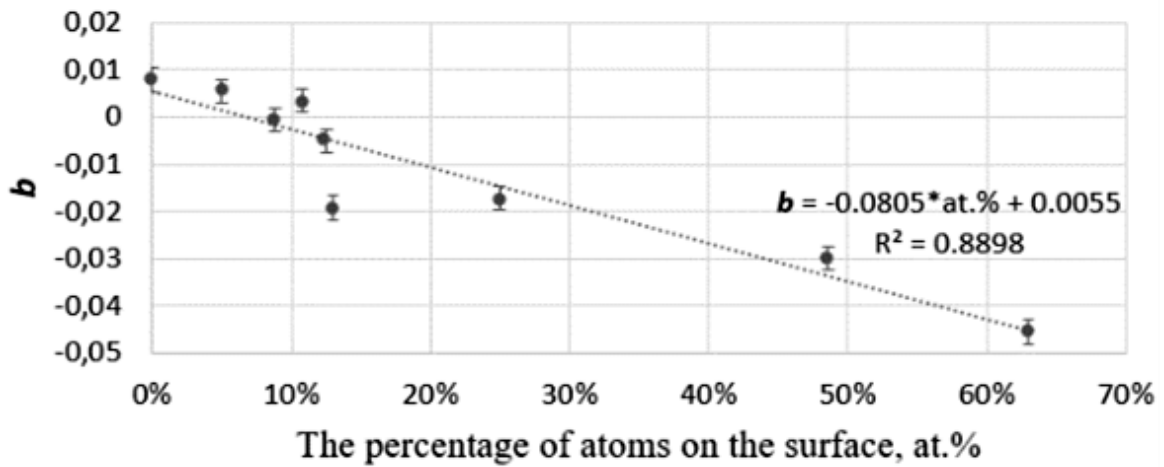


Fig. 2 – The dependence of the coefficient b on percentage of atoms on the surface

The presence of positive and negative areas of b indicates that there is a percentage of surface atoms where the CLTE is stable on whole temperature range. This study shows that minimal coefficient b is in case of 8,9 % of atoms on the fibers surface. It accords to the structure with diameter 10,8 nm.

Conclusions

The coefficients of linear thermal expansion (CLTE) of silver nanofibers and nanotubes depend on the size of nanostructure, especially on the percentage of atoms on the nanostructure surface and does not depend on kind of nanostructure.

Silver nanofiber with stable CLTE on the temperature range from 150 K to 450 K has 8,9 % of atoms on its surface and its diameter is 10,8 nm. This nanofiber or silver nanotube with the same percentage of surface atoms, may be used in MEMs/NEMs technologies as an analogues of carbon nanotubes having more perfect CLTE in compare with CLTE of carbon nanotubes.

References

1. X. Zang et al., Microelectron. Eng. (2014), <http://dx.doi.org/10.1016/j.mee.2014.10.023>
2. A. V. Dolbin et al., Fizika Nizkikh Temperatur, 2008, v. 34, No. 8, p. 860–862.
3. O. Filatov et al., Applied Nanoscience. (2018), <https://doi.org/10.1007/s13204-018-0770-4>

HOPPING CONDUCTION AND MAGNETORESISTANCE IN THE SINGLE-WALL CARBON NANOTUBES BUNDLES WITH RADIATION INDUCED DEFECTS

V. V. Vainberg, V. N. Poroshin, A.S. Pylypchuk, N.A. Tripachko, I.I. Yaskovets
Institute of Physics, Nat. Acad. Sci of Ukraine, Solid State electronics dept.
46 prospekt Nauki, Kiev 03028, Ukraine,
tel. (+38044) 525-10-80 E-mail: poroshin@iop.kiev.ua

Abstract

The electric transport properties and magnetoresistance (MR) of the metallic single-wall carbon nanotube bundles irradiated by the electron flux with the energy of ~ 1 MeV or the Co^{60} gamma quanta have been investigated in the temperature range $T=1.8 - 200$ K and in the magnetic fields up to 5 T. The power-law behavior of the conduction vs T is observed in the range of 50 through 200 K, that is characteristic for conduction of the quasi-one-dimensional systems in the model of the electron gas as the Luttinger liquid. The change of the power exponent α with the irradiation dose and its deviation as compared to α for the non-irradiated samples is connected with changing number of the conducting channels in the bundles in consequence of appearance of the radiation defects. For temperatures below 50 K the Mott three-dimensional hopping conduction is realized. Using the measured dependence of conduction on the temperature and electric field the energy density of electron states in the vicinity of the Fermi level, which participate in the charge transport, and the localization length of charge carriers in these states were determined. In the Mott-type hopping conduction region the MR was negative in the whole range of magnetic fields, while at the large fields an upturn to the positive change was observed. The mechanisms both of the negative and positive parts of MR are discussed.

1. Introduction

The structures based on the bulk of carbon nanotubes (CNT) are perspective to apply in contemporary electronics, photonics and sensors [1]. Their functional characteristics to a large extent are determined by a size, shape and mutual location of nanotubes. These factors in turn determine their morphological variety: bulks with a different extent of nanotubes orientation, bundle and network like structures, films, etc. Moreover, many properties depend on the defectiveness extent which may be changed, for example, by radiation treatment. It causes a large number of charge carriers transport mechanisms to appear in such structures: metallic conduction, hopping conduction, fluctuation tunneling, quantum corrections to conductivity under the conditions of weak localization of charge carriers etc.

The present paper is devoted to investigation of charge carriers transport under the electric and magnetic fields in the structures with CNT bundles. The structures are prepared by the uniaxial pressing of the CNT powder that results in the planar orientation of bundles in the plane perpendicular to the applied pressure direction. Formation of bundles is caused by mutual attraction of nanotubes due to the Van der Waals forces. Unlike the results of studies for such structures published earlier we have investigated the structures with radiation defects created in the course of irradiation by electron flux with the energy of ~ 1 MeV or Co^{60} gamma quanta. Mainly attention is paid to low temperatures where the conduction in consequence of random spatial location of nanotubes is caused by hops of charge carriers. The parameters characterizing the transport properties, such as the density of electronic states in the vicinity of the Fermi level g_F , participating in the charge transport, and the localization length of charge carriers in these electron states ξ , have been determined. These parameters are used to explain features of the magneto-transport in the structures under study.

2. Samples and experimental details

To fabricate structures the CNT powder produced by the Cheap Tubes Inc. Company, USA was used. It contains the 90 % of the single-wall nanotubes with the metallic conduction. The mean diameter of nanotubes is about 1.1 nm. The length is 5 through 30 μm . The powder was pressed at the room temperature, the pressure magnitude being of 1 GPa. By means of the

high resolution microscopy we found the obtained structure to be an aggregate of multi times intersecting and twisted bundles in the planes prevalingly oriented perpendicular to the applied pressure direction which provides a lot of contacts at intersection of nanotubes.

The samples to measure the dependences of the resistance on the temperature and the applied electric or magnetic field have the electric contacts fabricated by silver paste applied on the sample surface cut out of the structure. Irradiation of the samples was carried out at 300 K in the hydrogen ambient at the normal atmospheric pressure. The γ -radiation dose was up to $1.7 \cdot 10^7$ rad, the fluence magnitude of the high-energy electrons was in the range of $3 \cdot 10^{14}$ e/cm² through $6 \cdot 10^{14}$ e/cm². Measurements of the electric transport under weak electric fields were carried out in the dc regime (~ 10 μ A). In measurements at high (heating) fields the pulsed regime was used with the applied voltage pulse duration ~ 100 ns. In the magnetoresistance measurements the magnetic field strength up to 5 T was used.

3. Experimental results and discussion

The measured temperature dependences of conduction for samples with different kinds and doses of irradiation manifest similar behavior. Shown in Fig1 with both axes in the logarithmic scale are curves for the cases of irradiation by the high-energy electrons with the fluences of $3 \cdot 10^{14}$ and $6 \cdot 10^{14}$ e/cm² (samples S1 and S2, respectively) and γ -irradiation with the dose of $1.7 \cdot 10^7$ rad (sample S3).

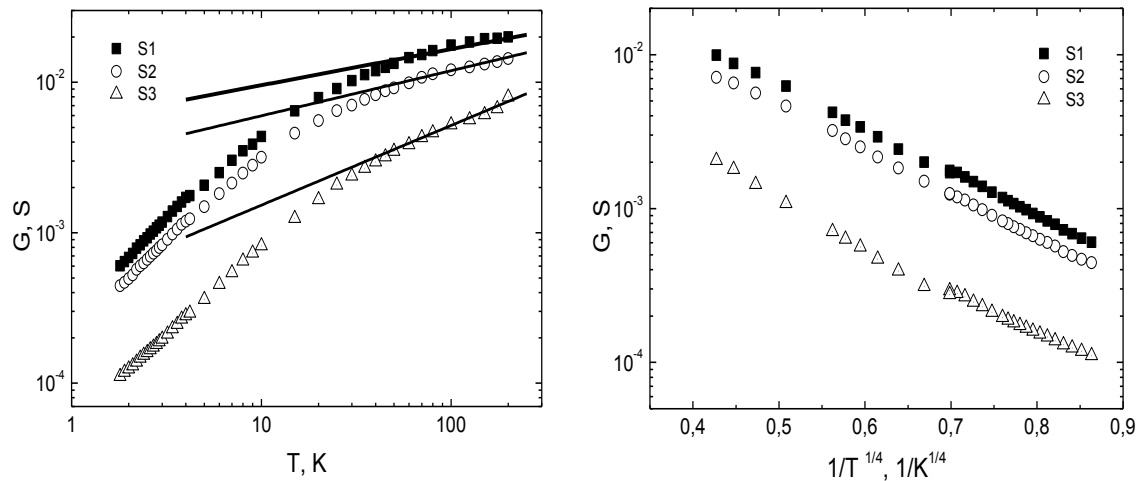


Fig. 1 – The conductance (G) vs temperature (T) dependences of the carbon nanotubes bundles in the double logarithmic co-ordinates, the solid line corresponds to the power function $G \sim T^\alpha$ (on the left), and on the function of reciprocal temperature to the $1/4$ power in the range 1.8 through 50 K (on the right)

It is seen that in the range of 50 through 200 K the results are well described by the power dependence $G \sim T^\alpha$ (the solid line in the figure), the power exponent equals to 0.24, 0.3, and 0.53, respectively. Such behavior of conduction in the weak electric field is characteristic for conduction of the quasi-one-dimensional systems in the model of the electron gas as the Luttinger liquid, which differs as compared to the Fermi model by presence of the Coulomb interaction resulting in correlated movement of charge carriers [2]. The change of the power exponent α with the irradiation dose and its deviation as compared to $\alpha \approx 0,4$ [3] for the non-irradiated samples is connected with changing number of the conducting channels in the CNT bundles in consequence of appearance of the radiation defects.

In the low temperature range from 50 down to 1.8 K the conduction quickly decreases with lowering temperature and the temperature dependence bears well expressed exponential character $G = G_0 \exp(-T/T_0)^{1/4}$. It is indicative of the variable range hopping (VRH) conduction mechanism with the variable hopping length described by the Mott law. The characteristic

temperature T_0 is determined by the independent of energy density of electron states in the vicinity of the Fermi level, which participate in the charge carriers transport, g_F , and the localization length of electrons in these states, ζ . That is $T_0 = C_T / (k_B g_F \zeta^3)$, where C_T is a constant. Note, the localization length in CNT is frequently considered as anisotropic. Then the localization length is geometrically averaged over directions along and transverse to the nanotube axis.

The data shown in Fig.1 enable to estimate the values of T_0 : 1874 K, 1677 K, 2346 K for the samples S1, S2 and S3, respectively. In order to determine the localization length one needs to know the density of states g_F , which, as it is known, depends on the structure morphology and must be determined for each sample. For this purpose we carried out measurements of the hopping conduction under the conditions of heating charge carriers by the applied electric field. The obtained dependences of the current in the sample on the electric field strength are depicted in Fig. 2.

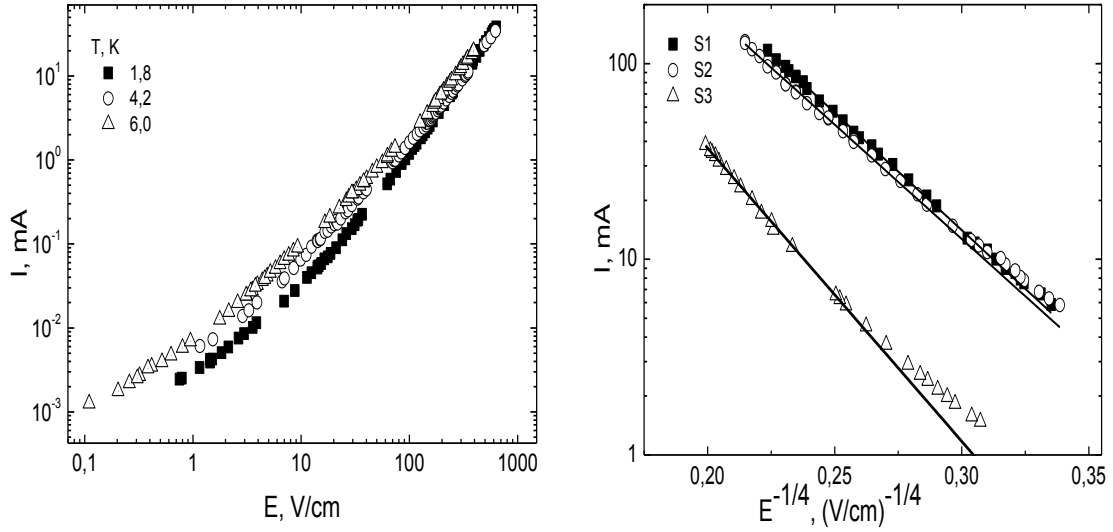


Fig. 2 – Current vs electric field strength dependences for the sample #S1 at different temperatures (on the left) and the current vs reciprocal value of the electric field to the $1/4$ extent for different samples in the electric field range corresponding to charge carriers heating up (on the right)

It is seen that at the electric field strength more than ~ 100 V/cm the dependences measured at different temperatures practically coincide. This indicates the fact that at such field strengths the hopping conduction is defined only by heating charge carriers due to the electric field. The current J vs electric field strength E dependence in this case is as follows

$$J \sim \exp \left[- \left(\frac{E_0}{E} \right)^{0.25} \right]; \text{ where } E_0 = \frac{C_E}{e g_F \zeta^4}$$

Here e is the electron charge, C_E is the constant ~ 1

As one can see in Fig.2, this dependence describes well the experimental results with the characteristic field E_0 values equal to $5.8 \cdot 10^5$, $5.2 \cdot 10^5$, $1.4 \cdot 10^6$ V/cm for the samples S1, S2 and S3, respectively. Using the obtained values of E_0 and T_0 one can determine (to the accuracy of the ratio of the constants C_E/C_T) the localization length of charge carriers:

$$\zeta = \frac{a k_B T_0}{e E_0}; \text{ where } a = \frac{C_E}{C_T}$$

The published papers give different values for the constant of a . We determined the values of the localization length and density of the electron states for the samples S1, S2 and S3 using the value $a=1$. They are listed in the table:

Sample	T_0 (K)	E_0 (V/cm)	ζ (cm)	g_F ($eV^{-1}cm^{-3}$)	b	n	c	m
S1	1874	$5.8 \cdot 10^5$	$9.31 \cdot 10^{-7}$	$5.9 \cdot 10^{19}$	0.018	1.48	0.0066	2.01
S2	1677	$5.2 \cdot 10^5$	$1.08 \cdot 10^{-6}$	$4.2 \cdot 10^{19}$	0.010	1.34	0.0065	1.91
S3	2346	$1.4 \cdot 10^6$	$8.2 \cdot 10^{-7}$	$6.9 \cdot 10^{19}$	0.015	1.31	0.0045	1.96

Note, the obtained values of the localization length in the range 8 through 10 nm are characteristic for the strong localization of charge carriers.

Now we consider the transverse magnetoresistance we observed under the conditions of the hopping conduction. Fig.3 illustrates the dependence of the relative magnetoresistance of the samples $(R(B) - R(0))/R(0)$ on the magnetic field B measured at 4.2 K

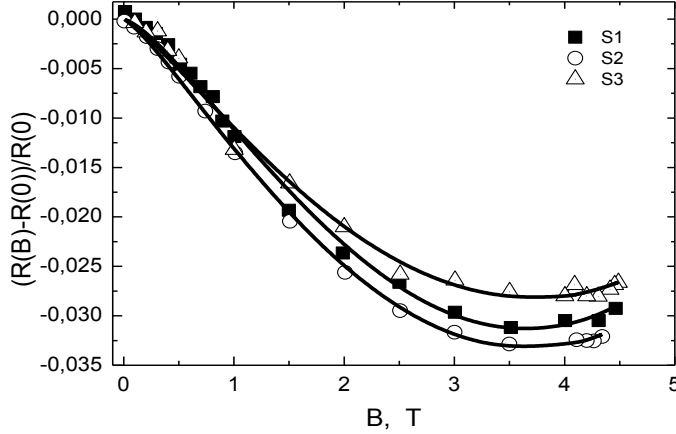


Fig. 3 – Dependence of the relative magnetoresistance on the magnetic field at 4.2.K. Solid lines – fitting by the formula (1)

In analysis of data on the Mott kind hopping conduction in the magnetic field we assumed the magnetoresistance changes to be caused by two contributions describing different mechanisms of the magnetic field influence on the wave function of charge carriers [4]:

$$\frac{R(B)-R(0)}{R(0)} = -bB^n + cB^m \quad (1)$$

This expression well describes the experimental data with parameters n, m, b and c listed in the table. The positive component with the exponent $m=2$ is usually connected with shrinkage of the envelop wave function at the localized electron state in the magnetic field. A small deviation of the obtained values of m from 2 may be caused by contribution of the spin-polarization mechanism which is explained by accounting for the Zeeman splitting of the energy band in the Fermi level vicinity where the hopping conduction arises. It accounts for double filled localized states and dependence of the hopping probability on the polarization extent of the spin part of the wave function in the magnetic field.

As for the negative contribution into the magnetoresistance, we note that with the exponent $n=1$ its nature is usually explained by the interference effects. However, our values of n considerably differ from 1 ($n=1.38 \div 1.41$). It cannot be explained by now within the frames of known theories.

4. References

1. Marcus Freitag, Carbon nanotube electronics and devices in “Carbon Nanotubes Properties and Applications”, Ed. Michael J. O’Connell, 2006 by Taylor & Francis Group, LLC.
2. B. A. Danilchenko, L. I. Shpinar, N. A. Tripachko, E. A. Voitsihovska, S. E. Zelensky, and B. Sundqvist, Applied physics letters **97**, (2010) 072106.
3. B A Danilchenko, N A Tripachko, E A Voitsihovska, I I Yaskovets, I Y Uvarova and B Sundqvist, J. Phys.: Condens. Matter **25** (2013) 475302
4. S. V. Demishev, A. D. Bozhko, V. V. Glushkov, E. A. Kataeva, A. G. Lyapin, E. D. Obratsova, T. V. Ishchenko, N. A. Samarin Physics of the Solid State, 50 (2008) 1386.

FORMATION FEATURES OF SILICON NANOCRYSTALS IN TIN-DOPED AMORPHOUS SILICON FILMS

Kolosiuk A.G., Rudenko R.M., Voitsikhovska O.O., Voitovych V.V., Krasko M.M., Povarchuk V.Yu.

Institute of Physics of the NAS of Ukraine
Ukraine, 03028, Kyiv, avenu Nauki 46,
tel. 044 5253973
E-mail: anjeyk@gmail.com

The process of the silicon crystalline phase formation in amorphous silicon films doped with tin is investigated. It is shown that metallic tin inclusions play a key role in the crystallization process of the studied samples a-SiSn (Sn ~1–10 at.%) at temperatures of 300–500 °C. The process of crystallization can be divided into two stages. In the first stage, tin metal inclusions are formed in the film volume due to the diffusion of tin atoms in the amorphous silicon matrix. In the second stage, the formation of the nanocrystalline silicon phase occurs due to the movement of silicon atoms from the amorphous to the crystalline phase due to the formed metal inclusions of tin. The presence of metallic tin inclusions provides the formation of silicon crystals at a much lower temperature than the temperature of solid phase recrystallization (~750 °C). The possibility of the relationship between the sizes of the formed nanocrystalline silicon and the sizes of metallic tin inclusions forming it is analyzed in the paper.

Trends in the development of modern electronics require the use of functional elements with dimensions of the order of several nanometers. Therefore, technologies for the formation of semiconductor nanostructures and their physical properties are being actively developed. Since silicon is the most widely used semiconductor material, considerable attention is paid to the study of nanocrystalline silicon (nc-Si), in particular in thin silicon films and silicon suboxide. The physical properties of thin films depends to a significant extent on the ratio of amorphous and nanocrystalline phases, the size and concentration of silicon nanocrystals [1-3]. Therefore, it is important to understand the mechanism of formation of nanocrystalline silicon.

The formation of nanocrystalline silicon with sizes up to 10 nm due to metal-induced crystallization has not been sufficiently studied. Usually, only the fact of the presence of silicon crystals with dimensions of several tens of nanometers is noted, however, the analysis of the preconditions for their formation is absent.

This work aimed to investigate the features of formation of nanocrystalline silicon in amorphous films obtained by simultaneous deposition of silicon and tin.

Materials and methods. Samples of tin-doped amorphous silicon a-SiSn were obtained by the method of thermal evaporation in vacuum of tin powders (PO-1 grade, 99.1% purity) and silicon (KEF-4.5 silicon). The tin content in the investigated samples was 0, 1, 4 and 10 at.%. The films were grown on silicon and quartz substrates at the temperature 300°C. The films were deposited on silicon and quartz substrates at a temperature of 300 °C. The film thickness was ~0.5–1 μm. The impurity content of the investigated films was monitored by the Auger-electron spectroscopy (JAMP-9500F Field Emission Auger Microprobe). To change the phase composition of the deposited films were subjected to isochronous annealing for 20 min in an argon environment in the temperature range from 300 to 1100 °C with an increment of 50 °C. Information on the phase composition of studied films was obtained by analyzing the Raman scattering spectra, which were registered at room temperature. Raman spectra were recorded at room temperature on a Jobin Yvon T-64000 spectrometer using excitation laser beam Ar⁺ with a wavelength of 488 nm. The average silicon crystallite sizes and the crystalline phase fraction were estimated according to the decomposition of the Raman spectra into components corresponding to the amorphous and crystalline phases within the phonon confinement model.

Detailed information on the method of obtaining films, their impurity composition, structural and optical characteristics is given in [2,3].

Results and discussion. We have previously established [2,3] that crystallization of the amorphous silicon phase occurs after annealing at 500 °C in samples containing 1 at.% tin, and in samples containing 4 and 10 at.% of tin crystalline phase is present immediately after deposition at 300 °C, and the size of the silicon crystallites is less than 10 nm. In both cases, these temperatures are lower than the crystallization temperature of the undoped amorphous silicon (750 °C).

The content of tin in the samples is higher than the solubility limit, so metal clusters will form in the volume of the films, which play a key role in reducing the crystallization temperature of the a-Si matrix. Since the film deposition temperature and the heat treatment temperature are higher than the tin melting temperature (231.9 °C), the cluster of tin probably be in a liquid state. The interaction of silicon with metal at relatively low temperatures (close to the eutectic temperature) without weakening the silicon bonds is unlikely because the Si-Si covalent bond is strong enough. One possible explanation for the weakening of silicon bonds in the presence of metal is the "screening model" proposed by S. Hiraki [4].

When metal tin is contacted with amorphous silicon, the process where silicon atoms penetrate the metal is the most energy-efficient. As a result, the Si-Sn alloy will be formed in the volume of the investigated films due to the tin clusters will dissolve the surrounding amorphous silicon matrix.

In general, the driving force behind the ordering of the structure of amorphous silicon is the difference in the chemical potentials of silicon atoms in the amorphous state and in the crystalline state. The solubility of silicon from the disordered phase is higher than the solubility of the ordered phase. The presence of this difference solubility causes the transport of silicon atoms from amorphous to crystalline phase through metallic tin.

Let us try to understand which factors are crucial for the formation of silicon crystallites with size of a few nanometers. Suppose that there is a relationship between the size of the crystallites of silicon being formed and the size of the tin clusters in which the amorphous phase dissolves. Also, consider that in the volume of the investigated samples, tin metal clusters are formed the same size. Each cluster is able of dissolving from an amorphous matrix an amount of Si atoms sufficient to form nanocrystalline silicon whose dimensions are experimentally obtained.

There is no crystalline phase after deposition in films with a tin content of ~ 1 at.%. It is observed only after annealing at 500 °C. Our mathematical calculations have shown that in these samples, tin clusters with a maximum size of about 10–15 nm can form over time $t \sim 1000$ s (the duration of deposition of the film on the substrate at 300 °C and its gradual cooling to a temperature of 200-250 °C). Tin clusters of this size can dissolve about 150 atoms of Si, which corresponds to the diameter of the spherical silicon nanocrystals size ~ 1.5-2 nm. From our estimates, crystallites of this size are an unstable formation at 300 °C, which will again pass into the amorphous phase. This explains the absence, after deposition, of the maximum Raman spectra corresponding to the crystalline phase of silicon for samples with a tin concentration of ~ 1 at.%. The calculations showed that the size of the tin clusters at a heat treatment of 500 °C should increase from 10-15 to 35 nm to allow the formation of nanocrystalline silicon with sizes exceeding critical. Thus, metal clusters of tin in the amorphous silicon matrix are quite mobile.

The formed clusters of tin will dissolve amorphous silicon, and then the silicon will be removed from the solution in the form of crystallites. That is, the process of crystallization can be considered as the movement of silicon atoms through the tin clusters from the amorphous to the crystalline phase. After mathematical calculations, we obtain that in the investigated a-SiSn films, the velocity of Si atoms in tin clusters must be $v \sim 10^{-2}$ cm/s. The obtained value is much greater than the rate of growth of the crystalline phase during thermal crystallization of amorphous silicon, but it is comparable to the speed of movement of the crystallization front. Such a rate of crystallization front will allow the samples to be crystallized in the order of tens

of seconds or less. This time is much shorter than the time of formation of tin clusters ($t \sim 1000$ s). Thus, the time required for the crystallization process of a-SiSn samples is mainly determined by the time of formation of metal tin clusters.

Therefore, the process of crystallization of the studied films can be divided into two stages. The first step is the formation of tin clusters in the process of cooling the film after deposition, or in the process of subsequent heat treatments. The second step is the dissolution of the silicon atoms from the amorphous matrix in tin clusters and their subsequent removal from the alloy outside in the form of a crystalline phase. The duration of the first stage is much longer than the second. It is determined by the diffusion of tin atoms in amorphous silicon, and its time can be about 1000–1500 seconds at temperatures of 300–500 °C. The duration of the second phase probably not exceed a few tens of seconds, as it is defined by relatively high speed of crystallization front, which is caused by the diffusion of silicon atoms through a drop of molten tin.

Conclusions

The results allow the following conclusions:

1. Tin metal clusters play a major role in the processes of nanocrystalline silicon formation in the investigated a-SiSn samples (Sn \sim 1–10 at.%) at temperatures of 300–500 °C.
2. The process of forming nanocrystalline silicon can be divided into two stages. The first stage is the formation of tin metal clusters in the deposition process and in subsequent heat treatments. This stage is lengthy (\sim 1000–1500 s) and is determined by the diffusion of tin atoms in amorphous silicon. The second stage is the dissolution of the surrounding amorphous matrix in the metal clusters of tin and output outside of the nanocrystalline silicon. This stage is short-term (<20 s) and is determined by the diffusion of silicon atoms from the amorphous to the crystalline silicon matrix through metallic tin clusters.
3. The analysis of the experimental results indicates that there is a relationship between the sizes of the crystallite silicon crystals that are formed and the size of the metallic tin inclusions that form them. The proportionality of the size of the formed nc-Si to the size of the metal inclusions may be of great practical importance, because it indicates a possible way of forming nanocrystalline silicon with predetermined sizes.

References

1. V.V. Voitovych, R.M. Rudenko, A.G. Kolosiuk, M.M. Krasko, V.O. Juhimchuk, M.V. Voitovych, S.S. Ponomarov, A.M. Kraitchinskii, V.Yu. Povarchuk, V.A. Makara, Effect of tin on the processes of silicon-nanocrystal formation in amorphous SiO_x thin-film matrices, *Semiconductors* **48**, N1, 73 (2014).
2. V.V. Voitovych, V.B. Neimash, N.N. Krasko, A.G. Kolosiuk, V.Yu. Povarchuk, R.M. Rudenko, V.A. Makara, R.V. Petrunya, V.O. Juhimchuk, V.V. Strelchuk, The effect of Sn impurity on the optical and structural properties of thin silicon films, *Semiconductors* **45**, N10, 1281 (2010).
3. R.M. Rudenko, V.V. Voitovych, M.M. Kras'ko, A.G. Kolosyuk, A.M. Kraichynskyi, V.O. Yukhymchuk, V.A. Makara, Influence of high temperature annealing on the structure and the intrinsic absorption edge of thin-film silicon doped with tin, *Ukr. J. Phys.* **58**, N8, 769 (2013).
4. A. Hiraki, Low temperature reactions at Si/ metal interfaces; What is going on at the interfaces? *Surface Science Reports* **3**, 357 (1984).

ON THE QUANTUM ELECTRODYNAMICS OF NANOSYSTEMS

Gritsunov A. V., Bondarenko I. N., Galat A. B., Glukhov O. V., Pashchenko A. G.
Kharkiv National University of Radio Electronics
61166, Kharkiv, Nauky ave., 14, dep. Microelectronics, electronic devices and appliances
Tel. +380 57 7021362
E-mail: gritsunov@gmail.com

Problems of quantum dynamics of nanoobjects essential for development of new nanoelectronic systems are discussed. According to the theory of natural oscillatory systems (NOSs), “interaction” between the objects is interpreted as a quantum-dynamic phenomenon meaning a stable trend arising from the quantum chaos. As an opposite, “interchange” is denominated as the permanent stochastic exchange with action quanta between different NOSs in 4D spacetime, being the physical base of the quantum chaos. The Tetrode-Wheeler-Feynman’s concept of “direct interparticle action” is reconciled with both the quantum radiation-absorption and the Coulomb interaction. A conservation law for the action is supposed as a necessary condition for the momentum-energy conservation. The “classic” conservation law for the momentum-energy is considered as derivative, being valid for the momentum as well as some physical value that is an integral over 3D space from a linear combination of stress-energy tensor principal diagonal terms. Such redefinition enables the unconditional quantization of the energy unlike “orthodox” quantum theory.

Introduction

The contemporary advance of electronic and robotic technologies to the nanoworld reanimates old fundamental problems of the quantum mechanics (QM) and the quantum electrodynamics (QED). Despite striking achievements in the engineering applications of these disciplines, there is no clear theoretical understanding the quantum world behavior yet. Such opinion is confirmed, e.g., by the recent discovery of abnormally high radiation-absorption factor for nanoscale emitting systems as well as other surprising quantum effects [1, 2]. It is obviously that new, more consistent, theory of QED phenomena is wanted.

Concepts of natural electromagnetic (EM) and electron-positron (EP) distributed oscillatory systems (NEMOS, NEPOS respectively), as real physical bases for the de Broglie matter waves and as alternatives to the “physical vacuum” of QED, were proposed by one of us [3]. A discipline named as “Theory of natural oscillatory systems” (TNOS) is developing in ResearchGate project of the same name [4]. Some fundamental problems of QED, in their specific interpretation, are considered in this paper.

Preliminary Physical Issues

The 4D pseudo Euclidean formalism with imaginary time (“1, 1, 1, i ”) is assumed. The Cartesian coordinate system is used; x , y , and z are the real spatial coordinates; t is a temporal coordinate with dimension of imaginary length. Four-vectors in the Minkowski spacetime are mixed-valued with real spatial components and imaginary temporal one.

Instead of the EM potential four-vector and de Broglie EP wavefunction, complex-valued four-vector aleph-functions $\vec{\aleph}^\gamma(x, y, z, t)$ and $\vec{\aleph}^e(x, y, z, t)$ respectively, each having real spatial components and imaginary temporal, are introduced for natural oscillatory systems (NOSs). EM aleph-function $\vec{\aleph}^\gamma$ is restricted with the Lorenz gauge $\vec{\nabla} \cdot \vec{\aleph}^\gamma \equiv 0$. EP aleph-function $\vec{\aleph}^e$ is restricted with both the Lorenz gauge $\vec{\nabla} \cdot \vec{\aleph}^e \equiv 0$ and a spatial flat rotation (“media 2D twisting”) condition, namely, $\aleph_\xi^e \equiv 0$ in some “privileged” rest frame system, where ξ is only

one of the spatial coordinates (arbitrary). In contrast to $\vec{\mathfrak{S}}^\gamma$, $\vec{\mathfrak{S}}^e$ has no “potential” eigenfunctions (with spin of zero) in one’s Fourier expansion, therefore, according to the angular momentum quantization rules, spins of NEPOS eigenmodes are of $\pm 1/2$, not of $-1, 0, +1$, as for NEMOS.

The physical senses of $\vec{\mathfrak{S}}^\gamma$ and $\vec{\mathfrak{S}}^e$ are local deviations of NEMOS and NEPOS respectively from their “undisturbed” states along the respective axes. According to such interpretation, both $\vec{\mathfrak{S}}^\gamma$ and $\vec{\mathfrak{S}}^e$ must be gauge-dependent (i.e., to tend to zero far off from a matter), but this is insignificantly in the quantum theory, because any invariable in the spacetime addition to $\vec{\mathfrak{S}}^\gamma$ or $\vec{\mathfrak{S}}^e$ has no action quantum, so, cannot be involved in the interaction.

So-called four-number $\vec{m} = \{m_x, m_y, m_z, im_t\}$, where $m_\tau = 0, \pm 1, \pm 2, \dots$; τ means one of spatio-temporal coordinates, is introduced to “elegant” enumeration of NEMOS and NEPOS eigenfunctions.

The Coulomb Interaction

The longstanding Wheeler-Feynman’s (and, earlier, Hugo Tetrode’s) idea of “advanced” EM interactions along with “retarded” ones [5] was recently reanimated by Y. Aharonov, “patriarch” of contemporary quantum theory. Such notion completely adjusts with the basic concepts of TNOS: “almost free” (i.e., “non-virtual”) photons contain too small action to store, e.g., total action of annihilating EP pair. Only “direct” collective transfer with multiple harmonic components of a NEMOS wave packet is possible.

The Coulomb interaction between fermions is a specific case of the radiation-absorption when photons are essentially “forced,” i.e., having relatively large actions. The “interaction” is interpreted as a stable trend in variation of the momenta or the momenta-energies of NEPOS wave packets arising from the quantum chaos. The latter is a result of random mutual conversion with action quanta (“interchange”) between NEPOS and NEMOS in 4D spacetime. If two or more immovable “electrons” are placed in their “common” EM potential, NEMOS performs a stochastic mutual exchange with momentum between ones (i.e., the Coulomb repulsion) in addition to the “localizing” effect for each wave packet taken separately [3]. For moving “electrons,” this exchange includes also energy.

The magnetic moment of “electron” is a result of the “uncertainty” in its own angular momentum. Stochastic changes of direction of an “electron rotation axis” are compensated by “mirror” variations in angular momentum of NEMOS, so, total angular momentum of the insulated system “electron in its own EM potential” remains objectively unchanged.

The Radiation-Absorption

The similar interaction process between atoms in the time domain transfers both momentum and energy and is known as “radiation-absorption.” Mechanism of the quantum EM interaction is supposed to be the same for both time-dependent (e.g., radiating-absorbing atoms) and static (e.g., mutually repulsive “electrons”) systems. We must put into our hypothesis the Tetrode-Wheeler-Feynman’s concept of “advanced” EM interactions along with “retarded” ones [5] to explain the temporal localization of EM wave packets, which transfer the energy.

E.g., if an excited atom #1 has transferred a quantum of its extra momentum-energy (and, respectively, negative and positive quanta of the action) to an atom #2 via a “photon,” this act may be still “rolled back” by an “antiphoton” (“the Schrödinger’s cat can be revived”). Only

if atom #2 has retransmitted the obtained quantum to an atom #3, this quantum no longer can be returned to atom #1 (“a measurement has been made, the cat is dead, sorry...”).

Why atom #3 cannot return the obtained quantum to atom #2, so, one will return it to atom #1 (remember, these processes cannot be described as “flowing in time,” so, “will” term is not quite suitable here)? Such situation is theoretically possible; however, the probability of the “rolling back” all chain of the events decreases dramatically as the number of possible variants of the events enlarges. Atom #3 can transfer the obtained quantum to an atom #4, or atom #5, *etc.*, not necessarily return it to the atom #2. Figuratively, the unhappy cat is a victim of the second law of thermodynamics.

Quantum oscillating systems having two and more stable or quasi-stable states (e.g., atoms) are, formally, the same “observers” as people with their “classic” apparatus. Just they seal the fate of the Schrödinger’s cat long before the box is opened. A “macroscopic observer” can be sure what has happened in the quantum system only when the above process has gone enough far to make a “rollback” practically impossible. Until then, the observer’s knowledge can be only probabilistic.

If a single excited atom is placed in the Universe, it would never radiate, because “almost free” photon cannot accumulate by oneself the difference between the actions of excited and unexcited atoms (neither positive nor negative parts of their total actions). Further, if only two atoms existed in the world, some is excited while other is unexcited at some instant, they would “beat” like two weakly coupled harmonic oscillators. The mutual coupling factor is defined by the fine-structure constant α as well as spatial characteristics of the atoms. Three and more mixed excited and unexcited atoms in the Universe, evidently, must oscillate like a network of harmonic oscillators weakly coupled each with another.

The Momentum-Energy Relations

According to TNOS [3, 4], the momentum-energy is a dynamic value arising from the “movement” of 3D world over 4D spacetime in the temporal direction. Excited NOS eigenmodes “vibrate” like animated cartoon from the point of view of a 3D observer. The frequency of this vibration describes the eigenmode’s energy, while the quickness and the direction of spatial displacement of the oscillation’s phase define its momentum. In other words, momentum-energy is defined as flow of the action through 3D world.

It is easy to see that the “orthodoxal” formula of QED for quantization of the total momentum-energy four-vector of a NOS \bar{m} -th eigenmode $\vec{W}_{\bar{m}} = \eta K_{\bar{m}} \vec{k}_{\bar{m}}$, where η is the Planck constant; $\vec{k}_{\bar{m}}$ is the wave four-vector of \bar{m} -th eigenmode; $K_{\bar{m}}$ is the mode occupation factor [4], is not so universal. First, this is valid only for “free” or matter-like eigenmodes, i.e., having $k_{\bar{m}^2} \leq 0$. Second, this not considers the existence of both positive and negative action quanta as well as the same sign of energy for “particles” (with $k_{\bar{m}t} > 0$) and “antiparticles” (with $k_{\bar{m}t} < 0$). Real 3D observer cannot determine actual sign of $k_{\bar{m}t}$ component in direct way. Only hypothetical “4D observer” can distinguish “positive” and “negative” directions of the wave vector for fermions. E.g., energies of “particle” and “antiparticle” have the same sign. The sign of \bar{m} -th eigenmode momentum depends on the relative orientation of $k_{\bar{m}\xi}$ and $k_{\bar{m}t}$ components.

Therefore, it would be reasonably to evaluate the total momentum-energy of individual eigenmodes and of a while NOS by means of integrating the respective components of the four-tensor of stress-energy density over all 3D volume of Universe. There are two form of this

tensor: “classic” $[w](x, y, z, t)$ and “quantum” $[p](x, y, z, t)$ ones. They differ only in the expressions for the principal diagonal terms.

The “classic” form is evaluated from the hypothesis of spacetime uniformity according to the Noether’s theorem. This results in conservative but not always quantized energy definition

$$w_{\tau\tau'} = \sum_{\tau'} \frac{\partial \mathfrak{N}_{\tau'}^*}{\partial \tau} \left[\frac{\partial h}{\partial (\partial \mathfrak{N}_{\tau'}^* / \partial \tau')} \right] - I_{\tau\tau'} h, \quad (1)$$

where $h(x, y, z, t)$ is the action four-density [1] for non-interacting NOS:

$$h = \frac{i}{2} \left[(\vec{\nabla} \mathfrak{N}_x)^2 + (\vec{\nabla} \mathfrak{N}_y)^2 + (\vec{\nabla} \mathfrak{N}_z)^2 + (\vec{\nabla} \mathfrak{N}_t)^2 + k_*^2 (\vec{\mathfrak{N}})^2 \right]; \quad (2)$$

k_* is a NEPOS cutoff wavenumber (a TNOS equivalent for “particle rest mass” m_*); $[I]$ is the unit four-tensor.

Substituting (2) to (1), one can see that the components of tensor $[w]$ are written as

$$w_{\tau\tau'} = 2i \frac{\partial \vec{\mathfrak{N}}}{\partial \tau} \cdot \frac{\partial \vec{\mathfrak{N}}}{\partial \tau'} - I_{\tau\tau'} h. \quad (3)$$

Evidently, “classically” defined stress-energy density (3) always ensures the total momentum-energy conservation in 3D Universe. Unfortunately, it can hardly be said that this agrees with the quantization basic principles. If energy is correlated with the temporal variation of a certain wave process, some forms of “classic” energy embodiment cannot be quantized (e.g., “energy” of EM potential of “rest electron”). The violation of the quantization rules at least for one of kinds of energy existence breaks down fundamentals of the quantum theory, because mutual transformation of “quantized” and “non-quantized” forms of energy cannot occur by discrete portions.

Unlike the classic EM theory, all components of the four-tensor of “quantum” stress-energy density $[p]$ of a NOS (including diagonal ones) are not based on the spacetime uniformity hypothesis and are defined in TNOS in simple and uniform manner

$$p_{\tau\tau'} = 2i \frac{\partial \vec{\mathfrak{N}}}{\partial \tau} \cdot \frac{\partial \vec{\mathfrak{N}}}{\partial \tau'} \quad (4)$$

differing from (3) in the principal diagonal terms. “Quantum” stress-energy density (4) is always quantized. E.g., a “quantum” energy always assumes some non-stationary (time-dependent) process existence, so, EM potential of the “rest electron” cannot possess any energy. However, the “quantum” energy, as a dynamic entity, is, generally, non-conservative value for 3D Universe (the momentum is conservative as usual). Conservation rules, following from the Noether’s theorem applied to the spatio-temporal coordinates, are fit now to other values, namely, linear combinations of the principal diagonal terms. E.g., for a hypersurface of $t = \text{const}$ (our 3D world), the value keeps:

$$w_{tt} = p_{tt} - \hbar = -p_{xx} - p_{yy} - p_{zz} + p_{tt} - k_*^2 (\vec{\mathfrak{S}})^2 \quad (5)$$

(actually, this is arithmetical sum of all components; the differing sign for p_{tt} is compensated by imaginary value of t). During an interaction between two and more “particles,” the “quantum” energy p_{tt} transfers to the “quantum” stress $p_{xx} + p_{yy} + p_{zz}$ and vice versa. This is an equivalent of mutual conversation of “kinetic” and “potential” classic energies.

Conclusion

Despite striking achievements in the engineering applications of QM and QED, there is no consensus in understanding the theoretical bases of quantum world behavior yet. Because characteristic sizes of nanorobot components are almost of the same order as typical de Broglie wavelengths for their parts, the design of those must be certainly performed according to the quantum laws, not classical. However, some fundamental bugs of “Copenhagen interpretation” make the outlook of further progress not quite definite.

TNOS considers spatially or spatio-temporally localized wave packets of NOSs as full-value equivalents of “elementary particles.” The proposed concept consistently describes behavior of de Broglie waves in conductors, semiconductors, and superconductors. The described results may be useful for the development of new nanoelectronic components and quantum computers.

References

- Wuttke, C. and A. Rauschenbeutel, “Thermalization via Heat Radiation of an Individual Object Thinner than the Thermal Wavelength,” arXiv: 1209.0536v3 [quant-ph] 18 Jul 2013.
- Slepyan, G., A. Boag, V. Mordachev *et al.*, “Anomalous Electromagnetic Coupling via Entanglement at the Nanoscale,” *New J. Phys.*, vol. 19, 023014, 2017.
- Gritsunov, A., I. Bondarenko, A. Pashchenko, and O. Babychenko, “Theory of Natural Oscillatory Systems and Advance in Nanoelectronics,” 14th Int. Conf. on Advanced Trends in Radioelectronics, Telecomm. and Computer Eng. (TCSET), Lviv-Slavske, Ukraine, p.p. 92-97, 2018.
- Gritsunov, A. V., “Theory of natural oscillatory systems,” ResearchGate project [Online]. Available: <https://researchgate.net/project/Theory-of-Natural-Oscillatory-Systems>
- Wheeler, J. A. and R. P. Feynman, “Classical Electrodynamics in Terms of Direct Interparticle Action,” *Rev. Modern Phys.*, vol. 21, no. 3, 1949.

THE VAN DER WAALS INTERACTION BETWEEN THE METALLIC NANOTUBES

N.I. Pavlishche, A.V. Korotun
 National University "Zaporizhzhia Politechnic"
 69063, Zaporizhzhya, Zhukovsky Str. 64, dep. Radioelectronics and telecommunication
 tel. (061) 764-67-33
 E-mail: andko@zntu.edu.ua

The Van der Waals interaction between two cylinder metallic nanoshell, the axes of which are parallel, has been studied. The expression for the free energy of the interaction per unit length has been obtained. The implementable case when the sizes of the shells are much less than the wavelength, the shells are made from the same material, they have the same geometrical dimensions, and the case of the dielectrically isotropic materials of the shells have been considered.

Introduction. The Van der Waals interaction, which is the consequence of the fluctuation effect of the electromagnetic forces, is under the investigation over many years [1]. However, these problems are of great current interest in the context of the development of the nanotechnologies. For example, in [2] one develops the approaches for the calculation of the Van der Waals forces between the nanostructures, right up to the close contact and linking, and also indicates the link between the microscopic theory and Lifshitz macroscopic theory; in [3] the Van der Waals interaction between the metallic nanowire and the surface on the “intermediate” distances has been considered, basing on Luttinger liquid approach; in [4] one studies the phononic heat-transfer mechanism, defined by the Van der Waals interaction, on the subnanometer distances between the metallic objects under the small potential differences.

However, the problem, connected with the Van der Waals interaction between 1D-structures, in particular, between the cylinder nanoshells, is still open, so this problem is important.

The body of the text. Let us consider the problem, connected with the finding of the free energy of the Van der Waals interaction per unit length for two long cylinder nanoshells with the thickness $t_i = b_i - a_i$ (a_i, b_i – the inner radius and the outer radius; $i = 1, 2$ – the number of the shell), which are situated on the big distance from each other ($R \gg a_i, b_i$). We assume (fig 1), that the shells are situated in the medium with the dielectric capacity τ_m , the materials of the core have the dielectric capacities τ_{1c} and τ_{2c} , the metal of the shells is anisotropic and its dielectric function forms the tensor

$$\tau_i = \begin{pmatrix} \tau_i^\perp & 0 & 0 \\ 0 & \tau_i^\perp & 0 \\ 0 & 0 & \tau_i^\parallel \end{pmatrix}. \quad (1)$$

The potentials in the domains I, II and III can be found as the solution of Helmholtz equation

$$\Delta_i \Phi_i^j = \frac{\tau_i^\parallel(\omega)}{\tau_i^\perp(\omega)} k^2 \Phi_i^j, \quad (2)$$

where $j = I, II, III$.

The solutions of the equation (2) can be expressed in terms of the modified cylinder functions

$$\begin{aligned}\Phi_1^I &= \sum_{m=-\infty}^{+\infty} A_{1m} I_m(kr_1) e^{im\varphi_1}; & \Phi_1^{II} &= \sum_{m=-\infty}^{+\infty} (B_{1m} I_m(i_1 r_1) e^{im\varphi_1} + C_{1m} K_m(i_1 r_1) e^{im\varphi_1}); \\ \Phi_2^I &= \sum_{m=-\infty}^{+\infty} A_{2m} I_m(kr_2) e^{im\varphi_2}; & \Phi_2^{II} &= \sum_{m=-\infty}^{+\infty} (B_{2m} I_m(i_2 r_2) e^{im\varphi_2} + C_{2m} K_m(i_2 r_2) e^{im\varphi_2}); \\ \Phi^{III} &= \sum_{m=-\infty}^{+\infty} (D_{1m} K_m(kr_1) e^{im\varphi_1} + D_{2m} K_m(kr_2) e^{im\varphi_2}),\end{aligned}\quad (3)$$

where $i_i = k \sqrt{\frac{T_i^{\square}}{T_i^{\perp}}}$.

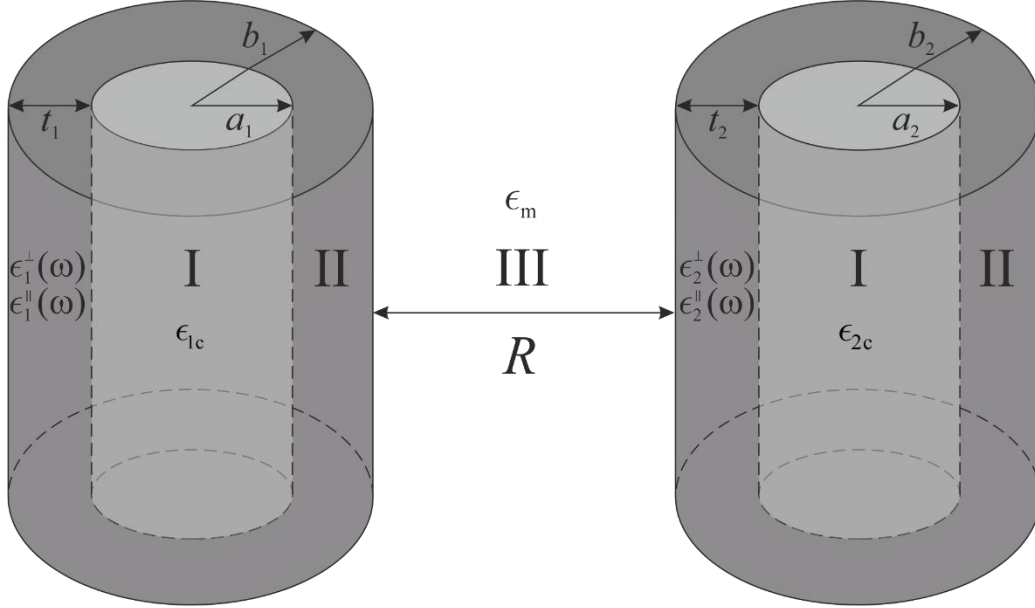


Fig. 1 – The geometry of the system

By Graf theorem

$$\begin{aligned}K_m(kr_2) e^{im\varphi_2} &= \sum_{p=-\infty}^{+\infty} K_{m+p}(kR) I_p(kr_1) e^{ip\varphi_1}, \\ K_m(kr_1) e^{im\varphi_1} &= \sum_{p=-\infty}^{+\infty} K_{m+p}(kR) I_p(kr_2) e^{ip\varphi_2},\end{aligned}$$

therefore

$$\begin{aligned}\Phi_1^{III} &= \sum_{m=-\infty}^{+\infty} \left[D_{1m} K_m(kr_1) + I_m(kr_1) \sum_{p=-\infty}^{+\infty} D_{2p} K_{m+p}(kR) \right] e^{im\varphi_1}; \\ \Phi_2^{III} &= \sum_{m=-\infty}^{+\infty} \left[D_{2m} K_m(kr_2) + I_m(kr_2) \sum_{p=-\infty}^{+\infty} D_{1p} K_{m+p}(kR) \right] e^{im\varphi_2}\end{aligned}\quad (4)$$

Using the boundary conditions of the equality of the potentials and the normal components of the electric displacement vector, where $r_1 = a_1$, $r_2 = a_2$ and $r_1 = b_1$, $r_2 = b_2$, we obtain

$$D_{1m} + \Delta_{1m} \sum_{p=-\infty}^{+\infty} D_{2p} K_{m+p}(kR) = 0; \quad D_{2m} + \Delta_{2m} \sum_{p=-\infty}^{+\infty} D_{1p} K_{m+p}(kR) = 0, \quad (5)$$

where

$$\Delta_{im} = \frac{I'_m(kb_i) - G_{im} I_m(kb_i)}{K'_m(kb_i) - G_{im} K_m(kb_i)}, \quad (6)$$

$$G_{im} = \frac{\sqrt{\tau_i^\perp \tau_i^\parallel} I'_m(i b_i) + E_{im} K'_m(i b_i)}{\tau_m I_m(i b_i) + E_{im} K_m(i b_i)}, \quad E_{im} = \frac{\frac{\sqrt{\tau_i^\perp \tau_i^\parallel}}{\tau_{ic}} I_m(ka_i) I'_m(i a_i) - I'_m(ka_i) I_m(i a_i)}{I'_m(ka_i) K_m(i a) - \frac{\sqrt{\tau_i^\perp \tau_i^\parallel}}{\tau_{ic}} I_m(ka_i) K'_m(i a_i)}. \quad (7)$$

The free energy is defined by the expression:

$$F(R) = k_B T \sum_{n=0}^{\infty} \int_{-\infty}^{+\infty} \frac{Ldk}{2\pi} \ln \det [\hat{\mathbf{I}} - \hat{\mathbf{N}}(k, i\omega_n)], \quad \omega_n = \frac{2\pi k_B T}{\hbar} n, \quad (8)$$

where $\hat{\mathbf{I}}$ – the identity matrix;

$$N_{lm} = \sum_{p=-\infty}^+ \Delta_{lm}(k, i\omega_n) \Delta_{2p} K_{m+p}(kR) K_{l+p}(kR). \quad (9)$$

As long as the domain $k \lesssim R^{-1}$ makes the major contribution, then $ka \ll 1$, $kb \ll 1$, $\frac{a}{R} \sqrt{\frac{\tau^\perp}{\tau^\parallel}} \ll 1$, $\frac{b}{R} \sqrt{\frac{\tau^\perp}{\tau^\parallel}} \ll 1$, and in (9) it is sufficient to take into account $\Delta_0(k, i\omega)$ and $\Delta_{\pm 1}(k, i\omega_n)$, hence, using the asymptotics of Infeld function and the asymptotics of McDonald function, under the small values of the argument, we obtain the following expressions, assuming that the material and the geometrical parameters of the shells are the same ($a_1 = a_2 = a$; $b_1 = b_2 = b$; $\tau_1^\perp = \tau_2^\perp = \tau^\perp$; $\tau_1^\parallel = \tau_2^\parallel = \tau^\parallel$; $\tau_{ic} = \tau_{2c} = \tau_c$):

$$\Delta_0 \cong \frac{\tau_c}{2\tau^\perp} k^2 ab \left(\frac{\tau^\perp}{\tau_m} - 1 \right) \left[\frac{k^2 ab}{2} \ln \frac{b}{a} + \frac{\tau^\perp}{\tau_c} \left(\frac{b}{a} - \frac{a}{b} \right) \right]; \quad (10)$$

$$\Delta_{\pm 1} \cong \frac{k^2}{2} \frac{b^2 \left(1 + \frac{\tau^\perp}{\tau_c} \right) \left(\frac{\sqrt{\tau^\perp \tau^\parallel}}{\tau_m} - 1 \right) - a^2 \left(1 + \frac{\tau^\perp}{\tau_m} \right) \left(\frac{\sqrt{\tau^\perp \tau^\parallel}}{\tau_c} - 1 \right)}{\frac{\sqrt{\tau^\perp \tau^\parallel}}{\tau_m} - \frac{a^2}{b^2} \left(\frac{\tau^\perp}{\tau_c} - 1 \right) \left(\frac{\sqrt{\tau^\perp \tau^\parallel}}{\tau_m} - 1 \right)}. \quad (11)$$

Supposing that the material of the shells is isotropic ($\tau^\perp = \tau^\parallel = \tau$), one can give the expressions (10) – (11) in the following form:

$$\Delta_0 \cong \frac{\tau_c}{2\tau} k^2 ab \left(\frac{\tau}{\tau_m} - 1 \right) \frac{\tau}{\tau_c} \left(\frac{b}{a} - \frac{a}{b} \right) = \frac{1}{2} k^2 ab \left(\frac{\tau}{\tau_m} - 1 \right) \left(\frac{b}{a} - \frac{a}{b} \right); \quad (12)$$

$$\Delta_{\pm 1} \cong \frac{k^2}{2} \frac{b^2 \left(1 + \frac{\tau}{\tau_c} \right) \left(\frac{\tau}{\tau_m} - 1 \right) - a^2 \left(1 + \frac{\tau}{\tau_m} \right) \left(\frac{\tau}{\tau_c} - 1 \right)}{\frac{\tau}{\tau_m} - \frac{a^2}{b^2} \left(\frac{\tau}{\tau_c} - 1 \right) \left(\frac{\tau}{\tau_m} - 1 \right)}. \quad (13)$$

After that, the expression for the free energy per unit length has the following form with the evaluated integral

$$\begin{aligned} F_L(R) &\cong -\frac{k_B T}{2\pi} \sum'_{n=0}^{\infty} \int_{-\infty}^{+\infty} dk \sum_{m=-\infty}^{+\infty} \sum_{p=-\infty}^{+\infty} \Delta_m(k, i\omega_n) \Delta_p(k, i\omega_n) K_{m+p}^2(kR) = \\ &= -\frac{k_B T}{4\pi R^5} \sum'_{n=0}^{\infty} \int_0^{\infty} dx \cdot x^4 \left\{ A_0(i\omega_n) K_0^2(x) + A_1(i\omega_n) K_1^2(x) + A_2(i\omega_n) K_2^2(x) \right\} = \\ &= -\frac{\pi k_B T}{2048 R^5} \sum'_{n=0}^{\infty} \left\{ 27 A_0(i\omega_n) + 45 A_1(i\omega_n) + 315 A_2(i\omega_n) K_2^2(x) \right\}, \end{aligned}$$

where the frequency functions are introduced

$$A_0(i\omega_n) = a^2 b^2 \left(\frac{b}{a} - \frac{a}{b} \right)^2 \left(\frac{\tau(i\omega_n)}{\tau_m} - 1 \right);$$

$$A_1(i\omega_n) = 2ab \left(\frac{\tau(i\omega_n)}{\tau_m} - 1 \right) \frac{b^2 \left(1 + \frac{\tau(i\omega_n)}{\tau_c} \right) \left(\frac{\tau(i\omega_n)}{\tau_m} - 1 \right) - a^2 \left(1 + \frac{\tau(i\omega_n)}{\tau_m} \right) \left(\frac{\tau(i\omega_n)}{\tau_c} - 1 \right)}{\frac{\tau(i\omega_n)}{\tau_m} - \frac{a^2}{b^2} \left(\frac{\tau(i\omega_n)}{\tau_c} - 1 \right) \left(\frac{\tau(i\omega_n)}{\tau_m} - 1 \right)};$$

$$A_2(i\omega_n) = \frac{b^4 \left(1 + \frac{\tau(i\omega_n)}{\tau_c} \right)^2 \left(\frac{\tau(i\omega_n)}{\tau_m} - 1 \right)^2}{\left[\frac{\tau(i\omega_n)}{\tau_m} - \frac{a^2}{b^2} \left(\frac{\tau(i\omega_n)}{\tau_c} - 1 \right) \left(\frac{\tau(i\omega_n)}{\tau_m} - 1 \right) \right]^2},$$

a

$$\tau(i\omega_n) = 1 + \frac{\omega_p^2}{\omega_n^2}$$

– Drude dielectric function.

Conclusions. The Van der Waals interaction between the cylinder metallic tubes with parallel axes has been studied within the framework of the macroscopic approach.

An asymptotic expression for the free energy of the interaction per unit length has been obtained for the small wavelength.

References

- [1] *Бараин Ю.С.* Силы Ван-дер-Ваальса. Москва: Наука, 1988. – 344 с.
 [2] *Dobson J.F., Gould T.* Calculation of dispersion energies // J. Phys.: Condens. Matter. 2012. V. 24, id. 073201.
 [3] *Makhnovets K.A., Kolezhuk A.K.* Finite-size nanowire at a surface: Unconventional power laws of the van der Waals interaction // Phys. Rev. B. 2017. V. 96, id. 125427.
 [4] *Волокитин А.И.* Эффект электрического поля в передаче тепла между металлами в экстремальном ближнем поле // Пис. ЖЭТФ. 2019. Т. 109, с. 783-788.

THE POLARIZABILITY OF THE METALLIC NANOCYLINDER, WHICH IS COVERED BY THE OXIDE LAYER

Ya.V. Karandas¹, A.V. Korotun¹, I.M. Titov²

¹National University "Zaporizhzhia Politechnic"

69063, Zaporizhzhya, Zhukovsky Str. 64, dep. Radioelectronics and telecommunication
tel. (061) 764-67-33

E-mail: andko@zntu.edu.ua

²UAD Systems

69002, Zaporizhzhya, Alexandrovska Str. 84

The paper deals with the frequency dependences of the polarizability of the bilayered metal-oxide nanocylinders. The expression for the polarizability has been obtained from the solution of the boundary problem of the electrostatics for the mentioned system. The particular cases of the "thin" and "thick" oxide layers have been considered. The approach for the calculation of the relaxation time, which takes into account the surface scattering, has been discussed. The graphs of the frequency dependences of the imaginary part of the polarizability for the nanocylinders Cu and Al, which are covered with the layer of the intrinsic oxide, have been given. The existence of the "violet" displacement of the maximums of the imaginary part of the polarizability under the increase in the radius of the nanocylinders, which is more substantial for the system Al@Al₂O₃, has been established. The calculations show the substantial increase in the values of the imaginary component of the polarizability for the nanocylinders of the aluminium and the maximums shift into the ultraviolet region.

Introduction. The one-dimensional metal structures attract the big attention of the researchers at the present time [1,2]. It is explained by the widespread application of such systems as the elements of the optical instruments, and also by the experience of the new physical effects in them, such as the surface-enhanced Raman scattering (SERS), the surface-enhanced fluorescence and the resonance scattering of the light. One of the main reasons, which cause these effects, is the surface plasmonic resonance, which depends on the geometry of the nanostructures and the dielectric properties of the metal and the medium, in which the nanostructure is situated.

The frequency of the surface plasmonic resonance can be found from the condition that the real part of the denominator of the expression for the polarizability of the system is equal to zero [3]. Among the other things, many optical characteristics can be expressed in term of the polarizability. In particular, the value of the section of the extinction is determined by the imaginary part of the polarizability. That is why the object of the given work is the study of the frequency dependence of the polarizability of the metallic nanocylinder, which is covered by the oxide layer and imbedded in the dielectric medium.

Setting up of the problem and the basic relations. Let us consider the metallic nanoconductor with the radius a , which is covered by the oxide layer with the thickness t ($t = b - a$).

The boundary electrodynamic problem of such 1D-structure consists of Laplace equation for each domain (fig. 1)

$$\Delta\varphi_i = \frac{1}{r} \frac{\partial}{\partial r} \left(r \frac{\partial \varphi_i}{\partial r} \right) + \frac{1}{r^2} \frac{\partial^2 \varphi_i}{\partial \phi^2} = 0 \quad (i=1, 2, 3) \quad (1)$$

with the boundary conditions of the equality of the potential and the normal component of the vector of the induction of the electric field on the interface

$$\varphi_1(a) = \varphi_2(a); \quad \varphi_2(b) = \varphi_3(b); \quad \tau(\omega) \frac{\partial \varphi_1}{\partial r} \Big|_{r=a} = \tau_{\text{ox}} \frac{\partial \varphi_2}{\partial r} \Big|_{r=a}; \quad \tau_{\text{ox}} \frac{\partial \varphi_2}{\partial r} \Big|_{r=b} = \tau_m \frac{\partial \varphi_3}{\partial r} \Big|_{r=b} \quad (2)$$

and the boundedness condition of the potential on the axis of the system

$$\left| \lim_{r \rightarrow 0} \varphi_i(r) \right| < \infty \quad (3)$$

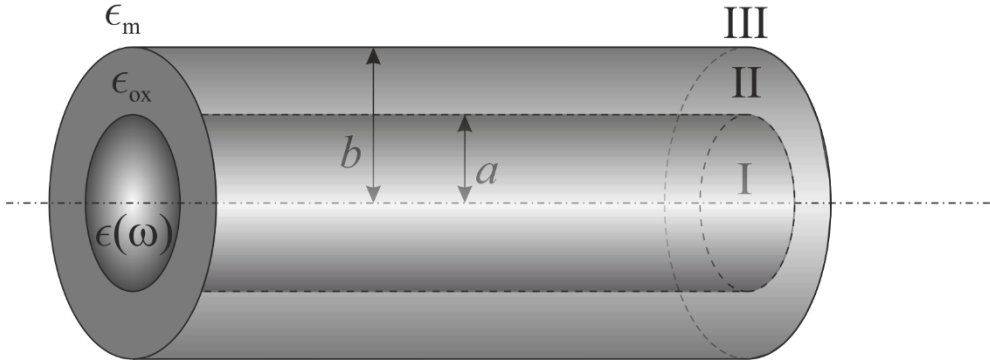


Fig. 1 – The geometry of the problem

The solutions of the equation in each of the domains have the form

$$\varphi(r, \phi) = \begin{cases} -\mathbf{E}_0 r \cos \phi, & r < a; \\ -\mathbf{E}_0 \left(Br + \frac{C}{r} \right) \cos \phi, & a < r < b; \\ -\mathbf{E}_0 \left(r - \frac{D}{r} \right) \cos \phi, & r > b. \end{cases} \quad (4)$$

After the substitution of the solution (4) into the boundary conditions (2) – (3), we obtain the expression for the polarizability of the considered system:

$$\alpha = b^2 \frac{(\tau + \tau_{\text{ox}})(\tau_{\text{ox}} - \tau_m) + Q^2 (\tau - \tau_{\text{ox}})(\tau_{\text{ox}} + \tau_m)}{(\tau + \tau_{\text{ox}})(\tau_{\text{ox}} + \tau_m) + Q^2 (\tau - \tau_{\text{ox}})(\tau_{\text{ox}} - \tau_m)}, \quad (5)$$

where the complex dielectric function of the metallic nanoconductor is determined by Drude expression:

$$\tau = \tau(\omega) = \tau_1 + i\tau_2 = \tau^\infty - \frac{\omega_p^2 \tau^2}{1 + \omega^2 \tau^2} + i \frac{\omega_p^2 \tau}{\omega(1 + \omega^2 \tau^2)}. \quad (6)$$

In this expression ω_p is the plasma frequency; τ^∞ is the component, which describes the contribution of the ion core of the metal; τ is the relaxation time.

The real part and the imaginary part of the polarizability have the form:

$$\text{Re} \alpha(\omega) = b^2 \frac{\text{Re} \Lambda}{\Xi}; \quad \text{Im} \alpha(\omega) = b^2 \frac{\text{Im} \Lambda}{\Xi}, \quad (7)$$

where we accept the following designations

$$\begin{aligned} \text{Re} \Lambda &= (\tau_{\text{ox}}^2 - \tau_m^2) \left[(\tau_1 + \tau_{\text{ox}})^2 + \tau_2^2 \right] + 2Q^2 (\tau_{\text{ox}}^2 + \tau_m^2) (\tau_1^2 + \tau_2^2 - \tau_{\text{ox}}^2) + Q^4 (\tau_{\text{ox}}^2 - \tau_m^2) \left[(\tau_1 - \tau_{\text{ox}})^2 + \tau_2^2 \right]; \\ \text{Im} \Lambda &= 4Q^2 \tau_{\text{ox}} (\tau_{\text{ox}}^2 + \tau_m^2) \tau_2; \end{aligned} \quad (8)$$

$$\Xi = (\tau_{\text{ox}} + \tau_m)^2 \left[(\tau_1 + \tau_{\text{ox}})^2 + \tau_2^2 \right] + 2Q^2 (\tau_{\text{ox}}^2 - \tau_m^2) (\tau_1^2 + \tau_2^2 - \tau_{\text{ox}}^2) + Q^4 (\tau_{\text{ox}} - \tau_m)^2 \left[(\tau_1 - \tau_{\text{ox}})^2 + \tau_2^2 \right].$$

Let us consider the limiting cases of the “thin” and “thick” oxide layers.

1. The approximation of the thin oxide layer $Q = 1 - q$, $q \rightarrow 0$, $Q \rightarrow 1$. In this case the expressions for the real part and the imaginary part have the following form:

$$\text{Re} \alpha(\omega) = b^2 \frac{\tau_1^2 + \tau_2^2 - \tau_m^2}{(\tau_1 + \tau_m)^2 + \tau_2^2} \left\{ 1 - q \left[2 - 2 \frac{\tau_1 (\tau_{\text{ox}}^2 - \tau_m^2)}{\tau_{\text{ox}} (\tau_1^2 + \tau_2^2 - \tau_m^2)} + G(\tau_1, \tau_2, \tau_{\text{ox}}, \tau_m) \right] \right\}; \quad (9)$$

$$\text{Im } \alpha = b^2 \frac{\tau_2 (\tau_{\text{ox}}^2 + \tau_m^2)}{\tau_{\text{ox}} ((\tau_1 + \tau_m)^2 + \tau_2^2)} \left\{ 1 - q \left[2 - G(\tau_1, \tau_2, \tau_{\text{ox}}, \tau_m) \right] \right\}, \quad (10)$$

where

$$G(\tau_1, \tau_2, \tau_{\text{ox}}, \tau_m) = \frac{(\tau_{\text{ox}}^2 - \tau_m^2)(\tau_1^2 + \tau_2^2 - \tau_{\text{ox}}^2) + (\tau_{\text{ox}} - \tau_m)^2 ((\tau_1 - \tau_{\text{ox}})^2 + \tau_2^2)}{\tau_{\text{ox}}^2 ((\tau_1 + \tau_m)^2 + \tau_2^2)}.$$

2. The approximation of the thick oxide layer $Q \rightarrow 0$

$$\text{Re } \alpha(\omega) = b^2 \frac{\tau_{\text{ox}} - \tau_m}{\tau_{\text{ox}} + \tau_m}; \quad \text{Im } \alpha(\omega) = 4b^2 Q^2 \tau_2 \tau_{\text{ox}} \frac{\tau_{\text{ox}}^2 + \tau_m^2}{(\tau_{\text{ox}} + \tau_m)^2 ((\tau_1 + \tau_{\text{ox}})^2 + \tau_2^2)}. \quad (11)$$

The relaxation time in the nanostructures can be substantially different from the similar value for 3D-metal. The reason of this is the preponderance of the scattering on the boundaries of the nanosystems over the contributions of the other scattering channels, for example, such as the scattering by phonons, the doping materials or the structure defects. In this case the formula (6) contains the value τ_{eff} instead of τ . The value τ_{eff} can be found from

$$\frac{1}{\tau_{\text{eff}}} = \frac{1}{\tau_{\text{bulk}}} + \frac{1}{\tau_s}, \quad (12)$$

where τ_{bulk} – relaxation time for 3D-metal, τ_s – relaxation time, which is connected with the scattering on the surface. In the case of the radial movement of the electrons in the nanocylinder this relaxation time can be determined by the relation [4]:

$$\frac{1}{\tau_s} = \frac{9\pi(3\pi)^{\frac{1}{3}} v_F}{64 a}, \quad (13)$$

where v_F – Fermi velocity of the electrons.

The calculation results and the discussion of them. The figures 2 and 3 show the results of the calculation of the frequency dependences of the imaginary part of the polarizability for the nanocylinders Cu and Al, which are covered with the layer of the corresponding oxide. The data for the calculations: the radii of the cylinders $a = 10, 20$ and 30 nm, the thickness of the oxide layer $t = 2$ and 10 nm.

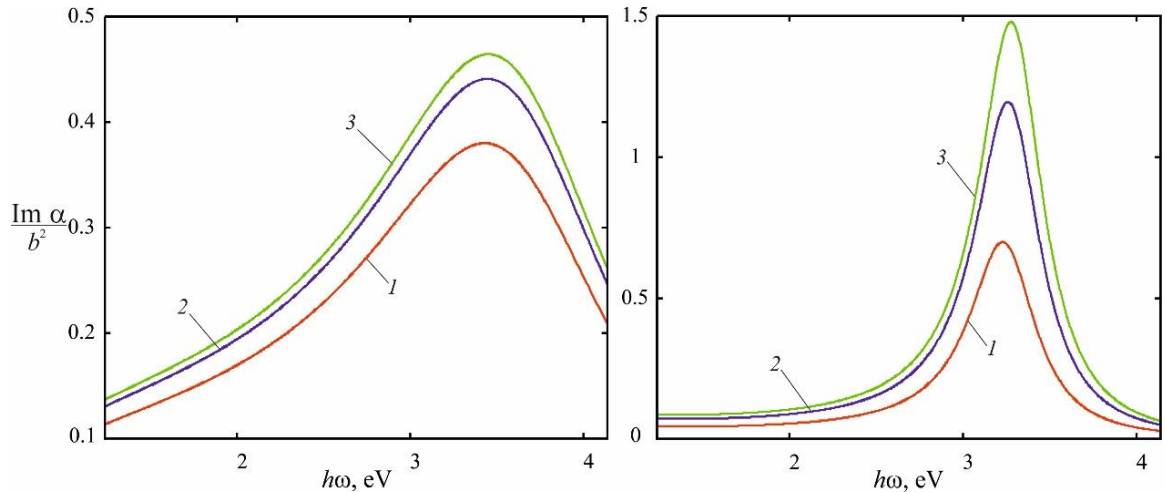


Fig. 2 – The frequency dependences of the imaginary part of the polarizability of the system Cu@Cu₂O for the “thin” (a) and “thick” (b) oxide shells with the different radius: 1 – $a = 10$ nm; 2 – $a = 20$ nm; 3 – $a = 30$ nm

We note that all the curves $\text{Im}\alpha(\omega)$ have one maximum, which is clearly defined in the case of the “thick” oxide layer. Among the other things, the value of this maximum increases when the radius of the cylinder increases and it runs into the “violet” shift, which is more substantial for $\text{Al@Al}_2\text{O}_3$. The clearly defined nature of the maximum for the nanocylinders Al is connected with the big concentration of the conduction electrons, and, correspondingly, the plasma frequency for Al. This translates to the fact that the maximum $\text{Im}\alpha(\omega)$ for the system $\text{Cu@Cu}_2\text{O}$ is situated in the visible region, and for $\text{Al@Al}_2\text{O}_3$ – in the ultraviolet region.

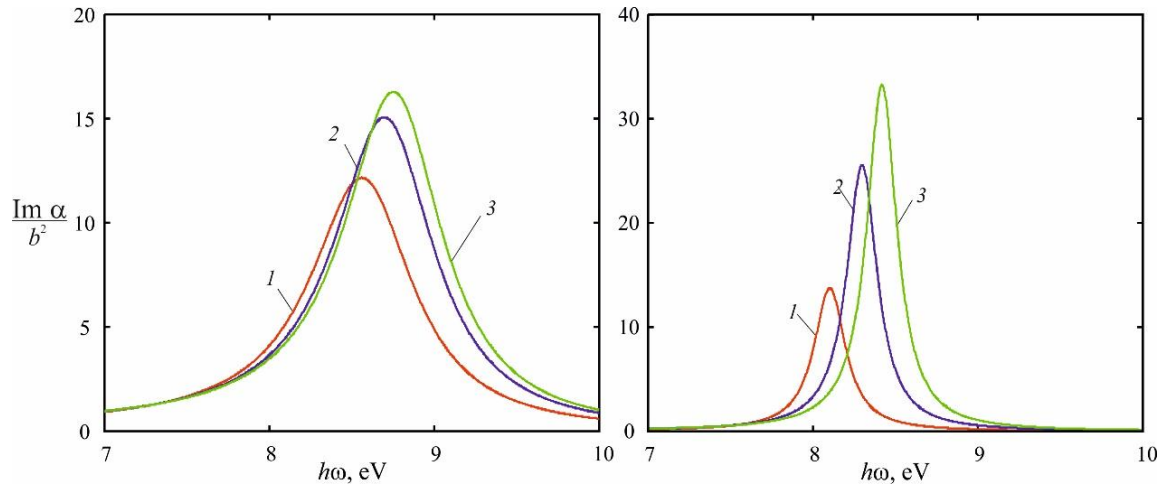


Fig. 3 – The frequency dependences of the imaginary part of the polarizability of the system $\text{Al@Al}_2\text{O}_3$ for the “thin” (a) and “thick” (b) oxide shells with the different radius: 1 – $a = 10$ nm; 2 – $a = 20$ nm; 3 – $a = 30$ nm

Conclusions. The relations for the real and imaginary parts of the polarizability of the bilayered metal-oxide nanocylinders have been obtained. The particular cases of the “thin” and “thick” oxide layers have been considered. The calculations of $\text{Im}\alpha(\omega)$ for the systems $\text{Cu@Cu}_2\text{O}$ and $\text{Al@Al}_2\text{O}_3$ have been performed.

It is established that the maximum value of $\text{Im}\alpha$ increases when the radius of the cylinder increases, and the “violet” shift of the maximum is more substantial for the nanocylinder $\text{Al@Al}_2\text{O}_3$.

It has been shown that the big concentration of the conduction electrons for Al results in an order of magnitude increase of the maximum values of the imaginary part and in the shift of the maximums from the visible region to the ultraviolet region in comparison with Cu.

References

- [1] Wu Z.-W., Ma Y.-W., Jiang Y.-Y., Li J., Yin X.-C., Zhang L.-H., Yi M.-F. Theoretical study of optimizing the refractive index sensitivity of dielectric-metal nanotube by tuning the geometrical parameters // *Opt. Commun.* 2019. V. 449, P. 57 – 62.
- [2] Zhao S., Zhu J. The effect of local dielectric environment on the resonance light scattering of Au–Ag bimetallic nanotube // *Appl. Phys. A.* 2017. – 9 p.
- [3] Maier S. A. *Plasmonics - Fundamentals and Applications*. New York, U. S. A.: Springer, 2007. – 224 p.
- [4] Kraus W. A., Schatza G. C. Plasmon resonance broadening in small metal particles // *J. Chem. Phys.* 1983. V. 79. P. 6130 – 6139.

RESEARCH OF ANOMALOUS PHOTOCONDUCTIVITY OF CRYSTAL SILICON WITH AMORPHOUS INCLUSIONS

O.Yu. Babychenko, A.V. Borodin
Kharkiv National University of Radio Electronics
61166, Kharkiv, Nauky ave. 14, Department of Microelectronics, Electronic Devices and Appliances,
tel. +38 (057) 7021362
E-mail: oksana.babychenko@nure.ua

Anomalous photoconductivity of crystalline silicon with amorphous cylindrical inclusions is investigated in this work. The obtained positive and negative photoconductivities are analyzed depending on the ratio of the Debye screening length, the function of the density of states, the degree of disorder of amorphous inhomogeneities and their geometry.

INTRODUCTION

Heterocompositions with thin and ultrafine structures (superlattices) can be considered as a new class of semiconductor materials, the fundamental properties of which are determined by the type of these structures, their thicknesses and the nature of the distribution of incoming doped impurities. The combination of the fundamental properties of the direct-gap structure (a – Si) and the indirect gap (c – Si) structure in a single (c-Si) crystal is the main difference between existing devices based only on (c-Si) or (a-Si) materials. In the (c – Si) structure, the carriers have a high mobility ($\mu_n \sim 1500$, $\mu_p \sim 500$) $\text{cm}^2/\text{V}\cdot\text{s}$, but an insignificant absorption coefficient of light, in addition to the short-wave region of the solar spectrum, which makes it necessary to use large thickness of photoconverters ($\geq 100 \mu\text{m}$). In the (a-Si) structure, charge carriers have a low drift mobility ($\mu_n \sim 10^{-1}$, $\mu_p \sim 10^{-3}$) $\text{cm}^2/\text{V}\cdot\text{s}$, but a very large absorption coefficient of light radiation, as well as a high concentration of recombination centers in the zone mobility. These factors determine the low efficiency of (a-Si) photo-converters [1-2]. The region of direct quantum transitions in the (c-Si) semiconductor is formed by nanoscale amorphous inclusions. Such a structure can be considered as a material with spatially inhomogeneous properties of amorphous and crystalline silicon. The presence of heterointerfaces with defects leads to the appearance of internal electric fields affecting the electrical transport of charge carriers in the crystalline part, but not affecting the total contact potential difference. Thus, it can be replaced by a combination of alternating cylindrical amorphous interlayers and silicon single crystals. The resulting charge carriers move in a periodic structure of crystalline silicon with parallel spaced cylindrical amorphous inclusions of radius r , which are periodically located in the bulk of the semiconductor with an average distance between the centers $2R$.

Photoconductivity of amorphous hydrogenated silicon

The calculations assume that the origin is on the axis of one of the amorphous cylinders. Under steady-state illumination, such an inhomogeneous spatial distribution of photocarrier concentrations is established, which ensures a balance between the processes of generation and recombination of nonequilibrium charge carriers. Due to the increased recombination of charge carriers on the surfaces of amorphous inclusions in the structure, a non-uniform distribution of photocarriers is established and bipolar diffusion of photocarriers to inclusions takes place. For a symmetric structure, the spatial distribution of the concentration of photocarriers is described by the following differential equation [3]

$$\frac{\partial \cdot \Delta n}{dt} = D_n \frac{\partial^2 \cdot \Delta n}{\partial x^2} - \frac{\Delta n}{\tau_n} + G \cdot \exp(-\kappa x), \quad (1)$$

where Δn - the concentration of excess holes; D_n - diffusion coefficient; τ_n - carrier lifetime, κ - absorption coefficient.

To solve equation (1), the following boundary conditions are used:

$$D \frac{\partial \Delta n}{\partial x} \Big|_{x=r} = +S \cdot \Delta n(r); \quad D \frac{\partial \Delta n}{\partial x} \Big|_{x=R} = -S \Delta n(R). \quad (2)$$

The first condition of equation (2) corresponds to the recombination of photocarriers on the surface of an amorphous cylindrical inclusion with a surface recombination rate, which depends on the state of the surface, and the second condition follows from the conditions of symmetry of the problem, which lead to the maximum concentration of photocarriers on the faces of the structure.

To solve equation (1), in addition to the boundary conditions, it is necessary to determine the density of states $N(E)$ in amorphous silicon, as well as the processes of photogeneration and carrier recombination, including at the boundaries of the contacting layers. The function of the density of states for the conduction band of amorphous silicon, taking into account the degree of disorder of its structure, has the form [2,4]:

$$N_c(E) = \frac{\sqrt{2} \cdot m_c^{*3/2}}{\pi^2 \cdot \hbar^3} \begin{cases} \sqrt{E - E_c}, & E \geq E_c + \frac{\gamma_c}{2} \\ \sqrt{\frac{\gamma_c}{2}} \cdot \exp\left(-\frac{1}{2}\right) \cdot \exp\left(\frac{E - E_c}{\gamma_c}\right), & E < E_c + \frac{\gamma_c}{2} \end{cases} \quad (3)$$

where m_c^* – the effective electron mass in the conduction band; E_c – the energy of the bottom of the disordered conduction band; $E_c + \gamma_c/2$ – the transition point between the quadratic and exponential distribution of the density of states of the conduction band; γ_c – width of tails of the conduction band. A measure of the disordering of the structure are the parameters γ_c .

Results of calculations and discussion

Fig. 1 shows the results of the solution of the problem. Calculations have shown that the photoconductivity of crystalline silicon with inclusions of cylindrical amorphous silicon increases with decreasing distances between the inclusions and decreases as the radius of inclusions increases. It is established that the photoconductivity is determined by the rate of surface recombination of photocarriers and can drop significantly with increasing S . The latter takes place in materials with a high concentration of amorphous inclusions, when there is a large surface area of inclusions per unit volume, i.e. when the ratio of the distance between inclusions to their radius reaches as large as possible. With a certain structure geometry, the presence of so-called negative photoconductivity occurs [5]. Negative photoconductivity is manifested in the fact that when the sample is illuminated, its conductivity does not increase, but decreases to a value less than dark.

The work also analyzed in more detail the obtained positive and negative photoconductivity depending on the ratio of the Debye screening length, the function of the density of states, the degree of disorder of amorphous inhomogeneities and degree of disorder of amorphous inhomogeneities and their geometry. Debye screening length is determined by the formula:

$$L_d = \left(\frac{\varepsilon_0 \cdot \varepsilon \cdot k \cdot T}{2 \cdot q^2 \cdot N_c(E)} \right)^{1/2} \cdot (\Phi_{1/2}(z))^{-1/2}, \quad (4)$$

where $\Phi_{1/2}(z)$ – the derivative of the Fermi function of order $1/2$ defined by the expression

$$\Phi_{1/2}(z) = \frac{2}{\sqrt{\pi}} \cdot \int_0^{\infty} \frac{\sqrt{x} \cdot \exp(x-z)}{(1 + \exp(x-z))^2} dx,$$

where $z = E_f/kT$ – the dimensionless Fermi energy in a semiconductor; $x = E/kT$ – dimensionless kinetic energy of electrons.

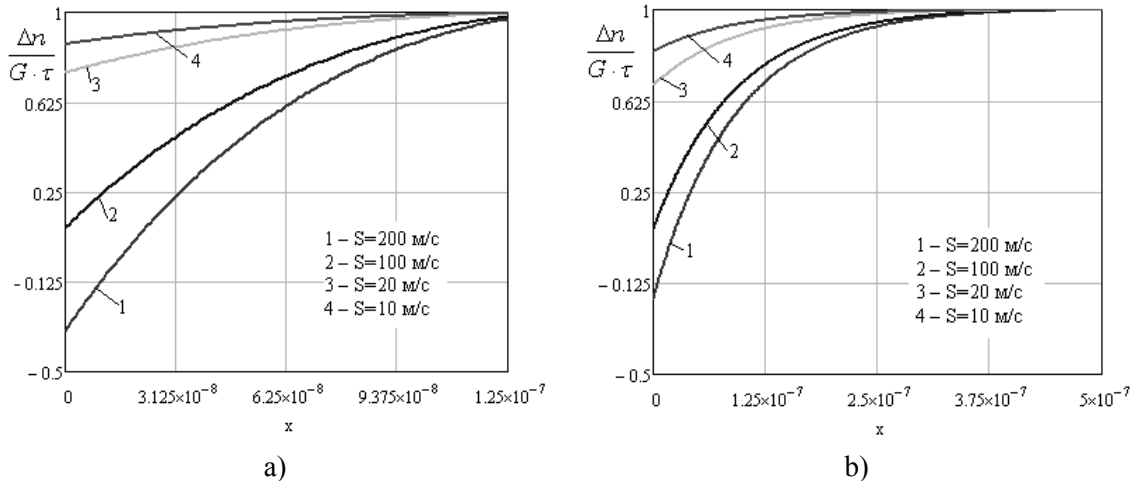


Fig. 1 – Dependences of the distribution of photocarriers in the sample at $r = 50$ nm and various values of the surface recombination rate. a) $R = 5r$, b) $R = 20r$

CONCLUSIONS

The photoconductivity modeling of the semiconductor structure, which is a crystalline silicon with uniformly located intersperses of amorphous silicon for the case of homogeneous generation of photoconductors, is carried out. On the basis of the results obtained, it can be argued that the photoconductivity of crystalline silicon with the inclusion of cylindrical amorphous silicon increases with decreasing distances between inclusions and decreases in the case of an increase in the radius of inclusions. A possible manifestation was detected at certain geometrical sizes of so-called negative photoconductivity. The presence of this effect is due to the formation on the surface of the investigated semiconductor structure of the inverse curvature of the zones due to sticking to so-called 'slow' surface surfaces of the main charge carriers.

REFERENCES

1. A.N.Dovbnia, V.P.Yefimov, G.D.Pugachev, V.S.Dyomin, N.A.Dovbnia, J.E.Gordienko, B.G.Borodin, S.V.Babychenko, T.A.Semenets /The influence of γ -irradiation and ^{238}U fragments on the properties of single-crystal Silicon. // Problems of atomic science and technology. Series "Nuclear Physics Investigations," Kharkov (Ukraine).-2006, # 3(47). -P. 179-181.
2. A.G. Pashchenko, O.Yu. Sologub. Definition of electronic states densities functions in amorphous silicon / Telecommunications and Radio Engineering, 73 (5):447-455 (2014).
3. А.Г. Пашченко, О.Ю. Сологуб / Определение функций плотностей электронных состояний в аморфном кремнии // Радиотехника. – 2012. – вып. 169. С.337 – 342.
4. Babychenko O.Y. States density distribution for determination of a-Si:H photoconductivity / O.Y. Babychenko, A.G. Pashchenko // Journal of Nano- and Electronic Physics. – 2017. - V. 9 No 5. - 05044(4pp)
5. Зуев В.О., Саченко А.В. Теоретичне дослідження поверхнево-чутливих фотоелектрів у Si // УФЖ. – 1973. – 18, №10. – С. 1680-1687.

**NANOPHOTONICS.
PROCESSES, STRUCTURES
AND DEVICES**

NANOPHOTONIC SOLID PHASE TRANSDUCER FOR HETEROGENEOUS DETECTION OF 5,6,11,12-TETRAPHENYLTETRACENE

Ghazi Khaled, A.V Kukoba, O.M. Bilash, K.M. Muzyka
Kharkiv National University of RadioElectronics
61166, Kharkiv, Nauky ave. 14, dep Biomedical Engineering
Tel. (057) 702-03-69
E-mail: myzika_katya@ukr.net

Abstract

In this work the nanophotonic solid phase transducer for aqueous detection of 5,6,11,12-tetraphenyltetracene as a representative member of polycyclic aromatic hydrocarbons (PAHs) with electrochemiluminescent properties was developed. The advantage and novelty of our approach is increase the surface concentration of the target analyte and, thus, to reduce the limit of electrochemiluminescent detection due to the transfer of the entire amount of analyte into the Langmuir-Blodgett nanolayer on the electrode (indium tin oxide). For a rational choice of the Langmuir-Blodgett amphiphilic matrix for model PAH, quantum chemical calculations were performed to supplement the experimental results. Interestingly, PMMA was found to be the best matrix for the preparation of homogenous supramolecular assembly. The optimal number of Langmuir-Blodgett monolayers on the ITO-electrode of the nanophotonical electrochemiluminescent transducer was 1. The surface pressure during creation of monolayers was in the range of $14 \div 16$ mN / m. The linear range of PAH concentrations was 10^{-10} - 10^{-13} M.

Introduction

The development of sensors to detect trace amounts of carcinogens, with high sensitivity is an important task for biomedical engineering, particularly polycyclic aromatic hydrocarbons (PAHs). This is due to the high hydrophobic nature and low aqueous solubility of the PAHs. PAHs are often present in the aquatic environment in trace concentrations. Therefore, the determination of PAHs in water particularly from industrial plants such as petroleum refineries is a complex analytical task. Electrochemiluminescence (ECL) is an analytical method that combines both electrical and luminescent characteristics. ECL is highly sensitive and has been used to investigate a particular group of PAHs such as benzepiren. The existing ECL methods for sensitive detection of PAHs require modification of the electrode with biomaterials such as DNA, nanomaterials that include carbon nanotubes, quantum dots etc all in an attempt to improve the aqueous solubility of the analyte. Other reported methods rely solely on the direct ECL detection based on quenching by the analyte [1].

Creating nanophotonical transducer with luminescent analytes on the electrode surface is possible using Langmuir-Blodgett (LB) technology [2]. LB technology results in mono- and multi-layer highly organized films with controlled thickness, orientation and high surface density of luminescent analytes, such as PAHs. However, despite the undoubted success in the LB technology, the problem still associated with the complexity of the formation of LB films with non-amphiphilic substances, such as PAHs.

In this investigation, 5,6,11,12-tetraphenyltetracene has been used as a model analyte. However, 5,6,11,12-tetraphenyltetracene is not an amphiphilic molecule and cannot form stable LB-monolayers that is uniformly distributed on the surface of the water subphase and, thus, LB-nanophotonical film. One of the approaches to solve this problem is to create LB films of mixed binary systems based on thermodynamically stable amphiphilic monomeric or polymeric compounds as matrices for immobilization of non-amphiphilic molecules.

The aim of this work is to develop a nanophotonical ECL-transducer based on LB technique for heterogeneous detection of 5,6,11,12-tetraphenyltetracene. Implementation of the aim can be achieved by addressing a number of technical problems such as, the rational choice of (i) langmuirogenic amphiphilic substances to form LB-layer (matrix material), (ii) the conditions of the formation of ordered LB-monolayer and their transfer from the aqueous subphase onto the sensor's electrode surface, (iii) the optimal number of LB-monolayers, (iv)

electrochemiluminescent detection of 5,6,11,12-tetraphenyltetracene based on developed nanophotonical transducer.

Quantum-chemical investigations of 5,6,11,12-tetraphenyltetracene complexes with stearic acid and polymethylacrylate

To better understand the nature of molecular interactions of LB systems with non-amphiphilic molecules quantum-chemical calculations were performed. Stearic acid and polymethyl methacrylate (PMMA) were used as amphiphilic molecules, and 5,6,11,12-tetraphenyltetracene as non-amphiphilic species. The amphiphiles are representatives of various classes of compounds that are used to obtain mixed binary systems with non-amphiphilic substances. Two-component complexes with most stable energies out of the 20 obtained were selected for complete optimization. The energy of interaction was calculated using the density functional (DFT) (functional M06-2X) with the cc-pvdz (M06-2X / ss-pvdz) as the basis set. All calculations were performed using the Gaussian03 program.

Calculations have shown that *all-trans* conformation in stearic acid molecule is 5.17 kcal / mole, while PMMA molecule is 14.07 kcal / mole more advantageous than curved.

Technology of the creation nanophotonic solid phase transducer

The formation of monolayers of 5,6,11,12-tetraphenyltetracene / PMMA and 5,6,11,12-tetraphenyltetracene / stearic acid system on the surface of ITO-electrodes has been provided using LT-102 LB trough, Microtestmachines, Co as described [3]. The surface structure of the monolayers obtained was controlled at the nanoscale by the atomic force microscope NT-206 of the same manufacturer.

Analytical studies were carried out with the help of ECL-analyzer ELAN-3D by the method of cyclic voltammetry with the simultaneous recording of the intensity of the ECL. The electrochemical and ECL studies of modified ITO electrodes were done in bidistilled water with tripropylamine (TPA) as a coreactant and LiClO₄ as a supporting electrolyte in three electrode electrochemical cell using cyclic voltammetry method with 100 mV/s scan rate. TPA was used as a well-known highly efficient ECL coreactant that obeys oxidative reduction ECL mechanism.

To measure the intensity of luminescence, a photoelectron multiplier with a multicellular photocathode of the photomultiplier-140 at a cathode -1400V voltage was used.

During the development of the ECL-technology, compression curves (π -A isotherms) of the binary system of stearic acid / 5,6,11,12-tetraphenyltetracene and PMMA / 5,6,11,12-tetraphenyltetracene were investigated. The surface pressure during formation of monolayers was in the range of 14 ÷ 16 mN / m. Based on the comparison of the luminescence intensity for stearic acid and PMMA-based LB-films with equal concentration of 5,6,11,12-tetraphenyltetracene, it can be concluded that the best results were achieved when using a PMMA matrix. The results of luminescent studies have shown that the ordered matrix of PMMA managed to incorporate 2.5 times more molecules of model PAH, and their surface concentration reached approximately 10¹⁴ molecules/cm².

Fig.1 shows an atomic force image of the surface of an ITO electrode modified with LB layers of the PMMA / 5,6,11,12-tetraphenyltetracene system. It clearly demonstrates that the polymer PMMA molecules are folded into flat globules about 100 nm in size. Perhaps this explains much higher concentration of model PAH in monolayer comparing to other investigated matrixes.

In order to test the developed nanophotonical transducer, different surface concentrations of 5,6,11,12-tetraphenyltetracene were immobilized in PMMA-monolayer. This transducer was placed in a three-electrode ECL cell.

The maximum ECL intensity was achieved when the number of LB-monolayers was equal to three. However, considering the fact that each additional monolayer requires a corresponding increase in the number of PAHs in the sample, the maximum sensitivity of the assay is reached with one LB-monolayer.

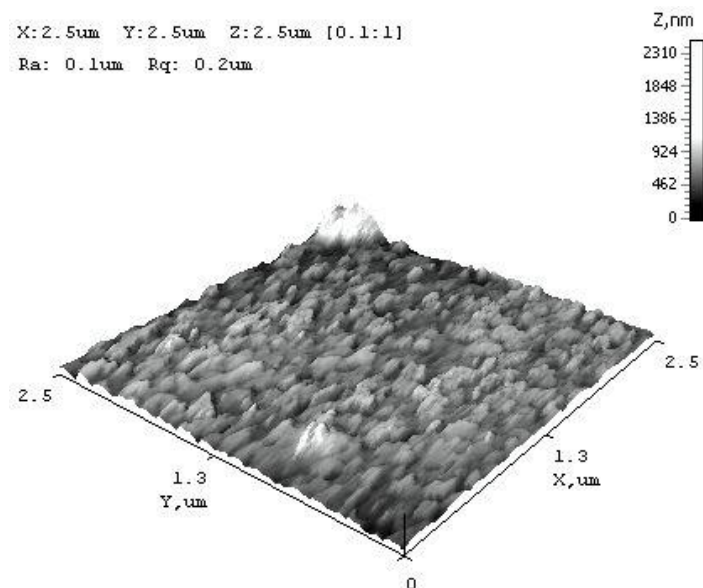


Fig. 1 – 3D Atomic force image of the surface of an ITO electrode modified with LB-layers of the PMMA / 5,6,11,12-tetraphenyltetracene system

Such behavior of analytic signal is likely associated with increased concentrations of radical cations of rubrene in the near-electrode zone when moving from one to three monolayers and reduced efficiency of electrochemical oxidation of rubrene with further increase of the number of monolayers.

Conclusions

The results of quantum-chemical calculations and luminescent studies have shown that PMMA is a better matrix than stearic acid for the preparation of homogeneous and stable “supramolecular assembly” of non-amphiphilic 5,6,11,12-tetraphenyltetracene. The optimal number of LB monolayers on the ITO-electrode of the ECL-transducer was 1. The surface pressure during creation of monolayers was in the range of $14 \div 16$ mN / m. The linear range of PAH concentrations was 10^{-10} - 10^{-13} M.

Thus, nanophotonic electrochemiluminescent transducer for heterogeneous detection of 5,6,11,12-tetraphenyltetracene was developed. The transfer of the model PAH from solution to supramolecular assembly on the surface of ITO electrode by means of LB technique allowed for achieving a low detection limit even without using of nano- and biomaterial-based amplification strategies.

References

1. J. Li, L. Yang, S. Luo, B. Chen, J. Li, H. Lin, Q. Cai, S. Yao Polycyclic aromatic hydrocarbon detection by electrochemiluminescence generating Ag/TiO(2) nanotubes // *Anal Chem.*, 2010, **82**, 7357-7361.
2. A. Kausar Survey on Langmuir–Blodgett films of polymer and polymeric composite // *Polymer - Plastics Technology and Engineering.*, 2017, **56**, 932-945, 2017.
3. G. Khaled, K. Muzyka Quantum-chemical investigations of rubrene complexes with stearic acid and polymethylmetacrylate in prediction of langmuirogenicity // *Sensor Electronics and Microsystem Technologies*, 2018, **4**, 32-38.
4. G. Khaled, A. Kukoba, O. Bilash, Yu. Zoludov, D. Snizhko, K. Muzyka Electroheliuminescent platform for solid phase determination of polycyclic aromatic hydrocarbons at ultra-trace level, *Radiotechnics (англ.) // AllUrk. Sci. Interdep. Mag.* 2018, **192**, 106 -112.

RISK FACTORS IN THE PULSED BEAM TECHNOLOGIES FOR THE ELECTRONIC CIRCUITS PRODUCTION

¹A.E. Pogorelov, ²Y.A. Pogoryelov

¹G.V. Kurdyumov Institute for Metal Physics, NAS of Ukraine,
03142 Kiev, Ukraine, Vernadsky ave. 36, dep. Physics for atomic transport processes,
Tel.: +(380) 97 927-49-12, E-mail: pog.alexander@gmail.com

²Department of Physics and Astronomy, Uppsala University, 751 21 Uppsala, Sweden

Annotation. This work raises the issue of possible risks arising during the beam treatment of materials used to fabricate electronic equipment components, as well as their studies and testing using various types of radiation. Based on the experimental results it is shown that non-stationary radiation exposure can result in a highly non-equilibrium state in the irradiated material. With the appropriate energy densities, it may be accompanied by the generation and directional movement of structural defects. In such state some of the processes in solids do not obey the laws of thermodynamic balance, which must be considered during the radiation treatments and measurements. In particular, this work discusses the examples of possible risks during the fabrication of passive electronic equipment components and the change of their parameters over the time. The possible negative impact of femtosecond laser pulses in the studies of magnetic multilayer film structures is considered. The evaluation studies conducted in this work reveal a number of physical processes that lead to the unusual results of mass and heat transfer under the conditions of artificially created non-equilibrium state in solids. The necessity to address these non-equilibrium physical processes occurring in solids with the application of radiation technologies and methodologies is substantiated.

Introduction. The commonly used solid state heat treatment methods, including doping, for the fabrication of the elements of electronic equipment should take into account a number of transfer processes that can significantly affect the final characteristics of the resulting products. First of all, they should include the processes of mass and heat transfer arising under highly non-equilibrium conditions created by a thermal pulse in a solid. Partial relaxation of the absorbed thermal energy in the crystal lattice of a number of solids results in the creation of a stress state, which leads to the formation of crystal lattice defects. The occurrence of such a state in an irradiated matter can lead to certain risks for both fabricated products and their operation, and a number of physical property studies using beam techniques.

Interacting with each other and with the stress field, the defects rush from the site of excitation into the depth of the material and create at the depth the desired concentration of the required element [1]. With correctly selected modes of pulsed heat exposure of a solid body it is possible to achieve concentrations of an element introduced from the surface that would exceed the maximum achievable in thermodynamically equilibrium conditions [2] (Fig. 1).

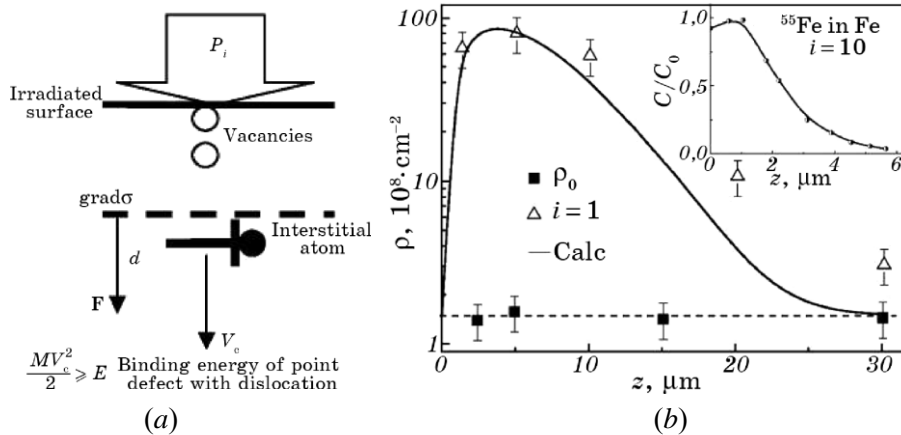


Fig. 1 – Effect of thermal stresses on the formation of structural defects, their interaction and penetration into the depth (a) with the formation of concentration at depth (b)

Results and discussion. At the same time, the effect of solid-phase penetration of the alloying element into the solid body during laser processing can have a negative effect in the process of laser scribing when trimming thin-film resistors. For the reasons described above, with this treatment, part of the resistive layer will be removed by laser ablation, and some will be introduced into the dielectric or semiconductor substrate (Fig. 2).

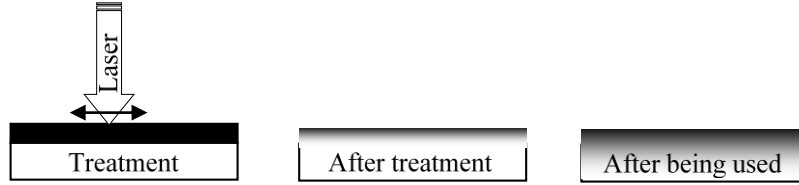


Fig. 2 – Probable scheme of resistor parameters degradation after ablative laser trimming

As such a resistor is used, the Joule heat generated by the flowing current will promote the diffusion processes and as a result the parameters of such an element may deviate from the original. A similar problem can arise when fabricating film inductances. In this case the surface diffusion should also be taken into account. Accounting for thermally activated processes is also important with respect to other, not only passive, electronic elements of hybrid circuits with a high degree of integration.

It is also important to take into account the possible influence of risk factors when studying physical properties of thin-film materials with the help of various pulsed-beam techniques. For example, a method of ultrafast demagnetization utilizing femtosecond laser pulses is used to study the magnetization dynamics in multilayer magnetic thin-film structures. Such technique is a much cheaper and compact alternative to a method of X-ray Ferromagnetic Resonance (XFMR), which requires a synchrotron radiation to study the magnetization dynamics [3]. In this case it is important to consider the possibility of a highly non-equilibrium state in the irradiated material caused by exposure to ultra-short laser pulses [2,4]. It may also be necessary to take into account the occurrence of thermally activated processes in a number of techniques which use femtosecond pulses of synchrotron radiation (Time-Resolved X-ray Diffraction, Extended X-ray Absorption Fine Structure, X-Ray Absorption Near Edge structure). According to estimates, using criteria for the duration of an irradiation pulse [4], non-equilibrium state in metal film can occur already at low energy densities.

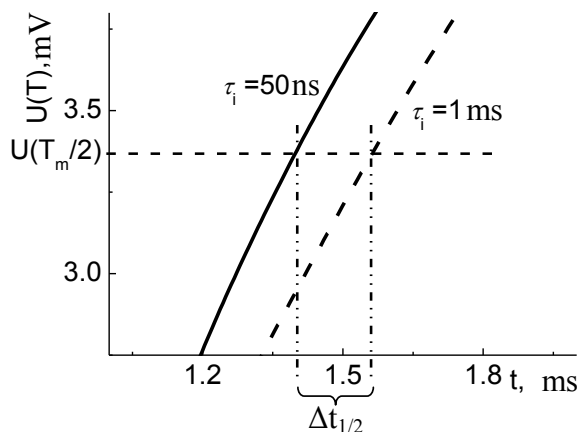


Fig. 3 – Dependence of the temperature propagation velocity on the dynamics of structural changes: *a* is the relaxation period of the non-stationary exposure mode ($\tau_i \sim 5 \cdot 10^{-8}$ s), *b* is the quasi-stationary exposure mode ($\tau_i \sim 10^{-3}$ s)

Another factor that should be considered when using thermal pulses to excite the non-equilibrium state in solid-state elements is a possible change of heat transfer parameters. Previously published results of thermophysical studies [4] have shown that the speed of temperature front (dT/dt) propagation depends on the dynamics of structural change in the substance residing in a highly non-equilibrium state. This was discovered experimentally when sequentially irradiating with pulsed laser a flat iron sample in two modes: quasi-stationary and highly non-stationary [4] (Fig. 3). Such regimes have ensured the passage of thermal front through the sample residing in the quasi-equilibrium

state, and then in a highly non-equilibrium state. In the first case, the thermal front passed through the crystal lattice with the initial number of structural defects, in particular, dislocations ($\rho \sim 10^8 \text{ cm}^{-2}$). According to [5], these defects have significant thermal resistance to the propagation of temperature front. In the second case additional dislocations (up to $\rho \sim 10^{10} \text{ cm}^{-2}$) were generated and together with the point defects and part of existing dislocations were moving in an iron lattice under the action of thermal stresses σ . This dislocation movement was provided by the Pich-Koehler force as a result of the interaction of boundary dislocations with the thermal-stresses σ (fig. 1a), which was moving in the same direction with the temperature front.

The explanation of this effect in [4] was associated not with the phonon-phonon interaction, but with the scattering of heat-transporting particles on moving defects in the crystalline structure of a solid. Such consideration of heat transfer under non-equilibrium conditions becomes possible if a ballistic component is added to the classical Fourier equation that takes into account the motion of scattering centers

$$Q = -\left(\frac{\partial T}{\partial x} + \tau \frac{\partial q}{\partial t}\right), \quad (1)$$

where τ is the inertia time, which for a given case of pulsed temperature action was associated with the scattering of heat carriers on moving edge dislocations. This equation is valid when the mean free path λ is equivalent to the distance between collisions of the particle carrying the temperature.

The greatest scattering of the temperature transporting particles occurs in a solid on dislocations. In this case, according to [5], the thermal resistance is carried out by a dislocation line. Thus, with a dislocation density ρ , the desired mean free path can be defined as $\lambda \sim (\rho)^{-1/2}$, and the time $\tau \sim \lambda / v$. The velocity v is determined by the speed of the thermal front movement, which is limited by the thermal diffusivity α of the substance, and therefore it can be written that $v \sim \sqrt{\alpha/t_r}$, where t_r is the relaxation time. As a result

$$\tau = \sqrt{\frac{t_r}{a\rho}}. \quad (2)$$

The time t_r can be defined as the lifetime of a heat source [2], the energy of which is sufficient to generate dislocations in a solid. The lifetime of a heat source with a short ($t_i \leq t_r$) laser pulse action was determined in [10] from the relation

$$t_r \cong \frac{B^2}{4T(0,t)^2} \left[t_i + \frac{T(0,t)^2}{B^2} \right]^2, \quad B = 2q\sqrt{\frac{a}{k}} \quad (3)$$

Estimating this time for $\tau_i = 5 \cdot 10^{-8}$ s according to the above formula, we obtain $t_r = 1.5 \cdot 10^{-5}$ s. Then, taking into account, the thickness of the layer in which the plastic flow of the material (Fe) occurs $h = \sqrt{at_r}$, will be $h \approx 18 \text{ }\mu\text{m}$. This value (as seen from Fig. 1b) fully includes the area in which mass transfer occurs, and corresponds well to the data of electron microscope studies, which indicate the presence of the increased dislocation density at these depths [2].

Dislocations are known to begin to form at shear stresses $\sigma > G/30$. If shear stresses arise due to thermal deformations then σ is defined as

$$\sigma = E\alpha\Delta T \frac{1+\nu}{1-\nu}, \quad (4)$$

where E - Young's modulus, ν - Poisson's ratio, α - linear expansion coefficient, ΔT - temperature difference.

Using this relationship (4), it is possible to determine the temperature range ΔT in which under the action of thermal stresses starts the movement of dislocations present in the crystal, as well as the generation of new ones. In the first case, it is sufficient to compare these stresses with the Peierls barrier $\sigma = (10^{-4} \div 10^{-2}) \cdot E$, determined by the Young's modulus of the material, and in the second, with the stresses at which dislocations generated by the shear modulus are generated.

Estimates show that the minimum temperature difference ΔT at which thermal stresses overcome the Peierls barrier is $\Delta T = 3.4 \div 340$ °C. Thus, dislocations in iron are mobile practically starting from room temperatures. But thermal stresses, leading to the generation of new dislocations, start with temperatures $\Delta T \sim 0.3T_m$ (only from 460 °C for the same material).

So, having determined the value of t_r from (3) and knowing from the experiment [3] the value $\Delta\tau = \Delta t_{1/2}$ (Fig. 3) it is possible using (2) to calculate the number of dislocations moving in the same direction with the heat flux that actively interact with heat carriers, as follows:

$$\Delta\rho = \frac{t_r}{a\Delta\tau} \approx 3 \cdot 10^3 \text{ cm}^{-2}$$

Thus, when estimating the time of thermal inertia τ (2) as the time of dispersion of the heat flux on dislocations it is important to consider these two factors: a) density of dislocations, which is determined by the above-mentioned threshold values; b) location of the dislocations line relative to the direction of heat flux propagation [5]. It is quite natural that the scattering of heat flux on the scattering centers moving in the same direction, the main of which are considered to be dislocations, will decrease. As shown, these values depend on the respective temperature ranges and material properties.

Conclusions. It is shown that when fabricating solid-state elements of the electronic equipment using methods of thermal pulse action, including commonly used laser methods, it is important to take into account the possible impact of a number of transport processes. Under the conditions of non-stationary irradiation with specific parameters a strongly non-equilibrium state may occur in a solid. It is characterized by the generation of structural defects and their directional movement from the irradiated surface deep into the material in the field of emerging thermal stresses. Such effect may be accompanied by an accelerated heat and mass transfer. This should be taken into account as a positive phenomenon for a local solid-state doping as well as a negative factor in tuning of the electronic equipment components, their long-term operation, as well as in a number of physical property studies.

References

1. Pogorelov A.E., Ryaboshapka K.P., Zhuravlev A.F. Mass transfer mechanism in real crystals by pulsed laser irradiation. // *Journal of Applied Physics*. – 2002. – V. 92. – P. 5766-5771.
2. Pogorelov O. E. Transport processes in solids under nonequilibrium conditions of excitation by a thermal pulse / Thesis for the scientific degree of Doctor of Physical and Mathematical Sciences in speciality 01.04.07 – solid state physics. — G. V. Kurdyumov Institute for Metal Physics of N.A.S. of Ukraine, Kyiv. – 2017. – P.330.
3. Y. Pogoryelov, M. Pereiro, S. Jana, A. Kumar, S. Akansel, M. Ranjbar, D. Thonig, O. Eriksson, D. Primetzhofer, P. Svedlindh, J. Akerman, O. Karis, and D.A. Arena, Non-Reciprocal Spin Pumping in Asymmetric Magnetic Trilayers, arXiv e-prints, arXiv:1812.09978, 2018.
4. Pogorelov A.E. Transport phenomena in a crystal induced by the energy pulse. *Metallofizika i noveishie tekhnologii*. – 2014. – V. 36. – N 3. – P. 383-389.
5. Oskotskii V.S., Smirnov I.A.. Defects in crystals and thermal conductivity / Leningrad: "Science", 1972. – P.160, (in Russian: В.С. Оскотский, И.А. Смирнов. Дефекты в кристаллах и теплопроводность / – Ленинград: Наука, 1972. – 160 с.)

PHOTOLUMINESCENCE OF THE MATRIX NANOCOMPOSITES OPAL – ACTIVE DIELECTRIC FILLED WITH EUROPIUM

O.V. Ohiienko¹, V.N. Moiseienko¹, D.O. Golochalov¹ and Bilal Abu Sal²

¹Oles Honchar Dnipro National University, Dnipro, pr. Haharina, 72, 49010, Ukraine

²Tafila Technical University, Tafila, P O Box 179, 66110, Jordan

E-mail: kombi21251@outlook.com

The work is devoted to the study of the effect of the nanocrystalline environment and photonic crystal effects on the photoluminescence spectra of the matrix nanocomposites opal-Bi₁₂SiO₂₀, opal-Bi₂TeO₅, opal-NaBi(MoO₄)₂ and opal-TeO₂ filled with europium (III) acetate hydrate C₆H₉EuO₆×H₂O). An increase in the integrated luminescence intensity of the matrix nanocomposite opal-Bi₁₂SiO₂₀:Eu³⁺ compared with other nanocomposites has been established. The luminescence of bismuth ions in the composition of the crystalline phases Bi₁₂SiO₂₀ and Bi₄Si₃O₁₂ was studied. The possibility of the participation of Bi³⁺ ions as a co-activator of luminescence in bismuth-containing nanocomposites is discussed.

The fabrication and research of optical properties of new luminescent materials on the basis of synthetic opals is of both fundamental and practical interest. In [1, 2] it is shown that europium (Eu³⁺) are promising material for filling opal pores. Of particular interest from the scientific and practical points of view are nanocomposites opal-active dielectric activated by fluorescent centres.

Bulk synthetic opals were grown by slow crystallization of monodisperse colloidal suspension of globules α -SiO₂ synthesized by modified Stober method [3]. Synthetic opals were obtained by the method of natural sedimentation under isothermal conditions at T=20°C. After the end of sedimentation, the evaporation of residual water was carried out by heating the bottom of cylindrical vessels to 50°C. For samples of the initial opals used in the work the values of the diameter of the globules and the interplanar distance were D=300nm and d=245nm. The spectral position of the center of the photon stop-band for the samples of the initial opals was 602nm. The filling of the pores of opal with active dielectrics was carried out using the melt method. Nanocomposites opal - Bi₁₂SiO₂₀, opal - Bi₂TeO₅, opal - NaBi(MoO₄)₂ and opal - TeO₂ were manufactured. The fact of filling the opal pores with melting were detected by shift of the Bragg reflection band maximum in the longwave region. Next, samples of nanocomposites were impregnated in an aqueous solution of the salt C₆H₉EuO₆×H₂O (99.9%), followed by drying at 23°C. Excitation of photoluminescence spectra was carried out in the geometry of "reflection" from the plane (111) of the sample by radiation of a semiconductor laser with λ_{ex} =405nm. The spectra were recorded in [111] ($\theta = 0^\circ$) direction and for $\theta = 30^\circ$ and 60° angles with [111] axis by a modified laser spectrometer based on the DFS-12 double monochromator. For comparison, the photoluminescence spectra of the salt solution and the essential opal infiltrated with C₆H₉EuO₆×H₂O were measured. Figure 1 shows the measured photoluminescence spectra Eu³⁺ ions in an aqueous solution of the salt C₆H₉EuO₆×H₂O, in the pores of opal and various nanocomposites. All the luminescence spectra of europium ions in the opal and nanocomposites pores are shifted to the long-wavelength region compared with the luminescence spectrum of an aqueous solution of salt. The reason for this may be a change in the structure of the coordination environment of europium ions in the nanopores of the opal matrix. Among the bismuth containing nanocomposites, the highest luminescence intensity was observed in the opal-Bi₁₂SiO₂₀:Eu³⁺ sample.

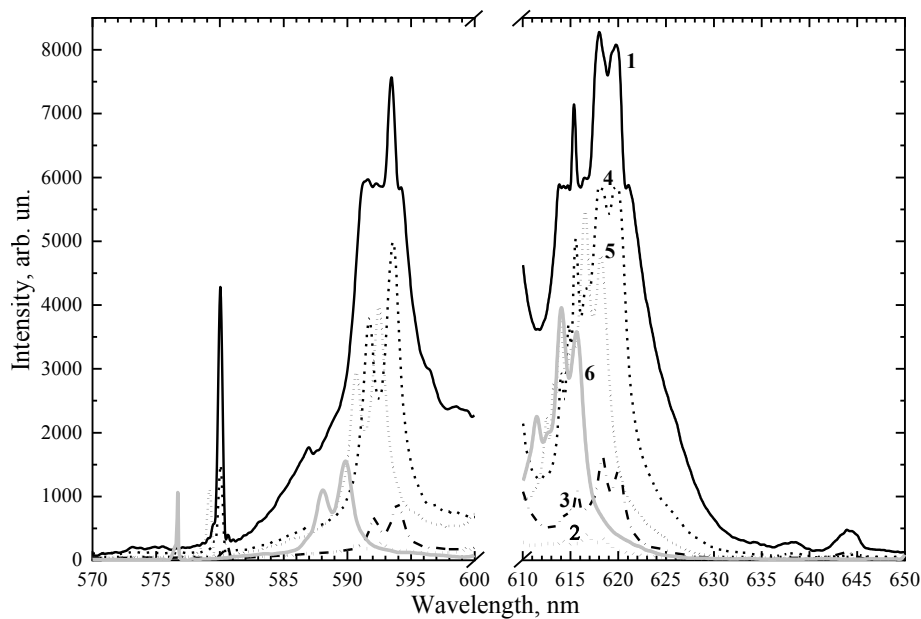


Fig. 1 – Photoluminescence spectra of the matrix nanocomposites opal – active dielectric infiltrated with salt europium (III) acetate hydrate: 1 – opal- $\text{Bi}_{12}\text{SiO}_{20}:\text{Eu}^{3+}$; 2 - opal- $\text{Bi}_2\text{TeO}_5:\text{Eu}^{3+}$; 3 – opal- $\text{NaBi}(\text{MoO}_4)_2:\text{Eu}^{3+}$; 4 – opal- $\text{TeO}_2:\text{Eu}^{3+}$; 5 – opal: Eu^{3+} ; 6 - aqueous solution of salt

For the opal- $\text{Bi}_{12}\text{SiO}_{20}$ matrix nanocomposite, it was found that the substance in the opal pores is in the crystalline state. This is confirmed by both, the characteristic form of the measured Raman spectra and X-ray diffractogram (figure 2). In addition, according to the Raman spectra and X-ray diffraction analysis in addition to $\text{Bi}_{12}\text{SiO}_{20}$, the phase of bismuth orthosilicate ($\text{Bi}_4\text{Si}_3\text{O}_{12}$) was revealed in the opal pores. Comparison of our results with literature data [2] allowed to establish a dominant presence in the pores of opals nanocrystals of bismuth orthosilicate $\text{Bi}_4\text{Si}_3\text{O}_{12}$, which is formed in the pores of the opal due to the interaction of the BSO melt with the SiO_2 globules.

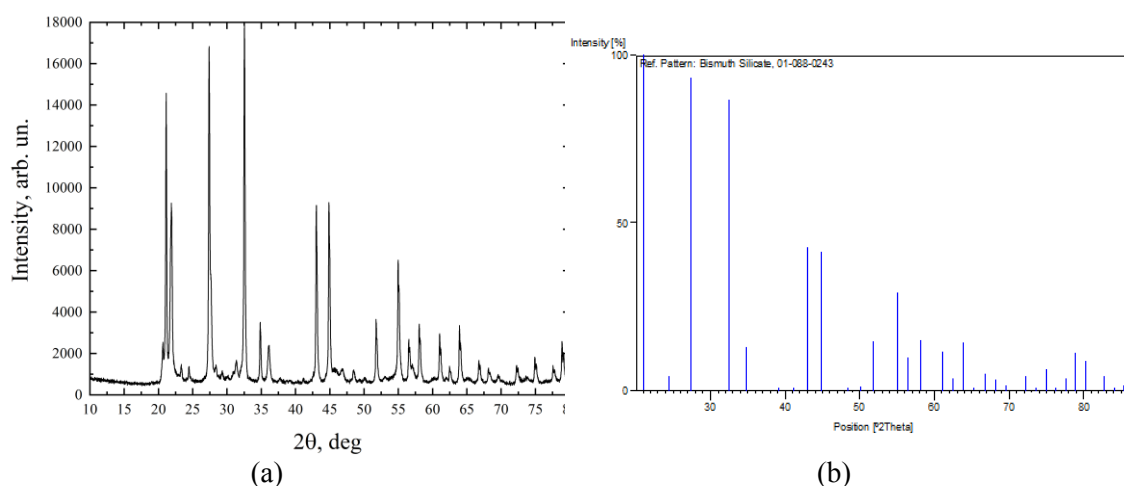


Fig. 2 – The X-ray diffractogram (CuK α -radiation) of the opal- $\text{Bi}_{12}\text{SiO}_{20}$ sample (a) and XRD Stick Pattern of the $\text{Bi}_4\text{Si}_3\text{O}_{12}$ [Crystal structure database ICSD] (b). Most intense peaks correspond to the crystal phase $\text{Bi}_4\text{Si}_3\text{O}_{12}$.

In the measured spectra, radiative transitions in the energy spectrum of europium ions ${}^5D_0 \rightarrow {}^7F_0$, ${}^5D_0 \rightarrow {}^7F_1$, and ${}^5D_0 \rightarrow {}^7F_2$ were observed for wavelengths of 580 nm, 592 nm and 619 nm, respectively. The following regularities were established: a) the red shift of the photoluminescence spectrum of Eu^{3+} ions in the opal and nanocomposites opal- $\text{Bi}_{12}\text{SiO}_{20}:\text{Eu}^{3+}$ and opal- $\text{TeO}_2:\text{Eu}^{3+}$ by 3 nm compared to the luminescence spectrum of the salt solution; b) the increase of the integrated intensity of luminescence of europium ions in the pores of the nanocomposite opal- $\text{Bi}_{12}\text{SiO}_{20}:\text{Eu}^{3+}$; c) the dependence of the intensity of the glow from the direction of observation for nanocomposite opal- $\text{Bi}_{12}\text{SiO}_{20}:\text{Eu}^{3+}$. The strongest angular dependence was demonstrated by the forbidden electro-dipole transition with $\lambda_{\text{max}}=580\text{nm}$ (figure 3).

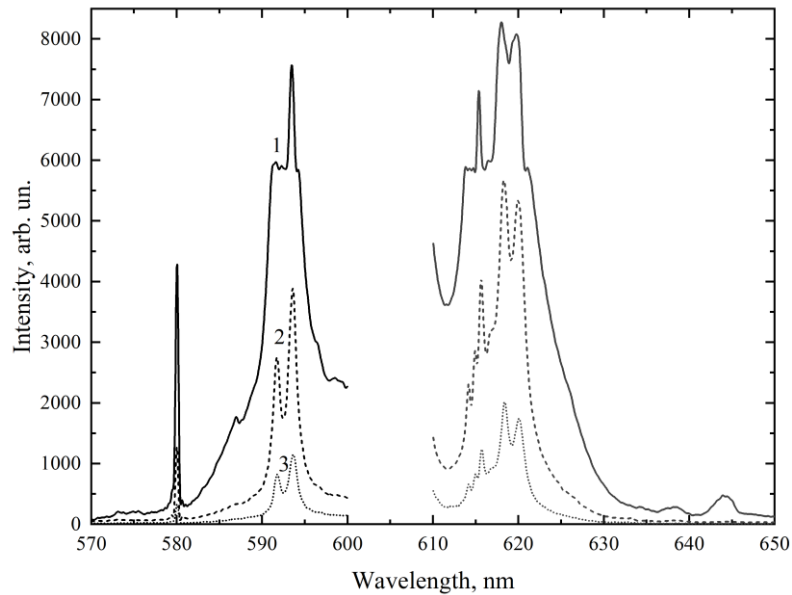


Fig. 3 – The dependence of the photoluminescence spectra of the nanocomposite opal–($\text{Bi}_{12}\text{SiO}_{20}$, $\text{Bi}_4\text{Si}_3\text{O}_{12}$), infiltrating by salt $\text{C}_6\text{H}_9\text{EuO}_6 \times \text{H}_2\text{O}$ from the direction of observation: 1 – $\theta = 0$, 2 – $\theta = 30^\circ$, 3 – $\theta = 60^\circ$

In order to clarify the mechanism for increasing the integral intensity of europium ions emission in the pores of the nanocomposite opal- $\text{Bi}_{12}\text{SiO}_{20}:\text{Eu}^{3+}$, we measured the photoluminescence spectra of the $\text{Bi}_{12}\text{SiO}_{20}$ crystal and the control sample $\text{Bi}_4\text{Si}_3\text{O}_{12}$. A control sample of the crystalline phase $\text{Bi}_4\text{Si}_3\text{O}_{12}$ was obtained by melting polycrystalline $\text{Bi}_{12}\text{SiO}_{20}$ powder at a temperature of 996°C , followed by recrystallization under the same temperature conditions in which the $\text{Bi}_{12}\text{SiO}_{20}$ melt was filled into the opal pores. Figure 4 (a) shows the photoluminescence spectra of the $\text{Bi}_{12}\text{SiO}_{20}$ crystal and the control sample $\text{Bi}_4\text{Si}_3\text{O}_{12}$, and figure 4 (b) shows the photoluminescence spectrum of $\text{Bi}_{12}\text{SiO}_{20}$ and $\text{Bi}_4\text{Si}_3\text{O}_{12}$ in opal pores. As can be seen from figure 4, a photoluminescence spectrum of $\text{Bi}_4\text{Si}_3\text{O}_{12}$ is shifted towards short wavelengths and has a markedly lower intensity. The photoluminescence spectrum of the nanocomposite opal-($\text{Bi}_{12}\text{SiO}_{20}$, $\text{Bi}_4\text{Si}_3\text{O}_{12}$), is the total contribution to the luminescence from $\text{Bi}_{12}\text{SiO}_{20}$ and $\text{Bi}_4\text{Si}_3\text{O}_{12}$. At the same time, the position and intensity ratio of the spectral components in the spectrum of the composite opal-($\text{Bi}_{12}\text{SiO}_{20}$, $\text{Bi}_4\text{Si}_3\text{O}_{12}$) differs from the photoluminescence spectra of the original $\text{Bi}_{12}\text{SiO}_{20}$ and $\text{Bi}_4\text{Si}_3\text{O}_{12}$ crystals (Figure 4 (b)). The observed spectra can be attributed to the luminescence of Bi^{3+} ions, which occupy an isolated position in the structure of crystals [4].

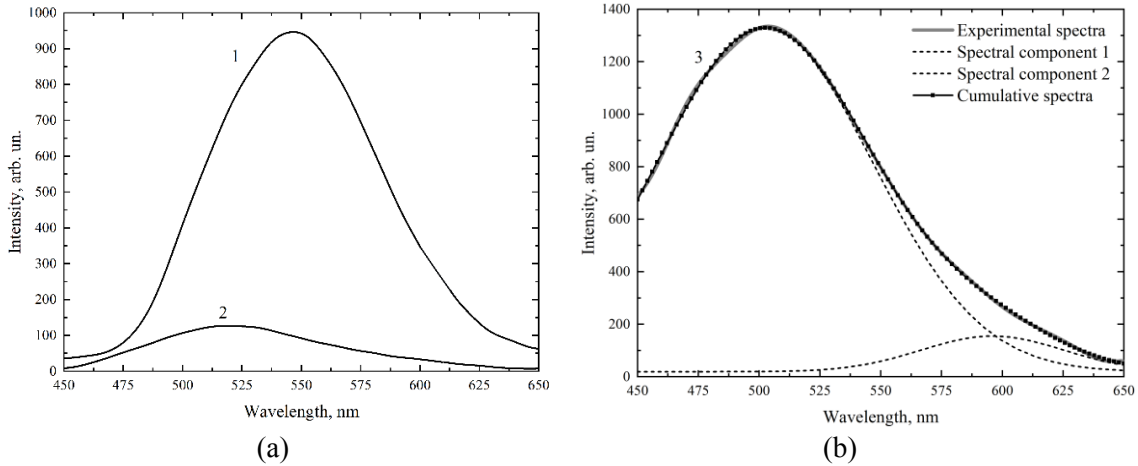


Fig. 4 – Photoluminescence spectra of a $\text{Bi}_{12}\text{SiO}_{20}$ crystal (1) and a control sample of $\text{Bi}_4\text{Si}_3\text{O}_{12}$ (2) (a) and photoluminescence spectra of the nanocomposite opal-($\text{Bi}_{12}\text{SiO}_{20}$, $\text{Bi}_4\text{Si}_3\text{O}_{12}$) with the results of decomposition into spectral components (b). All spectra are given to the same amount of substances

The results of measurements of the absorption and luminescence spectra of Eu^{3+} ions in glasses [5] demonstrate absorption at the ${}^7\text{F}_0 \rightarrow {}^5\text{D}_1$ (520-545 nm) and ${}^7\text{F}_0 \rightarrow {}^5\text{D}_0$ (580 nm) transitions. In this case, both photoluminescence spectra of $\text{Bi}_{12}\text{SiO}_{20}$ and $\text{Bi}_4\text{Si}_3\text{O}_{12}$ in the pores of opal overlap the absorption region of europium ions. Thus, it can be assumed that the increase in the integral intensity of emission of europium ions in the pores of the nanocomposite opal-($\text{Bi}_{12}\text{SiO}_{20}$, $\text{Bi}_4\text{Si}_3\text{O}_{12}$) (figure 1) is due to the participation in the optical processes of Bi^{3+} ions as a co-activator of luminescence of Eu^{3+} ions.

The main results of the work are as follows. The method for introducing the active dielectric melt into the pores of bulk synthetic opals was developed. It provides filling of pores up to 50 vol. % on average over the sample volume per cycle. It was established that as a result of crystallization of the melt, nanocrystals of active dielectric are formed in the pores of the opal. It has been established that the observed increase in the integrated luminescence intensity of the nanocomposite opal- $\text{Bi}_{12}\text{SiO}_{20}$ compared with other nanocomposites is due to the additional energy transfer to Eu^{3+} ions from Bi^{3+} ions, which are a co-activator of emission. This is confirmed by direct measurements of the photoluminescence spectra of nanocomposites opal-active dielectric. The absorption spectrum of the nanocrystalline dielectric phase in opal pores has an additional effect on the intensity of the luminescence spectra of nanocomposites.

[1] Li M, Zhang P, Li J, Zhou J, Sinitskii A, Abramova C, Klimonsky S O and Tretyakov Y D 2007 Directional emission from rare earth ions in inverse photonic crystals *Applied Physics V. B* 89 pp 251-255

[2] Zhang Y, Xu J, Cui U and Yang B 2017 Eu^{3+} -doped $\text{Bi}_4\text{Si}_3\text{O}_{12}$ red phosphor for solid state lighting: microwave synthesis, characterization, photoluminescence properties and thermal quenching mechanisms *SCIENTIFIC REPORTS* [7:42464/]

[3] St berW, Fink A, Bohn A 1968 Controlled growth of monodisperse silica spheres in the micron size range *J. Colloid Interface Sci.*, vol 26 pp 62-69

[4] Wan Z and Zhang G 2014 Controlled synthesis and visible light photocatalytic activity of $\text{Bi}_{12}\text{GeO}_{20}$ uniform microcrystals *SCIENTIFIC REPORTS* [4:6298/]

[5] Padlyak B V, Kindrat I I, Protsiuk V O and Drzewiecki A 2014 Optical spectroscopy of $\text{Li}_2\text{B}_4\text{O}_7$, CaB_4O_7 and LiCaBO_3 borate glasses doped with europium *Ukr. J. Phys. Opt.* vol 15 issue 3 pp 103-117

USAGE OF THE NONLINEAR METROLOGY INSTRUMENTS FOR RESEARCH THE LASER COOLING PROCESS

Kurskoy Yu. S.

Kharkov National University of Radioelectronics, Kharkov
61166, Ukraine, Kharkov, av. Nauki. 14, 057-702 14 84, E-mail: yurii.kurskyi@nure.ua

In the article the task of laser Doppler cooling of particles (atoms, ions and molecules), which has important applications for physics and metrology, is considered. It is shown that the laser cooling is the interaction process between a deterministic system of laser radiation and a chaotic system of moving particles. For monitoring and estimation of the cooling particles' parameters it's proposed to use the methods and instruments of Nonlinear Metrology that were designed for measurement of nonlinear dynamic systems parameters. The formula for estimating of the laser radiation Shannon entropy, as a function of a laser frequency, is obtained. The results allow to evaluate the change of the entropy of the cooling particles system after a given number of cycles "absorption – spontaneous emission of photons", which opens the new possibility for control of laser cooling process and estimate of temperature with small discrete values.

Keywords: Laser Cooling, Nonlinear Metrology, Shannon Entropy.

Introduction

One of the outstanding tasks in physics of the last quarter of the XX century was the task of cooling of gaseous substances to absolute zero temperature by braking the Brownian motion of particles (atoms, ions, molecules) using a laser radiation. The successful implementation of the cooling and retention of particles is important for physics, metrology and electronics, The particles, cooled to stop the thermal motion, can be observed more longer than moving particles, that is important for the high-resolution spectroscopy and the stabilization of laser frequency. When the temperature of particles' ensemble becomes close to 0°K it's possible to obtain the superfluidity status and the Bose-Einstein condensate, which can be used to create the quantum memory. The development of the cooling technology and retain of the cooled particles opens the new opportunities for metrological science to improve standard base, allows to obtain new reference points of frequency standards and improves the accuracy of global navigation systems. The perspective metrological tasks include the creating of optical clocks based on cooled single ions in electromagnetic traps and atoms trapped in the optical grid. It is assumed that the relative uncertainty of such clock frequency reaches values in 10^{-17} – 10^{-18} [1].

The laser cooling process bases on quantum-mechanical ideas about the absorption and radiation of energy by particles. Localized moving particles are irradiated by laser radiation with a frequency that is lower than a frequency of the atomic transition by the Doppler shift quantity. The particle absorbs a photon, is transferred from the primary energy state to an excited energy state. The particle's speed changes by the quantity of the recoil velocity. Then a particle, returning to the ground state, emits a photon with a frequency greater than the frequency of the absorbed photon. This process causes the loss of energy, slowdown the particles and, consequently, the decrease of substance's temperature. Thus, an impulse of a photon is passed to a particle when stimulated absorption and subsequent spontaneous emission of a photon.

For the next "excitation — spontaneous emission of photon" cycle the laser radiation frequency is reduced, adjusts to the particles' velocity. For N cycles, the one particle loses the impulse equal $\Delta p = N\hbar k$, here $\hbar k$ – the impulse of a photon. The number of cycles and the frequency of the cooling radiation are determined by the electronic configuration and velocity of particles [2]. This is the first stage of the laser cooling — the "Doppler laser cooling". It allows reach the temperature at the hundreds of μ K. For example, after Doppler cooling of the atoms of alkali metals their temperature is about 100 μ K. For more low temperatures other mechanisms of laser cooling are used: the subdoppler and cooling below the recoil level mechanisms. The

minimum temperature at subdoppler colling atoms is about 1 μK . Laser cooling below the one-photon level of recoil allows to obtain a temperature about 100 nK [3].

The practical realization of laser cooling and retaining of cooled particles requires a development of special methods for assessing and monitoring of particles' condition. The group of cooled particles may be represented in the form of an open nonlinear dynamic system with energy dissipation (NDS). Understanding of a specific character of such systems has led to create the methods and instruments of Nonlinear Metrology [4]. The universality of approaches, models and measurement instruments of variables of Nonlinear Metrology allows use them for measurement in various NDS physical and biological origin.

As an important instrument of Nonlinear Metrology theory the information Shannon entropy is accepted. It's used like a degree of order or chaotic condition of a system. In the framework of Nonlinear Metrology theory proposed the entropy scales for assessment and management of NDS's parameters [4]. The application of this instrument for estimation of cooled particles parameters will improve the reliability of the received information and to ensure control and management of desired parameters.

The task of this work is a usage of the nonlinear metrology instruments for research the laser cooling process.

Research Results

Let consider the Doppler laser cooling process as the interaction of two corresponded systems. The first system is an ensemble of N localized particles of the same substance — the "atom" system. The "atom" system is characterized by the mean velocity of particles and by the temperature T , which related by next expression:

$$T = \frac{\pi m}{8R} \langle v \rangle^2, \quad (1)$$

here: m — the molecular mass of the particles; R — the universal gas constant.

If the "atom" system is in equilibrium, the velocity distribution of particle $p(v)$ is expressed by the Maxwell distribution law:

$$p(v) = \frac{4}{\sqrt{\pi}} \left(\frac{m}{2kT} \right)^{\frac{3}{2}} \exp \left[-\frac{mv^2}{2kT} \right] v^2. \quad (2)$$

here: k — the Boltzmann constant.

The Brownian motion of "atom" system's particles, absorption and emission of photons during the cooling process let describe such system like an open, chaotic and dissipative NDS.

The second system is a laser radiation that characterized by a radiation frequency f_0 and the radiation line broadening Δf_0 — the "laser" system. In this case, the frequency distribution of intensity obeys the normal law or the Gaussian distribution [10]:

$$p(f) = \frac{1}{\Delta f_0 \sqrt{2\pi}} \exp \left[-\frac{(f - f_0)^2}{2\Delta f_0^2} \right]. \quad (3)$$

The frequency stabilized laser radiation is characterized by a high degree of coherence $\Delta f_0 / f_0 \ll 1$ (in scientific laboratories values $\Delta f_0 / f_0$ obtained at special units reach $\sim 10^{-15}$ - 10^{-17}). So the "laser" system can be described like a deterministic system. Its parameters stay in the certain frameworks during the time of observation. The laser operates in a pulsed mode, the pulse duration is determined by the interaction of laser radiation with particles.

Let consider the interaction of two systems from the position of the Information theory of measurement. For control of the systems conditions let use the information Shannon entropy that associated with the probability density $p(X)$, here X – the researched variable, by next expression $H = -p(X)\ln p(X)$ [4]. As it was said before it's often used like a degree of order or chaotic condition of NDS. The minimal value the Shannon entropy takes in the case of the normal Gaussian distribution, the maximum value — in the case of the uniform distribution. The entropy of a laser radiation is small, in a case of monochromatic radiation it equates zero. The entropy of an ensemble of particles is determined by the Maxwell distribution. Its value is intermediate between the entropy values for the normal and uniform distributions.

At the initial moment of time the "atom" system is characterized by the average velocity of the particles v_0 , temperature T_0 , and entropy $H_A(v_0, t_0)$. The "laser" system is characterized by the frequency of radiation $f_0 \pm \Delta f_0$, and entropy $H_L(f_0, t_0)$. After stop of interaction at the moment of time $t = \tau$ the systems' parameters are changed. The velocity of the particles decreases, the frequency of the spontaneous emission f increases in comparison with frequency f_0 , the spectral line of radiation Δf broadens. The "atom" system takes the next characteristics: v , T and $H_A(v, t)$; the "laser" system takes the next characteristics: $f \pm \Delta f$ and $H_L(f, \tau)$. This interaction continues for the number of cycles required to reach a given temperature of the material. For the "atom" system and the "laser" system the formulas for the Shannon entropy at the moments of time t_0 and τ have the next form:

$$H_A(v, t_0) = -p(v_0)\ln p(v_0), \quad H_L(f, t_0) = -p(f_0)\ln p(f_0), \quad (4)$$

$$H_A(v, \tau) = -p(v)\ln p(v), \quad H_L(f, \tau) = -p(f)\ln p(f). \quad (5)$$

Here: $H_A(v, \tau) < H_A(v, t_0)$ and the "atom" system becomes more orderly; $H_L(f, \tau) > H_L(f, t_0)$ the "laser" system becomes more chaotic. This situation is caused by the dependence of the Shannon entropy from the distribution density functions and the interval of values. Thus, when particles emit the photons with the frequency higher than the frequency of absorbed photons the particles velocity decreases, the peak of the Maxwell distribution function (2) increases and displaces to the direction of the small velocities. The entropy of the "atom" system reduces. The peak of the distribution function for laser intensity shifts toward the higher frequencies and corresponds to the resonant transition frequency for a given type of particles. Thus the value of Δf_0 increases in the due to the Doppler broadening, the value of line radiation broadening increases too.

The changing of systems conditions can be expressed using an information, which is acquired (information about the "atom" system I_A) or is lost (information about the "laser" system I_L) in the process of systems interaction [4]:

$$I_A = H_A(v, t_0) - H_A(v, \tau) = \Delta H_A, \quad I_L = H_L(f, t_0) - H_L(f, \tau) = \Delta H_L. \quad (6)$$

Using the information conservation law according to which "the amount of information in a closed system remains constant" from the (6) we obtain the equality:

$$|\Delta H_A| = |\Delta H_L|. \quad (7)$$

According to expression (7) the change of the "laser" system entropy by the module equals to the entropy change of the "atom" system. This equality allows analyzing the "laser" system settings change to estimate the parameters of the "atom" system.

The "atom" system entropy takes the minimum value $H_A(v)=0$ in the case when a thermal motion of the particles stops. The expression (7) at any moment of time can be represented in the next form:

$$|\Delta H_A(\Delta T)| = |\Delta H_L(\Delta f)| \quad (8)$$

The expression (8) solution taking into account expressions (2), (3), (6) allow to determine the connection between the entropy change of the "laser" system, the entropy and temperature of the "atom" system:

$$\Delta T = \Delta T [|\Delta H_L(\Delta f)|] \quad (9)$$

The expressions (3)–(9) allow to determine the entropy and temperature change of the "atom" system at the moments t_0 and τ the expression for the difference of entropy (6) ΔH_L :

$$H_L(f, t_0) = \ln(\Delta f_0 \sqrt{2\pi e}), \quad H_L(f, \tau) = \ln(\Delta f \sqrt{2\pi e}), \quad |\Delta H_L(\Delta f)| = \left| \ln \frac{\Delta f_0}{\Delta f} \right|. \quad (10)$$

Thus, the value of the "laser" system entropy depends of Δf changing (the value of the line radiation broadening). Measuring the frequency of spontaneous radiation and evaluating the entropy change (10) it's a possible to estimate the changes of entropy and temperature of the cooling particles system after any number of cycles "absorption – spontaneous emission of photons". It opens the new possibility for control of the cooling process and temperature estimates with small discrete value ΔT .

Conclusions

The task of laser Doppler cooling of particles (atoms, ions and molecules), which has important applications for physics and metrology, is considered. It is shown that the laser cooling is the interaction process between a deterministic system of laser radiation and a chaotic system of moving particles.

For monitoring and estimation of the cooling particles' parameters it's proposed to use the methods and instruments of Nonlinear Metrology that were designed for measurement of nonlinear dynamic systems parameters.

The formula for estimating of the laser radiation Shannon entropy, as a function of a laser frequency, is obtained. The results allow to evaluate the change of the entropy of the cooling particles system after a given number of cycles "absorption – spontaneous emission of photons", which opens the new possibility for control of laser cooling process and estimate of temperature with small discrete values.

References

1. Brazhnikov, D.V. Research of possibility of deep laser cooling of magnesium atoms for creating of new generation frequency standard. // Bulletin of NSU, Series "Physics", 2012, Vol. 7, Iss. 14, p.p. 6–18.
2. Letokhov V.S., Minogin V.G., Pavlik, B.D. Cooling and trapping of atoms and molecules by resonance laser field. // JETP. — 1977. — Vol. 72. — pp. 1328–1342.
3. Balykin A, Atom optics and its applications // Bulletin of the Russian Academy of Sciences. — 2011. — Vol. 81, No. 4. — pp. 291–315
4. Machekhin Yu.P., Kurskoy Y.S. Fundamentals of nonlinear metrology. // LAP Lambert Academic Publishing. — 2014. — 240 p.

RESEARCHING OF SPIN-EFFECTS IN SEMICONDUCTORS WITHOUT AN INVERSION CENTER FOR PHOTOELECTRIC ENERGY CONVERSION

N.N. Chernyshov, A.V. Belousov*, I.A. Chernyshova, M.A.F. Alkhaldeh

Kharkiv National University of Radio Electronics;

61166, Kharkiv National University of Radio Electronics

tel. +7(910)7375198; +38(093)0436635

E-mail: mykola.chernyshov@nure.ua

The Federal State Budget Educational Institution of Higher Education

“Belgorod State Technological University named after V.G. Shukhov”;

46, Kostyukova street, Belgorod, 308012, Russian Federation

E-mail: ntk@intbel.ru

ABSTRACT

The scientific article is devoted to a theoretical study of the tunneling of electrons through semiconductor barriers. It is shown that the tunneling process itself in such systems is spin-dependent and the transparency of the structures depends on the orientation of the electron spins even for symmetric barriers in the absence of an external magnetic field. The microscopic nature of this effect consists in the spin-orbit splitting of electronic states in the barrier, which is cubic in the wave vector. The actuality of the article is considering the theory of spin-dependent tunneling for single barriers and for resonant two-barrier structures. It is shown that the dependence of the tunnel transparency of the structures on the mutual orientation of the spin and the electron wave vector can be used for spin injection and for the electrical detection of the spin state of electrons. The influence of the spin-orbit interaction on the tunneling passage of charge carriers through non-centrosymmetric semiconductor barriers can manifest itself during the injection of free charge carriers from ferromagnets into a semiconductor through a potential barrier. The scientific novelty lies in the fact that, in the study of tunneling magnetoresistance in the structure of Fe/GaAs/Au, an anisotropic dependence of resistance on the magnetization of the Fe layer in the interface plane was found. Model calculation of the injection of electrons from Fe to Au through a semiconductor barrier GaAs taking into account the effect, enabled to explain the anisotropy observed experimentally.

Key words: potential barriers, tunneling, electronic spin, wave vector, spin-orbit splitting, two-barrier structures.

INTRODUCTION

Spin-dependent tunneling phenomena physics has recently attracted much attention and has been investigating the injection of spin-oriented charge carriers from magnetic materials into semiconductor structures [1-3]. Spin injection (transfer of particles with non-equilibrium spin polarization) can be carried out in an external magnetic field in structures with spatial inhomogeneity of the effective q -factor. Injection of electrons with a no equilibrium spin due to a jump of q -factor at the interface of the contact and semiconductor, was first observed in n -type InSb by nuclear magnetic resonance by the change in the spin polarization of nuclei. It was shown later that the efficiency of such a spin injection method significantly increases with the transfer of charge carriers from a semimagnetic semiconductor layer, in which, due to the giant Zeeman splitting effect, free carriers are significantly polarized in spin in weak magnetic fields. This makes it possible to record the spin orientation of injected charge carriers by optical methods using photo or electroluminescence polarization, which has been demonstrated for various semiconductor compounds. The possibility of injection of spin-oriented electrons from semimagnetic CdMnTe into the bulk CdTe layer [4], from BeMnZnS to the GaAs/AlGaAs quantum well [5], and also from GaMnAs holes to the InGaAs/GaAs quantum well [6]. It was shown in [7] that effective controlled spin injection can be carried out using tunnel diodes based on semimagnetic semiconductors. In this case, the resonance structure acts as a spin filter: depending on the applied voltage and the external magnetic field, electron tunneling occurs through different spin levels, which are energy-shifted relative to each other due to Zeeman splitting. Such spin-

dependent electron tunneling in an external magnetic field was studied for structures based on semi-magnetic ZnMnSe/BeTe and (Zn, Mn, Be) Se [8] semiconductors. It has recently been established that the difference between the effective q -factor of free electrons leads to a spin-dependent photoemission of electrons from the surface of semiconductors to vacuum. For the practical implementation of spin injectors that work effectively at room temperature, the use of ferromagnetic structures seems promising. The possibility of injection of spin-oriented charge carriers from a ferromagnet into a semiconductor is shown in [9]. Experimentally, spin injection from a ferromagnet was carried out by tunnel scanning microscopy methods in the works on the injection of electrons from a Ni needle onto the (110) surface of bulk GaAs [10]. The spin orientation of electrons on the GaAs surface was detected by the polarization of the luminescence. However, in layered heterostructures, the effective transfer of a spin through the ferromagnet – semiconductor interface could not be observed for a long time. It was pointed out in the theoretical work [9] that the fundamental reason for the low efficiency of spin injection in heterostructures is the strong difference in the conductivity of a ferromagnetic material and a semiconductor. It was shown in [10] that this problem could be solved if charge carrier injection is carried out through a tunneling barrier located between a ferromagnet and a semiconductor. Experimental results indicate that the degree of spin polarization of injected electrons reaches a few tens of percent at room temperature. Recently it has been shown that asymmetric tunnel barriers themselves based on nonmagnetic structures can be used as spin filters. It has been shown that the Rashba spin – orbit interaction on nonequivalent interfaces of asymmetric structures leads to the dependence of the tunnel transparency of barriers on the orientation of electron spins even in the absence of an external magnetic field. Such an effect is possible only in asymmetric systems with resonant tunneling through two-barrier and three barrier structures.

1. TUNNELING THROUGH A SINGLE BARRIER

It is convenient to begin the analysis of spin-dependent tunneling with the classical problem of the passage of particles through a single rectangular barrier. Consider electron tunneling with a wave vector $\mathbf{k} = \mathbf{k}_{//}, \mathbf{k}_z$ over the potential barrier of height V_b and thickness b , grown from a semiconductor with a zinc blende grating along the crystallographic direction $z//[001]$, where $\mathbf{k}_{//}$ the component of the wave vector is in the interface plane, the normal component of the wave vector. The Hamiltonian describing the propagation of electrons in the conduction band in each layer of the heterostructure, in the approximation of the effective mass, takes the form

$$\hat{H} = -\frac{\hbar^2}{2m^*} \frac{\partial^2}{\partial z^2} + \frac{\hbar^2 \mathbf{k}_{//}^2}{2m^*} + V(z) + \hat{H}_b, \quad (1)$$

where m^* the effective mass, which may be different in different layers, $V(z)$ is the profile of the potential energy of electrons that is, created by the heterostructure, $V(z) = V_b$ in the barrier and $V(z) = 0$ in the contact regions, \hat{H}_b is the Hamiltonian of the spin-orbit interaction.

In semiconductors with a zinc blende lattice, the spin-orbit splitting of the conduction band is cubic in the wave vector and is described by the Dresselhaus Hamiltonian [9]

$$\hat{H}_b = \gamma [\hat{\sigma}_x \mathbf{k}_x (\mathbf{k}_y^2 - \mathbf{k}_z^2) + \hat{\sigma}_y \mathbf{k}_y (\mathbf{k}_z^2 - \mathbf{k}_x^2) + \hat{\sigma}_z \mathbf{k}_z (\mathbf{k}_x^2 - \mathbf{k}_y^2)], \quad (2)$$

where γ the parameter characterizing the force of the spin-orbit interaction, $\hat{\sigma}_\alpha$ ($\alpha = x, y, z$) the Pauli parameters, $x//[100]$, $y//[010]$, $z//[001]$ are the cubic axes of the crystal.

In the study of electron tunneling along the z axis, the component of the wave vector in equation (2) should be considered as an operator $-i\partial/\partial z$. We assume that the kinetic energy of the incident particles is much smaller than the height of the barrier V_b . In this case, the main contribution to the Hamiltonian of the spin-orbit interaction in the barrier \mathbf{k}_z^2 is determined by the equation

$$\hat{H}_b = \gamma (\hat{\sigma}_x \mathbf{k}_x - \hat{\sigma}_y \mathbf{k}_y) \frac{\partial^2}{\partial z^2}. \quad (3)$$

The spin-orbit interaction (3) takes the form similar to the first term in the Hamiltonian (1), which describes the kinetic energy of an electron along the growth of the structure. Hamiltonian (3) is diagonalized by spinors

$$\chi_{\pm} = \frac{1}{\sqrt{2}} \begin{pmatrix} 1 \\ \mp e^{-i\varphi} \end{pmatrix}, \quad (4)$$

which correspond to electronic states with opposite spin orientation. Here the polar angle of the wave vector is $\mathbf{k} = (\mathbf{k}_{//} \cos \varphi, \mathbf{k}_{//} \sin \varphi, k_z)$.

2. SPIN ORIENTATION DEPENDENCIES

Particles in spin states χ_{\pm} propagate inside the barrier with preservation of the spin for various indicators of the attenuation of the wave function for the values of the parameter $\gamma > 0$. Spatial orientations of electron spins in their own states χ_{\pm} depend on the direction of the wave vector $\mathbf{k}_{//}$ in the interface plane and determined by the equation

$$s_{\pm} = \pm \frac{1}{2} (-\cos \varphi, \sin \varphi, 0). \quad (5)$$

Electronic spins in their own states s_{\pm} oriented along the wave vector $\mathbf{k}_{//}$, if vector $\mathbf{k}_{//}$ directed along the cubic axes of the crystal [110] or [010], and is perpendicular to the wave vector $\mathbf{k}_{//}$, if $\mathbf{k}_{//}$. We assume that the tunneling occurs without scattering processes. In this case, the component of the electron wave vector in the plane of the interfaces $\mathbf{k}_{//}$ is conserved, and particles with spins s_{\pm} pass through the barrier with the spin conservation. In the basis of Eigen states χ_{\pm} Hamiltonian (1) with spin-orbit interaction (3) is diagonal along spin indices and takes the form

$$\mathbf{H}_{\pm} = -\frac{\partial^2 \hbar^2}{\partial z^2 2m_{\pm}} + \frac{\mathbf{k}_{//}^2 \hbar^2}{2m^*} + V(z), \quad (6)$$

where m_{\pm} is the effective mass of electrons along the growth axis of the structure, modified by the spin-orbit splitting of the conduction band, $m_{\pm} = m^* \left(1 \pm 2 \frac{\gamma m^* \mathbf{k}_{//}}{\hbar^2} \right)^{-1}$.

The function $u_{\pm}(z)$, describing the sum of the incident and reflected wave in region I and the wave in region III, takes the form

$$\begin{cases} u_{\pm}^{(I)}(r) = \exp(i\mathbf{k}_{\pm} z) + r_{\pm} \exp(-i\mathbf{k}_{\pm} z); \\ u_{\pm}^{(III)}(r) = A_{\pm} \exp(\mathbf{q}_{\pm} z) + B_{\pm} \exp(-\mathbf{q}_{\pm} z); \\ u_{\pm}^{(II)}(r) = t_{\pm} \exp(i\mathbf{k}_{\pm} z), \end{cases} \quad (7)$$

where $r_{\pm}; t_{\pm}$ are the amplitude transmission and reflection coefficients of particles with spin s_{\pm} , \mathbf{q}_{\pm} are the indicators of wave functions in the barrier,

$$\mathbf{q}_{\pm} = \mathbf{q}_0 \left(1 \pm 2 \frac{\gamma m_2 \mathbf{k}_{//}}{\hbar^2} \right)^{-1/2}; \quad (8)$$

$$\mathbf{q}_0 = \sqrt{\frac{2m_2 V_b}{\hbar^2} - \mathbf{k}_{\pm}^2 \frac{m_2}{m_1} - \mathbf{k}_{//}^2 \left(\frac{m_2}{m_1} - 1 \right)}$$

the attenuation coefficient of the wave function without taking into account the spin-orbit interaction, m_1 and m_2 are the effective masses in the contact regions and inside the barrier. The use of boundary conditions at the interfaces allows writing a closed system of linear equations and coefficients $t_{\pm}, r_{\pm}, A_{\pm}, B_{\pm}$ and determine the dependence of the transmission and reflection coefficients on the orientation of the electron spins. Since we are interested in spin tunneling due to the splitting of the electron spectrum in the barrier, we will use standard boundary conditions for the continuity of the wave function ψ_{\pm} and flow $(1/m_{\pm}) \partial \psi_{\pm} / \partial z$ at heterojunctions.

In addition, we will neglect the spin-orbit interaction in the contact layers I and III, since the spin splitting due to cubic in $\mathbf{k}_{//}$ terms in these regions is small. The calculation shows that the transmission coefficients t_{\pm} for compounds with moderate spin-orbit interaction $\gamma m_z \mathbf{k}_{//} / \hbar^2 \ll 1$ and sufficiently wide $\exp(-b\mathbf{q}_0) \ll 1$ barriers have the form [10]

$$t_{\pm} = t_0 \exp\left(\pm \gamma \frac{m_z \mathbf{k}_{//}}{\hbar^2} \mathbf{q}_0 b\right); \quad (9)$$

$$t_0 = -4i \frac{m_z \mathbf{k}_z \mathbf{q}_0}{m_i (\mathbf{q}_0 - i\mathbf{k}_z m_z / m_i)^2} \exp(-\mathbf{q}_0 b - i\mathbf{k}_z b)$$

the transmission coefficient calculated without taking into account the spin-orbit splitting of the spectrum. The general problem of the passage of electrons with an arbitrary initial spin orientation set by a spinor χ through a barrier based on a semiconductor with a zinc blende grating can be solved by decomposing the Hamiltonian (3) into proper spin states χ_{\pm} . To analyze spin-dependent tunneling, it is convenient to introduce the polarization efficiency of the structure

$$P = \text{th}\left(2\gamma \frac{m_z \mathbf{k}_{//}}{\hbar^2} q_0 b\right). \quad (10)$$

CONCLUSION

For a fixed value of the longitudinal wave vector $\mathbf{k}_{//}$, the polarization efficiency of the tunnel structure increases with increasing spin-orbit coupling constant γ and barrier thickness b . To achieve higher polarization efficiency values, thick barriers must be used. It should be noted that an increase in the barrier thickness leads to a significant decrease in its transparency and, consequently, to a decrease in the tunneling flux of electrons. The calculation results indicate that the polarization efficiency can reach several percent for reasonable barrier thicknesses. Structures based on the GaAs compound and its solid solutions are the most effective spin filters due to the large value of the product γm^* in these materials.

REFERENCES

1. R.H. Silsbee. "Spin orbit induced coupling of charge current and spin polarization," J. Phys.: Condens. Matter., vol. 16, 2004, p.179.
2. R. Fiederling, M. Keim, G. Reuscher, W. Ossau, G. Schmidt. "Injection and detection of a spin-polarized current in a light emitting diode," Nature (London), vol. 402, 1999, p.787.
3. Th. Gruber, M. Keim, R. Fiederling, G. Reuscher, W. Ossau, G. Schmidt. "Electron spin manipulation using semi magnetic resonant tunneling diodes," Appl. Phys. Lett., vol. 78, 2001, p.1101.
4. S.F. Alvarado, "Observation of spin-polarized-electron tunneling from a ferromagnetic into GaAs," Phys. Rev. Lett., vol. 68, 1992, p.1387.
5. V.P. Labella, D.W. Bullock. "Spatially resolved spin-injection probability for gallium arsenide," Science, vol. 292, 2001, p.1518.
6. E.I. Rashba, "Theory of electrical spin injection: Tunnel contacts as a solution of the conductivity mismatch problem," Phys. Rev., vol. B62, 2000, p.16267.
7. H.J. Zhu, M. Ramsteiner, H. Kostial, M. Wassermeier, H.-P. Schonherr, K.H. Ploog. "Room-temperature spin injection from Fe into GaAs," Phys. Rev. Lett., vol. 87, 2001, p.016601.
8. P.R. Hammar, M. Johnson. "Spin-dependent current transmission across a ferromagnetic insulator two-dimensional electron gas junction," Appl. Phys. Lett., vol. 79, 2001, p.2591.
9. V.F. Motsnyi, J. De Boeck, J. Das, W. Van Roy, G. Borghs. "Electrical spin injection in a ferrimagnet/tunnel barrier/semiconductor heterostructure," Appl. Phys. Lett., vol. 81, 2002, p.265.
10. N.N. Chernyshov. "Study the photovoltaic effect in the spin resonance for crystals without inversion centre," Zbior artykulow naukowych. Warszawa, 02.2016, pp.53-58.

**SPECIFIC DIRECTIONS
IN NANO-ELECTRONICS
AND MODELING**

MODELING OF THE KEY CHARACTERISTICS ALL BACK-CONTACT SILICON SOLAR CELLS

A.V. Sachenko¹, V.P. Kostylyov¹, V.M. Vlasyuk¹, R.M. Korkishko¹, I.O. Sokolovskyi¹,
M. Evstigneev²

¹V. Lashkaryov Institute of Semiconductor Physics, NAS of Ukraine, 41 prospect Nauky, 03028
Kyiv, Ukraine, e-mail: vkost@isp.kiev.ua

² Department of Physics and Physical Oceanography, Memorial University of Newfoundland,
St. John's, NL, A1B 3X7 Canada

Abstract

The key parameters of silicon solar cells with back contact and rear metallization (SC-BC), such as the short-circuit current, open-circuit voltage, and photoconversion efficiency, are modeled theoretically. Among other recombination channels, the model accounts for the non-radiative Auger recombination assisted by the deep recombination center and recombination in the space-charge region. It is established that these mechanisms are important in the typical commercial SC-BC in the maximal-power regime. The theory is developed for calculating the efficiency as a function of the SC-BC thickness. In particular, the theory is applied to model the SC-BC produced by SunPower Corp.

Introduction. Depending on the surface recombination velocity on the illuminated surface S_0 and on the total surface recombination velocity on the front and rear surfaces S_s , two mechanisms determine the optimal SC-RM thickness, at which the output power is maximal. The first mechanism dominates when the efficiency exceeds 24% under the AM1.5 conditions and is related to an essential increase of photon mean free path in the textured silicon SC.

The one-dimensional theory developed here allows one to calculate the photoconversion efficiency η and other key parameters of SC-BC, such as the short-circuit current I_{SC} , open-circuit voltage V_{OC} , and the I - V curve fill factor FF . It is valid when the following criteria are fulfilled: (1) $L_d \gg d$, (2) $S_s \ll D_A/d$, where L_d is the electron-hole pair diffusion length, d is the base thickness, S_s is the total recombination velocity on the front and the rear surfaces, and D_A is the ambipolar diffusion coefficient. Then, one can neglect the spatial non-uniformity of the excess carrier concentration, $\Delta n(x)$, where x is the coordinate perpendicular to the SC surface. This simplifies significantly the analysis of the SC-BC.

In the theoretical modeling of the SC-BC characteristics, the following recombination mechanisms in silicon are taken into account: Shockley-Read-Hall recombination with the lifetime τ_{SRH} , non-radiative exciton Auger recombination assisted by deep impurities with the lifetime τ_{nr} , surface recombination on the front and rear surfaces with the respective velocities S_0 and S_d , radiative recombination with lifetime τ_r , band-to-band Auger recombination, and the space-charge region (SCR) recombination with the velocity S_{SC} . In contrast to the traditional SC, recombination on the front surface plays an important role in the SC-BC, so that the condition $S_0 \ll D_A/d$ may not always be fulfilled.

The theoretical dependence of the photoconversion efficiency η on the SC-BC base thickness d is obtained. Two mechanisms are operative in forming the short-circuit current dependence on the thickness. The first one accounts for the increase of the photon mean-free path in the textured SC-BC, and the second one is related to the effect of the recombination velocity on the illuminated surface, S_0 .

Results and discussion. The general algorithm for calculating of the photoconversion efficiency in the SC-BC is described [1].

As shown in the work [2], the external quantum efficiency EQE in a textured p-n junction-based silicon SC, as well as in a heterojunction SC, is described in the long-wavelength region by an empirical expression

$$EQE(\lambda, b) = \left(1 + b/4\alpha(\lambda)d \cdot n_r^2\right)^{-1}, \quad (1)$$

where b is a numerical coefficient greater than 1. Here, it is assumed that in the long-wavelength region, the external quantum efficiency is approximately the same as the internal quantum efficiency $EQE(\lambda, b) = T(\lambda) \cdot IQE(\lambda, b) \approx IQE(\lambda, b)$, because the transmission coefficient $T(\lambda)$ in this part of the spectrum is close to 1.

Shown in Fig. 1 are the experimental curves $EQE(\lambda)$ for the SC-BC from [3] and their approximation by the expression (1). The coefficient b , at which the theory agrees well with the experiment in the long-wavelength region, equals 1.6. As seen in Fig. 1, the expression (1) quite accurately describes $EQE(\lambda)$ in the wavelength range from 800 to 1200 nm. Hence, for this SC-RM one can determine the light-generated current density according to

$$J_L(d, b) = q \left[\int_{\lambda_0}^{800} I_{AM1.5}(\lambda) EQE(\lambda) d\lambda + f \int_{800}^{\lambda_m} I_{AM1.5}(\lambda) EQE(\lambda, b) d\lambda \right], \quad (2)$$

where $\lambda_0 = 300$ nm, $\lambda_m = 1200$ nm, $I_{AM1.5}(\lambda)$ is the spectral photon flux under the AM1.5 conditions, $EQE(\lambda, b)$ is given by (1), and the coefficient $f \leq 1$ should be chosen such that for $\lambda = 800$ nm, the values $EQE(\lambda)$ and $EQE(\lambda, b)$ are the same.

In order to model the SC-BC, one needs to determine the recombination parameters τ_R and b_r , which describe the recombination in SCR S_{SC} . Here τ_R is the lifetime of the Shockley-Reed Hall in the SCR, b_r - the ratio of capture cross-sections hole to electron. They can be found from the dark I - V curves. Because we could not find the dark I - V curves in the literature on these SC, just the illuminated ones, we have measured them on some commercial SC-BC with the area $A_{SC} = 153$ cm² and the base thickness $d = 165$ μ m. The experimental dark current density $J_r(V)$, shown in Fig. 2 was fitted by the theoretical expressions above. In the modeling, the Shockley-Read-Hall recombination time was taken to be $\tau_{SRH} = 10$ ms. The same figure shows light I - V for commercial SC-BC.

As a result of this fitting, the following parameters have been obtained: the net surface recombination velocity at low injection $S_{0s} = 4$ cm/s, the SCR recombination time $\tau_R = 20$ μ s, the ratio of the electron to hole capture coefficient $b_r = 2 \cdot 10^{-2}$.

Using the approach developed in [1], taking into account (1) and (2), it is possible to obtain for CETM the dependence $\eta(d)$ and determine the optimal value optimal SC-BC thickness d_{opt} .

It should be noted that the result obtained is valid only if the criterion $S_0 d / D_A \ll 1$ is fulfilled. It is well-known that surface recombination on the front (illuminated) surface of silicon SC-BC decreases the short-circuit current density J_{SC} according to

$$J_{SC} = J_L(d, b) \left[1 + S_0(\Delta n) d / D_A(\Delta n)\right]^{-1}, \quad (3)$$

where $D_A(\Delta n) = (n_0 + p_0 + 2\Delta n) \times \left[(n_0 + \Delta n) / D_p(\Delta n) + (p_0 + \Delta n) / D_n(\Delta n) \right]^{-1}$ is the ambipolar diffusion coefficient, $D_p(\Delta n)$ and $D_n(\Delta n)$ are the hole and electron diffusion coefficients, which are related to the respective mobilities by Einstein's relation.

We are analysing the case of n-type doping, i.e. $n_0 \gg p_0$. We also consider the general case when the excess carrier concentration Δn is not bounded from above and may exceed the equilibrium majority concentration n_0 .

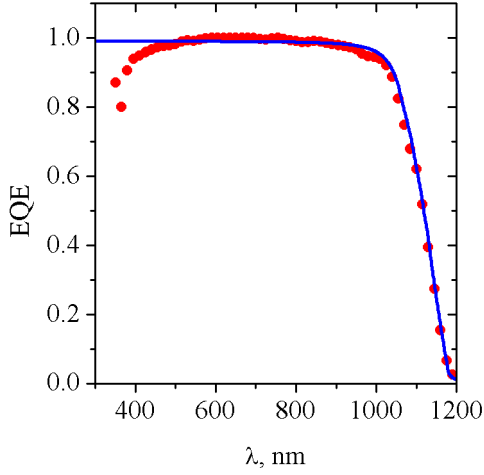


Fig. 1 – Experimental (symbols) and theoretical (solid line) external quantum efficiency for the SC from [3]

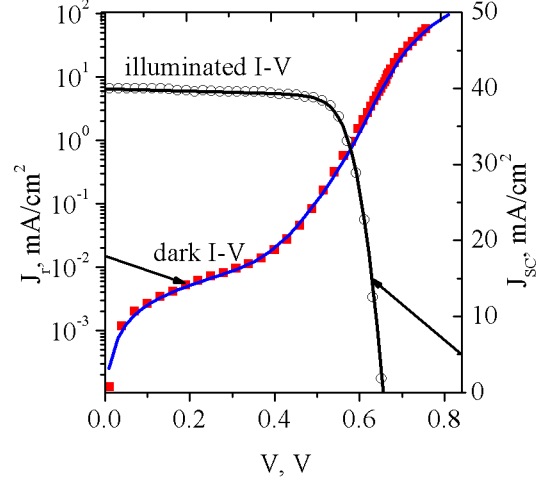


Fig. 2 – Experimental (symbols) and theoretical (solid line) dark I-V and illuminated I-V curves of the commercial SC by SunPower

Let us evaluate the effect of the surface recombination velocity S_0 and base thickness d on the photoconversion efficiency in the SC-BC. Strictly speaking, the values of D_p and D_n are not fixed when $\Delta n \geq n_0$. To simplify the analysis, let us consider the situation when D_p and D_n have their low-injection values, $D_{p0} = 11.25 \text{ cm}^2/\text{s}$ and $D_{n0} = 33.75 \text{ cm}^2/\text{s}$, and the resistivity of silicon is sufficiently high. We also take into account that $S_0(\Delta n) = S_{00}(1 + \Delta n/n_0)$, where S_{00} is the low-injection recombination velocity on the front surface. Then, the expression (3) assumes the form

$$J_{sc} = J_L(d, b) \left[1 + S_{00}(1 + \Delta n/n_0) d \left(\left((n_0 + \Delta n)/D_{p0} \right) + (\Delta n/D_{n0}) \right) / (n_0 + 2\Delta n) \right]^{-1}. \quad (4)$$

Fig. 3a shows the theoretical photoconversion efficiency $\eta(d)$ for the commercial SC-RM, obtained using the same calculation scheme as in the previous case, but with $S_{0s} = 4 \text{ cm/s}$. The curve 1 is obtained under the assumption that surface recombination velocity does not affect the short-circuit current, whereas the curves 2 and 3 correspond to the low-injection front surface recombination velocity S_{00} of 0.4 and 0.6 cm/s. As seen from Figs. 4 and 5, the commercial SC tested is characterized by a smaller drop in both the maximal efficiency and the optimal thickness as S_{00} is increased. The maximal η -value is 21.8 %, which differs by only 0.5% from the efficiency at $d = 165 \text{ }\mu\text{m}$. The initial optimal thickness d_{opt} is about 322 μm .

Finally, shown in Fig. 3b are the efficiency vs. base thickness curves for the SC-BC with the record efficiency of 25.2 % from Ref. [4]. The following parameter values were assumed: $\tau_{SRH} = 10 \text{ ms}$, doping level $9 \cdot 10^{14} \text{ cm}^{-3}$, $\tau_R = 20 \text{ }\mu\text{s}$, and $b_r = 2 \cdot 10^{-2}$. From fitting the experimental open-circuit voltage with the theory, it was found that $S_{0s} = 0.42 \text{ cm/s}$. Then, but comparing the theoretical and experimental efficiency at the thickness 130 μm , the specific

series resistance value of $0.25 \Omega \cdot \text{cm}^2$ was found. Finally, the curves $\eta(d)$ were built, see Fig. 3b (curve 1). As seen in this figure, the maximal efficiency has the value of 25.2% at the optimal thickness $d_{opt} = 141 \mu\text{m}$. The curves 2-4 correspond to the low-injection front surface recombination velocity S_{00} of 0.04, 0.07 and 0.1 cm/s. Again, as in the previous case, the efficiency values at $d = 141 \mu\text{m}$, are practically the same at different S_{00} .

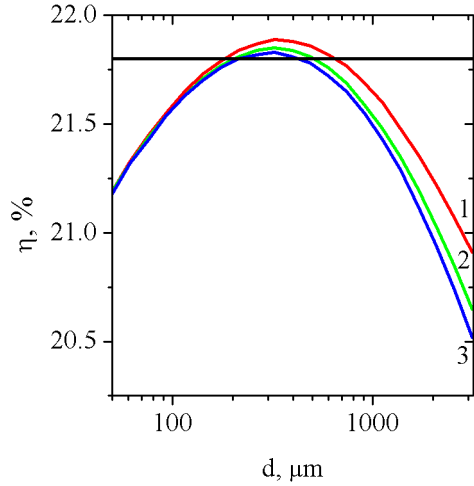


Fig. 3a – Thickness dependence of the photoconversion efficiency for the SC by SunPower. The curves 1-3 are built for $S_{00} = 0, 0.4, \text{ and } 0.6 \text{ cm/s}$

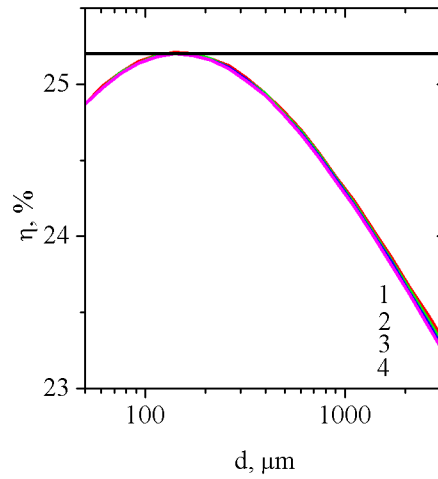


Fig. 3b – Thickness dependence $\eta(d)$ for the SC from [4]. The curves 1-4 are obtained for $S_{00} = 0, 0.04, 0.07 \text{ and } 0.1 \text{ cm/s}$

Conclusions. The results of our analysis show that two mechanisms are operative in the thickness dependence of the photoconversion efficiency in the SC-BC. The first one is related to an increase of the photon mean free path in the textured SC, and is the more pronounced the smaller the value of the parameter b in the expression (1). The other mechanism has to do with the recombination velocity on the front surface. The effect of surface recombination on the illuminated surface on the short-circuit current in the SC-BC analyzed is the smaller the lower the net surface recombination velocity on the front and rear surfaces. Besides, the value of S_0 is always smaller than S_d , which is taken into account in the calculations. The open-circuit voltage is affected only by the total front plus rear surface recombination velocity S_s .

The higher S_s the larger the optimal base thickness d_{opt} at which the photoconversion efficiency is maximal, and the bigger the shift of d_{opt} to the smaller values as S_0 is increased. At the same time, the curves $\eta(d)$ in the thickness range between 150 and 350 μm in the silicon SC-BC produced by SunPower are rather flat, hence using the thickness of $(150 \pm 30) \mu\text{m}$ does not lead to a significant reduction of the efficiency as compared to the maximal values.

References

1. A.V. Sachenko, V.P. Kostilyov, V.M. Vlasyuk, et al. SPQEO, 22 (3) pp. 5-13 (2019).
2. A.V. Sachenko, V.P. Kostilyov, A.V. Bobyl, et al. Technical Physics Letters 44 (10) pp. 873-876 (2018).
3. http://eshop.terms.eu/_data/s_3386/files/1379942540-sunpower_c60_bin_ghi.pdf
4. D. D. Smith, G. Reich, M. Baldrias, et al., Photovoltaic Specialists Conference (PVSC), 2016 IEEE 43rd, 3351–3355, IEEE. (2016).

OPTIMIZATION OF FREQUENCY AND ENERGY CHARACTERISTICS OF DISK MONOPOLE ANTENNA

Mayboroda D.V., Pogarsky S.A., Pshenichnaya S.V., Anikeeva K.S., Smirnova K.O.

V.N.Karazin Kharkiv national university
61022, Kharkiv, sq. Svobody, 4, Kharkiv national university
Named after v.N.Karazin, Department of Ultra High Frequencies
E-mail: Sergey.A.Pogarsky@univer.kharkov.ua

The results of numerical simulation of frequency characteristics of complex radiating structure based on disk microstrip monopole with 3rd iteration quasi-fractal topology are presented. The structure has been excited in two stages: by coplanar waveguide segment and segment of coaxial waveguide with step change of inner conductor diameter. Simulation has been performed in a free version of CST. The structure has been found to be dual-band, and with operating bands sufficient for ultra-wideband signals processing.

Introduction

Modern telecommunication technologies development causes application of an increasing number of new communication types. The main requirement to devices providing new types of communication is miniaturization without the main technical characteristics worsening. The particular attention is being paid to opportunity of ultra-wideband signals transmission. Today, planar antenna systems with so-called canonical topology (rectangle, disk, ring and their modifications), meeting almost all the modern requirements except high power signals transmission [1], are the most common.

The use of certain topology enables various operating modes realization, formation the specified characteristics of radiated fields. Topologies based on axially-symmetric structures are the most attractive because of their unique properties. The foremost one is the ability to form circularly (elliptically) polarized fields. However, these structures have significant disadvantage – the existence of degenerate modes. There are well-known ways of removing the degeneracy in these structures [2, 3]. The main idea of them is creation of tortuous paths for currents flowing on the monopole surface. One of the possible implementations is the use of fractal (quasi-fractal) structures. It should be mentioned, that implementation of the so-called physical fractal is almost impossible because real structures have finite dimensions and high iteration order (δ) can not be realized. Besides, the broadbandness effect appears only at low iteration order (δ).

This paper demonstrates one of the ways to optimize the frequency and energy characteristics of a quasi-fractal monopole.

Model under study

There are well-known papers, which consider quasi-fractal structures based on disk monopole [4, 5]. The feature of explored structures is a grounded back side of dielectric plate (excitation type is not important in this case). The structures provide multi-frequency operating mode (in a certain sense, broadbandness could be mentioned). However, relative bandwidth equals from 1 to 3%. In this case ultra-wideband signals processing is impossible. The physical reason of narrowbandness is being explained below. Resonance and energy accumulation occurs between grounded plane and microstrip disk (with all the possible topology variations). This region is limited because dielectric plates, that are thin in comparison with the resonant wavelength, are used for most applications. The dielectric substrate thickness increasing leads to some expansion of operating frequency band, however, the possibility of surface waves excitation increases, which eventually causes antenna efficiency decrease.

One of the possible solutions is a fundamental design change, such as grounded plane removing. Technically, it leads to an increase in resonant volume (dielectric substrate and a free

space region), but, at the same time, it causes radiation from the opposite side of the structure. Therefore, some special type of disk resonator excitation has to be chosen. In this case, the best option is excitation by coplanar transmission line.

Fig. 1 demonstrates the design of quasi-fractal monopole with unshielded coplanar line segment as an exciter.

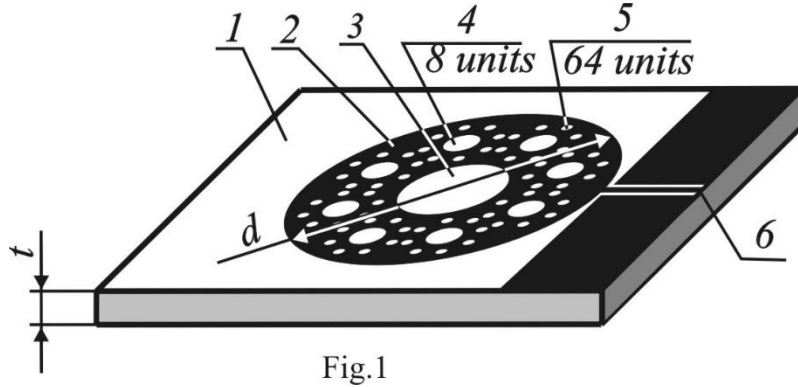


Fig. 1 – uses the following notations: 1 – dielectric substrate, 2 – base microstrip disk; 3 – 1st iteration element; 4 – 2nd iteration elements; 5 – 3rd iteration elements; 6 – coplanar transmission line segment elements. Dielectric plate with the standard dimensions 60x48 mm has been used as a

substrate. The base microstrip disk diameter is $d = 35$ mm. The dielectric substrate thickness is $t = 0.5$ mm. Permittivity ϵ_r was being varied in order to determine sensitivity of studied characteristics to this parameter

The input impedance of microstrip radiator is known to vary within interval from 120 to 240 Ohm and its topology is not very important. The key factor is a ratio between resonant wavelength and the radiating aperture size. Considering ratio between sizes of structure elements, coplanar line segment length can not exceed 12.2...12.4 mm, which is obviously not enough for smooth change from structure input impedance to disk input impedance. For this reason, it is necessary to use an additional matching element, e.g. segment of coaxial line with step change of inner conductor diameter.

This structure characteristics has been numerically analyzed using free version of CST. Initially, the possibility of obtaining optimal matching within the widest possible frequency range has been studied. In fact, it determines total device bandwidth and the ability of ultra-wideband signals processing.

Frequency dependences of $|S_{11}|$ for different ϵ_r are presented in Fig. 2. Values of ϵ_r are being varied from 2.4 to 3.9. Obviously, antenna turns out to be dual-band within whole frequency range under consideration. The operating frequency range is determined in accordance to IEEE standard: return loss has to exceed -10 dB ($|S_{11}| \approx 0.396$), which corresponds to $VSWR \approx 2$. The low-frequency bandwidth is $\Delta F \approx 5.88$ GHz at $\epsilon_r = 2.4$ and somewhat narrower for other ϵ_r (about $\Delta F \approx 5.26$ GHz), and lower frequency of the band does not change, which is caused by topology of base disk radiator. The upper frequency of low-frequency band almost does not change as well (for curve 1 it is slightly shifted to high-frequency region, considering significantly smaller ϵ_r). This frequency depends on the 1st iteration aperture topology. After normalizing by central frequencies, relative bandwidths obtained are equal to 1.387 and 1.338 respectively.

High-frequency bands turn out to be narrower than low-frequency ones (4.9 GHz and 4 GHz, respectively). It should be noted, that both the widest bands of acceptable matching and minimum of $|S_{11}|$ can be realized at $\epsilon_r = 2.4$. General trend is the operating band narrowing, and when ϵ_r equals 3.6 and 3.7 the matching quality is high. However, in the narrow band, as ϵ_r increases to 3.8 and 3.9, the band of acceptable matching significantly widens, but matching quality worsens. Such dependences behavior is caused by 2nd and 3rd iteration slot

inhomogeneities, dimensions of which are comparable to resonant wavelengths excited in the structure.

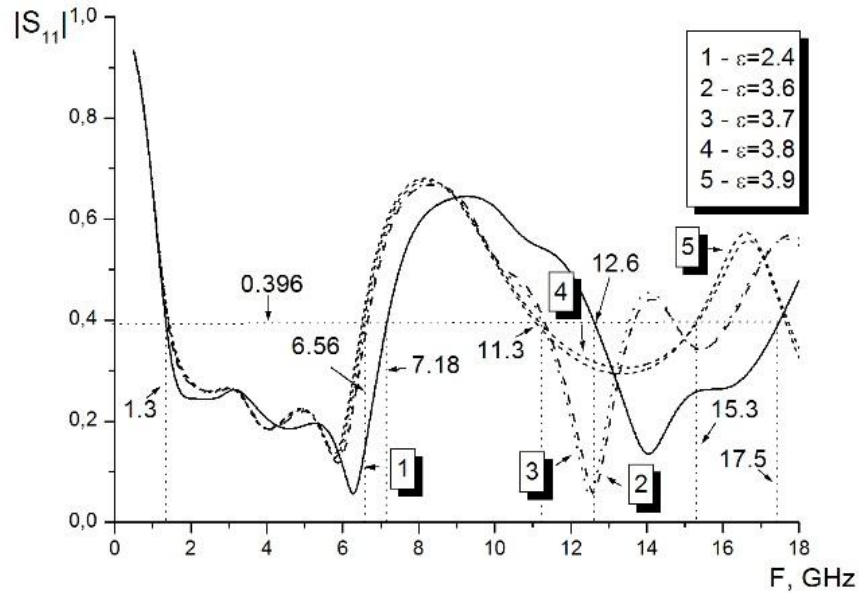


Fig. 2

Conclusions

The numerical experiments have revealed the opportunity of using quasi-fractal microstrip structure as a broadband dual-band radiating antenna. Bandwidth ratio in low-frequency region equals 5.5. In high-frequency region, the operating band is somewhat narrower. The obtained dependences demonstrate rather weak sensitivity of $|S_{11}|$ to small (to 5%) changes of ϵ_r . Integrated approach to the problem of radiating module matching with external exciting circuits has revealed the opportunity of operating frequency band widening.

References

1. K. L. Wong, Compact and Broadband Microstrip Antennas, John Wiley & Sons. 2003.
2. D.V. Mayboroda, and S.A. Pogarsky, Electrodynamic characteristics of the disc microstrip radiator with structural auxiliary elements, Telecommunications and Radio Engineering, **74**(13), pp. 1147-1155, 2015.
3. L. N. Lytvynenko, S. A. Pogarsky, D. V. Mayboroda and A. V. Poznyakov, Microstrip Antenna With Complex Configuration Of Radiators, Int. Conf. on Antenna Theory and Techniques (ICATT), 2017, Kyiv, Ukraine, pp. 254-256.
4. D.V. Mayboroda, S.A. Pogarsky and E.A. Shaulov, Fractal Antenna, UA Patent, 2017, No. u 2017 08267.
5. S.A. Pogarsky, D.V. Mayboroda, Optimization of the integral parameters of disk microstrip antennas with radiators of complex geometry, Journal of Telecommunications and Radio Engineering, **75** (9), pp. 763-769, 2016.

HIGH-FREQUENCY ELECTRODYNAMICS OF NANOSTRUCTURED HIGH- T_c SUPERCONDUCTOR FILMS

A.L.Kasatkin¹⁾, V.P. Tsvitkovsky¹⁾, A.O.Pokusinskii²⁾

¹⁾ G.V. Kurdyumov Institute for Metal Physics of NAS of Ukraine,
Dep.of Superconductivity, 36 Vernadsky ave., 03142 Kiev
tel. (067) 503-15-03
E-mail: tsvad55@gmail.com

²⁾ Kiev T. Shevchenko National University,
Faculty of Radio Physics, Electronics and Computer Systems,
4-g Glushkov ave., 03187 Kiev

Theoretical model for microwave response of nanostructured high- T_c superconductor (HTS) film with implanted dielectric nanoparticles or ion radiation induced point-like or extended linear (columnar) structural defects with a nanosize cross-section in the films interior, is developed, and the microwave surface resistance $R_s(T, H, \omega)$ is calculated both for the Meissner and mixed states of superconductor film in the presence of applied dc magnetic field. Obtained results indicate that dielectric nanoparticles or nanosized radiation defects can significantly improve superconductor characteristics at microwave frequencies. Namely, this artificial nanostructure leads to the decrease of the surface resistance in the Meissner state and eliminates Abrikosov vortices oscillations and related microwave energy losses in the mixed state of the film, thus decreasing the Abrikosov vortices contribution to the R_s value in the mixed state of HTS film. Obtained results indicate that implantation of dielectric nanoparticles or point-like and columnar radiation defects can significantly improve the superconductor film characteristics in the microwave frequency range. This effect was observed in some recent experiments performed on HTS films

1. Introduction

Implantation of dielectric phase nanoparticles in the interior of high-temperature superconductors (HTS) is a modern trend in fabrication of superconducting materials with high current carrying capability [1]. The positive role of implanted dielectric nanoparticles as well as artificially induced point or extended linear defects, produced by heavy ion irradiation of superconducting samples [2], consists mainly in enhancement of Abrikosov vortices pinning and preventing their dissipative motion under the Lorentz force action caused by transport current flow through the superconductor. Besides that, dielectric nanoparticles (as well as radiation defects) implanted in the matrix of HTS film can significantly improve its characteristics at microwave frequencies. Namely, these implanted nanosized objects can decrease the surface resistance in the Meissner state [3] and eliminate Abrikosov vortices oscillations and related microwave energy losses, thus decreasing the Abrikosov vortices contribution to the R_s value in the mixed state of type-II superconductor [4].

In the present work we consider effect of point-like or columnar defects addition on the microwave surface resistance value $R_s(T)$ in the Meissner state of superconductor and demonstrate how this treatment can significantly decrease $R_s(T)$ value at least at low temperatures. Also we develop a theoretical model for high frequency response of Abrikosov vortices in the mixed state of 3D anisotropic superconductor which contains: a) separate nanoparticles or nanosized point radiation defects, which act like strong zero-dimensional pinning sites, and b) nanorods or columnar heavy ion irradiation tracks, which are extended linear pinning sites for vortices. We consider vortices as an elastic strings and calculate the surface resistance $R_s(n_i, B, I_{rf}, \omega, T)$ dependencies for both mentioned cases. Obtained results indicate that implantation of dielectric nanoparticles or radiation defects can significantly improve the superconductor characteristics in the microwave frequency range. This effect was observed in some recent experimental works [4].

2. Microwave surface resistance $R_s(T, \bar{\lambda})$ of nanostructured superconducting film

The microwave surface resistance of a rather thick superconducting film with $d > 2\lambda$, being in the Meissner state (d – is the films thickness, λ – is the London penetration depth of a weak magnetic field), can be described by the well-known relation [3]:

$$R_s(T, \omega) = \frac{\mu_0^2 \omega^2}{2} \lambda^3(T) \sigma_1(T, \omega) \quad (1)$$

$$\sigma_1(T, \omega) = \frac{e^2}{m^*} n_N(T) \frac{\tau(T)}{1 + (\omega\tau(T))^2}; \quad \sigma_2(T, \omega) = \frac{1}{\mu_0 \omega \lambda^2(T)} = \frac{e^2}{m^* \omega} n_S(T) \quad (2)$$

here $\sigma_1(T, \bar{\lambda})$ is the real part of the complex microwave conductivity $\hat{\sigma}(T, \bar{\lambda}) = \sigma_1(T, \bar{\lambda}) + i\sigma_2(T, \bar{\lambda})$. In the framework of the two-fluid model of superconductor the expressions for $\sigma_1(T, \bar{\lambda})$ and $\sigma_2(T, \bar{\lambda})$ are given by Eq.(2); $n_N(T)$ and $n_S(T)$ are concentrations of normal electrons and those in the superfluid condensate, respectively; $\tau(T)$ – is the relaxation time for normal electrons. Within the phenomenological model $\tau^{-1}(T) = \tau_o^{-1} + \tau_i^{-1} + \tau_{e-ph}^{-1}(T)$. Here τ_o , τ_i , $\tau_{e-ph}(T)$ are electron momentum relaxation times for processes of electron scattering by natural defects in the pristine film, by implanted nanoparticles, and phonons, respectively. From (1) one can see that decrease in the total relaxation time $\tau(T)$ due to implantation of dielectric nanoparticles (or radiation defects) in the matrix of superconductor first leads to decrease of σ_1 and then, in accordance to (1), to decrease of the surface resistance R_s , as it is illustrated by Fig.1 where results of $R_s(T)$ calculation on the base of Eq.(1) are demonstrated for different nanoparticles concentrations at some suitable values of other parameters taken from the corresponding literature (see, e.g. [3]).

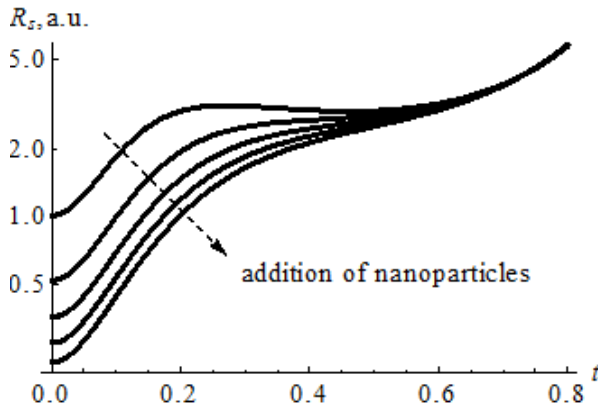


Fig. 1 – Effect of added dielectric nanoparticles and/or radiation defects on the surface resistance $R_s(T)$ of HTS film at different temperatures (t – is the reduced temperature : $t=T/T_c$)

This decrease of R_s , caused by implantation of additional electron scattering centers – dielectric nanoparticles or radiation defects in the interior of superconductor film, should be mostly pronounced at low temperatures and at not too high concentration of such kind nanosize scattering sites, because increase in the electron momentum relaxation rate due to increase of electron scattering also leads to significant increase of the penetration depth λ . The latter, accordingly to Eq.(1), leads to the competition of opposite dependencies λ and σ_1 on concentration of these additional scattering sites. So, there should be an optimal concentration of nanoparticles or radiation defects (correspondingly τ_i) to get the minimal value of R_s for other fixed parameters (e.g., $T, \bar{\lambda}$).

3. Vortex oscillations and RF-losses in superconductors with strong vortex pinning

In the present work we also develop a theoretical model for high frequency response of Abrikosov vortices in the mixed state of 3D anisotropic superconductor with dielectric nanoparticles, which act like strong point-like pinning sites. We consider vortices as elastic strings and calculate the surface resistance $R_s(n_i, B, \vec{j}, T)$ in the linear regime (at small amplitudes of rf field H_{rf}). At not too high dc magnetic fields B one has for the total surface resistance R_s : $R_s(n_i, B, \vec{j}, T) = R_{s,e}(n_i, \vec{j}, T) + R_{s,v}(n_i, B, \vec{j}, T)$, where $R_{s,e}$ is given by Eq. (1), while $R_{s,v}$ term corresponds to contribution of oscillating vortices. Using phenomenological model for rf vortex dynamics [5] and disregarding collective effects in the vortex ensemble, we have obtained expression for $R_{s,v}$ which resembles contribution of vortex oscillations for the cases, schematically shown in Fig.2 - (a) and (b), namely: when elastic vortex strings are strongly pinned by point-like pinning sites (dielectric nanoparticles or point-like radiation defects), as it is demonstrated in Fig.2a and in the case of extended linear (columnar) pinning sites – see Fig.2b. In the latter case one can expect that the main contribution to $R_{s,v}$, at least at high enough temperatures $T \delta T_c$, arises due to thermally excited vortex kinks, which connect two parts of the whole vortex line situated on two adjacent neighboring columnar pinning sites and can viscously move along the columns axis (z -axis in Fig.2b) under the Lorentz force action. Below both these cases are considered.

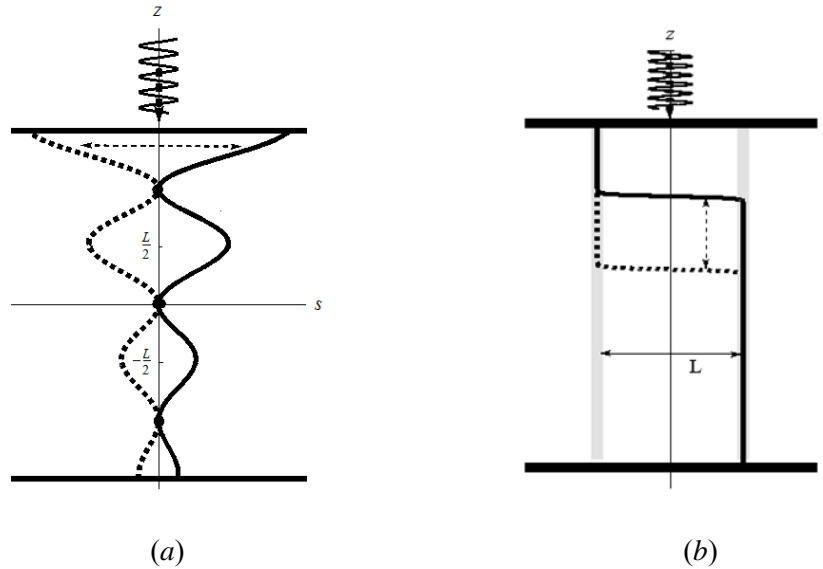


Fig. 2 – (a) – rf- oscillations of elastic vortex string pinned by point-like pinning sites;
(b) - rf- oscillations of vortex kinks in superconductor with columnar defects

In the case of point-like pinning sites we suppose that elastic vortex strings are rigidly pinned at discrete points r_i inside a rather thick superconducting plate (thickness $d > 2\lambda$), where nanoparticles or point-like radiation defects are randomly distributed (Fig.2a). We suppose the average distance between neighboring nanoparticles L being much less than the London penetration depth λ , and intervortex distance $a_\phi \approx \left(\frac{\phi_0}{B}\right)^{1/2}$; $L = n_i^{-1/3} \ll a_\phi, \lambda$; $\phi_0 \equiv \frac{\pi \hbar c}{e}$ - is

the flux quanta ($2.07 \text{ G} \oplus \text{cm}^2$). At these conditions, vortex segments between adjacent pinning sites along the vortex line in a microwave field behave themselves like nearly independent overdamped oscillators. Using the well-known Gittleman-Rosenblum model for rf-losses of oscillating vortices and related surface resistance $R_{s,v}$ [5] one can obtain for contribution to the microwave surface resistance due to oscillating vortex segments in considered model:

$$R_{s,v} \propto \frac{B}{B_{c2}} \rho_n \frac{\omega^2}{\omega_p^2 + \omega^2}; \quad \omega_p = \frac{12P}{\eta L} \quad (3)$$

In Eq. (3) ρ_n – is the resistivity in the normal state ($T > T_c$); ω_p – is so called “pinning frequency” [5]; η – is the viscosity coefficient for vortex motion. Increase in nanoparticles concentration leads to decrease in L and growth of ω_p , thus leading to decrease of the surface resistance in accordance with Eq. (3).

For the case of implanted columnar pinning sites (nanorods or radiation tracks), the main contribution of trapped vortices to the microwave losses in the film proceeds, as we believe, due to viscous oscillations of vortex kinks, connecting parts of the whole vortex line pinned on adjacent columnar defects, as it is shown schematically in Fig.2b. We suppose a rigid pinning exerted on vortices by columnar defects and free viscous motion of vortex kinks. For this case one can obtain the contribution to the surface resistance due to kinks viscous oscillations in form:

$$R_s(B, \omega, T) = C \frac{B}{\eta \omega} \exp\left[-\frac{\varepsilon_\phi L}{kT}\right] \quad (4)$$

It should be noticed that in this case the frequency and temperature dependencies of R_s , caused by vortex oscillations essentially differ from those obtained for point-like pinning sites in (3).

4. Conclusion

Obtained results indicate that implantation of dielectric nanoparticles or radiation defects can significantly improve the superconductor film characteristics in the microwave frequency range. This artificial nanostructure can essentially decrease the surface resistance value of the superconducting film being in the Meissner state and also eliminate Abrikosov vortices oscillations and related microwave energy losses, thus decreasing the Abrikosov vortices contribution to the R_s value in the mixed state of HTS film. Such kind of nanoparticles influence on the microwave response of HTS films was observed in some recent experiments [3,4].

The work is supported by the NAS of Ukraine through the project of specialized program “ Nuclear and radiation technologies for the energy sector and community needs” (Reg. No. K-4-7-10 from 01.03.2019)

References

1. Maiorov, S. A. Baily, H. Zhou, et.al. “Synergetic combination of different types of defect to optimize pinning landscape using BaZrO₃-doped YBa₂Cu₃O₇”, *Nature Mater.* 8, 398 (2009).
2. R. Gerbaldo, G. Ghigo, L. Gozzelino, et.al., “Nanostructuring Superconductors By Ion Beams: A Path Towards Materials Engineering, Multidisciplinary Applications of Nuclear Physics with Ion Beams”, *AIP Conf. Proc.* 1530, 95 (2013).
3. R. Woerdenweber, P.Lahl, and J.Einfeld, “Improvement of the microwave properties of Y-Ba Cu-O films with artificial defects”, *IEEE Trans. Appl. Supercond.* 11, 2812 (2001).
4. S. Sato, T. Honma, S. Takahashi, et.al., “Introducing Artificial Pinning Centers Into YBCO Thin Films to Improve Surface Resistance in a DC Magnetic Field”, *IEEE Trans. Appl. Supercond.* 23, 7200404 (2013).
5. M. Golosovsky, M. Tsindlekht, and D. Davidov, “High-frequency vortex dynamics in YBa₂Cu₃O₇”, *Supercond. Sci. Technol.* 9, 1 (1996).

DIELECTRIC NONLINEARITY OF STRUCTURES Pt-Bi₁₂SiO₂₀:Ga-Pt

Panchenko T.V.*, Karpova L.M.**

*Oles Honchar Dnipro National University

49010, Dnipro, 72 Gagarin Avenue, Dep. Physics, Electronics and Computer Science,

** Ukrainian State University of Chemical Technology

49005, Dnipro, 8 Gagarin Avenue, Dep. Mechanics,

tel.(067) 98-35-466

e-mail: panchtv141@gmail.com

The temperature dependences of the real part of the dielectric constant ϵ , nonlinear current-voltage and voltage-farad characteristics before and after polarization, thermally stimulated depolarization current in structures Pt-Bi₁₂SiO₂₀:Ga-Pt were investigated. It is shown that metal nanoparticles Ga in a dielectric matrix of Bi₁₂SiO₂₀ under conditions of blocking contacts provide nonlinearity of these characteristics and a significant increase ϵ in the range 300 – 670 K and hysteresis of the current and capacity. The evolution of hysteresis loops has been examined. The results obtained explained by involving such factors as the formation of Schottky barriers, electron injection from electrodes, and the role of nanoparticles Ga in increasing the contribution of the quasi-dipole mechanism to polarization processes. It by the method of thermal depolarization analysis is revealed.

Introduction. Crystals of sillenites Bi₁₂MO₂₀ (BMO, where M = Si, Ge, Ti) are actual materials of functional electronics. They possess by a unique combination of various practically useful properties (photorefractive, acoustooptic, piezo-, photo- and dielectric) and demonstrate pronounced non-linear effects, which are used, in particular, in the devices for the recording, storing and processing of optical information. Recently, there has been an interest in these and other dielectric materials containing metal nanoparticles [1, 2]. It is shown, for example, that Co nanoparticles make it possible to control the dielectric properties of Bi₁₂GeO₂₀ crystals [2].

This paper presents the results of a study of the influence of Ga nanoparticles on temperature dependences of the real part of the dielectric constant ϵ , current-voltage (CVCs) and voltage-farad characteristics (VFCs) of Bi₁₂SiO₂₀:Ga crystals in the non-polarized and thermoelectret state in the Pt-Bi₁₂SiO₂₀:Ga-Pt structures.

Essence. Undoped Bi₁₂SiO₂₀ (BSO) crystals and Ga doped crystals Bi₁₂SiO₂₀:Ga (BSO:Ga) were grown by the Czochralski method. The content of Ga was 4·10⁻³ wt.%. Pt-Bi₁₂SiO₂₀-Pt (Pt-BSO-Pt) and Pt-Bi₁₂SiO₂₀:Ga-Pt (Pt-BSO:Ga-Pt) structures were created by cathodic spraying of Pt electrodes to 200 mkm polished BSO:Ga plates. The dependences of the current on the dc voltage I(U) (CVCs) and capacitance C(U) (VFCs) on the dc bias voltage were measured. The voltage was changed with a step of ±2V, it increased and decreased with a reversal of the sign within: U = 0÷200÷0÷-200÷0 V for the forward and reverse branches of the CVCs and VFCs characteristics. The measurements were carried out at T=300 K. The thermoelectret state (TES) was formed at temperature, voltage and time of polarization T_p= 300 K, U_p =100V and t_p=30 min., respectively. The thermally stimulated depolarization (TSD) current I(T) and the temperature dependences of the real part of the dielectric constant ϵ (T) were measured in the range T=300-800K. The measurements were automated using a micro-computer.

For non-polarized BSO and BSO: Ga crystals, the positive and negative branches of the I (U) and C (U) curves are non-linear, asymmetric relatively to the vertical (I, C) and horizontal (U) axes, and are characterized by hysteresis. The polarization of the crystals leads to an increase in the current and capacitance of the investigated crystals, and the indicated features of the CVCs and the VFCs characteristics appear more clearly. In addition, these features of the I (U) and C (U) curves should be supplemented by the dependence of their type on the number of measurement cycles with reversal of the sign of the voltage U and, especially, on the presence of Ga nanoparticles. They change the nature of the nonlinearity of forward moves of the CVCs characteristic from exponential to power, while the reverse moves remain power (Fig. 1).The

hysteresis type also depends on the presence of Ga. For undoped BSO, an excess of the reverse current over the direct current is observed (“positive hysteresis”), while for BSO: Ga, the forward current exceeds the reverse current (“negative hysteresis”). The repetition of measurement cycles leads to a decrease in the area of the hysteresis loops of the CVCs, which determines the energy dissipation in crystals, the loops become more symmetrical.

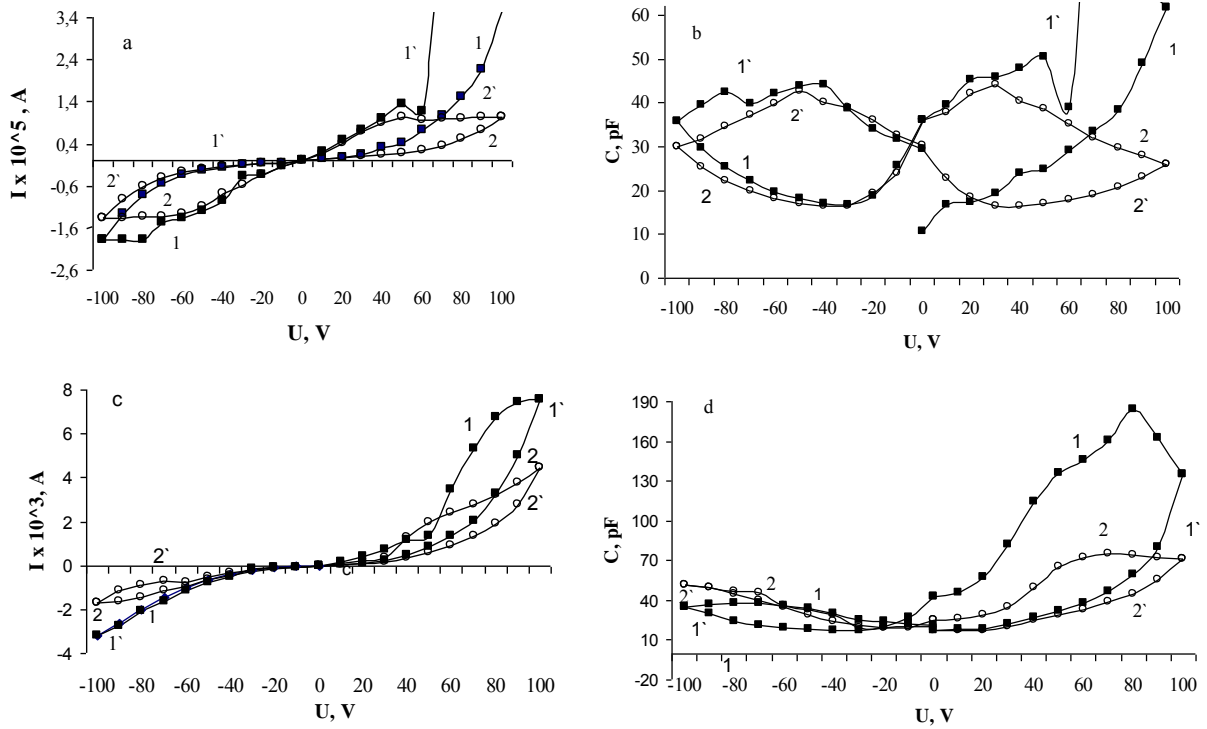


Fig. 1 – CVCs (a, c) and VFCs (b, d) of BSO (a, b) and BSO:Ga (c, d) crystals in the thermo-electret state for the first (curves 1 and 1') and the second (curves 2 and 2') measurement cycle. Curves 1, 2 correspond to forward scanning, curves 1' and 2' – to reverse one

The characteristics of the VFCs characteristics for BSO crystals are similar to those of the CVCs. Doping of Ga changes the appearance of the VFCs characteristic and violates the indicated analogy, however, the negative nature of hysteresis persists (Fig. 1).

To analyze the results, it is necessary to take into account the mechanisms of TES formation. The temperature dependences of the dielectric constant $\epsilon(T)$ and the temperature spectra of current TSD $I(T)$ observed before and after the polarization of the samples indicate a significant effect of Ga nanoparticles (Fig.2). They cause a low-temperature shift of the TSD spectrum $I(T)$, an increase in intensity and a change in the shape of its main peak with a structured dome-shaped for BSO ($T_{max} = 693$ K) to a narrow one that is close to symmetrical for BSO: Ga ($T_{max} = 500$ K), and - the appearance of additional peaks with $T_{max} = 360$ и 390 K (Fig. 2, a, b). Such a metamorphosis of the spectra indicates the participation in the polarization of electrically active defects with different thermal activation energies E_a and a different accumulated polarization charge Q_p . Before polarization, the $\epsilon(T)$ dependences of the BSO: Ga crystals, as well as the TSD spectra $I(T)$, are shifted toward lower temperatures relative to those for BSO. After polarization, the shift of the $\epsilon(T)$ curves for BSO:Ga crystals increases, while low-temperature peaks are not prescribed (Fig.2, c, d). The polarization charge $Q_p = \int I(t)dt$ with $T = T_0 + \beta t$, where $T_0 = 300$ K, $\beta = 0.16$ K/s is significantly higher than for undoped crystals.

The formation of TES is associated not only with the ratio of the contributions of the charge-space and quasi-dipole polarizations, but also with the conditions on the contacts.

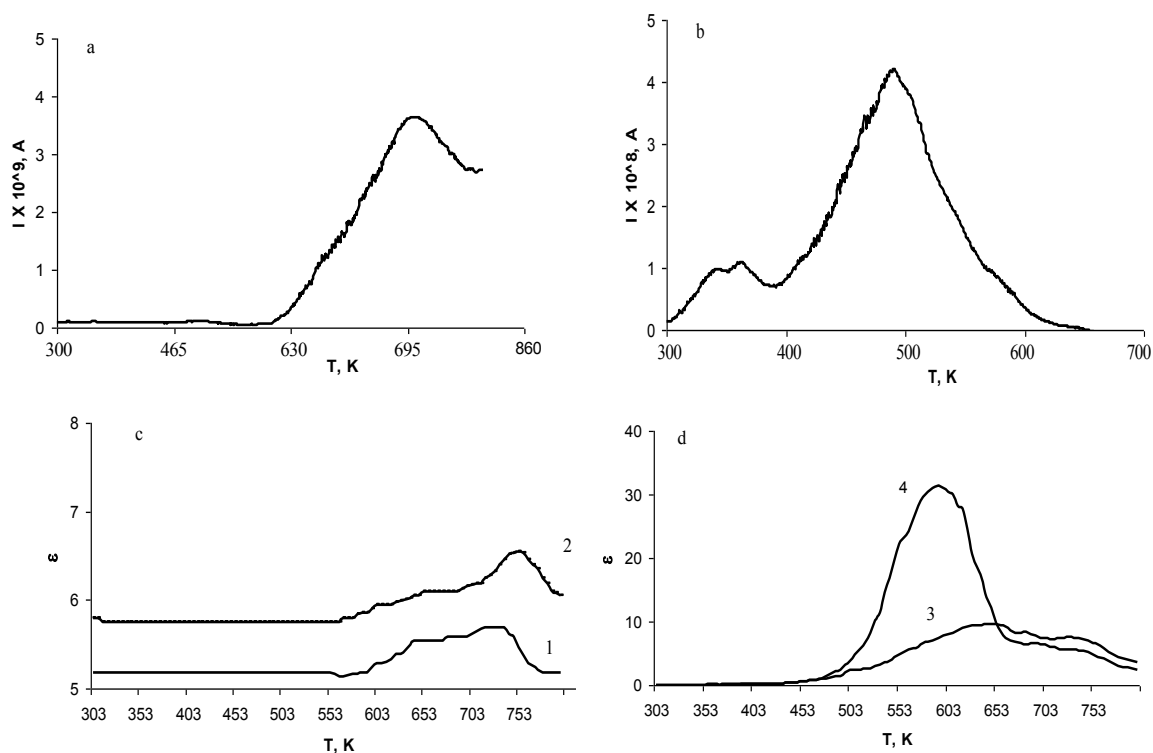


Fig. 2 – TSD (a) current spectra $I(T)$ of BSO (a) and BSO: Ga (b) crystals after polarization and temperature dependences of the dielectric constant $\varepsilon(T)$ of BSO (c, 1, 2) and BSO: Ga (d, 3, 4) crystals to (1, 3) and after (2,4) polarization

Taking into account that the work function of BSO is $A_1 = 4.5$ eV, and from the Pt electrodes $A_2 = 5.6$ eV, we see that Schottky barriers should arise at the Pt-BSO contacts. Since Ga nanoparticles cause a significant increase in electrical conductivity, the ratio between A_1 and A_2 may change so that at Pt-BSO: Ga contacts, injection of electrons from Pt will be possible.

Conclusion. Thus, the obtained features of the CVCs and the VFCs characteristics, and the $\varepsilon(T)$ and TSD $I(T)$ dependences of the Pt-BSO:Ga-Pt structures can be explained by the influence of Ga nanoparticles on the change in the type of contacts from blocking on injecting, as well as on the change in the ratio contributions of the main mechanisms of polarization in favor of a quasi-dipole.

Despite the fact that metal nanoparticles can react with the surrounding dielectric matrix and form oxide inclusions, the effect of Ga indicates the need for further study of composite materials based on BMO crystals.

References

1. Р.А.Ганеев, А.И.Ряснянский, А.Л.Степанов, Т.Усманов. Нелинейный оптический отклик наночастиц серебра и меди в ближнем ультрафиолетовом спектральном диапазоне. Физика твердого тела. 2004, т.46, вып. 2, с. 341-346.
2. С.Filipic, A.Rlos, M.Gajc, D.A.Pawlac, J.Dolinsek, A.Levstic. Dielectric relaxation in pure and Co-doped $\text{Bi}_{12}\text{GeO}_{20}$ single crystals. Journal of advanced dielectrics. 2015., v.5, №3, p.p.15500223-1 – 15500223-5.

CALCULATING OF SOLAR CELL ABSORPTION EFFICIENCY AND ENERGY CHARACTERISTICS

A.B. Galat, V.V. Bilous
Kharkiv National University of Radio Electronics
61166, Kharkiv, Nauky ave. 14, Department of Microelectronics, Electronic Devices
and Appliances,
tel. (057) 702-13-62
E-mail: oleksandr.galat@nure.ua

The solar cell efficiency is strongly dependent on its structure (the number of layers and their sizes) and material properties. First of all we have to optimize light absorption of the structure by choosing proper material and its thickness. On the other hand, the maximum efficiency is determined by the processes in the p-n junction (generation, recombination, current transfer, losses). In this case, the optimal structure can differ from the calculated one only with allowance for absorption. The optimum size of layer thickness and its ratio is not always clear.

The light absorption efficiency of some light transformers calculated in this work using analytical method. The calculations take into account the spectrum of sunlight AM1.5, the dependence of the conversion rate and absorption coefficients from light quantum energy. Calculations of energy characteristics are performed using free program SCAPS version 3.3.07.

Change of basic energy parameters, got at a calculation (V_{OC} - idle voltage, J_{SC} – current of short circuit, FF - factor of filling, η - efficiency) corresponds to the change of light absorption efficiency.

1 Introduction

Solar cells are made in the form of structures based on crystalline (c-Si) and hydrogenated amorphous silicon (a-Si: H), cadmium telluride (CdTe), indium diselenide ($CuInSe_2$ - CIS), gallium diselenide ($CuGaSe_2$ - CGS), and $CuIn_{1-x}Ga_xSe_2$ - CIGS solid solutions, etc. The cost of solar energy is still too high, and the costs of manufacturing and disposing of solar cells hinder their distribution. Improving the efficiency of photoconverters depends primarily on their absorption capacity and the conversion rate of solar energy into electrical energy. Absorbency is determined by the dependence of the absorption coefficient of the material on the wavelength in the range of solar radiation. The most effective in this regard are solid solutions of $CuIn_{1-x}Ga_xSe_2$ - CIGS (for single junction structures). The calculations of the absorptivity of solar cells, that are made on the basis of various materials [1, 2], are based on the known spectral distributions of the absorption coefficients of materials in the range of the main flux of solar radiation.

In order to adequately compare the efficiency of light absorption by different materials, their absorption coefficient should be taken into account in the range of at least 0.3 ... 2.5 μm , in which more than 99% of the solar energy reaching the Earth's surface is located. Therefore, the efficiency of the photoconverter must be calculated taking into account the ratio of the values of absorbed to the incident power in the specified spectral region. Obviously, such a wide range requires the use of several active layers (tandem photovoltaic cells) for maximum absorption effect [2].

At the same time, the energy characteristics of solar cells are determined by the ability of the structure to convert the absorbed light into electric current in an external circuit. This process depends on the efficiency of generation, current transfer, minimization of losses in the structure.

The paper presents the results of calculations of the absorptivity of the most promising materials of solar photoconverters. The calculations were made on the basis of an improved technique [1, 2] and allow comparing the absorption efficiency of the spectrum of 0.3 ... 2.5 μm

for multilayer thin-film structures. The calculations of the energy characteristics of such structures using numerical methods were also performed.

2 Method of calculating the absorption efficiency of a multilayer solar cell

The spectrum of solar radiation is studied in sufficient detail and presented in publications. The distribution obtained by the American Society for Testing and Materials (ASTM) [3] for certain atmospheric conditions and geographic location was used. This distribution was used for calculations in this work (Fig. 1). The upper graph is the spectral power density of solar radiation outside the atmosphere (AM0). The average is actually the AM1.5 dependence used in the work, taking into account the radiation scattered by the atmosphere (according to Rayleigh's law). The lower chart is the direct solar izkucheniya AM1.5. Accounting for radiation scattered by the atmosphere, as can be seen from the graphs, adds power mainly in the visible part of the spectrum. In general, this additive is about 10%.

The distribution is presented in the range of 0.25 ... 4.0 μm , however, as can be seen from Fig. 1, most of the AM1.5 Global power flow of interest to us is in the range of 0.3 ... 2.5 μm . It is logical for all studied materials to use the same range of 0.3 ... 2.5 microns, which was done in this work.

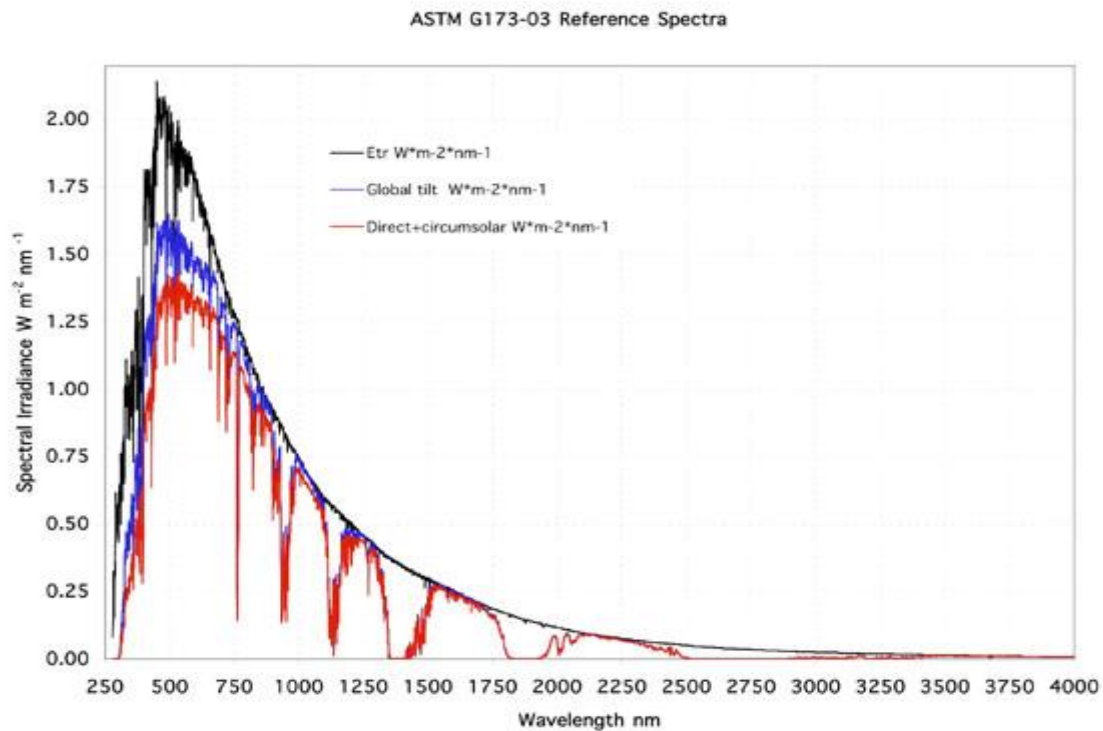


Fig. 1 – Distribution of spectrum of sunny radiation of AM0 (Etr), AM1.5 taking into account dispersion of light (+10%) (Global), direct AM1.5 (Direct)

To confirm, calculations were made of the power density of the radiation spectrum of the Sun AM1.5 Global, cut from above by the wavelength [1]. Calculations show that in the range of 0.3 ... 2.5 μm , 99.1% of the total power of solar radiation falls on the Earth. The literature data for measuring the power density of the Sun give 0.846 kW / m^2 for AM1.5 Direct + and 0.93 kW / m^2 for AM1.5 Global, which is in good agreement with the calculation. Since the solar spectrum is represented by a discrete function [3], it is possible to use these data directly in the calculations of the absorptivity. The spectral dependences of the absorption coefficients are

represented by experimental curves with a sufficiently large error; when these dependencies are discretized, an additional error is introduced.

Considering this, the above dependences were processed, the spectrum range of interest to us was divided into subranges of 10 ... 50 nm in size (the size is dictated by the required accuracy of the calculations). For the calculations of the absorption capacity A the expression was used [1]

$$A = \frac{\sum_{k=1}^K [F_k \cdot \lambda_k \cdot [1 - (\prod_{m=1}^M e^{-\alpha_{mk} \cdot d_m})]]}{\sum_{k=1}^n [F_k \cdot \lambda_k]}, \quad (1)$$

where F_k – solar power power density AM1.5 Global, averaged over the k-th subband of the spectrum;

λ_k – wavelength corresponding to the middle of the k-th subband of the spectrum;

α_{mk} – material absorption coefficient of the m-th layer, averaged over the k-th subband of the spectrum;

d_m – material thickness of the m-th layer;

k – number of the subrange of the spectrum;

m – number of the layer of material in the structure;

K – number of subranges of the spectrum into which the main emission range is divided;

M – number of layers of various materials in the structure of the photoconverter.

In each subrange we determine the average value of the functions F_k , α_{mk} , λ_k . These data arrays are used in the program for direct calculations.

3 Calculation of the absorption efficiency and energy characteristics

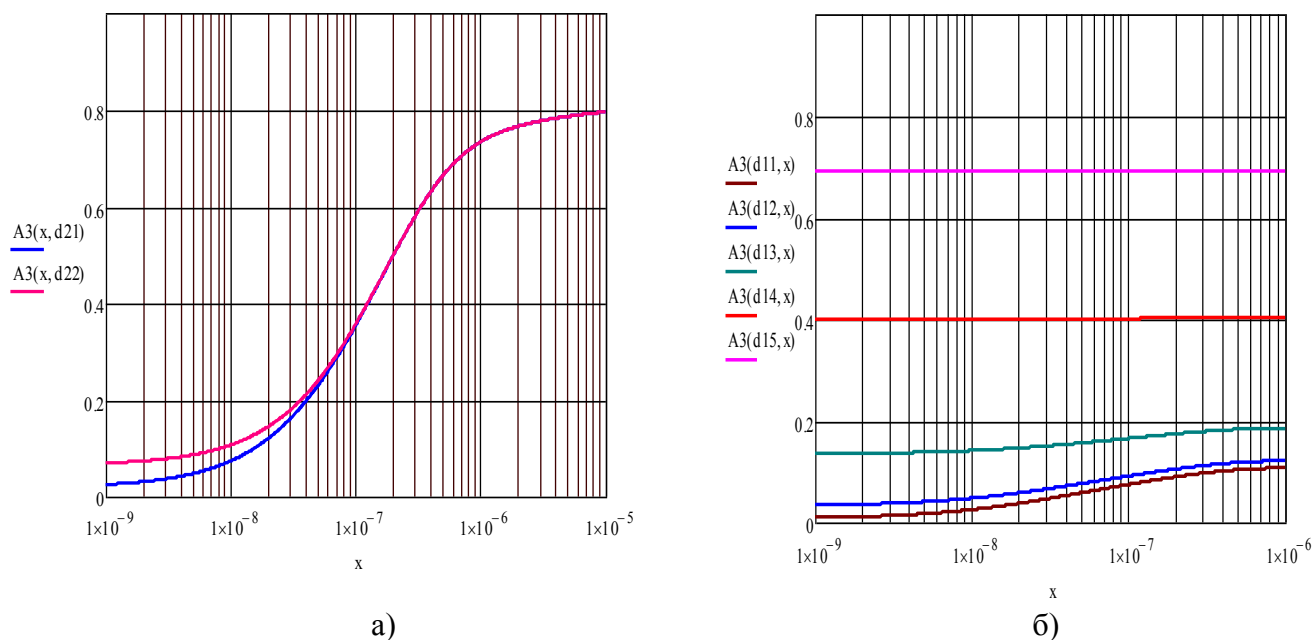
Absorbance calculations are presented for a single junction CdS / CIS bilayer structure, which is considered one of the most promising [2,4]. The results of the calculations make it possible to more adequately estimate the absorption of radiation in the spectral range of 0.3 ... 2.5 μm , as well as reasonably compare the absorption capacity of various materials used for solar converters [4].

Calculations of energy characteristics are performed using the free program SCAPS version 3.3.07 [5]. The main results of the calculations are given in Table. 1. Designations: W - CIS layer thickness, V_{oc} - no-load voltage, J_{sc} - short circuit current, FF - IVC filling factor, η - efficiency.

Table. 1 – The results of the calculation of main photovoltaic converter parameters

W, mkm	2	3	4	5	6	7	8
V_{oc} , V	0.610	0.621	0.626	0.629	0.630	0.631	0.632
J_{sc} , mA/cm ²	33.8	34.7	35.2	35.5	35.7	35.8	35.9
FF, %	79,6	80.4	80.7	80.9	81.0	81.1	81.1
η , %	16.5	17.3	17.8	18.1	18.2	18.3	18.3

For an example in fig. 2 shows the calculations of the absorption capacity of the two-layer structure of CdS / CIS with a change in the thickness of the layers from 1 to 10,000 nm.



a - when changing the thickness of the CIS layer and the thickness of the CdS layer of 10 and 80 nm, b - when the thickness of the CdS layer changes and the values of the thickness of the CIS layer are 1, 5, 25, 125 and 625 nm

Fig. 2 – Absorbency of CdS / CIS two-layer structure

4 Conclusions

In this paper, it is proposed to use analytical calculations of the absorptive capacity of multilayer solar cells and numerical calculations of their energy characteristics to determine the optimal structure of the solar cell. Analytical estimates of radiation absorption by different materials make it possible to choose the thickness of the layers in the first approximation, and the energy characteristics calculated by the SCAPS program make it possible to refine all the parameters of the solar cell structure. The results of the calculations show that the relative change in the energy parameters of solar cell (V_{OC} - idle voltage, J_{SC} - short circuit current, FF – IVC filling factor, η - efficiency) when changing the thickness of the main absorbing layer GIS practically repeats the change in the absorption capacity of the structure obtained by the analytical method .

1. Галат А.Б. Расчет поглощательной способности солнечных фотопреобразователей // 9-я Международная научная конференция «Функциональная база нанoeлектроники». Сб. науч. трудов. – Харьков: ХНУРЭ, 2017. – С.103–106.

2. Новиков Г.Ф., Гапанович М.В. Солнечные преобразователи третьего поколения на основе Cu-In-Ga-(S,Se)/ Успехи физических наук. – 2017. – Т.187. –№2. – С.173–191.

3. <http://www.astm.org/>

4. Натарова Ю.В. Исследование фотоэлектрических преобразователей на основе различных полупроводниковых материалов /Ю.В. Натарова, А.Б.Галат , А.С. Гнатенко //Журнал нано- та електронної фізики, 2018, Том 10 № 4, 04023-1–04023-6

5. SCAPS Manual / Burgelman M., Decock K., Niemegeers A. et al. URL: <https://users.elis.ugent.be/ELISgroups/solar/projects/scaps/SCAPS%20manual%20november%202018.pdf> (дата звернення – 05.01.2019)

NANOSATELLITES OF THE POLYITAN SERIES: RESULTS OF EXPERIMENTS AND PROSPECTS FOR DEVELOPMENT

¹*B.Rassamakin, ¹M.Ducheiko, ¹N.Bayskov, ¹S.Ostapchuk, ²A.Lauch,*

³*E.Lanevsky, ¹V.Hominich, ¹R.Melnyk, ¹I.Starovit*

¹National Technical University of Ukraine “Igor Sikorsky Kyiv Polytechnic Institute”, Ukraine;

²CB “Centr”, Smila, Ukraine;

³Diona LLC, Kyiv, Ukraine

bmrass@gmail.com

This article gives general information about the goals, requirements of missions and describes how these requirements are expressed in the development of nanosatellites (NS) of the PolyITAN series of CubeSat standard. The report also discusses the integration of electronics with the design and payload, provides information on the applied manufacturing methods and tests of NS of various modifications for performing tasks in orbit. The analysis of the results of flight tests of the NS (PolyITAN-1 and PolyITAN-2) and potential capabilities of the developed NS “PolyITAN-3” (assessment of the quality of shooting when sensing the Earth from an altitude of 400 ... 350 km) and “PolyITAN-4” (features of simulating the environment and plant growth under microgravity and cosmic radiation).

1. Model of nano-satellite “PolyITAN-1”

Leading universities of the world are now actively encouraging students to create nano-satellites - small spacecraft, the so-called international standard “CubeSat” (U1 format (single unit) corresponds to a mass of about 1 kg and dimensions of 10×10×10 cm). In addition to solving purely educational purposes, such spacecraft in the future may be used in the implementation of a number of scientific, technical and social projects for different purposes. Standard “CubeSat” makes it possible to create miniature satellites weighing 1-10 kg in a short period of time (1-3 years) and with relatively small means. Such work is carried out in dozens of scientific centers around the world. The rapid development of the element base gives hope for the commercial application of these spacecraft. The establishment of such satellites allows the space research at relatively low financial cost and it is actual for Ukrainian conditions with its high potential in the field of designing and developing of space technology [1-6].

Restrictions on mass, volume and surface area, in particular solar cells, require the development of extremely efficient design of CubeSat standard nanosatellites (NS). According to it, Igor Sikorsky Kyiv Polytechnic Institute has created the NS series named **PolyITAN**. Launched in 2009, the NS “PolyITAN-1” project is a joint activity of researchers, teachers and students of a number of faculties of the KPI, who first created the space electronic platform of the NS.

Objectives of KPI “PolyITAN-1” nano-satellite launch: the development and research of solar sensors for small satellites; check of the power circuitry between the solar panels and batteries, developed at the University; improvement and adaptation of digital radio information and control commands transmission to the space environment; exploration of space influence to the operation of electronic subsystems; study the functioning of the navigation subsystem of global signal receiver GPS / GLONASS.

Nano-satellite was launched into orbit 19.06.2014 with the carrier rocket “Dnepr” as a part of the cluster starts. Beacon EM0UKRI of “PolyITAN-1” satellite has been heard in the early hours after the launch at the telemetry control and collection center of the university NTUU “KPI”, it also was recorded by radio amateurs of Japan, Germany, Britain and others. Today, nano-satellite is operating in low-Earth Sun-synchronous orbit at a distance about 620 km from the Earth, duration of its circulation is 97.8 minutes. At every 5th out of 16 daily turns around the Earth in a short time (2-9 minutes) it is possible to communicate with the spacecraft from the ground station established in KPI. During these moments developers get information about the functioning of the nanosatellite subsystems, required for future work.

1.1 The design and subsystems of nano-satellite “PolyITAN-1”

Nanosatellite “PolyITAN-1” is a typical single block nano-satellite CubeSat 1U format. It is a cubic frame carcass, which houses electronic circuits (Fig. 1, a).

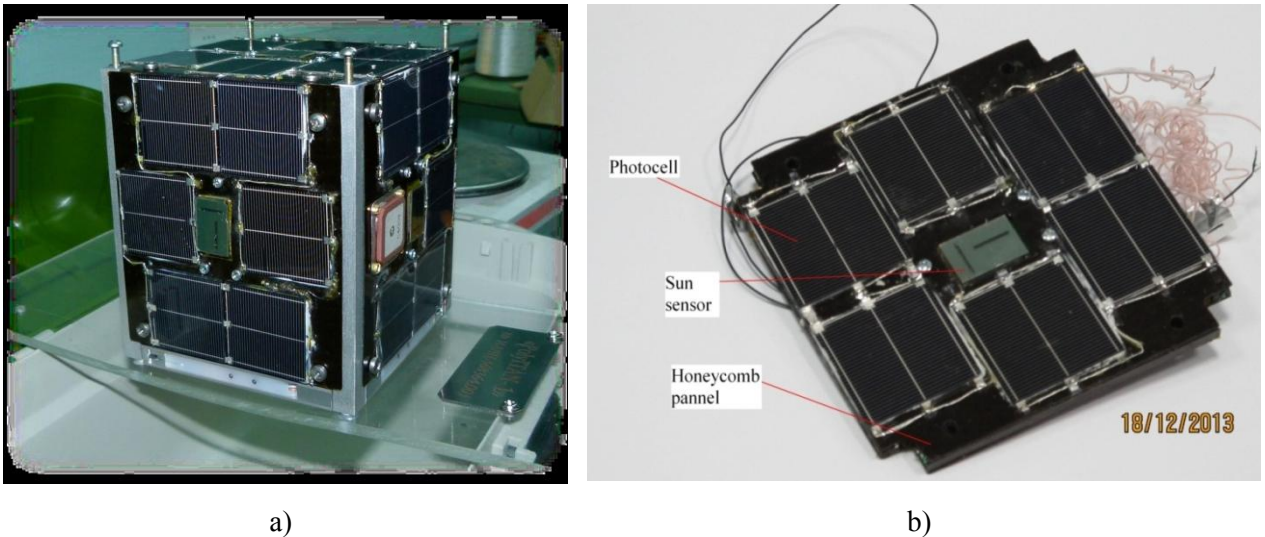


Fig. 1. General view of the university nanosatellite “PolyITAN-1”(a) and Solar battery on honeycomb carbon fiber frame and the coordinates of the Sun Sensor (b)

The side faces of the cube are ultra-light multilayer honeycomb panels frames of carbon fiber and aluminum honeycomb, the so-called "sandwich panels" (Fig. 1, b). They are designed for temperature control, protection against electromagnetic radiation and placing on them the photovoltaic solar panels. Solar panels are silicon photovoltaic cells (29 units) with conversion efficiency up to 20%. On the side of the cube, which is directed to Earth in the flight, there are 4 radio remote antennas unfolding in orbit. On the three adjacent panels of the cube there are placed Sun coordinate sensors.

The satellite structure includes a subsystem boards with electronic components, which are typical for this class of nano-satellites.

Power supply system (PSS) includes: solar cells as the primary power source; battery (optional power supply); electronic control board of the power supply system, which is designed to monitor and control the energy state of the battery and ensure the supply of the various subsystems of the onboard complex. The features of the designed power supply system are: the presence of an individual subsystem controlling the charge of battery cells; hot backup subsystem; built-in protection for over-current and thermal protection. PSS provides: maximum power selection mode from the solar battery; energy saving mode with low power consumption of other systems; the ability to monitor the voltage and current of the solar and rechargeable batteries; the ability to monitor the temperature of the basic units.

The structures of a data processing system are:

a). on-board computer (BC), which coordinates the work of the on-board service complex subsystems and provides operating with a data of payload and on-board complex. BC composition: software, optimized in time (sequence diagram of BC operation) and power consumption (energy saving sleep mode); a beacon function for radio telemetry on request; multi-layer circuit board with processor ARM Cortex-M4;

b). navigation subsystem that includes a receiver of signals of standard accuracy navigation system GPS/GLONASS and receiver antenna;

c). orientation and stabilization control subsystem (OSCS) is designed to: quenching the initial angular velocity of nano-satellite after separation from the launch vehicle and its orientation in the orbital coordinate system; provide three-axis orientation of the nano-satellite with a given accuracy; determining the orientation of the nano-satellite in normal / standby mode. OSCS includes electromagnets, Sun coordinate sensors (located on the faces of the nano-satellite), a magnetometer and an angular velocity sensor.

Features of the transceiver subsystems (radio): the electronic board and software are own development of NTUU "KPI"; includes redundant channels; there are provided low-power modes of radio channels; applied AX.25 protocol in Modbus protocol environments [1]; hardware implementation provides a high quality output. The communication subsystem comprises: an electronic unit, comprising two receivers and two transmitters 145 MHz and 437 MHz; antenna-feeder devices of receiving and transmitting equipment for these frequency bands; high-frequency waveguide cables set; set of connecting cables. It has been proposed and produced a fundamentally new scheme and subsystem solutions, defined the energy potentials of radio system and main expected performance characteristics.

The results of the analysis of the basic nano-satellite characteristics and parameters, calculations of the radio system energy potential “ground control station (GCS) – nanosatellite” and “nanosatellite – GCS” were confirmed by the flight experiment.

1.2 The ground control station

The nanosatellite ground control station (Fig.2) is made on the basis of the transceiver ICOM-910H with the following parameters: a transmitter power of 35 watts, the receiver sensitivity of 0.18 mV, FM and CW modulation. The developed version of the radio and control subsystem includes two radio link: A radio link “up” (ground control and receive station - satellite (“uplink”), which is used to transfer command information; and radio link “down” (satellite - ground control and receive station (“downlink”), used for the transmission of telemetry and other information.

The composition of ground segment of nanosatellite control, including: radio transmitter (RT) of command information, radio receiver (RR) for receiving information from the on-board systems, radio modem for the primary message processing, separate antenna systems of RT and RR, antennas tracking guidance and display control system, personal computer, tachometer with software for RT and RR control, software for antennas tracking guidance and display control system. The composition of the board includes: radio transmission device for transmitting information from the on-board systems, radio receiver for command information, radio modem for primary messages processing, separate antenna systems of RT and RR.

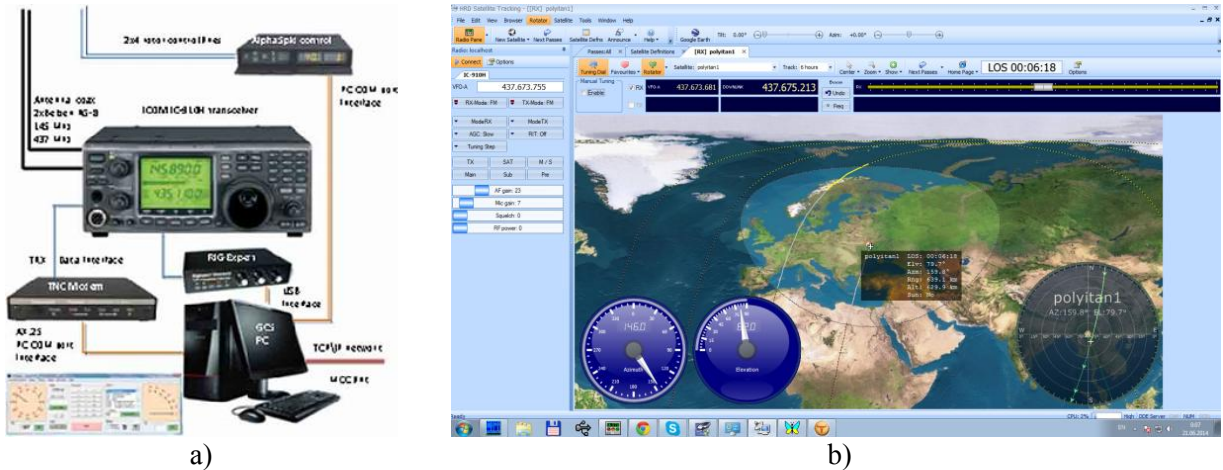


Fig. 2. The ground control station of nano-satellite scheme (a) and specialized program view (b)

Whereas it is necessary to provide at the frequency 437 MHz the reception of data from the ground station, and their transfer to it, it was considered possible variants of transceivers, minimizing weight and size.

2. Model of nano-satellite “PolyITAN-2-SAU”

At present, the PolyITAN-2-SAU launched into the near-Earth orbit is part of the scientific space network of the QB50 project intended for studying the thermosphere. The main task of the QB50 project is to study the Earth's climate change. The NS carries a payload on board – an experimental sensor for analyzing the oncoming gas flow FIPEX, capable of distinguishing and measuring the characteristics of atomic and molecular oxygen, which is the main element at altitudes of 90-420 km from the earth's surface. This is important for the assessment of thermosphere models.

2.1. Object of Study

Structurally, NS “PolyITAN-2-SAU” is the successor of the previous model (NS “PolyITAN-1”) designed at NTUU “KPI” and launched into Earth orbit in 2017 (finished mission in 2019 when was burned in the Earth’s atmosphere) . The results of the first run and participation in QB50 mission allowed significant changes in the NS design. Thus, “PolyITAN-2-SAU” is a 2U (2-Unit) format, with a payload,

which is a thermosphere composition analyzer FIPEX. This is the main difference compared to the first model (PolyITAN-1 is a 1U), which is caused by a special range of tasks to be carried out of the NS.

The key to finding innovative solutions is the need to comply with the requirements of the NS QB50 project, under which the payload is ready to be installed on the projected satellite. Thus these are size, layout, set of subsystems, which should provide integration, and the ability to manage the already developed FIPEX (Fig.3).

Payload is FIPEX (Flux-Probe-Experiment) – parser of the thermosphere composition, developed at Dresden Technical University, which is able to distinguish and measure the behavior of atomic oxygen, as a key element in the lower thermosphere, in the time domain [7].

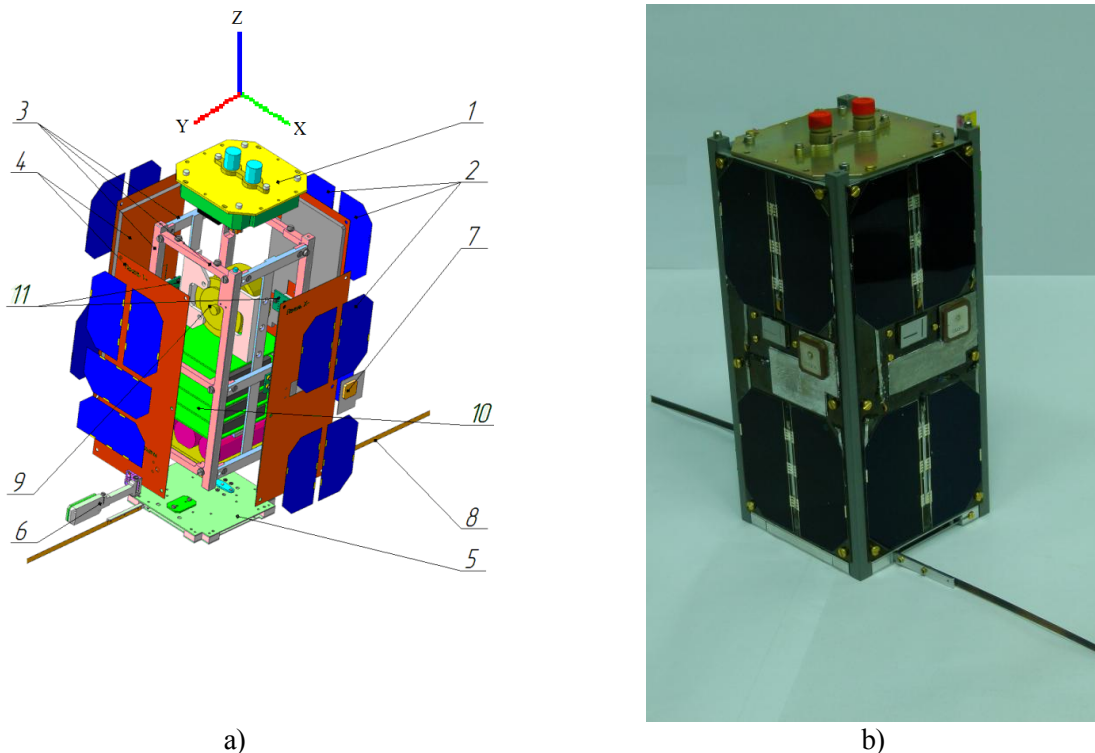


Fig. 3. Engineered (a) and real (b) view of “PolyITAN-2-SAU”:

1 – payload (FIPEX); 2 – solar battery; 3 – satellite case; 4 – honeycomb panel; 5 – aerial module; 6 – magnetometer with deployment mechanism; 7 – GPS/GLONASS aerial; 8 – radio aerial; 9 – flywheel; 10 – electronic platform; 11 – Sun direction sensor.

2.2. Thermal vacuum testing

Thermal vacuum testing, during which was simulated the effect of space factors on the NS and its parts, is one of the important stages in the development of “PolyITAN-2-SAU”. Significant factors of space for the thermal vacuum test are: low temperature, vacuum, space blackness, Sunlight and reflected radiation from the Earth [3, 6–8].

During its orbital motion, NS continuously falls under various influences – Sun radiation, Earth radiation etc., which significantly affect the thermal state and thermal mode of the NS systems, and thus the reliability and efficiency of the NS elements in flight.

At various intervals, the impact of these factors will vary: depending on the NS position in orbit and on the functioning conditions of its systems the carcasses surfaces will be exposed to variable heat flows of different intensity, which will determine the thermal state of subsystems and elements of NS, including its electronic equipment [6, 7].

One of the main characteristics that determine the readiness of the NS PolyITAN-2-SAU to start is conformity of the temperature conditions of the electronic platform and equipment of the NS to their operating temperature range. Thus the result of thermal vacuum test should conclude that during the imitation of external and internal heat evolution, temperatures of NS elements do not exceed their permissible limits. Also during the test there was made the checkup of the functional ability of the satellite subsystems to perform their tasks at the orbit, and confirmation of the correct thermal regulation

of NS systems. Also, tests are needed to fulfill international QB50 project requirements. This includes checking performance and capability to control the payload under the impact of space factors.

To carry out the necessary tests simulating thermal vacuum chamber TVC-0.2 [7] was used, which is the single set of tools and equipment that provides the necessary space conditions simulation. This camera is designed specifically for the NS research, elements of space technology and small-sized spacecraft. This camera is located in the NTUU “KPI”, a general view and a block diagram of modeling facility TVC-0.2 is shown in Fig. 42. The diameter of the cylindrical part of the chamber is 0.5 m, height is 0.6 m. The pumping system consists of the oil diffusion pump H-2 T-3 and two fore-vacuum pumps. Pumping speed equals to 1500 l/s, and the ultimate pressure test is 10^{-5} Pa. Imitation of solar flux is carried out by solar radiation simulator (SRS), a xenon lamp.

The optical system in the working zone of the chamber provides a radiant heat flux, the power and spectral characteristics of which are close to the solar radiation of the open space. Solar radiation imitator is located outside the chamber and let the beam of light pass through the inspection hole. Earth radiation simulator (ERS) (4) is copper heater formed as a plate which is fixed directly under the NS. The measuring system is designed to measure temperature dependences, and uses copper-constantan thermocouple and copper resistance thermometers as sensors, which are attached to the NS, as well as temperature sensors, which are structurally a part of the NS, and are located on the electronic platform and the battery unit.

As a result of the test, rotation of NS around the Earth was simulated and the temperature dependence of its components, on which temperature sensors were placed, was received. The Fig. 4 shows the temperature dependence of the inner sides of honeycombed structure which serves as frame, i.e. the temperature distribution on its planes.

The graph is divided into 3 parts, which correspond to three different simulation cycles of NS turnover in its orbit. Also the graph shows the temperature of creoscreens TVC-0.2, i.e. the temperature of the surrounding space of the NS. It can be seen that the maximum temperature corresponds to the temperature of the parts and Z+ and Y+ in the beginning of the cycle, as solar radiation falls on these faces at a small angle relative to the normal line. At the same time the coldest face of X+, as in the process of rotation NS Sun's rays almost do not fall on it. It can be stated repeatability of values from cycle to cycle, what is a necessary condition for thermal vacuum tests. Temperature limits varies ($-55...+20^{\circ}\text{C}$), which corresponds to the capabilities of the normal operation of the NS, as well as correlate with previously conducted mathematical modeling.

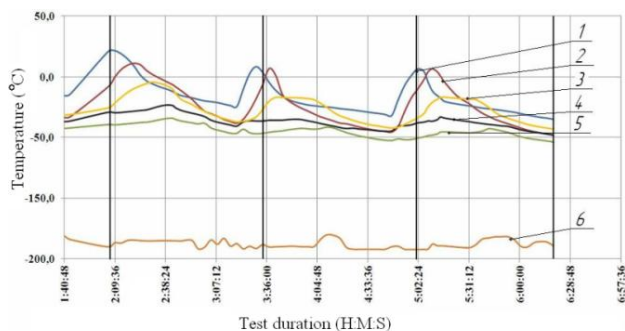


Fig. 4. Distribution of temperatures on the inner sides of the NS honeycombs: 1 – side Z+; 2 – side Y–; 3 – side X–; 4 – side X+; 5 – side Y+; 6 – cryo shields.

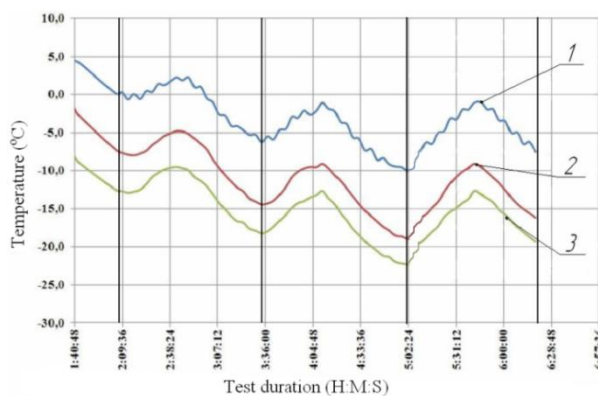


Fig. 5. Distribution of temperature on the electronics boards of NS: 1 – radio channel board; 2 – CPU board; 3 – FIPEX board.

Fig. 5 is a graph showing changes in temperature values on the control board of the payload, on the radio board and the CPU board. As can be seen from the chart, board temperature does not significantly dependent on external factors and changed slightly from the Sun to the shadow mode ($2...3^{\circ}$). The maximum temperature is presented on radio board ($+3...-10^{\circ}$), then the CPU board ($-5...-20^{\circ}$) and the control board of payload ($-10...-23^{\circ}$). Based on the data it can be stated that the electronic system of NS is within acceptable temperature limits. Also worth noting the practical independence of temperature between the NS of orbital position, and fluctuations in the radio card, which can be observed in the course of the experiment — those are the results of the performance of this NS element. As a result, thermal vacuum tests: - studied the temperature distribution on the modules, assemblies and construction

elements of the NS, electronic board surfaces, depending on the external radiant heat fluxes corresponding to movement of NS by the proposed orbit; - revealed the limits of temperature fluctuations of the NS elements caused by modeling of changes in its orbital position; - confirmed the performance of the NS equipment under conditions consistent with the orbital.

According to test results, it can be concluded that the engineering model of the NS sustains thermal loads and can operate in space in normal mode.

2.3. Strength and dynamic analysis

“PolyITAN-2-SAU” is made according to the non-hermetic scheme in the CubeSat satellite bus. One of the most important stages in the design and ground testing is the task of ensuring the strength of the NS at various stages of its life cycle, including a comprehensive calculation and experimental analysis of the dynamics and strength of the NS.

The main and most responsible from the point of view of the mechanical loads acting on the NN is the stage of launching into orbit. At this stage, the NS experiences maximum quasistatic overloads [10], harmonic and random vibrations, impulse and acoustic effects. At the launch stage, NS is located in the launch container ISIS-POD. The NS lower end faces are supported by a spring pusher, the upper ones on the cover of the launch container.

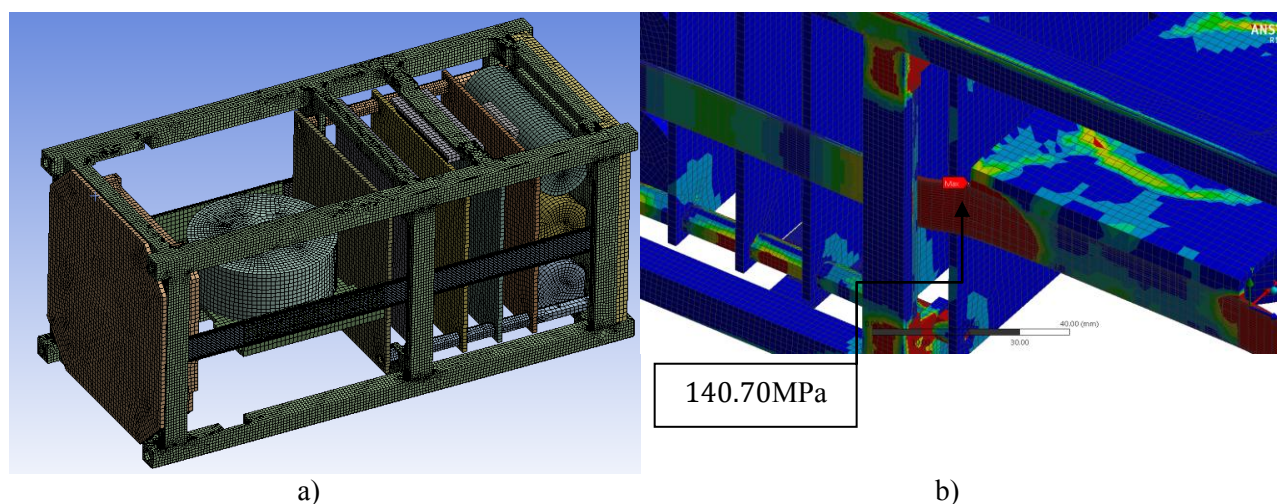


Fig. 6. “PolyITAN-2-SAU” Finite Element Model (a) and distribution of stresses in the bridge of the support frame in the section of fastening of the SOS bracket for the X-axis overload option (b).

The dynamic and strength cycle of work implies:- Static analysis;- Modal analysis;- Harmonic and random vibration analysis. According to the requirements of QB50 and ECSS-E-HB-32-26A, for nanosatellite there is no need to check the strength of acoustic and impulse actions due to small overall dimensions of the NS and the conditions for placing the ISIS-POD on the carrier rocket adapter.

The finite-element model (FEM) of the NS generated in the ANSYS [10] and shown in Fig. 6a. For approximation of the framework, scientific module (FIPEX), stacking racks of the EP, batteries and antenna module we used 20 hexagonal finite elements (FE) SOLID186. To approximate the SOS brackets and electronic circuit boards we used FE SHELL181 with 4 layers in thickness. The articulation of plate and volumetric FE was carried out by means of massless absolutely rigid bonds based on two-node beam elements BEAM188. Conjugating fragments of FEM with different partition densities, contact elements of CONTA174 were used with the same type of FE. The obtained rational FEM NS, consisting of 326,300 elements with 1,221,504 nodes (Fig. 6a), was used for static, modal, harmonic and random vibration analysis.

In quasistatic analysis, the conditions for placing the NS in the shipping container were taken into account by setting zero displacements ($u_x = u_y = u_z$) of the frame supporting surfaces, with the exception of longitudinal ($u_z \neq 0$) for the side ribs (Fig. 6b). It was found that the largest Mises stresses

occur in the frame bridge (material - D16) near the attachment points to the SOS brackets (Fig. 6b). In turn, in the stacking rack of the EP (material - L63), the stress is realized during overload in the vicinity of the contacts with the central board. Among the electronic circuit boards of the EP, the lower one is the most loaded, for which in case of an overload at the points of contact with the stacking racks.

The strength of NS is determined from the following conditions:

a). The absence of plastic deformation under the action of limit loads.

b). The absence of destruction in the structural elements of the NS under the action of design loads.

As a result, it was established that the maximum total von Mises stresses (179.06 MPa) occur in the frame bridge near the mounting locations of the SOS brackets when the NS is loaded in the direction of the X axis. In this case, the factor of safety for the limit $\eta_L = 1.12$ and ultimate loads $\eta_U = 1.30$. For the developed design of the NA PolyItan-2-SAU, a rational combined ECM is constructed, containing volumetric, shell, beam and contact EC. Calculated way, amplitude-frequency characteristics and parameters of VAT in PolyItan-2-SAU structural elements are determined on the basis of a single CEM under the action of quasistatic overloads, harmonic and random vibrations corresponding to the elimination stage. It is established that, in accordance with the requirements, the considered PolyItan-2-SAU design is rational in terms of strength.

3. Future projects of PolyITAN series

The mission of the project “PolyITAN-3” (for Earth sensing) is creation of 3U CubeSat nanosatellite by developing, modeling and researching effective service subsystems to provide a payload – an optoelectronic scanner with a capability of shooting in the range of up to 30 m when operating in orbit at altitudes up to 700 km.

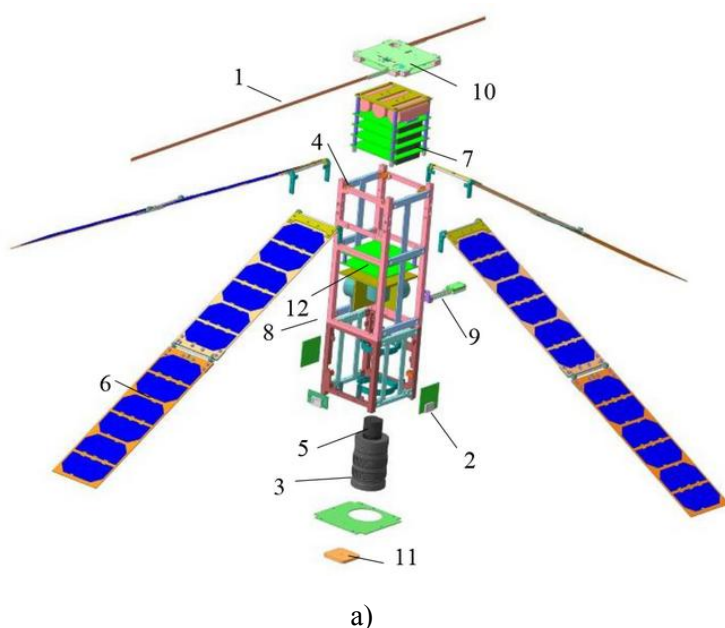


Fig. 7. “PolyITAN-3” engineering model (a): 1 – antenna 144/435 MHz, 2 – solar sensor, 3 – camera lens, 4 – frame, 5 – camera, 6 – solar panels, 7 – electronic platform, 8 – flywheel, 9 – magnetometer, 10 – antenna module, 11 – high-speed antenna, 12 – electromagnet board; and real photo (b).

“PolyITAN-3” (Fig. 7) is 3U CubeSat satellite with camera for remote sensing. This feature is associated with new challenges in the thermal control system and the power supply of the satellite. Solar panels have the form of 4 wings, each wing consists of two modules of six elements. The modules are connected in the wing by the mechanism of opening and connected in series. In addition, a high-speed radio link module is used. It has the following properties: 5.7 GHz 800 kB, 2 W; and will be used for transfer of images to the earth station.

All previous work has been carried out, such as selection and development of equipment, electric and thermal calculations, etc. A thermal model of the nanosatellite was created, and a numerical calculation was also carried out in the ESATAN-TMS program. Now the satellite is being assembled, and scheduled to produce thermal-vacuum test.

The feature of the “PolyITAN-4-BIO” mission

Plants are an indispensable component of bioregenerative life support systems for long-term space missions (long-haul flights and extraterrestrial bases), as the plants act as oxygen and water regenerators, a source of food and utilization of vital products. Summarizing the numerous biological experiments conducted on different spacecraft, we can conclude that microgravity is not a factor that limits the growth, development and reproduction of plants. An important condition for the successful cultivation of plants in space is the use of elite seeds and maintaining certain conditions for plants cultivation. It is impossible to predict the stability of plants in life support systems to space flight conditions over long flights, since almost all plant objects grown on space platforms are annual plants with a short life cycle (up to 6 months), and the duration of most experiments on board The International Space System (ISS) did not exceed 30 days. It is advisable to conduct long experiments with plants in simplified, compared with those used on the ISS, growth chambers, in order to establish a record for the duration of stay of higher plants in the active physiological state in space flight (up to 3 years). Such an experiment can be carried out on the platform of a small satellite CubeSat, using the technology created and successfully tested in space conditions created by National Technical University of Ukraine “Igor Sikorsky Kyiv Polytechnic Institute” and microcosm technology – growing plants in a closed gas environment, which was developed in the National Botanical Garden. M.M. Grishka NAS of Ukraine. In a unique experiment at this institution, the plants show the ability to grow in a closed gas environment for a long time (currently the duration of the experiment is 12 years).

Carrying out the experiment and promoting it in the media has a powerful image component and will promote the promotion of cosmonautics and the attraction of young people to pre-scientific space exploration.

The technology of the developed unit for long-term cultivation of plants in microgravity can be applied for the implementation of space experiments in the future, as well as being a tested basis for the creation of new cultivation chambers for growing plants aboard spacecraft. With plant life support system (temperature and lighting) from on-board telemetry and model experiments on plant growing is created in a stationary unit under stationary conditions with observation of the condition of plants growing in a stationary unit. Creating such a system will allow for various biological experiments on the CubeSat platform.

The proposed space experiment is unparalleled and will be the first attempt at long-term exposure of several species of plants in space flight in a power unit. Information on the resilience of such an artificial ecosystem to the long-term impact of microgravity is a prerequisite for the creation of bioregenerative life support systems and the implementation of their long-term space missions.

The feature of the “**PolyITAN-4-BIO**” mission is current impossibility to give a positive forecast for the stability of higher plants in the conditions of space flight during long flights; since almost all vegetable objects that have been grown on space platforms are annual plants with a short life cycle, and the duration of most of the experiments aboard the ISS did not exceed 30 days. Plants are considered as a source of food and oxygen in bioregenerative life support systems of long space missions. The satellite design includes a hermoblock with a system for maintaining the viability of plants: fibrous substrate, grating for a substrate, NIR-camera for shooting (observing the state of plants), fan with protection, LED lighting, system for monitoring the environment inside.

Hermetically sealed block potentials an technical data

- Led light with regulation of brightness and emission band; Top-light with intensity 300 W/m² (white 225 W/m², red 75 W/m²). Light period is equal to Earth light period (16 hours day and 8 hours night).
- Opaque coating provides isolation from sunlight.
- Supporting of the predetermined temperature 18±10 °C.
- Humidity sensors, 4 humidity probes during the day.
- CO₂ quantity control (2 probes per minute).
- Fan with guard group for gases convection providing inside the block.

- Camera with possibility of monitoring in IR spectrum, taking of pictures from one and more pictures per day.
- Block dimensions are less than 80x80x160 mm, it weight less than 2 kg.

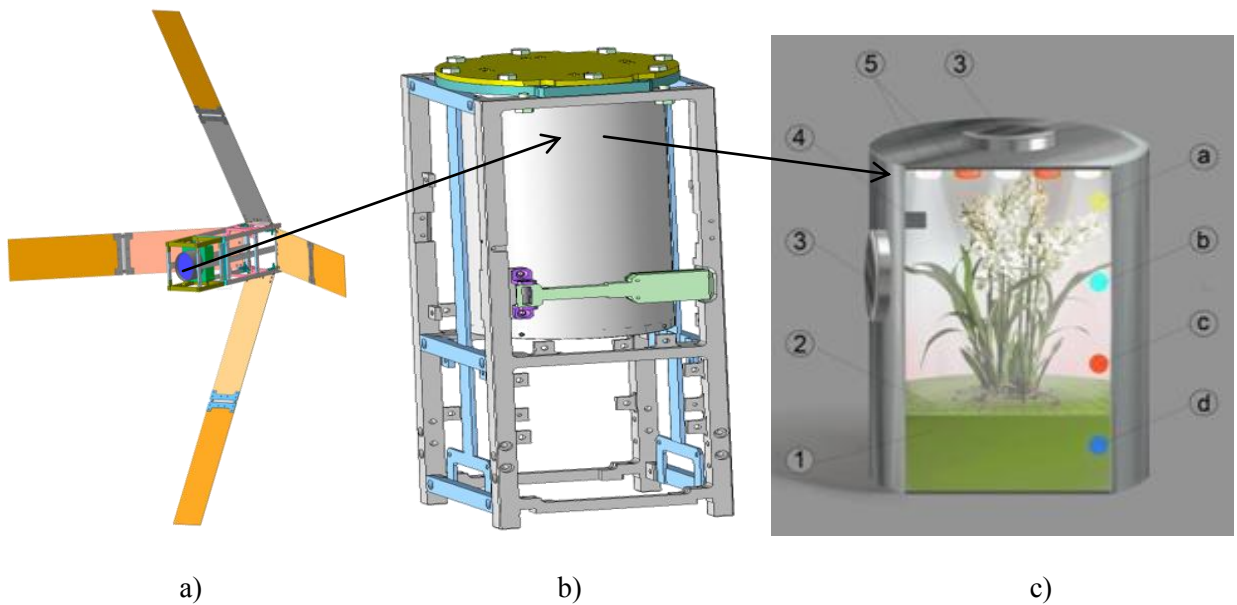


Fig. 8. General view “PolyITAN-4-BIO” (a); Placing of hermoblock in the case of “PolyITAN-4-BIO” (b); Hermoblock composition (c) include plant’s life support systems: 1 – fibrous substrate, 2 – holding mesh for the substrate, 3 – NIR-camera (to monitor the state of the plant) 4 – fan with protection, 5 – LED light; and the environmental monitoring system inside the unit: a – light sensor, b – CO₂ sensor, c – temperature sensor, d – substrate humidity sensor.

Expected results: selection the optimal plant composition with the best growth characteristics and the value of the minimum-sufficient level of water with the mineral component for plant nutrition.

SUMMARY AND CONCLUSIONS

Aerospace technology and manufacturing techniques were used in the design and manufacturing of nanosatellites series “PolyITAN”. Architecture of “PolyITAN” nanosatellite allowed to avoid problems that occur with a reduction in scale structures of satellite systems for their use in small and nano-satellites. This was made possible thanks to realization of the key differences between large satellites and satellites CubeSat, the development of new sub-systems and systems specially designed for use in CubeSat format nanosatellites.

“PolyITAN” nanosatellites provides high-performance electronic platform for testing new materials in space, carrying out scientific experiments and testing of technologies.

Benefits of “PolyITAN” Platform:

- High precision positioning using GPS + GLONASS (Galileo optional).
- The cost of mass production is lower by 40-60% than in the US and European counterparts.
- The presence of a complete set of satellite system at University (satellite into orbit and ground station).
- Start services, support and maintenance.
- The possibility of supply of separate components and subsystems.
- Scalable platform in accordance with the Cubesat standard.
- Using for a wide range of applications (radio communication, Earth sensing, scientific experiments, etc.).
- Use of carbon fiber honeycombs for heat control and radiation protection.
- The full nano-satellite development cycle

Analysis of the functional characteristics of “PolyITAN-1” subsystems and test of the impact of external damaging factors are still going on in the orbit. However, all tests up to this day have been successful and the results are compared with the design.

ACKNOWLEDGEMENTS

This work was supported by participants and sponsors of the project “PolyITAN-2-SAU”: Academician Mikhalevich Foundation, Kalinin Foundation (Ukraine), Boeing-Ukraine Ltd.

REFERENCES

1. B.M. Rassamakin, N.F. Baiskov, S.A. Ostapchuk, S. M. Khairnasov, A.S.Menzhega, A.B. Rassamakin, N.A. Pershin, D.S. Smakovsky: Development and research of subsystems of NTU “KPI” “POLYITAN-1” nano-satellite with carbon-fiber honeycomb // 12-a Ukrainska konferentsiya z kosmichnih doslidzhen, Eupatoriya, October 3-7, 2012. – p. 109 (in Russian).
2. A.G. Laush, B.M. Rassamakin, N.F. Baiskov, S.V. Ostapchuk: Testing of orbital flight parameters of nano-satellite using GNSS simulator // 13-aUkrainskakonferentsiya z kosmichnihdoslidzhen, Eupatoriya, October 2-6, 2013. – p. 127 (in Ukrainian).
3. B.M. Rassamakin, N.F. Baiskov, S.A. Ostapchuk, S. M. Khairnasov, O.V. Budonny, A.B. Rassamakin, A.S. Menzhega, N.A. Pershin, R.V. Antipenko, E. J. Kovalenko, D.S. Smakovsky, S.E. Martenyuk, V.I. Khominich: University nano-satellite POLYITAN-1 // 14-a Ukrainskakonferentsiya z kosmichnihdoslidzhen, Uzhgorod, October 8-12, 2014. – p. 24 (in Russian).
4. B. Rassamakin: The First Ukrainian Nanosatellite – PolyItan-1: Development, Simulation, Flight Tests // 5-th International Space Conference SEMW 2014, 21-23 October 2014. – p. 26.
5. B.M. Rassamakin, N.F. Baiskov, S.A. Ostapchuk, S.M. Khairnasov, A.B. Rassamakin, A.S. Menzhega, N.A. Pershin, R.V. Antipenko, E.Y. Kovalenko, D.S. Smakovsky, S.E. Martenyuk, V.I. Khominich, M.G. Dusheyko: University nano-satellite POLYITAN-1: Results of flight tests // 15-a Ukrainska konferentsiya z kosmichnih doslidzhen, Odessa, August 24-28, 2015. – p. 45 (in Russian).
6. E.Y. Kovalenko, B.M. Rassamakin, N.F. Baiskov: Electrical power system of POLYTAN series CUBESAT nanosats. // 7th European CubeSat Symposium, 9 - 11 September 2015, Liège, Belgium, – p. 29.
7. B.M. Rassamakin, N.F. Baiskov, S.W. Ostapchuk, A.V. Pinchuk, E.U. Kovalenko, E.V. Lanevsky, S. M. Khairnasov, A. B. Rassamakin, V. I. Khominich, N. M. Bendasiuk, “Engineering model of POLYITAN-2-SAU nano-satellite for the study of the atmosphere at altitudes of 380-90 km”, 15th Ukrainska konferencia z kosmichnih doslidgen, 24 – 28 August, 2015, Odessa.
8. B.M. Rassamakin, V.A. Rogachiv, S.M. Khairnasov, E.S. Zavadskaja and V.I. Khominich, “Experimental simulation of nanosatellites heat modes”. Tekhnologiya i Konstruirovanie v Elektronnoi Apparature, 2013, no. 4, – pp. 27-30. (in Russian).
9. L. V. Kozlov, M. D. Nusinov, A. I. Akishin et al. “Modelling of the thermal modes of the spacecraft an its environment”, Modelirovanie teplovykh rezhimov kosmicheskogo apparata i okruzhayushchei ego sredy. Moskow, Mashinostroenie, 1971. (in Russian).
10. A.S. Tsybenko Stress-Strain State Investigation of Polyitan-2 Nano-Satellite under the Ascent-Stage Quasi-Static Overload Conditions / A.S. Tsybenko, B.M. Rassamakin, A.A. Rybalka. // Strength of Materials. – 2017. – no. 49. – pp. 381–387.

TABLE OF CONTENTS

METHODS OF FORMATION, DIAGNOSIS AND RESEARCH OF NANOSTRUCTURES	
Yu.T. Zholudov, V.S. Vasytkovskyi, M.I. Slipchenko, O.V. Slipchenko, B.N. Chichkov FORMATION OF SEMICONDUCTOR QUANTUM DOTS FOR ELECTROCHEMILUMINESCENT ASSAY BY LASER FRAGMENTATION	6
V.A. Smyntyna, V.M. Skobeeva, K.A. Verheles, N.V. Malushin TECHNOLOGICAL FEATURES FORMATION SPECTRA OF LUMINESCENCE CdS QD	11
V.P. Kostylyov, A.V. Sachenko, V.M. Vlasiuk, S.D. Kobylanska, P.V. Torchyniuk SYNTHESIS AND CHARACTERIZATION OF ORGANIC-INORGANIC PEROVSKITE WITH NON-CONTACT METHODS	16
R.M. Korkishko, V.M. Vlasyuk, B.F. Dvernikov, V.V. Chernenko and V.P. Kostylyov MOBILE COMBINED PHOTOVOLTAIC / WIND POWER STATION FOR POWER SUPPLY OF ELECTRONIC EQUIPMENT IN THE FIELD CONDITIONS	20
R.M. Korkishko, V.M. Vlasyuk, V.V. Chernenko, O.A. Serba and V.P. Kostylyov PHOTOELECTRIC CHARACTERISTICS OF DIFFUSION-FIELD SILICON SOLAR CELLS AT HIGH EXCITATION LEVELS	24
O.V. Kovalenko, V.Y. Vorovsky, M.F. Bulaniy, O.V. Khmelenko, O.I. Kushnerov LOW-TEMPERATURE FREEZE-DRYING METHOD FOR THE SYNTHESIS OF ZnO:Mn NANOKRYSTALS	28
A.P. Bukivskii, I.G. Vertegel, R.V. Gamernyk, Z.D. Kovalyuk and Yu.P. Gnatenko FORMATION OF NANOSTRUCTURAL PbI₂-PbMnI₂ COMPOSITE MATERIALS	32
I.P. Studenyak, O.V. Kovalchuk, S.I. Poberezhets, M. Timko, P. Kopčanský DIELECTRIC PROPERTIES AND ELECTRICAL CONDUCTIVITY OF 6CB LIQUID CRYSTAL WITH Cu₆PS₅Br SUPERIONIC NANOPARTICLES	35
Slipchenko N.I., Liu Chan, Borodkina A.N., Panchenko A.Yu. ESTIMATION OF THE RESOLVING ABILITY OF OPEN COAXIAL UHF SENSOR	39
I.N. Bondarenko, G.N. Bendeberya, E.A. Gorbenko LOCAL MICROWAVE HEATING	43
I.N. Bondarenko, Yu.Ye. Gordienko, A.S. Nechiporenko, A.Yu. Panchenko MICROWAVE LOCAL DIAGNOSTICS OF BIOOBJECTS	47
Tyurin A.V., Bekshaev A.Ya., Zhukov S.A. LUMINESCENCE STUDIES OF THE DYE SELF-DESENSITIZATION PROCESSES OF TYPE II	51

I.M. Shcherban, Yu.Ye. Gordienko	55
FEATURES OF THE USE OF MICROWAVE MICROSCOPY IN NANO-ELECTRONICS TECHNOLOGY	
NANO-ELECTRONIC SENSORS AND INFORMATION SYSTEMS. NANO-ELECTRONIC SENSORS FOR BIO-ENGINEERING	
V.N. Borshchov, N.I. Slipchenko, O.M. Listratenko, O.V. Kravchenko, O.V. Syddia	60
NEW APPROACHES TO CREATION OF HIGH-EFFICIENCY RECEIVERS OF SOLAR RADIATION FOR CONCENTRATOR SOLAR MODULES	
Lepikh Ya.I., Borshchak V.A., Lavrenova T.I., Zatovskaya N.P., Balaban A.P.	66
NANOCOMPOSITES BASED ON RUTHENIUM SEMICONDUCTOR COMPOUNDS FOR GIC ELEMENTS AND SENSORS	
Kukla O.L., Mamykin A.V., Pud A.A., Ogurtsov N.A., Noskov Yu.V., Mikhaylov S.D.	70
NANOSTRUCTURED ELECTROCONDUCTIVE COMPOSITE MATERIALS FOR DETECTING PHOSPHORUS AND CHLOROROGANIC SUBSTANCES	
V.P. Karnaushenko, A.V. Borodin, Y.S. Vasylyev, M.I. Piataikina.	74
INTEGRATION OF HARD BLOCKS INTO FPGA NANOSTRUCTURE	
S. N. Osinov, V. F. Zavorotnyi, B. I. Lupyna, O. V. Borisov	79
Thermoresistive Transducers Used Heat Exchange Technology	
PHYSICS AND THEORY OF NANOSTRUCTURES FOR ELECTRONICS	
Yu. M. Penkin, V. A. Katrich, M. V. Nesterenko, S. L. Berdnik	85
EVALUATION OF EFFECTIVE PERMITTIVITY OF QUARTZ NANOCOMPOSITES WITH FULLERENE INCLUSIONS	
V.G. Udovitskiy, M.I. Slipchenko, O.Yu. Kropotov, P.V. Turbin, B.M. Chichkov, O.V. Slipchenko	89
MORPHOLOGY AND MICROSTRUCTURE OF CATHODE DEPOSIT OBTAINED AT PLASMA-ARC SYNTHESIS OF CARBON NANOTUBES	
Yu.A. Vronska, S.M. Zakharov, I.O. Shmatko, O.A. Shmatko, S.M. Kedrovskiy	95
GENERAL KINETICS OF Pb-Sn SOLID SOLUTIONS CELLULAR PRECIPITATION	
O.V. Filatov ^{1,2} , O.M. Soldatenko ² , S.M. Soldatenko ²	99
SIZE INFLUENCE OF SILVER NANOPARTICLES ON THE COEFFICIENT OF Ag LINEAR THERMAL EXPANSION	
V. V. Vainberg, V. N. Poroshin, A.S. Pylypchuk, N.A. Tripachko, I.I. Yaskovets	102
HOPPING CONDUCTION AND MAGNETORESISTANCE IN THE SINGLE-WALL CARBON NANOTUBES BUNDLES WITH RADIATION INDUCED DEFECTS	

Kolosiuk A.G., Rudenko R.M., Voitsikhovska O.O., Voitovych V.V., Krasko M.M., Povarchuk V.Yu. FORMATION FEATURES OF SILICON NANOCRYSTALS IN TIN-DOPED AMORPHOUS SILICON FILMS	106
Gritsunov A. V., Bondarenko I. N., Galat A. B., Glukhov O. V., Pashchenko A. G. ON THE QUANTUM ELECTRODYNAMICS OF NANOSYSTEMS	109
N.I. Pavlishche, A.V. Korotun THE VAN DER WAALS INTERACTION BETWEEN THE METALLIC NANOTUBES	114
Ya.V. Karandas, A.V. Korotun, I.M. Titov THE POLARIZABILITY OF THE METALLIC NANOCYLINDER, WHICH IS COVERED BY THE OXIDE LAYER	118
O.Yu. Babychenko, A.V. Borodin RESEARCH OF ANOMALOUS PHOTOCONDUCTIVITY OF CRYSTAL SILICON WITH AMORPHOUS INCLUSIONS	122
NANOPHOTONICS. PROCESSES, STRUCTURES AND DEVICES	
Ghazi Khaled, A.V Kukoba, O.M. Bilash, K.M. Muzyka NANOPHOTONIC SOLID PHASE TRANSDUCER FOR HETEROGENEOUS DETECTION OF 5,6,11,12-TETRAPHENYLTETRACENE	126
A.E. Pogorelov, Y.A. Pogoryelov RISK FACTORS IN THE PULSED BEAM TECHNOLOGIES FOR THE ELECTRONIC CIRCUITS PRODUCTION	129
O.V. Ohiienko, V.N. Moiseienko, D.O. Golochalov and Bilal Abu Sal PHOTOLUMINESCENCE OF THE MATRIX NANOCOMPOSITES OPAL – ACTIVE DIELECTRIC FILLED WITH EUROPIUM	133
Kurskoy Yu. S. USAGE OF THE NONLINEAR METROLOGY INSTRUMENTS FOR RESEARCH THE LASER COOLING PROCESS	137
N.N. Chernyshov, A.V. Belousov*, I.A. Chernyshova, M.A.F. Alkhawaldeh RESEARCHING OF SPIN-EFFECTS IN SEMICONDUCTORS WITHOUT AN INVERSION CENTER FOR PHOTOELECTRIC ENERGY CONVERSION	141
SPECIFIC DIRECTIONS IN NANOELECTRONICS AND MODELING	
A.V. Sachenko, V.P. Kostylyov, V.M. Vlasyuk, R.M. Korkishko, I.O. Sokolovskyi, M. Evstigneev MODELING OF THE KEY CHARACTERISTICS ALL BACK-CONTACT SILICON SOLAR CELLS	146

Mayboroda D.V., Pogarsky S.A., Pshenichnaya S.V., Anikeeva K.S., Smirnova K.O. OPTIMIZATION OF FREQUENCY AND ENERGY CHARACTERISTICS OF DISK MONOPOLE ANTENNA	150
A.L.Kasatkin, V.P. Tsvitkovsky, A.O.Pokusinskii HIGH-FREQUENCY ELECTRODYNAMICS OF NANOSTRUCTURED HIGH-T_c SUPERCONDUCTOR FILMS	153
Panchenko T.V., Karpova L.M. DIELECTRIC NONLINEARITY OF STRUCTURES Pt-Bi₁₂SiO₂₀:Ga-Pt	157
A.B. Galat, V.V. Bilous CALCULATING OF SOLAR CELL ABSORPTION EFFICIENCY AND ENERGY CHARACTERISTICS	160
B.Rassamakin, M.Ducheiko, N.Bayskov, S.Ostapchuk, A.Lauch, E.Lanevsky, V.Hominich, R.Melnyk, I.Starovit NANOSATELLITES OF THE POLYITAN SERIES: RESULTS OF EXPERIMENTS AND PROSPECTS FOR DEVELOPMENT	166

Collection of Scientific Works

X INTERNATIONAL SCIENTIFIC CONFERENCE

Functional Basis of Nanoelectronics

Responsible for the release of materials: Prof. Slipchenko M.I.

Collection materials are published in the author's version without editing

Signed to print 10.09.2019. Format 60x84/16. Paper offset. Garniture of TimesNew.
Cond. print. p. 20,0. Edition 100 copies. Order. № 0910/3-19.

Printed from original layout in Private owned enterprise FLP Petrov V. V.
State register of legal entities and physical persons-businessmen.
Record № 2480000000106167 from 08.01.2009.
Ukraine, 61144, Kharkov, str. Gvardeitsev Shironinzev, 79v, ap. 137,
tel. (057) 78-17-137. e-mail:bookfabrik@mail.ua